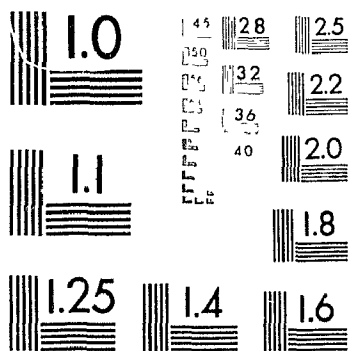


# 1

PM-1 3½"x4" PHOTOGRAPHIC MICROCOPY TARGET  
NBS 1010a ANSI/ISO #2 EQUIVALENT



PRECISION<sup>SM</sup> RESOLUTION TARGETS



National Library  
of Canada

Acquisitions and  
Bibliographic Services Branch

395 Wellington Street  
Ottawa, Ontario  
K1A 0N4

Bibliothèque nationale  
du Canada

Direction des acquisitions et  
des services bibliographiques

395, rue Wellington  
Ottawa (Ontario)  
K1A 0N4

*Your file* *Votre référence*

*Our file* *Notre référence*

## NOTICE

The quality of this microform is heavily dependent upon the quality of the original thesis submitted for microfilming. Every effort has been made to ensure the highest quality of reproduction possible.

If pages are missing, contact the university which granted the degree.

Some pages may have indistinct print especially if the original pages were typed with a poor typewriter ribbon or if the university sent us an inferior photocopy.

Reproduction in full or in part of this microform is governed by the Canadian Copyright Act, R.S.C. 1970, c. C-30, and subsequent amendments.

## AVIS

La qualité de cette microforme dépend grandement de la qualité de la thèse soumise au microfilmage. Nous avons tout fait pour assurer une qualité supérieure de reproduction.

S'il manque des pages, veuillez communiquer avec l'université qui a conféré le grade.

La qualité d'impression de certaines pages peut laisser à désirer, surtout si les pages originales ont été dactylographiées à l'aide d'un ruban usé ou si l'université nous a fait parvenir une photocopie de qualité inférieure.

La reproduction, même partielle, de cette microforme est soumise à la Loi canadienne sur le droit d'auteur, SRC 1970, c. C-30, et ses amendements subséquents.

**Seismic Nature of Middle Continental Crust:  
Comparison of Laboratory Velocity and LITHOPROBE  
Seismic Reflection and Refraction Data from the Britt Domain,  
Southwestern Grenville Province, Canada**

By

Changxing Long

Submitted in Partial Fulfillment of the Requirements for  
the Degree of Doctor of Philosophy

at

Dalhousie University  
Halifax, Nova Scotia  
May, 1994

© Copyright by Changxing Long, 1994



National Library  
of Canada

Acquisitions and  
Bibliographic Services Branch

395 Wellington Street  
Ottawa, Ontario  
K1A 0N4

Bibliothèque nationale  
du Canada

Direction des acquisitions et  
des services bibliographiques

395, rue Wellington  
Ottawa (Ontario)  
K1A 0N4

*Your file* *Votre référence*

*Our file* *Notre référence*

THE AUTHOR HAS GRANTED AN IRREVOCABLE NON-EXCLUSIVE LICENCE ALLOWING THE NATIONAL LIBRARY OF CANADA TO REPRODUCE, LOAN, DISTRIBUTE OR SELL COPIES OF HIS/HER THESIS BY ANY MEANS AND IN ANY FORM OR FORMAT, MAKING THIS THESIS AVAILABLE TO INTERESTED PERSONS.

L'AUTEUR A ACCORDE UNE LICENCE IRREVOCABLE ET NON EXCLUSIVE PERMETTANT A LA BIBLIOTHEQUE NATIONALE DU CANADA DE REPRODUIRE, PRETER, DISTRIBUER OU VENDRE DES COPIES DE SA THESE DE QUELQUE MANIERE ET SOUS QUELQUE FORME QUE CE SOIT POUR METTRE DES EXEMPLAIRES DE CETTE THESE A LA DISPOSITION DES PERSONNE INTERESSEES.

THE AUTHOR RETAINS OWNERSHIP OF THE COPYRIGHT IN HIS/HER THESIS. NEITHER THE THESIS NOR SUBSTANTIAL EXTRACTS FROM IT MAY BE PRINTED OR OTHERWISE REPRODUCED WITHOUT HIS/HER PERMISSION.

L'AUTEUR CONSERVE LA PROPRIETE DU DROIT D'AUTEUR QUI PROTEGE SA THESE. NI LA THESE NI DES EXTRAITS SUBSTANTIELS DE CELLE-CI NE DOIVENT ETRE IMPRIMES OU AUTREMENT REPRODUITS SANS SON AUTORISATION.

ISBN 0-612-05165-X

Name \_\_\_\_\_

Dissertation Abstracts International is arranged by broad, general subject categories. Please select the one subject which most nearly describes the content of your dissertation. Enter the corresponding four digit code in the spaces provided

--	--	--	--

U·M·I

SUBJECT TERM

SUBJECT CODE

**Subject Categories**

**THE HUMANITIES AND SOCIAL SCIENCES**

**COMMUNICATIONS AND THE ARTS**

Architecture 0729  
 Art History 0377  
 Cinema 0900  
 Dance 0378  
 Fine Arts 0357  
 Information Science 0723  
 Journalism 0391  
 Library Science 0399  
 Mass Communications 0708  
 Music 0413  
 Speech Communication 0459  
 Theater 0465

**EDUCATION**

General 0515  
 Administration 0514  
 Adult and Continuing 0516  
 Agricultural 0517  
 Art 0273  
 Bilingual and Multicultural 0282  
 Business 0688  
 Community College 0275  
 Curriculum and Instruction 0727  
 Early Childhood 0518  
 Elementary 0524  
 Finance 0277  
 Guidance and Counseling 0519  
 Health 0680  
 Higher 0745  
 History of 0520  
 Home Economics 0278  
 Industrial 0521  
 Language and Literature 0279  
 Mathematics 0280  
 Music 0522  
 Philosophy of 0998  
 Physical 0523

Psychology 0525  
 Reading 0535  
 Religious 0527  
 Sciences 0714  
 Secondary 0533  
 Social Sciences 0534  
 Sociology of 0340  
 Special 0529  
 Teacher Training 0530  
 Technology 0710  
 Tests and Measurements 0288  
 Vocational 0747

**LANGUAGE, LITERATURE AND LINGUISTICS**

Language  
 General 0679  
 Ancient 0289  
 Linguistics 0290  
 Modern 0291  
 Literature  
 General 0401  
 Classical 0294  
 Comparative 0295  
 Medieval 0297  
 Modern 0298  
 African 0316  
 American 0591  
 Asian 0305  
 Canadian (English) 0352  
 Canadian (French) 0355  
 English 0593  
 Germanic 0311  
 Latin American 0312  
 Middle Eastern 0315  
 Romance 0313  
 Slavic and East European 0314

**PHILOSOPHY, RELIGION AND THEOLOGY**

Philosophy 0422  
 Religion  
 General 0318  
 Biblical Studies 0321  
 Clergy 0319  
 History of 0320  
 Philosophy of 0322  
 Theology 0469

**SOCIAL SCIENCES**

American Studies 0323  
 Anthropology  
 Archaeology 0324  
 Cultural 0326  
 Physical 0327  
 Business Administration  
 General 0310  
 Accounting 0272  
 Banking 0770  
 Management 0454  
 Marketing 0338  
 Canadian Studies 0385  
 Economics  
 General 0501  
 Agricultural 0503  
 Commerce Business 0505  
 Finance 0508  
 History 0509  
 Labor 0510  
 Theory 0511  
 Folklore 0358  
 Geography 0366  
 Gerontology 0351  
 History  
 General 0578

Ancient 0579  
 Medieval 0581  
 Modern 0582  
 Black 0328  
 African 0331  
 Asia Australia and Oceania 0332  
 Canadian 0334  
 European 0335  
 Latin American 0336  
 Middle Eastern 0333  
 United States 0337  
 History of Science 0585  
 Law 0398  
 Political Science  
 General 0615  
 International Law and Relations 0616  
 Public Administration 0617  
 Recreation 0814  
 Social Work 0452  
 Sociology  
 General 0626  
 Criminology and Penology 0627  
 Demography 0938  
 Ethnic and Racial Studies 0631  
 Individual and Family Studies 0628  
 Industrial and Labor Relations 0629  
 Public and Social Welfare 0630  
 Social Structure and Development 0700  
 Theory and Methods 0344  
 Transportation 0709  
 Urban and Regional Planning 0999  
 Women's Studies 0453

**THE SCIENCES AND ENGINEERING**

**BIOLOGICAL SCIENCES**

Agriculture  
 General 0473  
 Agronomy 0285  
 Animal Culture and Nutrition 0475  
 Animal Pathology 0476  
 Food Science and Technology 0359  
 Forestry and Wildlife 0478  
 Plant Culture 0479  
 Plant Pathology 0480  
 Plant Physiology 0817  
 Range Management 0777  
 Wood Technology 0746  
 Biology  
 General 0306  
 Anatomy 0287  
 Biostatistics 0308  
 Botany 0309  
 Cell 0379  
 Ecology 0329  
 Entomology 0353  
 Genetics 0369  
 Limnology 0793  
 Microbiology 0410  
 Molecular 0307  
 Neuroscience 0317  
 Oceanography 0416  
 Physiology 0433  
 Radiation 0821  
 Veterinary Science 0778  
 Zoology 0472  
 Biophysics  
 General 0786  
 Medical 0760

Genesys 0370  
 Geology 0372  
 Geophysics 0373  
 Hydrology 0388  
 Mineralogy 0411  
 Paleobotany 0345  
 Paleocology 0426  
 Paleontology 0418  
 Paleozoology 0985  
 Palynology 0427  
 Physical Geography 0368  
 Physical Oceanography 0415

**HEALTH AND ENVIRONMENTAL SCIENCES**

Environmental Sciences 0768  
 Health Sciences  
 General 0566  
 Audiology 0300  
 Chemotherapy 0992  
 Dentistry 0567  
 Education 0350  
 Hospital Management 0769  
 Human Development 0758  
 Immunology 0982  
 Medicine and Surgery 0564  
 Mental Health 0347  
 Nursing 0569  
 Nutrition 0570  
 Obstetrics and Gynecology 0380  
 Occupational Health and Therapy 0354  
 Ophthalmology 0381  
 Pathology 0571  
 Pharmacology 0419  
 Pharmacy 0572  
 Physical Therapy 0382  
 Public Health 0573  
 Radiology 0574  
 Recreation 0575

Speech Pathology 0460  
 Toxicology 0383  
 Home Economics 0386

**PHYSICAL SCIENCES**

**Pure Sciences**  
 Chemistry  
 General 0485  
 Agricultural 0749  
 Analytical 0486  
 Biochemistry 0487  
 Inorganic 0488  
 Nuclear 0738  
 Organic 0490  
 Pharmaceutical 0491  
 Physical 0494  
 Polymer 0495  
 Radiation 0754  
 Mathematics 0405  
 Physics  
 General 0605  
 Acoustics 0986  
 Astronomy and Astrophysics 0606  
 Atmospheric Science 0608  
 Atomic 0748  
 Electronics and Electricity 0607  
 Elementary Particles and High Energy 0798  
 Fluid and Plasma 0759  
 Molecular 0609  
 Nuclear 0610  
 Optics 0752  
 Radiation 0756  
 Solid State 0611  
 Statistics 0463

**Applied Sciences**  
 Applied Mechanics 0346  
 Computer Science 0984

Engineering  
 General 0537  
 Aerospace 0538  
 Agricultural 0539  
 Automotive 0540  
 Biomedical 0541  
 Chemical 0542  
 Civil 0543  
 Electronics and Electrical 0544  
 Heat and Thermodynamics 0348  
 Hydraulic 0545  
 Industrial 0546  
 Marine 0547  
 Materials Science 0794  
 Mechanical 0548  
 Metallurgy 0743  
 Mining 0551  
 Nuclear 0552  
 Packaging 0549  
 Petroleum 0765  
 Sanitary and Municipal System Science 0790  
 Geotechnology 0428  
 Operations Research 0796  
 Plastics Technology 0795  
 Textile Technology 0994

**PSYCHOLOGY**

General 0621  
 Behavioral 0384  
 Clinical 0622  
 Developmental 0620  
 Experimental 0623  
 Industrial 0624  
 Personality 0625  
 Physiological 0989  
 Psychobiology 0349  
 Psychometrics 0632  
 Social 0451

**EARTH SCIENCES**

Biogeochemistry 0425  
 Geochemistry 0996



DALHOUSIE UNIVERSITY

FACULTY OF GRADUATE STUDIES

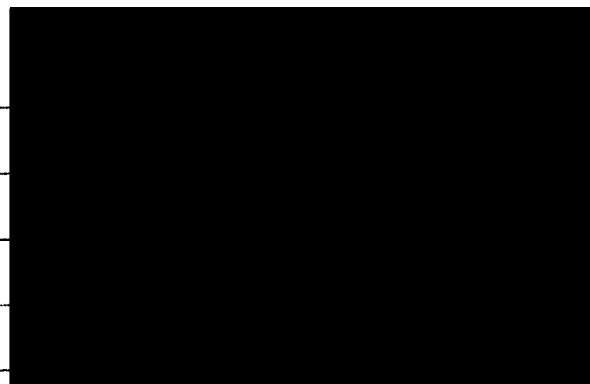
The undersigned hereby certify that they have read and recommend to the Faculty of Graduate Studies for acceptance a thesis entitled "Seismic Nature of Middle Continental Crust: Comparison of Laboratory Velocity and LITHOPROBE Seismic Reflection and Refraction Data from the Britt Domain Southwestern Grenville Province, Canada"

by CHANGXING LONG

in partial fulfillment of the requirements for the degree of Doctor of Philosophy.

Dated March 30, 1994

External Examiner \_\_\_\_\_  
Research Supervisor \_\_\_\_\_  
Examining Committee \_\_\_\_\_



D A L H O U S I E U N I V E R S I T Y

DATE: April 28, 1994

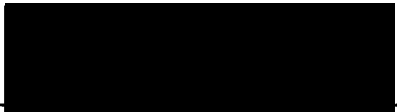
AUTHOR: Changxing Long

TITLE: Seismic Nature of Middle Continental Crust:  
Comparison of Laboratory Velocity and LITHOPROBE  
Seismic Reflection and Refraction Data from the  
Britt Domain, Southwestern Grenville Province, Canada

DEPARTMENT OR SCHOOL: Earth Sciences Department

DEGREE: Ph.D CONVOCATION: Autumn YEAR: 1994

Permission is herewith granted to Dalhousie University to circulate and to have copied for non-commercial purposes, at its discretion, the above title upon the request of individuals or institutions.



Signature of Author

THE AUTHOR RESERVES OTHER PUBLICATION RIGHT, AND NEITHER THE THESIS NOR EXTENSIVE EXTRACTS FROM IT MAY BE PRINTED OR OTHERWISE REPRODUCED WITHOUT THE AUTHOR'S WRITTEN PERMISSION.

THE AUTHOR ATTESTS THAT PERMISSION HAS BEEN OBTAINED FOR THE USE OF ANY COPYRIGHTED MATERIAL APPEARING IN THIS THESIS (OTHER THAN BRIEF EXCERPTS REQUIRING ONLY PROPER ACKNOWLEDGMENT IN SCHOLARLY WRITING) AND THAT ALL SUCH USE IS CLEARLY ACKNOWLEDGED.

## Table of Contents

Table of Contents	iv
List of Figures	vii
List of Tables	ix
Abstract	x
Acknowledgements	xi
<b>Chapter 1. INTRODUCTION</b>	<b>1</b>
Seismic Studies of Continental Crust	1
Objectives of This Study	3
Outline of the Following Chapters	5
<b>Chapter 2. GEOLOGICAL AND GEOPHYSICAL BACKGROUND</b>	<b>7</b>
Regional Geologic Setting	7
Geology of the Britt Domain	15
Gneiss Associations	17
Key Harbour Gneiss Association	18
Bayfield Gneiss Association	19
Nadeau Island Gneiss Association	20
Ojibway Gneiss Association	21
Sand Bay Gneiss Association	21
Monocyclic Granodiorite and Related Plutonic Rocks	22
Mafic Intrusions and Anorthosite	23
Structural Geology	25
Summary of Geologic Events	27
Previous Geophysical Studies	28
1982 COCRUST Experiment	33
GLIMPCE Profile J	35
LITHOPROBE Lines 30 and 31	40
The Unresolved Problems	43
<b>Chapter 3. LABORATORY VELOCITY MEASUREMENTS</b>	<b>44</b>
Sample Descriptions	44
Granitic - Intermediate Orthogneiss	48
Paragneiss	50
Mafic and Ultramafic Rocks	50
Experimental Methods	52
Specimen Preparation	53
Velocity Measurements	55



Experimental Results	59
Velocity - Pressure Relationships	68
Compressional Wave Velocity - Density Relationships	70
Poisson's Ratio	75
Seismic Anisotropy and Shear Wave Splitting	78
Average Properties of the Britt Domain	92
<b>Chapter 4.    REFRACTION EXPERIMENT AND COMPARISON                     WITH LABORATORY DATA</b>	<b>95</b>
1992 LITHOPROBE Abitibi-Grenville Refraction Experiments	95
Data Acquisition	96
Data Processing	99
Data Interpretation	100
Travel Time Fit	100
Error Analysis of Travel Time Fit	131
Synthetic Amplitude Analysis	133
Interpretation of the Resultant Model	139
Comparison of In-situ and Laboratory Data	142
3 - 15 km Depth Zone	145
15 km - Moho	146
0 - 3 km Depth Zone	147
Velocity Anisotropy of the GFTZ	151
<b>Chapter 5.    SYNTHETIC REFLECTION MODELLING</b>	<b>153</b>
Reflectivity of Thin Mafic Layers	155
Thin Bed Resolution	155
Model Construction and Modelling Techniques	156
Modelling Results	159
Reflection Patterns Due to Lithologic Variation	162
Modelling Technique	162
Folded Structures	164
Hypothetical Models for the Britt Domain	172
Model Construction	172
Synthetic Sections	179
Discussion	188
Wide-angle Reflection Character of Folded Structures	188
Problem	188
Modelling Technique	189
Results	191
<b>Chapter 6.    CONCLUSIONS</b>	<b>194</b>
Laboratory Seismic Properties of Britt Domain Rocks	194
Granitic Gneisses	196
Granodiorite Gneisses	196
Diorite Gneisses	197

Paragneisses	197
Mafic Rocks	198
Other Lithologies	198
Summary	199
Results from Abitibi-Grenville Refraction Experiment.	200
Synthetic Reflection Modelling and Data Interpretation	203
Reflectivity	203
Thin Mafic Layers	203
Larger Scale Lithologic Contacts	204
Reflection Patterns	205
'Shingles' on Profile J	205
Discussion on the Nature of Seismic reflectivity in the Continental Crust	207
Appendix I. Refraction Sections along Line AB	210
Appendix II. Reflectivity of Regularly Spaced Thin Layers	218
Appendix III. Detailed Distribution of Mafic Layers along Key River	221
References	228

## List of Figures

2.1	Geological Map of the Southwestern Grenville Province	8
2.2	Subdivision of the Central Gneiss Belt	11
2.3	Geological Map of the Britt Domain	16
2.4	Vertical Magnetic Gradient Map of Georgian Bay Area	30
2.5	Bouguer Gravity Map of Georgian Bay Area	31
2.6	Location Map of Previous Seismic Lines	32
2.7	Crustal Velocity Models along COCRUST Refraction Lines	34
2.8	Profile J Reflection Section	36
2.9	Profile J Refraction Section	37
2.10	Velocity Model of Profile J	39
2.11	LITHOPROBE Line 30 Reflection section	41
2.12	Gravity Profile and Reflection Section across Parry Sound Domain	42
3.1	Location Map Showing Sample Sites	45
3.2	Ternary Diagram for Orthogneiss Samples	49
3.3	Core Orientation Convention	54
3.4	Sample Assembly	56
3.5	Velocity-Pressure Plot for Sample B-43	58
3.6	Velocity-Density Plot for Britt Samples	71
3.7	Velocity-Density Diagram for Lithologic Groups	73
3.8	Velocity-Density Plot for Mafic Samples	76
3.9	Schematic Diagram Showing V <sub>p</sub> -V <sub>s</sub> Fields of Britt Lithology	77
3.10	V <sub>p</sub> Anisotropy-Pressure Plot for Sample B-43	81
3.11	V <sub>p</sub> Anisotropy-Modal Biotite-Biotite Alignment Plot for Paragneiss Samples	85
3.12	Preferred Orientation of Biotite for Sample B-22	86
3.13	V <sub>p</sub> Anisotropy-Modal Hornblende Plot for Mafic Rocks	89
4.1	Location Map for the 1992 Abitibi-Grenville Refraction Experiment	97
4.2	Seismic Sections (V <sub>p</sub> ) Recorded along Line AB and Associated Ray Diagrams	101
4.3	Selected Seismic Sections (V <sub>s</sub> ) along Line AB	122
4.4	Velocity Model for Refraction Line AB	127
4.5	Residual Time plot for the Britt Domain	132
4.6	Residual Time Plot for the Dip of the Grenville Front Tectonic Zone	132
4.7	Residual Time Plot for Layer 3	134
4.8	Synthetic Refraction Profiles for Selected Shot Points	135
4.9	Velocity-Depth Plot for Britt Domain	143
4.10	Temperature-Corrected V <sub>p</sub> -Depth Plot	144
4.11	Velocity-Pressure Plot for Saturated Sample B-44	148
5.1	Mafic Dike Distribution along Key River	158
5.2	Synthetic Seismogram for Thin Mafic Layers	160

5.3	Blue-up of GLIMPCE Line J over Britt Domain	163
5.4	Synthetic Reflection Model for a Simple Folded Boundary	165
5.5	Synthetic Sections fir Model with Simple Folded Boundary	166
5.6	Synthetic Reflection Model for Second Order Folds	168
5.7	Unmigrated Synthetic Reflection Section for Model with Second Order Folds	169
5.8	FK-Migrated Synthetic Reflection Section	170
5.9	Synthetic Reflection Sections	171
5.10	Synthetic Model for Pods of Gabbro	173
5.11	Synthetic Sections for Model with Gabbro Pods	174
5.12	Locations of Reflection Models	175
5.13	Hypothetical Model for Southern Britt Domain	176
5.14	Hypothetical Model for Northern Britt Domain	177
5.15	Unmigrated Synthetic Reflection Section for Southern Britt Model	180
5.16	Unmigrated Synthetic Reflection Section for Northern Britt Model	181
5.17	FK-Migrated Synthetic Reflection Section for Southern Britt Model	182
5.18	FK-Migrated Synthetic Reflection Section for Northern Britt Model	183
5.19	Northern Britt Model with No Second Order Folds	185
5.20	Unmigrated Section for Northern Britt Model with No Second Order Folds	185
5.21	FK-Migrated Section for Northern Britt Model with No Second Order Folds	187
5.22	Wide-Angle Reflection Model for Folded Structures	190
5.23	Wide-Angle Reflection Section for Folded Structures	192
6.1	Average Velocity-Pressure Plot for Britt Domain	195
6.2	Schematic Diagram of Velocity Structure along Profile AB	201
6.3	Schematic Diagram of Velocity Structure along Profile J	206

## List of Tables

3.1	Mineralogy of Britt Samples	46
3.2	Compressional Wave Velocities of Britt Rocks	60
3.3	Shear Wave Velocities of Selected Britt Samples	67
3.4	Average Velocity Increases of Britt Lithologies from 20 - 200 MPa	69
3.5	Average Densities and Velocities of Britt Lithologic Groups	72
3.6	$V_p$ Anisotropy of Britt Samples	79
3.7	$V_s$ Anisotropy of Selected Britt Samples	80
3.8	Average $V_p$ Anisotropy of Britt Lithologic Groups	83
3.9	Contribution of Biotite to Anisotropy of Selected Paragneiss Samples	88
3.10	Shear Wave Splitting in Selected Samples	91
3.11	Average Properties of the Britt Domain	93
4.1	Depth and Charge Size of Shots along Line AB	98
4.2	Physical Properties of Individual Layers in the Model for Line AB	130
5.1	Laboratory-Derived Reflection Coefficients for Britt Domain Rocks	154

## Abstract

The Britt Domain in the southwestern Grenville Province of the Canadian Shield is believed to be a deep (ca. 30 km) exposure of high grade (upper amphibolite facies) mid crustal rocks of predominantly granitic and granodioritic composition. Vertical reflection data across the Britt Domain show a series of subhorizontal, discontinuous reflections and wide-angle records reveal a complex 'shingling pattern' of crustal arrivals. This work addresses the overall velocity structure of the middle crust exposed in the Britt domain and the origin of these reflections based on laboratory velocity measurements, in-situ seismic data and surface geology.

Laboratory studies of eighty velocity samples from the Britt Domain show that average (area-weighted mean) P- and S wave velocities at 600 MPa are 6.36 km/s and 3.67 km/s respectively, and the average velocity anisotropy is weak. Strong reflection coefficients occur between mafic rocks and granitic rocks and intermediate coefficients occur between diorite and other lithologies. Shear zones do not generate significant reflection coefficients because they occur within granitic gneisses and impedance contrasts are difficult to develop in this lithology.

In-situ refraction data (LITHOPROBE Abitibi-Grenville line AB) demonstrate a uniform velocity structure to a depth of 15 km in the central Britt Domain with a P-wave velocity of 6.15 km/s, an S-wave velocity of 3.55 km/s and linear vertical gradients at depth of 0.02 km/s/km and 0.01 km/s/km, respectively. Comparison of laboratory and refraction data suggests that the upper crust of the Britt Domain is granodioritic in composition. The lower crust beneath the Grenville Front Tectonic Zone in the central Britt Domain appears to be composed of diorite at the top but becomes increasingly mafic toward the Moho.

One and two-D seismic modelling shows that scattered bodies of mafic-intermediate gneiss within the host gneisses of granitic composition are the most likely causes of reflectivity in this area. Large scale folded structures are probably responsible for the 'shingles' revealed by wide angle reflection. These structures are not revealed on near vertical reflection records probably because rugosity (second order folds) of the boundaries and velocity heterogeneity above them break the reflectors into segments on the seismic section, and they could not be recovered by conventional interpretation routines. While strong lower crustal reflectivity in extensional terranes may be due to lithologic lamination, this study also suggests that such reflections in compressional settings may be produced by merged reflections from the peaks and troughs of deep seated folds.

## Acknowledgements

This work could not have been accomplished without help from a large number of people at different institutions, including Dalhousie University, the Memorial University of New Foundland, the Geological Survey of Canada, the Atlantic Geoscience Centre and the LITHOPROBE Seismic Processing Centre in Calgary. My utmost thanks, however, go to M. H. Salisbury, my research supervisor, for his advice during my years at Dalhousie.

I would also like to thank N. G. Culshaw who introduced me to the geology of the research area. The laboratory velocity measurements was greatly helped by R. Iuliucci. Gordon Brown milled my velocity samples and made my thin sections.

The refraction data could not have been acquired or used in this thesis without help from many people. I thank R. F. Mereu, who was in charge of the 1992 LITHOPROBE refraction experiment and allowed me to participate in the project, Isa Asudeh and Steve Parry, who provided help in data processing and Ian Reid for his expertise in data interpretation and for allowing me to access his programme.

The synthetic reflection data were generated at Memorial University and Dalhousie University. Many thanks go to Jeremy Hall at the Memorial University and Keith Loudon at Dalhousie and their working groups, who allowed me to use their computing facilities and gave me helpful advice and suggestions.

## Chapter 1

### INTRODUCTION

#### Seismic Studies of Continental Crust

In the past few decades, a large number of deep seismic reflection and refraction profiles have been carried out in the continental crust by several groups, including COCORP and the USGS in the United States, LITHOPROBE in Canada, DEKORP in Germany, BIRPS in Great Britain, ECORS in France and ACORP in Australia. Rapid growth of the deep reflection and refraction data base has greatly improved our knowledge of the seismic structure of continental crust, especially seismic velocities and reflectivity of the middle-lower crust. Although there is considerable diversity in the velocity-depth models for different tectonic settings, a recent compilation of 90 deep refraction profiles (Holbrook, et al., 1992) shows that: (1) in general, a three-layer crust, with velocities increasing with depth, is a useful model; in most tectonic environments, the middle and lower crust together comprise about 2/3 of the total crust, (2) mid-crustal velocities range for the most part, from 6.4-6.7 km/s and (3) the lower-crustal velocity distribution is bimodal, with values of 6.7-6.8 km/s and 7.1-7.3 km/s.

On the other hand, the most important contributions of crustal reflection studies in the last 15 years are the discovery of high reflectivity in the lower continental crust.



and the recognition of distinct reflectivity patterns in different tectonic regimes. Although deep seismic reflection coverage is still limited, some particularly distinctive reflection patterns can be correlated with specific tectonic settings (Mooney and Meissner, 1991). (1) Young extensional lower crust is usually strongly reflective with multiple subhorizontal sets of reflections which terminate at the top of a seismically transparent mantle. These reflections have been attributed to: (a) the presence of free aqueous fluids in a lower crust with stratified porosity, (b) subhorizontal shear zones, mylonite zones or fabrics caused by ductile shearing and (c) the presence of mafic sills and layered intrusions associated with underplating or partial melting in the upper mantle (Warner, 1990). (2) Compared with young extensional areas, more complex reflectivity patterns consistent with pervasive thrusting and indentation are associated with compressional orogens (Sadowiak et al., 1991). Among the most prominent features are dipping bands of reflections outlining seismic duplexes, ramp and flat structures and open wedges. Repeated and stacked upper crustal sections have been revealed in some orogenic belts. (3) Investigation of Precambrian crust shows pronounced subhorizontal features within the upper and middle crust. The lower crust is often relatively transparent and Moho reflections are weak in such regions. However, some recent profiles show that lower Precambrian crust is also reflective (Behrendt et al., 1988).

The ultimate purpose of crustal seismic studies, however, is to determine the structure and composition of the crust as a function of depth (i.e., to map in the third dimension), but it is often difficult to interpret crustal velocity and reflectivity in terms of petrology. Laboratory  $V_p$  and  $V_s$  studies can be used to estimate crustal composition at depth, if the results are constrained by geologic settings in which deep crust or structures analogous to those at depth are exposed, as in high grade metamorphic terranes and crustal cross-sections such as the Ivrea Zone (Fountain and Burke, 1991), the Kapuskasing Uplift (Fountain et al., 1990) and the Grenville Front Tectonic Zone (Burke, 1991).

#### Objectives of This Study

This work addresses the overall velocity structure of the middle crust exposed in the Britt domain of the Grenville Province and the origin of the scattered subhorizontal reflections revealed by vertical reflection profiling through a combined study of rock properties, seismic refraction and reflection modelling. The Britt domain in the Grenville province offers an excellent opportunity to investigate the seismic nature of a fairly typical segment of Precambrian middle crust because: (1) it is similar in overall composition to exposures of the middle crust in continental shields worldwide (Nockolds, 1954; Poldervaart, 1955); (2) it is a large coherent block of weakly to moderately deformed

middle crust exposed in oblique (shallow-dipping) cross section; (3) it has been extensively studied in terms of geology (e.g. Culshaw et al., 1988, 1989; Davidson and Bethune, 1988); and (4) a large set of seismic data has been acquired in the area under the COCRUST, GLIMPCE and LITHOPROBE programs. In particular, the recently completed 1992 LITHOPROBE Abitibi-Grenville transect provides new refraction data directly under the Britt domain (Irving et al., 1993), the GLIMPCE experiment provides high resolution, coincident refraction/ reflection data in the offshore extension of the Britt domain under Georgian Bay (Green et al., 1989; Mereu et al., 1989) and the COCRUST experiment provides regional refraction coverage to the east (Mereu et al., 1986).

The specific objectives of this study are thus to: (1) determine the average seismic properties of the Britt domain, (2) estimate its bulk composition vs depth, and (3) determine the causes of Britt domain reflectivity (lithology or deformation?) and the types of structures responsible for the reflection patterns observed (do areas dominated by folded structures generate scattered, subhorizontal reflections?). The results can also be used to interpret previous in-situ seismic data in the region and the results will add to the growing data base for understanding the seismic nature of deep continental crust.

The methods and procedures used in this study include:

(1) Determination of the acoustic properties of exposed Britt domain rocks from laboratory high pressure measurements.

(2) Determination of the average  $V_p$ ,  $V_s$ , Poisson's ratio and seismic anisotropy of the middle crust from area-weighted means of (1).

(3) Determination of the refraction structure of the Britt domain from forward modelling, ray tracing and amplitude analysis of results from the recent LITHOPROBE in-situ seismic experiment and comparison with GLIMPCE and laboratory results in order to estimate the average composition of the crust at depth.

(4) Synthetic modelling of the reflectivity of the middle crust using laboratory velocities, densities and geology as constraints and comparison with available reflection data in the region.

(5) Comparison of the results with refraction and reflection results elsewhere.

#### Outline of the Following Chapters

The regional geologic setting, lithology, structure and tectonic history of the research area are summarized in chapter two. The major results from previous geophysical work are also described in this chapter, including the 1982 COCRUST refraction experiment, the 1986 GLIMPCE reflection/

refraction experiment over Lake Huron and magnetic and gravity surveys in the area. Chapter three presents laboratory velocity measurements for the Britt domain, including sample collection, petrographic analysis of rock samples, measurement techniques and results. The average properties of each lithology, as well as averages for the whole area are also assessed in this chapter; these include bulk densities, S-wave and P-wave velocities, seismic anisotropy and Poisson's ratio. LITHOPROBE 1992 Abitibi-Grenville refraction data (line AB across the Britt domain) are interpreted in chapter four and the bulk composition at depth is estimated by comparison between refraction and laboratory results. Based on laboratory velocity and surface geology, one and two dimensional reflection modelling techniques are then employed in chapter five to investigate the causes of Britt domain reflectivity and the types of reflection geometries which could give rise to the reflections observed. Chapter six presents the conclusions of this study and a general discussion on the seismic nature of mid-lower continental crust.

## Chapter 2

### GEOLOGICAL AND GEOPHYSICAL BACKGROUND

#### Regional Geologic Setting

The Grenville Province, the youngest structural division of the Canadian Precambrian Shield, outcrops within a belt approximately 1900 km long and roughly 400 km wide. It extends to the northeast from the Great Lakes and is bounded by the Grenville Front on the northwest and the Appalachian orogen on the southeast. High grade metamorphic rocks, chiefly gneisses and migmatites of diverse origin and complex structure, characterize much of the Grenville Province (Davidson, 1984). The last major period of tectonism, referred to as the Grenville or Grenvillian orogeny, took place between 1.15 and 1.0 Ga (Stockwell, 1964, 1982), although rocks in many parts of the province record events of various earlier ages (Davidson, 1984).

The Grenville Province has been divided into subprovinces or belts according to two independent classification schemes. On the basis of rock assemblages and structural style, Wynne-Edwards (1972) divided the province in central Ontario into the Grenville Front Tectonic Zone (GFTZ), the Central Gneiss Belt (CGB) and the Central Metasedimentary Belt (CMB; Fig.2.1). A later classification by Rivers et al. (1989) divides the Grenville Province into the Parautochthonous Belt (PB), the Allochthonous Polycyclic

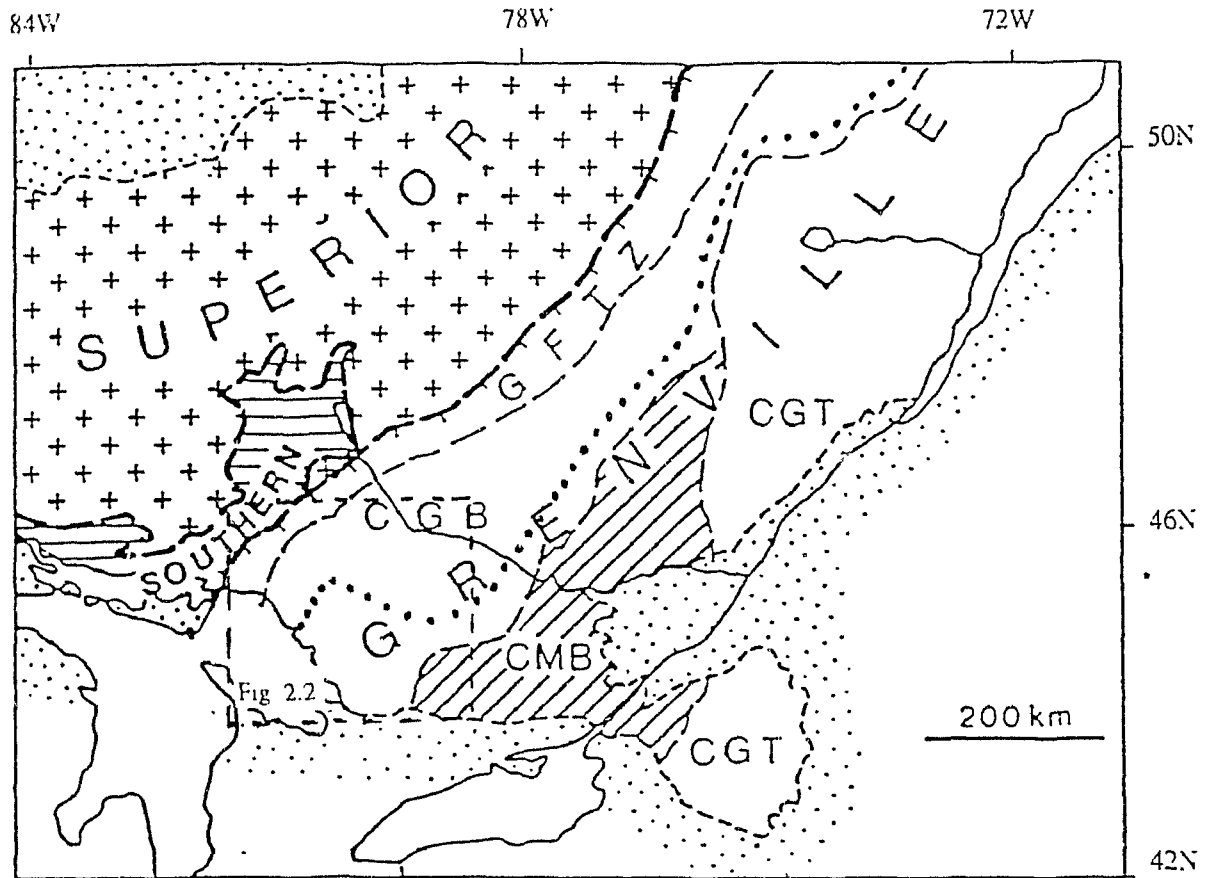


Fig. 2.1 Subprovinces in the southwest Grenville province after Wynne-Edwards (1972). The figure is from Davidson (1986). GFTZ = Grenville Front Tectonic Zone, CGB = Central Gneiss Belt, CMB = Central Metasedimentary Belt, CGT = Central Granulite Terrane, stipple = Paleozoic cover, dotted line = boundary between Parautochthonous Belt and Allochthonous Polycyclic Belt (Rivers et al., 1989). Inset shows location of Figure 2.2.

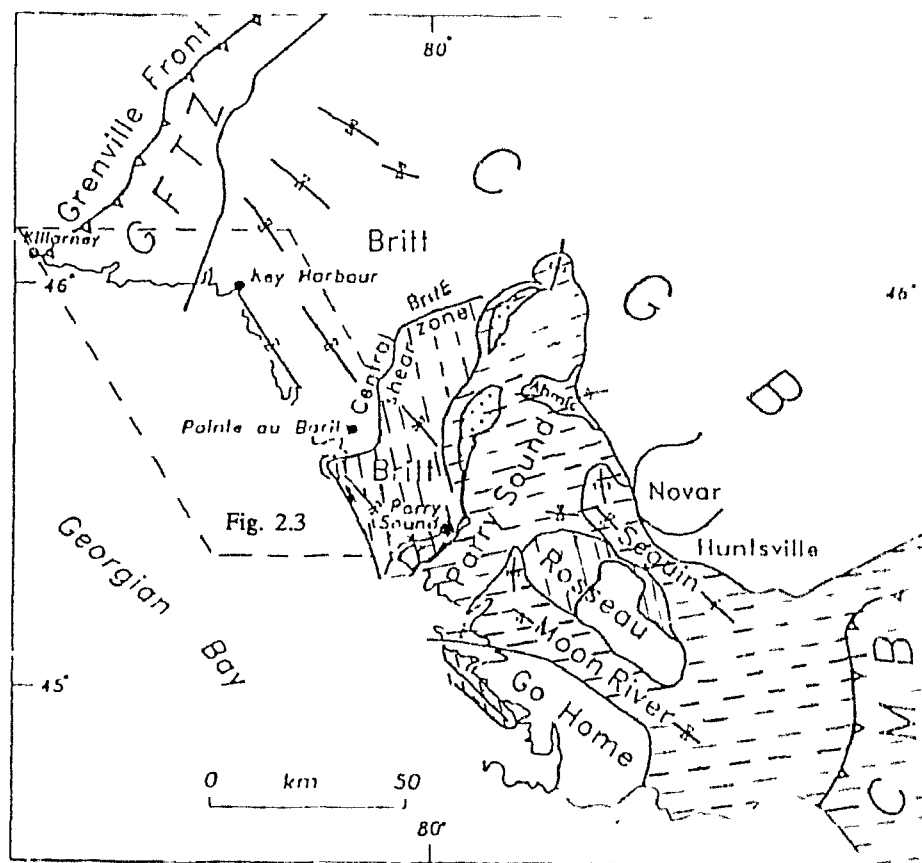
Belt (APB) and the Allochthonous Monocyclic Belt (AMB). This subdivision was based on geological, geophysical and geochronological data and a structural/tectonic framework that had been developed since Wynne-Edwards's division; the boundary between the parautochthonous and allochthonous belts is shown in Figure 2.1. Compared to Wynne-Edwards's classification, the PB includes the GFTZ and the northern CGB; the APB and AMB are composed of the southern CGB and the CMB, respectively. The two schemes complement each other and elements of both are used in the following description.

The northwest edge of the Grenville Province in Ontario is a broad zone of intense deformation, termed the Grenville Front Tectonic Zone (GFTZ). Its northwest limit, the Grenville Front, marks the junction of Archean and Proterozoic rocks with uplifted middle-lower crustal rocks of the Grenville orogen (Davidson, 1986; Green et al., 1989). Its southeast boundary, with the CGB, is defined by a major shear zone (Davidson and Bethune, 1988). The rocks within the GFTZ form northeast-striking lenticular bodies with intervening ductile shear and mylonite zones of various scales (Davidson and Bethune, 1988; Green et al., 1988). Generally, foliation and layering dip moderately southeast and carry pronounced downdip lineations. Kinematic indicators in the mylonite zones reveal a consistent southeast over northwest sense of transport (Davidson, 1984, 1986). Granitic-granodioritic orthogneiss is the major rock type within the GFTZ. The few orthogneisses that have been dated

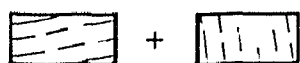


yield igneous crystallization ages ranging from ca. 1700 Ma (Krogh et al., 1971; Davidson et al., 1992) to ca. 1450 Ma (Bethune, 1993). While the absolute ages of most gneisses in the GFTZ are not known, field relations indicate that most of them probably fall in this age range, including an important component of ca 1450 Ma granitoids which are common in the Britt domain to the southeast (Van Breemen et al., 1986; Corrigan et al., in press). Paragneisses of various compositions are present only in the northwest part of the GFTZ (Davidson and Bethune, 1988; Burke, 1991). Metamorphic grade, no more than greenschist facies in the Killarney complex, increases abruptly to at least middle amphibolite facies across the front and continues to rise to the southeast, locally reaching granulite facies (Green et al., 1988). The rocks are polymetamorphic, bearing evidence of metamorphism at about 1450 Ma as well as a Grenvillian imprint. The Grenvillian metamorphism becomes more pervasive eastwards. The high grade metamorphic rocks with ca. 1450 Ma metamorphic ages (U-Pb, zircon, Krogh, 1989; Bethune et al., 1990) in the western GFTZ were exhumed by thrusting at or shortly before ca. 980 Ma (Haggart et al., 1993).

In contrast to the southeast-dipping GFTZ, structures in the Central Gneiss Belt (CGB) are characterized by northwest-trending folds and shear zones of various scales. Based on the lithology, metamorphic grade and structural style, the CGB is further divided into several domains (Fig. 2.2) separated by 1-2 km wide ductile shear and mylonite zones



Allochthon (Rivers et al, 1989)



Allochthon (Culshaw et al., in press)

Fig. 2.2 Schematic map showing domains/subdomains and major synforms within the Central Gneiss Belt. Abbreviations as in Figure 2.1. Dots = anorthosite gneiss. Inset shows location of Figure 2.3. Taken from Culshaw et al. (in press).

(Culshaw et al., 1983; Davidson et al., 1982; Davidson, 1984). These boundary shear zones usually have a moderate to shallow dip and wholly or partly circumscribe the domains. These shear zones and the mylonites associated with them show a dominant southeast-over-northwest sense of transport (Davidson et al., 1982; Davidson, 1984, 1986; Culshaw et al., 1983). U-Pb dating on zircons from pegmatites emplaced during thrusting yields ages of  $1159 \pm 5-4$  Ma in the Parry Sound Shear Zone (van Breemen et al., 1986) and ca. 1103 Ma and 1097 Ma in the Parry Sound/Moon River and Parry Sound/Seguin boundary thrust zones (van Breemen and Davidson, 1990, Nadeau, 1990). According to the division of Rivers et al. (1989), the first order boundary between the PB and APB lies within the CGB (Fig. 2.2) along the Parry Sound Shear Zone (the PSSZ), but the work of Culshaw et al. (in press) implies that the boundary lies along the Central Britt Shear Zone (the CBSZ). The parautochthonous CGB (northern Britt domain plus two windows south of the CBSZ, the Go Home and southern Rosseau subdomains; Culshaw et al., in press) is composed of ortho- and paragneisses and abundant granitic-granodioritic megacrystic plutons which are similar to those in the GFTZ. The allochthonous CGB to the south of the CBSZ includes the southern Britt domain, the Parry Sound domain and the Seguin, Moon River and northern Rosseau subdomains (Culshaw et al., in press). The southern Britt domain is composed mainly of gneisses of supracrustal origins while the Parry Sound domain is dominated by mafic to granitoid orthogneiss with well-

layered mafic to felsic granulite and minor pelite, calc-silicate rocks, quartzite and marble. The igneous crystallization age for a principal member of the Parry Sound domain (the McKellar orthogneiss) is  $1425 \pm 75$  Ma (van Breemen et al., 1986), while recent geochronological data from the southwestern Parry Sound domain indicate an additional episode of granitoid plutonism between ca. 1360 and 1280 Ma (Wodicka, per. comm.). Igneous crystallization of two anorthosite bodies has been dated at  $1163 \pm 3$  Ma (Parry Island; Wodicka, per. comm.) and  $1350 \pm 50$  Ma (Whitestone; van Breemen et al., 1986). The other sub-domains are characterized by migmatitic granodioritic gneiss with minor supracrustal gneiss and amphibolite. Gneisses in the Parautochthonous CGB display pre-Grenvillian metamorphism (granulite facies; ca. 1450 Ma; Ketchum et al., in press) overprinted by upper amphibolite facies Grenvillian metamorphism. The allochthonous CGB underwent only the granulite (Parry Sound domain) to amphibolite facies Grenvillian metamorphism. The Central Metasedimentary Belt Boundary Zone (the CMBBZ), a major ductile high strain zone of gneissic tectonites, transported gneisses and porphyroclastic gneisses bounds the CGB on the southeast. The CMBBZ is about 10 km thick, 200 km long and dips gently to the southeast; a wide variety of kinematic indicators suggest prevailing overthrusting to the northwest (Culshaw et al., 1983; Davidson, 1984; Hanmer and Ciesielski, 1984; Hanmer and McEachern, 1992; Easton, 1992).

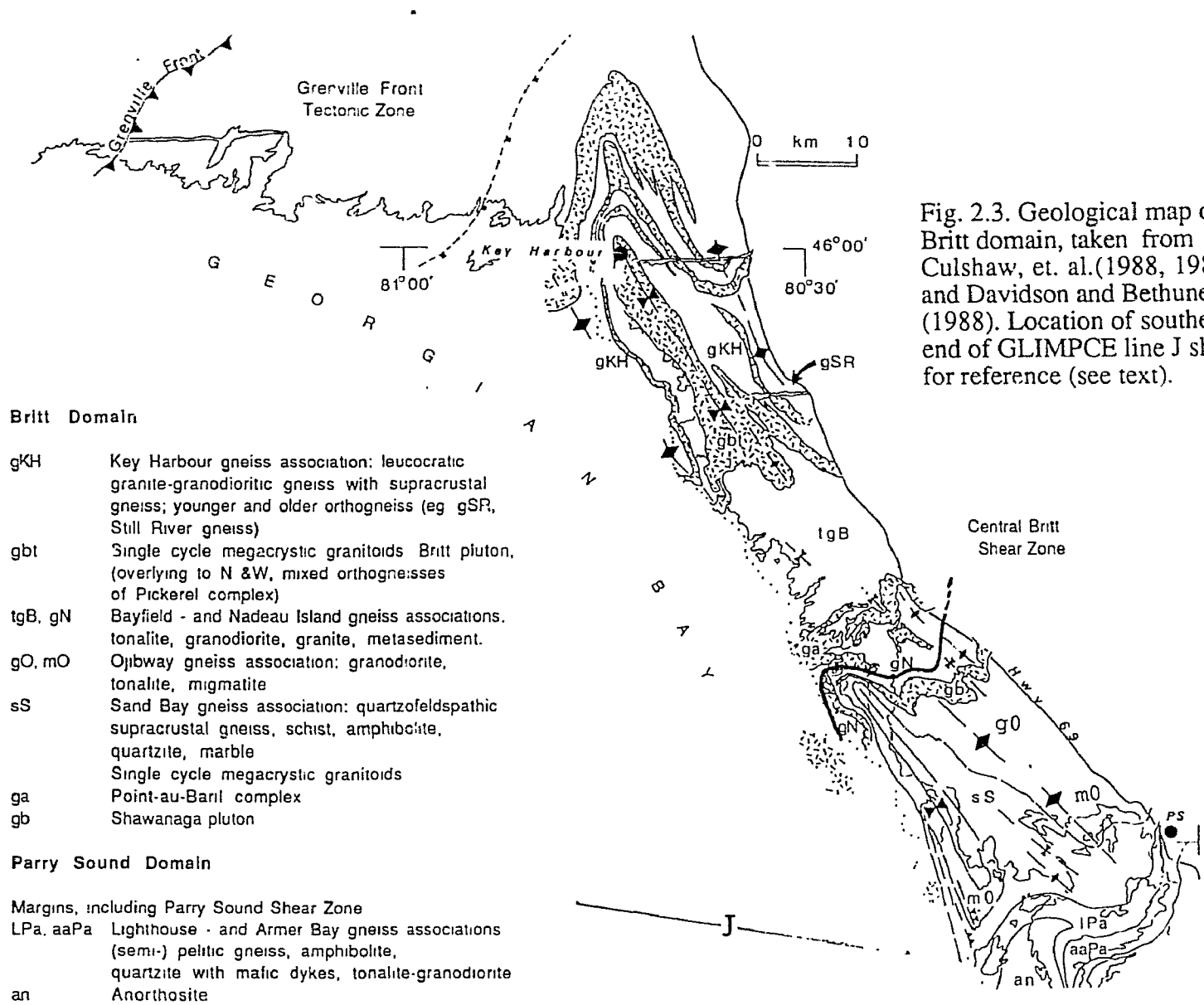
Compared with the CGB, large amounts of supracrustal rocks, the Grenville Supergroup, are present in the Central Metasedimentary Belt (the CMB). Sedimentation and volcanism between 1300 and 1250 Ma, followed by plutonism and metamorphism at roughly 1140 to 1070 Ma, characterize much of the CMB (Easton, 1992). The major rocks of supracrustal origin include marble, metavolcanic rocks, fine- to medium-grained clastic metasediments, quartzite and quartzofeldspathic gneiss. Plutonic rocks in the CMB range in composition through tonalite, syenite, monzonite and gabbro (Davidson, 1986). The metasedimentary rocks exposed in the CMB may represent a marginal basin while the tonalite suite may represent fragments of the remnant arc adjacent to the basin (McEachern et al., 1993). The metamorphic grade varies from greenschist to granulite facies (Davidson, 1986; Easton, 1992). From northwest to southeast, attitudes of layering and map-units change gradually from shallowly southeast-dipping through vertical along the St. Lawrence River to northwest-dipping in New York State (Davidson, 1986). The CMB can also be further divided into several lithologic terranes (see Easton, 1992).

In the past twenty years, several hypothetical models for the geological evolution of the Grenville Province have been proposed. They can be categorized into two groups: (1) internal dismemberment and imbrication of a single continent due to major shearing and thrusting (e.g. Wynne-Edwards, 1972, 1976; Baer, 1981; Woussen et al., 1986) and (2) plate

tectonic models involving an ocean closure (e.g. Donaldson and Irving, 1972; Dewey and Burke, 1973; Young, 1980; Windley, 1986; Corriveau, 1990; Hanmer and McEachern, 1992; McEachern and van Breemen, 1993).

### Geology of the Britt Domain

The research area for this study is a corridor along the northeast shore of Georgian Bay. It lies within the CGB and extends from the southeast margin of the GFTZ through the Britt domain to the Parry Sound Shear Zone (Fig. 2.3). The Britt domain is composed of parautochthonous and allochthonous rocks separated by the CBSZ (Culshaw, et al., in press). Gneisses of diverse origins and abundant (30%) middle Proterozoic plutonic rocks (ca. 1450 Ma) of varied composition characterize the Britt domain. The metamorphic grade associated with the Grenvillian tectonism is upper amphibolite facies (e.g. Culshaw et al., 1988; Anovitz and Essene, 1990; Jamieson et al., 1992; Jamieson et al., in press; Corrigan et al., in press). In places, granulite-facies enclaves dating from ca. 1450 Ma have been preserved (Ketchum, 1992; Ketchum et al., in press), and there is evidence for earlier events (> ca. 1698 Ma, Corrigan et al., in press). U-Pb Monazite (Corrigan et al., in press) and metamorphic zircon ages (Culshaw, per. comm.) suggest that the metamorphic peak in the Britt domain was attained in the interval 1050-1035 Ma. Metamorphic data from many areas



suggest that the present erosion surface represents Grenvillian orogenic depths in excess of 20 km (e.g. Wynne-Edwards, 1972; Anovitz and Essene, 1990). The emplacement age of regional post-tectonic pegmatites suggests that tectonism ceased in the Britt domain by 990-988 Ma (Ketchum et al., 1993; Corrigan et al., in press).  $\text{Ar}^{40}/\text{Ar}^{39}$  data indicate that most of the Britt domain had cooled below 450 °C by 960-970 Ma and 300 °C by 900 Ma (Culshaw et al., 1991).

In the following sections, the terms "monocyclic" and "polycyclic" refer to rock units that have undergone, respectively, one or more than one orogenic event. Specifically, 'polycyclic' refers to rocks which have undergone Grenvillian and pre-Grenvillian events and 'monocyclic' to those only metamorphosed during the Grenvillian event.

#### Gneiss Associations

From Key Harbour to the Parry Sound Shear Zone (Fig. 2.3), the gneisses are divided into five major rock groupings, termed "gneiss associations" (Culshaw et al., 1988, 1989) that are separated by sheet-like foliated plutons of monocyclic granitoid rocks. The term refers to a group of gneisses of varied composition that are consistently intermixed on a scale too small to map but which together form a map unit. One or more of the members of the gneiss association may occur in places in bodies large enough to form a mappable unit within the gneiss association. In



addition, there may be important differences in tectonic history between individual gneiss associations (Culshaw et al., 1991). From northwest to southeast, these groups are named the Key Harbour, Bayfield, Nadeau Island, Sand Bay and Ojibway gneiss associations (Culshaw et al., 1988; 1989). The Key Harbour, Bayfield and Nadeau Island gneiss associations below the CBSZ are predominantly composed of polycyclic rocks and belong to the Parautochthon, while the Sand Bay and Ojibway gneiss associations above the CBSZ are formed of monocyclic rocks and have been assigned to the Allochthon (Culshaw et al., in press).

#### *Key Harbour gneiss association*

The Key Harbour gneiss association (gKH, Fig. 2.3) is situated in the northwest part of the Britt domain. Its southeast limit coincides with the northern boundary of the Britt pluton (gbt, Fig. 2.3). Culshaw et al. (1988) distinguished three members of this gneiss association: the Key Harbour gneiss, Free Drinks mafic gneiss and Still River mafic gneiss. The Key Harbour gneiss is largely composed of polycyclic layered, migmatitic, leucocratic, pink to grey ortho- and paragneisses. The paragneiss is quartzofeldspathic and generally contains some biotite and minor garnet. It is associated with minor pods or layers of sillimanite gneiss, quartzite and garnet amphibolite (Culshaw et al., 1991). The orthogneisses are predominantly granitic in composition, but include less abundant gneisses of intermediate composition

(Corrigan et al., in press). Older granitoids of this suite were intruded at ca. 1689 Ma (Corrigan, 1990) by the Key Harbour leucogranite which constitutes about half of the Key Harbour area. All rock types of the Key Harbour gneiss contain variable amounts of fine-grained disrupted mafic dikes which are absent in the younger middle Proterozoic granitoids (Culshaw et al., 1988; Corrigan et al., 1993).

The Free Drinks mafic gneiss lies along the west side of the monocyclic Britt pluton and occupies an area about 10 km long and 1 km wide which strikes northwest. It is composed of gabbroic, leucogabbroic, tonalitic and minor granitic gneiss of plutonic origin (Culshaw et al., 1988). The Still River mafic gneiss (gSR, Fig. 2.3) lies in the eastern portion of the Key Harbour association. It is composed of amphibolite and intermediate, mesocratic gneiss as well as variable amounts of pink leucogneiss. All of the above lithologies may be strongly deformed, resulting in straight gneiss of polymodal composition.

#### *Bayfield gneiss association*

The Bayfield gneiss association (tgB, Fig. 2.3) is bounded by the monocyclic Britt pluton on the northwest and the monocyclic Point-au-Baril complex (ga in Fig. 2.3) on the southeast. It is composed of polycyclic rocks. The major rock type is a migmatitic metatonalite - granodiorite orthogneiss (ca.1700-1800 Ma, U-Pb zircon, Culshaw, per. comm.), the Bayfield gneiss (Culshaw et al., 1988). This is associated

with a variety of granitoid gneisses of plutonic origin, together with which it evidently forms a single plutonic complex. Associated but not necessarily genetically related rock types include (Culshaw et al., 1988): (1) pink and grey biotite leucogneiss of dominantly supracrustal origin, (2) small bodies of pink, leucocratic, alaskitic biotite granite which cut the metatonalite, and (3) a belt of metasedimentary gneisses which consists of garnet-rich quartzofeldspathic rock interlayered with (semi-) pelitic gneiss. Two sets of metamorphosed mafic dikes which crosscut the pre-Grenvillian leucosomes (ca. 1450 Ma granulite facies metamorphism) occur throughout the Bayfield gneiss association.

#### *Nadeau Island gneiss association*

This gneiss association (gN, Fig. 2.3) lies between the Point-au-Baril plutonic complex on the north and the Sand Bay and Ojibway gneiss association (sS, gO, Fig. 2.3) on the south. It is composed of polycyclic rocks and deformed on its south side within the CBSZ. Orthogneisses of granitic, granodioritic and tonalitic composition characterize much of the association and probably form a single plutonic complex. An igneous crystallization age of ca. 1600 Ma has been determined for one member (Culshaw, per. comm., 1994). Metasedimentary rocks including pelitic and semipelitic types, calc-silicate rocks and amphibole-bearing garnet-biotite gneisses are also a substantial component, more voluminous than in the Bayfield gneiss association (Culshaw

et al., 1988). Although the rocks are largely overprinted by Grenvillian upper amphibolite facies metamorphism and deformation, pre-Grenvillian granulites (1452-1433 Ma; Ketchum et al., 1992, 1993) are documented in low strain zones. The Nadeau Island association contains scattered pods and bodies (up to 1 km in largest dimension) of meta-gabbro and also contains crosscutting mafic dikes similar to those in the Bayfield gneiss association.

#### *Ojibway gneiss association*

The Ojibway gneiss association lies above the CBSZ. The dominant lithology is a grey granodioritic-tonalitic orthogneiss in the north (gO, Fig. 2.3) which grades into leucosome-rich migmatite in the south (mO, Fig. 2.3) at higher structural levels (Culshaw et al., 1991). The igneous crystallization age of the orthogneiss is ca. 1450 Ma (U-Pb, zircon; Culshaw, per. comm.). Rocks of this association are only affected by the Grenvillian events and lack the abundant crosscutting mafic dykes observed in the gneiss associations described above.

#### *Sand Bay gneiss association*

The Sand Bay gneiss association also lies above the CBSZ and the boundary between the Ojibway and Sand Bay gneiss associations is complexly folded. This gneiss association appears to be entirely composed of gneiss of supracrustal origin, including abundant migmatitic quartzofeldspathic

gneiss and smaller amounts of grey, plagioclase-quartz-biotite schist, named the Dillon schist (Culshaw et al., 1988). The migmatitic quartzofeldspathic gneiss is associated with minor amounts of amphibolite, marble, calc-silicate rocks and quartzite. The maximum depositional age of the Dillon schist and quartzite is 1350-1400 Ma ( U-Pb, detrital zircons, Culshaw, per. comm., 1994). Since the age of Sand Bay gneiss association is younger than the igneous crystallization age of the orthogneiss of the Ojibway, it indicates an unconformable or tectonic contact between the Sand Bay gneiss association and the Ojibway gneiss association (Culshaw et al., in press).

Although they contain globular and pod-like mafic bodies, the monocyclic Ojibway and Sand Bay gneiss associations, unlike the underlying polycyclic gneiss associations, lack cross-cutting mafic dikes and monocyclic megacrystic granitoids and contain no evidence of pre-Grenvillian metamorphism. These gneiss associations are interpreted to be allochthonous, ie. transported onto the underlying Parautochthonous belt along the CBSZ (Culshaw et al., in press).

#### Monocyclic Megacrystic Granitoids and Related Plutonic Rocks

Metaplutonic rocks, dominantly granitoid with compositions ranging from granite and quartz syenite through granodiorite to diorite, occupy about 30% of the region. Megacrystic textures are common in these rocks. They have

been mapped as individual plutons or complexes of varied compositions: the Pickerel complex, Britt pluton, Point-au-Baril complex and Shawanaga pluton (Fig.2.3). The Britt pluton, the largest pluton in the region, has been dated at  $1456 \pm 9 - 6$  Ma (Van Breemen et al., 1986) and the Point-au-Baril complex and Shawanaga pluton at  $1460 \pm 12 - 8$  Ma (Culshaw et al., in preparation). Other dated monocyclic granitoids include the Mann Island granodiorite ( $1442 \pm 6 - 7$  Ma; Corrigan et al., in press) in the Key Harbour area and the 'marginal orthogneiss' ( $1346 \pm 69 - 39$  Ma; Van Breemen et al., 1986) in the southeasternmost Britt domain. These plutonic rock units are usually extremely elongated, folded and metamorphosed, but unlike the host gneisses which had complex structural and metamorphic histories, they only show the effect of a single structural/metamorphic episode (the Grenvillian orogenic event), and thus are termed 'monocyclic' (Culshaw et al., 1988).

#### Mafic Intrusions and Anorthosite

Small (several meters or less in dimension) rounded bodies, dykes and angular fragments of mafic rocks are scattered throughout the region. They can be subdivided on the basis of their age (relative to metamorphic events) and/or lithology. The oldest group is composed of small bodies of amphibolite that resemble mafic dykes or sills that have been broken into angular fragments (Culshaw et al., 1988). They are restricted to polycyclic host gneisses.

The second group is composed of more widespread dykes that crosscut polycyclic and monocyclic plutonic rocks. They are foliated and variably metamorphosed by Grenvillian metamorphism but crosscut pre-Grenvillian leucosomes in polycyclic rocks. Thus they separate Grenvillian and pre-Grenvillian metamorphism (Culshaw et al., 1988). This group is probably equivalent to the Sudbury dykes which have an age of ca.  $1238 \pm 4$  Ma (Krogh et al., 1987; Davidson and Bethune, 1988). Subordinate, small, often globular-shaped, bodies of olivine metagabbro with coronitic textures occur above the CBSZ within the allochthonous Sand Bay and Ojibway gneiss associations; they are members of the ca. 1170 Ma coronitic metagabbro suite elsewhere in the CGB (Davidson and van Breemen, 1988; van Breemen and Davidson, 1990; Culshaw et al., in press). One such body within the Ojibway gneiss association is dated at ca. 1150 Ma (Heaman and LeCheminant, in press). Garnet-clinopyroxene bearing mafic rocks of eclogitic affinity also occur at this structural level of the Britt domain. They are few in number and occur along the CBSZ where they are associated with small bodies of gneissic anorthosite (Culshaw et al., in press). Rocks of this type record a high pressure metamorphic event and since they do not occur below the CBSZ (Culshaw et al., 1988, 1989) they and their host rocks have been interpreted to have been exhumed from deep levels along the CBSZ (Culshaw et al., in press).

In addition to the small bodies discussed above there are also several plutons of gabbro and metagabbro. These

occur below the CBSZ as rounded bodies up to one or two kilometers in diameter. Although the rocks are recrystallized, primary igneous textures are locally recognizable (Culshaw et al., 1988). The absolute age of these gabbros is unknown although they lack polymetamorphic textures and are therefore probably <1450 Ma (Culshaw, per. comm., 1994)

Anorthosite (an, Fig. 2.2, 2.3) occurs within the Parry Sound Shear Zone in large bodies and sheets in addition to the small bodies associated with the CBSZ. Anorthosite also occurs as a sheet to the west of Key Harbour within the Pickerel complex.

### Structural Geology

Although pre-Grenvillian fabrics locally exist in the parautochthonous Britt domain (north of the CBSZ), Grenvillian structures dominate. The most significant tectonic fabric is the SE-NW trending lineation that, together with other structures of various scales, indicates thrusting and/or extension under pervasively ductile conditions parallel to this trend.

Northwest-trending folds of various types and scales, from outcrop-scale sheath and cylindrical folds to map-scale "a" type folds, are among the most significant structural features of the Britt domain (Fig. 2.2, 2.3; Davidson et al., 1982; Schwerdtner, 1987; Culshaw et al., 1988; in press). These folds have low amplitudes and hinges aligned parallel



to the SE trending, subhorizontal, stretching lineation. Field relations indicate that folds above the CBSZ are formed during or after post-thrusting extension on the CBSZ in the ductile mid-lower crust. Field relations of those below the CBSZ are not as clear but have been interpreted as products of thrusting (Schwerdtner, 1987), possibly with an extensional component (Jamieson et al., in press).

The principal shear zones in this area include the Central Britt Shear Zone (CBSZ) and the Parry Sound Shear Zone (PSSZ). The CBSZ has an orthogonal width of 3 km and dips gently southeast (Culshaw et al., 1989; Ketchum et al., 1993; Culshaw et al., in press). The CBSZ contains the boundary between parautochthonous rocks to the north and allochthonous rocks to the south and is characterized by strongly deformed rocks consisting of straight gneiss, porphyroclastic gneiss and mylonite. Kinematic indicators suggest a late ductile history of extension (upper amphibolite facies, ca. 1020-1000 Ma; Ketchum et al., 1993) with the hanging wall displaced to the southeast (Ketchum et al., 1993; Culshaw et al., in press). However, the CBSZ likely originated as a thrust because (Culshaw et al., in press): (1) high pressure rocks (eclogite) occur exclusively in the hangingwall; (2) there is an abrupt change in history across the zone that is difficult to explain in terms of normal stratigraphic successions; (3) at the northern end of the shear zone the kinematic indicators that indicate thrusting are not completely overprinted by extensional ones.

The PSSZ, which separates the Britt domain and the Parry Sound domain, is similar to the CBSZ in scale. Shear-sense indicators imply southeast-over northwest-thrusting (ca. 1160 Ma, van Breemen et al., 1986; Davidson, 1984; Culshaw et al., 1989) followed by extensional deformation.

The youngest significant structures are ENE-trending brittle normal faults. These faults usually have a displacement on the order of tens of meters, but some of them show movement of several hundreds meters (Culshaw et al., 1989).

#### Summary of Geologic Events

In recent years, detailed geological mapping along the north and northeast shores of Georgian Bay (e.g. Culshaw et al., 1988, 1989; Davidson and Bethune, 1988; Bethune, 1989), new geochronology data (e.g. Corrigan, 1990; Culshaw et al., 1991; Corrigan et al., in press; Ketchum et al., 1993; Culshaw, per. comm.) and thermobarometry data (e.g. Anovitz and Essene, 1990; Corrigan, 1990; Jamieson et al., in press) have led to a better understanding of the geologic history of the area. The major events include:

(1) Pre-Grenvillian metamorphism and plutonism. At least two metamorphic events occurred in the early Proterozoic, separated by plutonism at ca. 1698 Ma. Although absolute ages are not well constrained, the intrusion of the Key Harbour leucogranite at ca. 1698 serves as the minimum age of the first event and the maximum age of the second. Mineral

assemblages suggest both metamorphic events attained at least uppermost amphibolite facies conditions (Corrigan et al., in press). Granulite facies metamorphism at 1450 ma is documented in the central Britt domain (Ketchum et al., in press) and may well correspond to the second pre-Grenvillian event.

(2) Emplacement of mid-Proterozoic granitoids (ca. 1450 Ma) along or close to the boundaries between gneiss associations.

(3) Regional emplacement of the Sudbury dykes (ca. 1240 Ma). These widespread dikes serve as an important marker of pre-Grenvillian and Grenvillian metamorphism.

(4) The Grenvillian tectonometamorphic event (ca. 1050-1035 Ma), including northwest-directed thrusting, late southeast-directed extension and regional high grade metamorphism (upper amphibolite facies).

(5) South-side-down normal faulting under brittle-ductile and brittle crustal conditions comprise the post-Grenvillian history.

### Previous Geophysical Studies

Between 1987-1989, the Geological Survey of Canada conducted a systematic, digitally recorded aeromagnetic survey in Ontario. Based on this data and previously digitized aeromagnetic survey data in Ontario, a detailed

vertical magnetic gradient map of Ontario was produced by the Ontario Geological Survey in 1991 (Gupta, 1991). Figure 2.4 shows the vertical magnetic gradient map of the Georgian Bay area. Three distinct features, among others, can be seen in Figure 2.4: (1) strong northeast signatures coincide with the GFTZ and Parry Sound Shear Zone, (2) pronounced northwest-trending features over the Britt domain and Georgian Bay coincide with the northwest-trending folds observed within the Britt domain, (3) notable east-west signatures in the Point-au Baril area can be related to the Central Britt Shear Zone.

The Bouguer gravity map of the Georgian Bay area (McGrath, 1988) is shown in Figure 2.5. Two prominent Bouguer gravity anomalies occur, a low over the Killarney complex which coincides with the GFTZ and a high over the Parry Sound domain. It is worth noting that the Britt domain and most of Georgian Bay between these two anomalies have comparable Bouguer gravity values, suggesting the rocks under each have similar densities.

In addition, major seismic studies have been conducted in the southwestern Grenville province in recent years, and have provided critical information on the structure and tectonic evolution of the Grenville Orogen. Figure 2.6 shows the location of deep seismic refraction and reflection lines which have been conducted across the GFTZ and/or the CGB by COCRUST, GLIMPCE and LITHOPROBE.

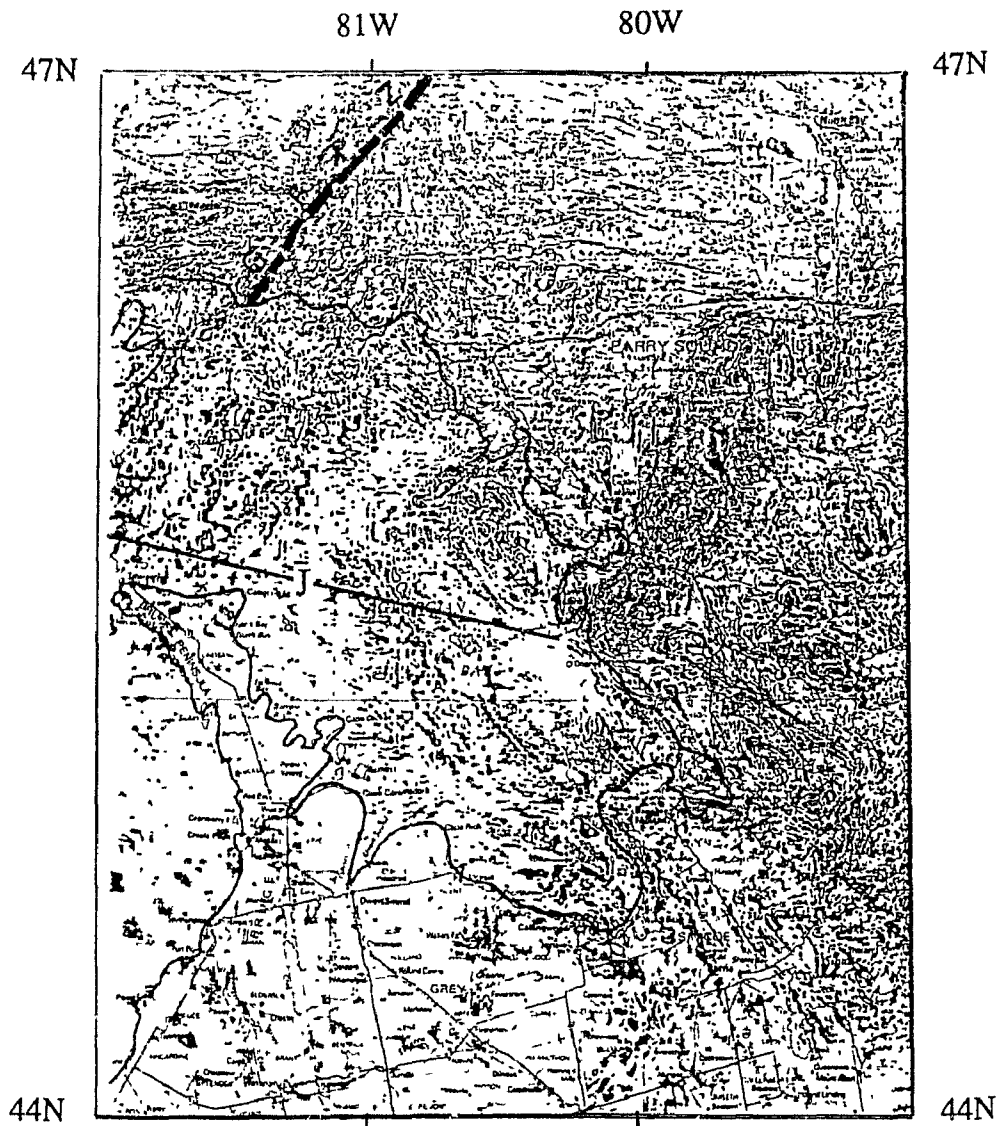


Fig. 2.4 Vertical magnetic gradient map showing northwest-trending features in the Britt domain and similar features under seismic line J (from Map 2591, Ontario Ministry of Northern Development and Mines, 1991).

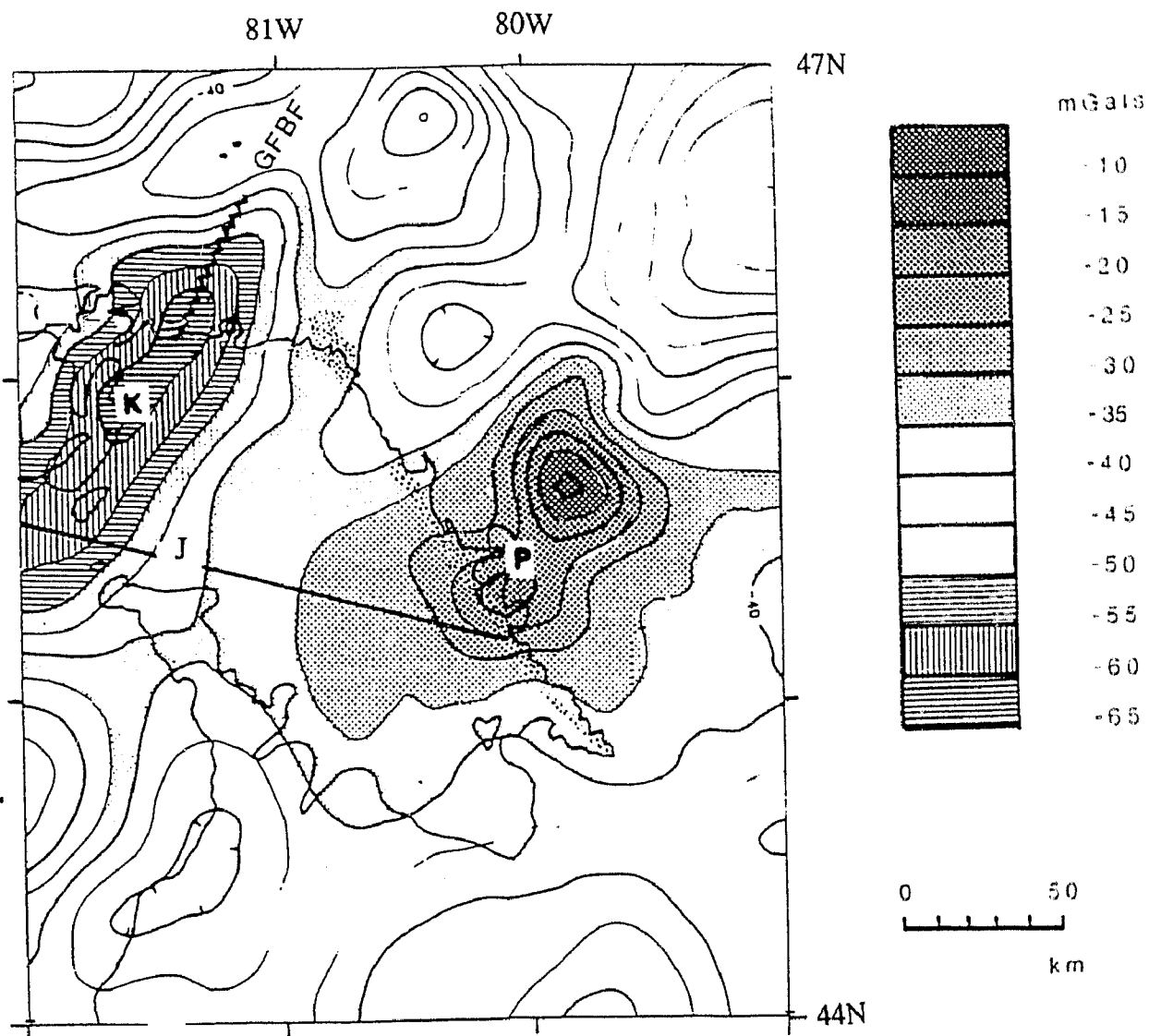


Fig. 2.5 Bouguer gravity map showing the Killarney gravity low (K) and Parry Sound gravity high (P). The region between the two anomalies has rather uniform gravity features (from McGrath et. al., 1988). Location of GLIMPCE line J shown for reference.

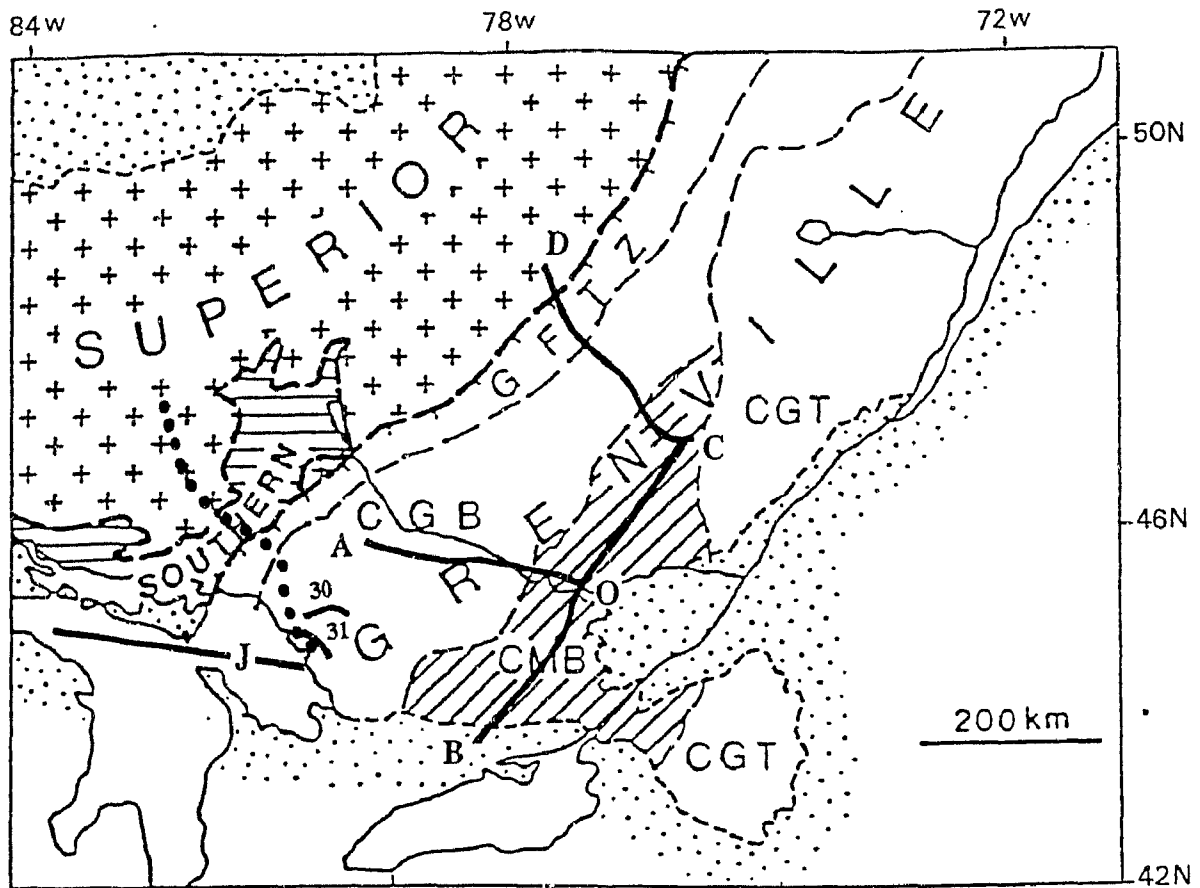


Fig. 2.6 Summary figure showing seismic lines conducted in southwestern Grenville Province and referred to in text. DC, AO, and BC are 1982 COCRUST refraction lines; J, 1986 GLIMPCE reflection/refraction line; 30 and 31, 1991 LITHOPROBE reflection lines. Heavy dotted line shows location of 1992 LITHOPROBE Abitibi-Grenville refraction line AB. Abbreviations as in Fig. 2.1

### The 1982 COCRUST Experiment

A long-range seismic refraction/wide-angle reflection experiment was conducted by the Canadian Consortium for Crustal Reconnaissance Using Seismic Techniques (COCRUST) in 1982. Three seismic lines, each approximately 300 km in length, are shown in Figure 2.6. The main tectonic features of interest traversed by the lines are the Grenville Front, the boundary between the Central Gneiss Belt and the Central Metasedimentary Belt of the Grenville Province and the Ottawa-Bonnechere Graben. The major results of this study include (Mereu et al., 1986):

(1) Near-surface seismic velocities vary from 5.8 to 6.4 km/s and regional differences in velocity gradients, particularly in the upper crust, are pronounced (Fig. 2.7).

(2) There was no strong evidence for any intermediate depth crustal seismic discontinuity.

(3) All three major tectonic features, the Grenville Front, the Ottawa Graben and the CMB-CGB boundary are deep-seated features which extend to Moho. They are marked by changes in the character of velocity gradients within the crust as well as changes in crustal thickness (Fig.2.7).

(4) The Moho is a sharp, well defined discontinuity beneath the CGB but is irregular and poorly defined under major portions of the Ottawa Graben.



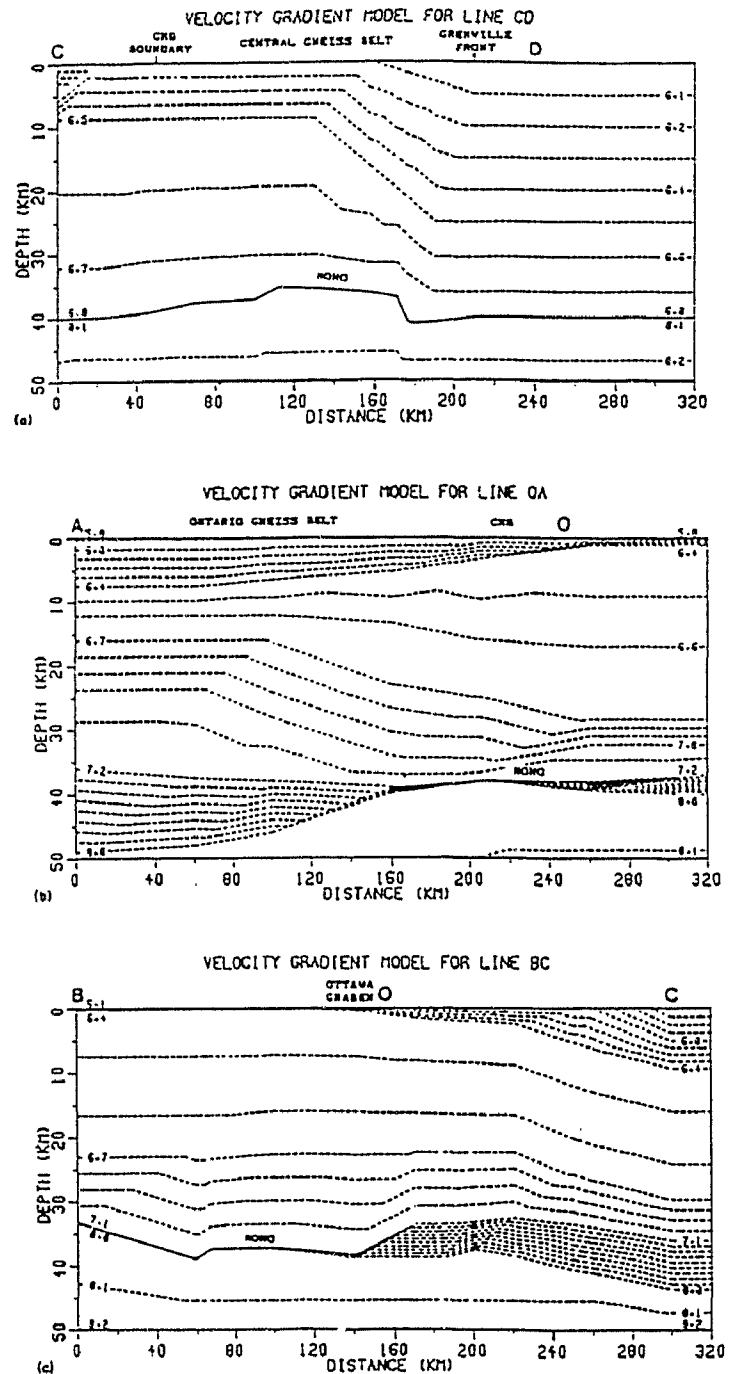


Fig. 2.7 Velocity models for COCRUST lines (a) CD, (b) OA, and (c) BC. The models were derived from synthetic seismogram analysis. Dotted lines indicate velocity contour lines in km/s. From Mereu et al., 1986.

### GLIMPCE Profile J

The Great Lakes International Multidisciplinary Program on Crustal Evolution (GLIMPCE) has recorded a number of deep seismic reflection and refraction profiles in the Great Lakes region (GLIMPCE seismic refraction working group, 1989; Green et al., 1988, 1989). Among them the multichannel reflection and coincident refraction/wide-angle reflection profile, line J, extends 350 km in a WNW-ESE direction across the Manitoulin terrane in the west, the Grenville Front Tectonic Zone (GFTZ) in the centre, and the Britt domain in the east (Fig. 2.6). An F-K migrated reflection section of the eastern part of profile J and the coincident refraction/wide-angle reflection data are presented in Figures 2.8 and 2.9, respectively.

Based on the reflection character (Fig. 2.8), the seismic section partitions into three units laterally, and these coincide with the major tectonic units named above and shown along the top of Figure 2.8. A two-layer structure is defined for the Manitoulin terrane with a highly reflective lower crust and a less reflective upper crust, separated by a band of strong reflections at about 5s two-way travel time (Green et al., 1988, 1989). Green et al. (1989) interpret the lower crust as the attenuated Superior cratonic margin, the upper crust as a composite terrane consisting of displaced Huronian strata plus younger granites and rhyolite, the remains of an exotic mass that collided with the Superior cratonic margin during the Penokean orogeny, and the

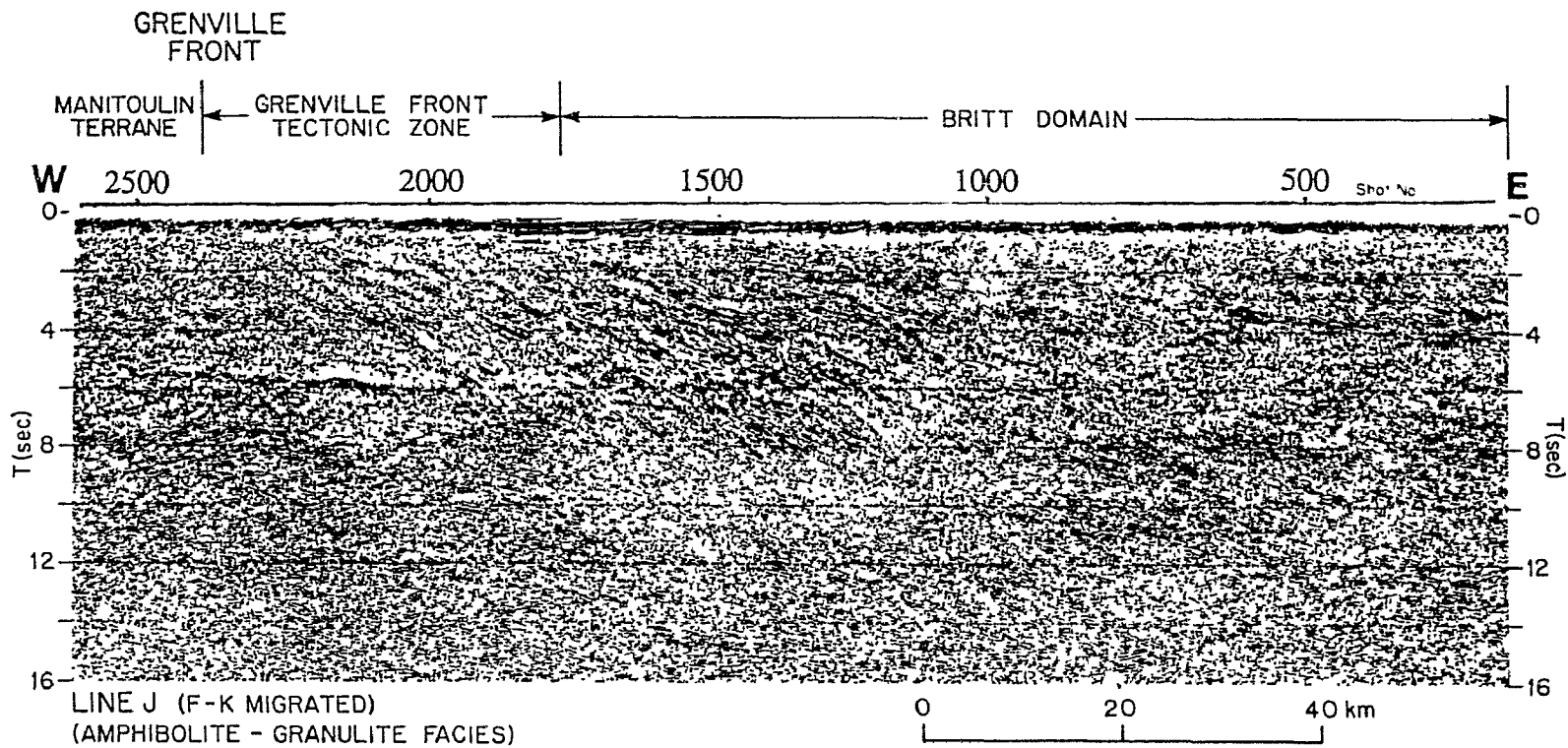


Fig. 2.8 F-K migrated seismic reflection data for eastern part of GLIMPCE profile J, from Green, et al. (1990). Vertical axis is two way travel time and horizontal axis is distance. Note the dipping reflectors in the GFTZ and subhorizontal reflectors in the Britt domain. Selected shotpoints indicated along top of profile.

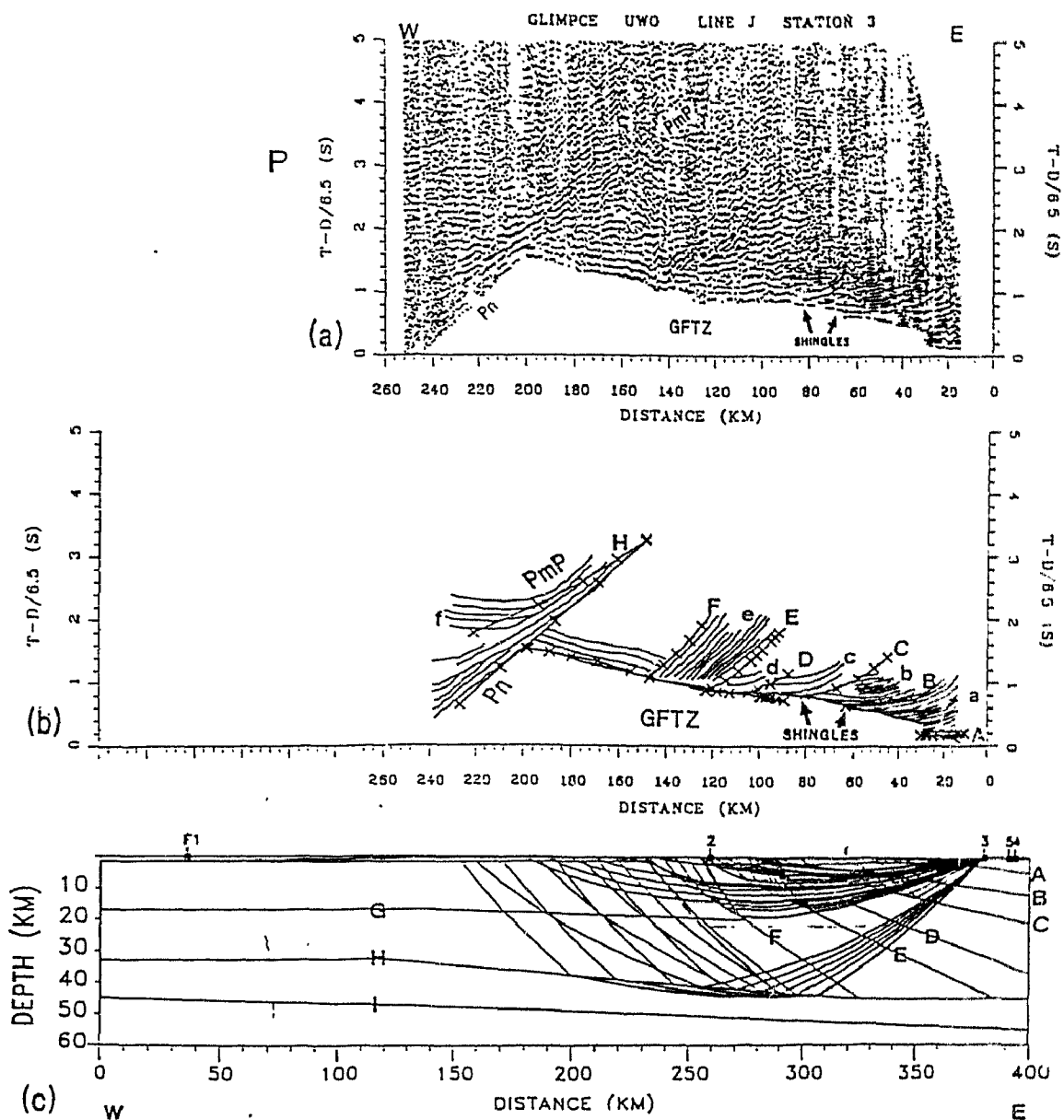


Fig. 2.9 (a) P wave record section for line J recorded at Parry Sound station 3. (b) Comparison of theory and observation. Continuous lines in groups a,b,c,d,e, and f are observed reflection hyperbolae. A,B,C,D,E,F, and H are theoretical ray trace-travel time branches associated with the corresponding model interfaces in (c), ray trace diagram for station 3 arrivals.

intervening discontinuity as the master Penokean decollement.

The GFTZ is characterized by strong southeast-dipping reflections. The apparent dips decrease southeastward from 35 to 25 degrees, and the strength and density of the reflections change markedly to the southeast. These strong dipping reflections are recorded down to about 9s and weaker events can be traced to as deep as 15s travel time. The reflections were interpreted by Green et al. (1988, 1989) as mylonite zones and highly strained contacts between gneissic and migmatitic rocks of varied lithologies. However, detailed velocity data from laboratory measurements and in situ experiments shows they may be due to clusters of thin mafic dykes within the host orthogneiss and to strained contacts between contrasting lithologies (Burke, 1991).

Farther to the east, the Britt domain is characterized by numerous discontinuous subhorizontal reflections and lozenge-shaped reflection packages. The strength and density of these reflections are moderate and uniform throughout the whole crust and their origin is still open to discussion.

Figure 2.9a is a wide-angle reflection/refraction time-distance plot of P waves recorded along line J . One of the interesting features on this section is the 'shinglelike' pattern of arrivals observed at moderate range, a phenomenon attributed to wide-angle reflection from numerous dipping layers within the crust (Fig. 2.9b, 2.9c; Mereu and Epili, 1990; Epili and Mereu, 1991). Figure 2.10 shows the velocity model for profile J (Epili and Mereu, 1991).

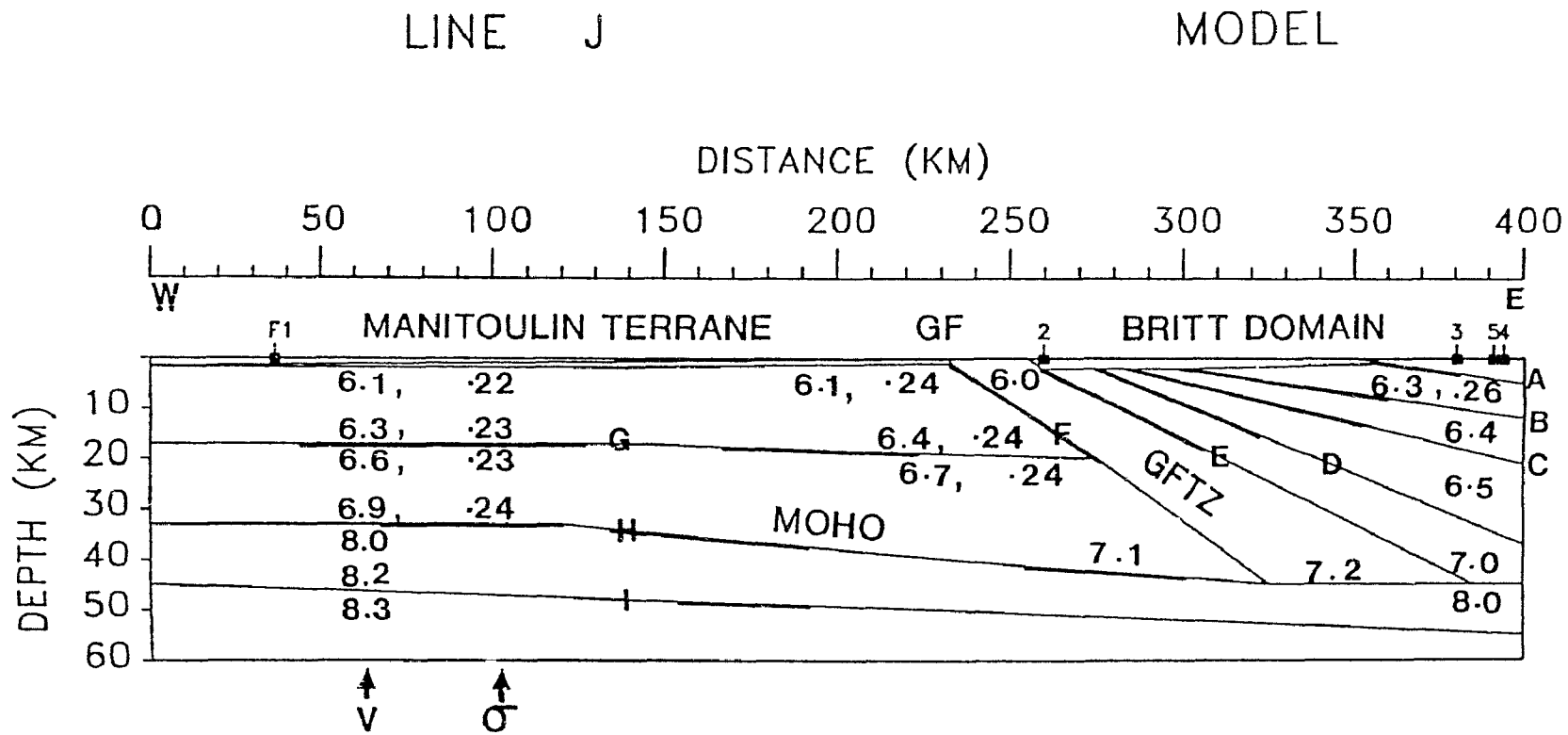


Fig. 2.10 P-wave velocity and Poisson's ratio ( $\sigma$ ) model for profile J (Epili and Mereu, 1991)

LITHOPROBE Lines 30 and 31

New seismic images of Grenville crustal structure were acquired within the western Grenville province in 1991 (White et al., 1993). Lines 30 and 31 cross the Parry Sound domain and extend into the Britt domain (Fig. 2.6). Predominantly east-dipping reflectors (A,B, in Fig. 2.11) are observed in the upper 10 km of the crust on line 30 in the vicinity of the Parry Sound Shear Zone, consistent with surface observations. The seismic section of line 31 shows reflectors dipping inward (A,B,F, Fig.2.12b) from the shear zones bounding the Parry Sound domain, converging at a depth of about 6 km. This geometry is in agreement with gravity profiles (Lindia et al., 1983; Fig. 2.12a). A prominent reflection beneath the Parry Sound domain (H,G, Fig. 2.11; 2.12b) is correlated to the CBSZ. The Parry Sound domain was interpreted as an allochthonous mass of lithologically distinct granulite facies rocks emplaced on a dominantly amphibolite facies lower deck composed of Britt domain lithologies on the northwest and Rosseau subdomain lithologies on the southeast (Davidson and Morgan, 1981; Davidson et al., 1982); the seismic and gravity data support this geological interpretation. Apart from the dipping reflectors which are associated with the shear zones, apparent sub-horizontal reflectors, which increase in reflectivity within the lower crust (E,C, Fig.2.11; 2.12b), characterize both of the seismic sections.

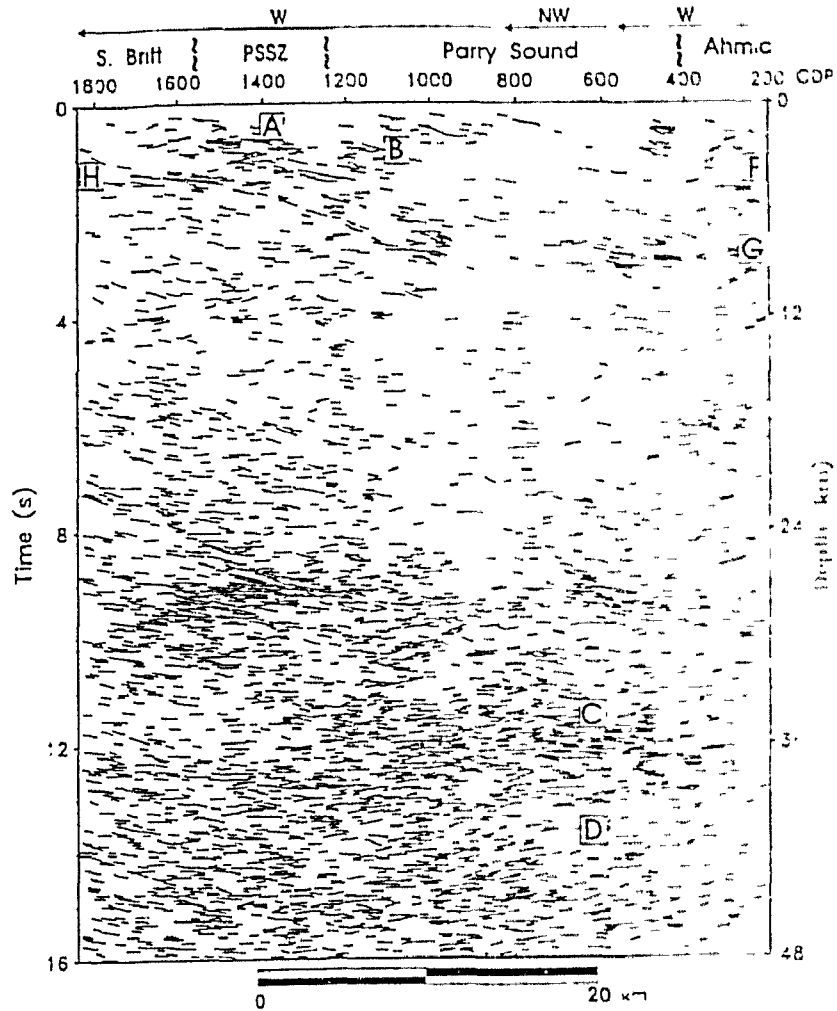
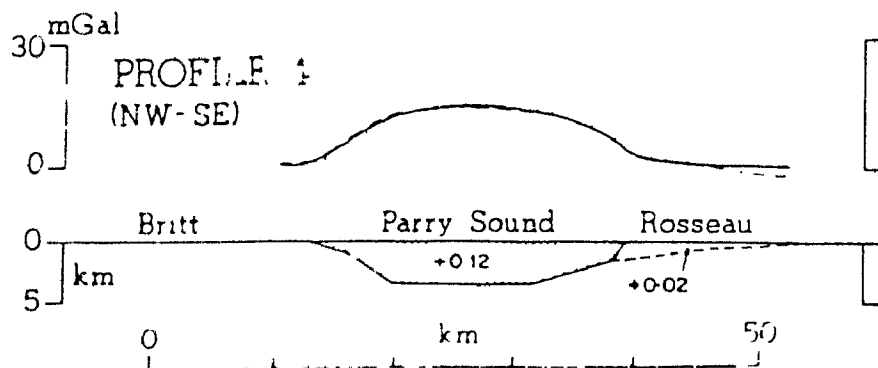
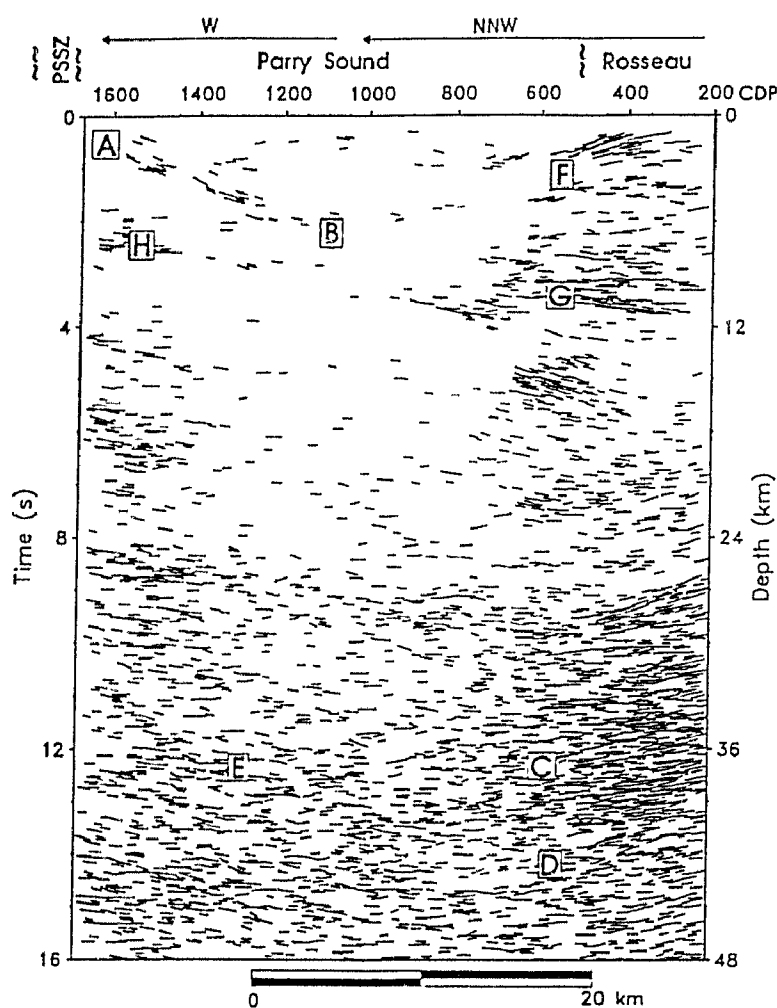


Fig. 2.11 Line drawing of LITHOPROBE reflection line 30. Labels are referred to in the text. Seismic profile orientation, CDP numbers and geological boundaries are identified across the top of the line drawings. From White et al., 1993.





(a)



(b)

Fig. 2.12 (a) Gravity profile at same location as line 31 showing bowl-shaped Parry Sound domain (Lindia et al., 1983). (b) Line drawing of LITHOPROBE reflection line 31. Labels are referred to in the text. Seismic profile orientation, CDP numbers and geological boundaries are identified across the top of the line drawing. From White et al., 1993.

### The Unresolved Problems

Regarding the present seismic data, three major problems remain unresolved:

(1) Since the Britt domain is in part allochthonous, it is not clear how far the surface geology extends in depth.

(2) Reflection profiles consistently show a moderate crustal reflectivity characterized by subhorizontal, scattered reflections. However, their origin is unclear.

(3) Although the "shingles" revealed by wide angle data from the Britt domain have been interpreted in terms of a series of dipping layers, vertical reflection data do not show these structures and surface geology does not support this interpretation. Thus, an alternative interpretation seems to be required.

To address these problems, laboratory studies of rock properties are essential. They can provide not only useful evidence for the interpretation of velocity models in terms of petrology, but also the parameters required by synthetic modelling to determine the potential causes of reflectivity. Finally, the results of laboratory measurements on the Britt domain rocks will provide baseline data on the velocity and density range of felsic gneisses which will be particularly useful since previous physical property studies have paid relatively little attention to these lithologies.

## Chapter 3

### LABORATORY VELOCITY MEASUREMENTS

#### Sample Descriptions

Eighty-four rock samples were collected for velocity measurements from the research area described in chapter one at the sites shown in Figure 3.1. The basic sampling criterion was to obtain field-oriented samples that are representative of each of the lithologic units mapped by Culshaw, et al. (1988, 1989) and Davidson and Bethune (1988). For units displaying a wide range in composition and deformation, more than one sample was taken in order to determine the range of velocity and anisotropy associated with each unit. Rocks that lacked secondary mineral alteration and visible fractures were chosen for laboratory measurements.

Thin section analyses were made for all rock samples to determine (1) modal mineralogies, (2) textures and fabrics and (3) mineral alteration. Modal mineralogies were determined by point-counting with at least 1000 points counted on each slide. Potassium feldspars were stained by sodium-cobaltinitrate to aid in identification where necessary. Mineralogical data for the velocity samples are summarized in Table 3.1 and the petrography based on thin section analysis is described below.

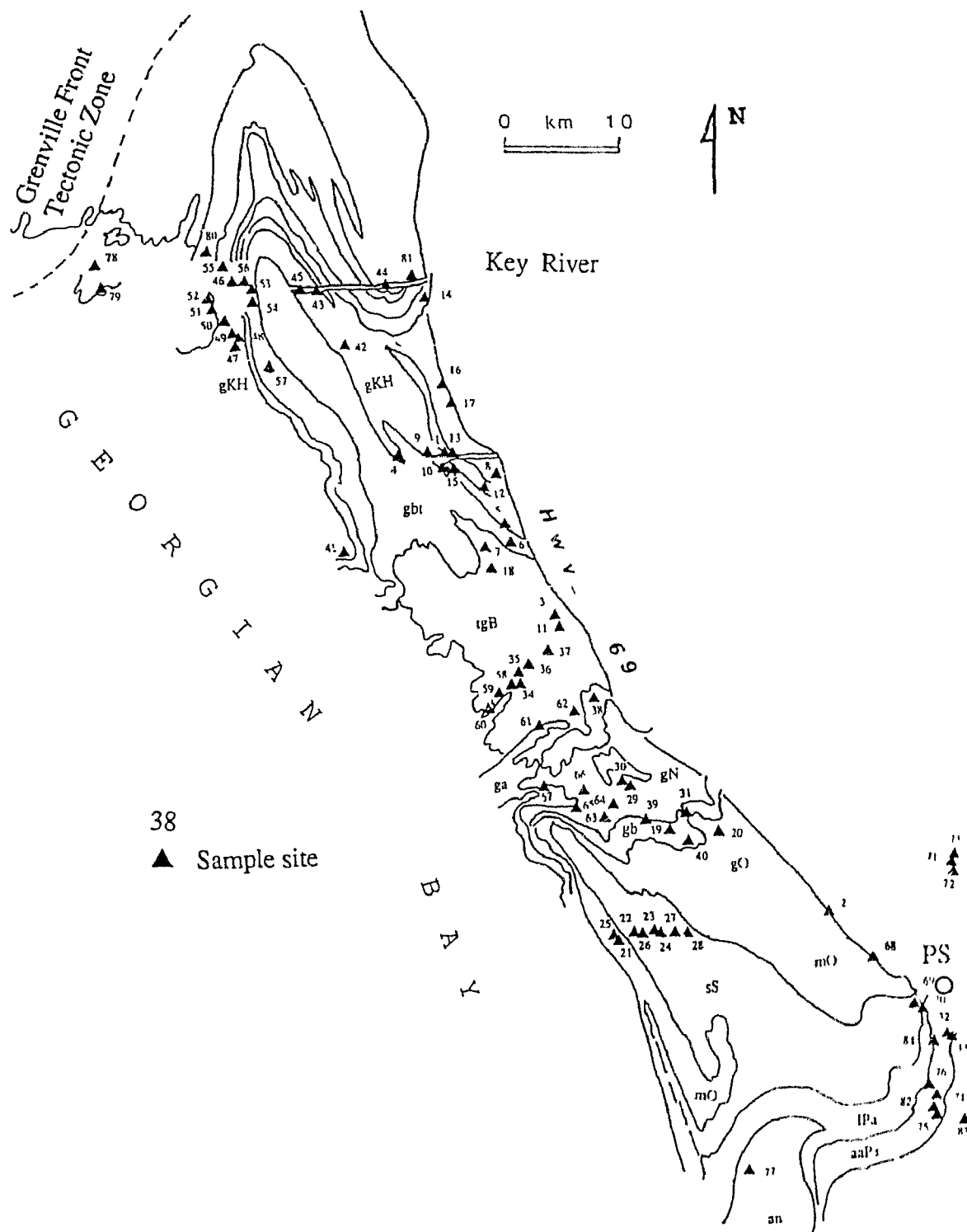


Fig.3.1 Location map of velocity sample sites. Symbols as in Figure 2.3. PS denotes Parry Sound.

Table 3.1 Mineralogy of Britt Samples (vol.%)

Sample	Lithology	Otz	Plg	Ksp	Bio	Hb	Px	Gt	Opg	Ap	Zir	Sph	Chl	Mus	Epi
B 1	Granodiorite	20.8	50.9	13.3	6.1	2.5	0.0	0.0	0.4	0.1	0.1	0.5	0.3	0.0	0.0
B 2	Granite	23.1	10.1	53.8	6.2	2.4	0.0	0.0	0.0	0.1	0.0	0.9	0.0	0.0	1.4
B 3	Metadiabase	4.2	13.9	0.0	0.1	48.4	15.7	17.6	3.6	0.5	0.0	0.0	0.0	0.0	0.0
B 4	Granite	27.9	45.3	20.3	5.2	0.1	0.0	0.0	0.1	0.0	0.0	0.4	0.3	0.1	0.1
B 5	Granite	27.3	2.6	66.4	3.4	0.0	0.0	0.0	0.1	0.1	0.0	0.1	0.0	0.0	0.0
B 6	Granodiorite	20.9	57.7	10.5	3.5	6.4	0.0	0.0	0.3	0.3	0.1	0.1	0.2	0.0	0.0
B 7	Granodiorite	20.8	58.8	8.4	5.3	6.1	0.0	0.0	0.0	0.1	0.1	0.1	0.1	0.0	0.2
B 8	Granite	25.3	15.2	42.7	5.8	0.0	0.0	0.0	0.0	0.1	0.0	0.5	0.0	0.0	0.4
B 9	Granite	43.9	3.9	47.2	4.4	0.0	0.0	0.0	0.4	0.1	0.1	0.0	0.0	0.0	0.0
B 10	Granite	20.5	38.1	34.4	5.7	0.0	0.0	0.0	0.7	0.1	0.0	0.3	0.0	0.2	0.0
B 11	Granite	22.9	2.6	67.3	6.5	0.0	0.0	0.1	0.2	0.1	0.1	0.0	0.2	0.0	0.0
B 13	Amphibolite	2.6	29.6	0.5	5.3	34.1	10.1	10.5	5.6	0.9	0.0	0.0	0.8	0.0	0.0
B 14	Granodiorite	40.1	38.3	11.2	1.8	6.8	0.0	0.2	0.5	0.2	0.2	0.0	0.7	0.0	0.0
B 15	Granite	42.1	8.3	47.9	1.1	0.0	0.0	0.1	0.4	0.0	0.1	0.0	0.0	0.0	0.0
B 16	Diorite	7.6	66.2	1.2	12.5	10.4	0.0	0.0	0.0	0.2	0.1	0.0	1.5	0.0	0.3
B 18	Granite	38.4	5.5	54.6	1.1	0.0	0.0	0.1	0.0	0.0	0.1	0.0	0.1	0.1	0.0
B 19	Paragneiss	30.2	18.9	31.6	14.9	0.0	0.0	3.5	1.6	0.0	0.1	0.0	0.0	0.1	0.0
B 20	Granite	22.5	4.9	60.0	10.5	0.0	0.0	0.0	0.0	0.1	0.0	0.0	0.6	0.2	1.2
B 21	Granite	27.0	5.5	63.9	2.9	0.0	0.0	0.0	0.5	0.0	0.0	0.0	0.1	0.1	0.0
B 22	Paragneiss	20.5	15.4	40.2	18.0	0.0	0.0	0.0	3.9	0.1	0.0	0.0	0.0	1.9	0.0
B 23	Metadiabase	1.1	43.9	1.0	0.3	50.4	0.0	0.0	0.0	0.3	0.1	2.9	0.0	0.0	0.0
B 24	Granite	81.3	6.6	0.0	10.2	0.0	0.0	0.0	1.5	0.3	0.1	0.0	0.0	0.0	0.0
B 25	Diorite	17.4	14.3	2.6	5.6	9.1	0.0	0.6	0.0	0.2	0.1	0.1	0.0	0.0	0.0
B 26	Paragneiss	5.0	5.5	74.4	15.0	0.0	0.0	0.0	0.0	0.1	0.0	0.0	0.0	0.0	0.0
B 28	Granite	31.4	11.3	52.1	2.5	0.0	0.0	0.0	2.5	0.1	0.0	0.1	0.0	0.0	0.0
B 29	Granite	21.8	29.2	36.4	4.1	7.2	0.0	0.0	0.0	0.1	0.1	0.1	0.0	0.1	0.0
B 30	Paragneiss	0.5	52.8	7.1	34.8	0.0	0.0	1.5	0.7	0.1	0.1	0.1	0.0	2.3	0.0
B-31	Amphibolite	1.4	38.2	0.0	3.5	39.8	0.2	13.9	2.8	0.2	0.0	0.0	0.0	0.0	0.0
B 32	Amphibolite	4.2	23.3	1.5	0.6	38.6	27.4	0.0	2.3	0.0	0.0	0.0	2.1	0.0	0.0
B 33	Granite	50.8	3.1	39.9	3.5	1.0	0.0	0.0	1.5	0.0	0.1	0.0	(Calcite	0.1)	
B 34	Amphibolite	7.6	42.3	1.2	7.1	39.9	0.0	0.1	1.1	0.2	0.0	0.1	0.3	0.0	0.1
B 35	Granite	25.2	5.7	63.1	4.6	0.0	0.0	0.0	0.0	0.1	0.0	0.0	0.5	0.7	0.1
B 36	Granite	23.0	13.5	59.8	2.5	0.0	0.0	0.0	1.0	0.1	0.1	0.0	0.0	0.0	0.0
B-37	Amphibolite	3.1	48.3	0.0	7.0	41.1	0.0	0.0	0.2	0.1	0.0	0.2	0.0	0.0	0.0
B-38	Paragneiss	22.8	53.5	1.3	13.4	5.9	0.0	2.2	0.2	0.2	0.1	0.2	0.1	0.0	0.0
B 39	Paragneiss	37.9	39.3	0.0	21.5	0.0	0.0	1.1	0.1	0.1	0.0	0.0	0.0	0.0	0.0
B-40	Granite	21.5	14.7	53.2	10.1	0.0	0.0	0.1	0.1	0.1	0.1	0.0	0.0	0.0	0.0
B 41	Granite	20.5	5.0	62.3	11.6	0.0	0.0	0.0	0.5	0.1	0.0	0.0	0.0	0.0	0.0
B-42	Metadiabase	0.5	46.4	0.0	23.8	0.0	9.4	13.7	4.6	1.6	0.0	0.0	0.0	0.0	0.0
B 43	Granite	40.8	27.0	30.0	0.3	0.7	0.0	0.0	0.8	0.1	0.1	0.0	0.1	0.1	0.0
B 44	Granodiorite	31.8	59.1	2.9	6.1	0.0	0.0	0.0	0.0	0.1	0.0	0.0	0.0	0.0	0.0
B-45	Metadiabase	1.2	23.4	0.0	5.3	59.0	0.0	6.4	3.2	0.1	0.0	0.0	0.5	0.0	0.9
B-46	Granite	20.7	31.7	33.2	9.3	3.1	0.0	0.1	0.8	0.2	0.0	0.3	0.2	0.0	0.2
B 47	Granite	27.3	5.5	62.2	0.0	0.9	0.0	0.0	2.1	0.1	0.0	0.0	1.9	0.0	0.0
B-48	Diorite	7.9	68.9	0.0	10.3	11.6	0.0	0.5	0.7	0.1	0.0	0.0	0.0	0.0	0.0
B 49	Granite	30.0	0.6	67.0	1.5	0.0	0.0	0.0	0.2	0.1	0.1	0.0	0.4	0.1	0.0
B 50	Granite	43.3	19.8	35.7	0.5	0.0	0.0	0.0	0.5	0.1	0.0	0.0	0.0	0.1	0.0
B 51	Granite	24.1	10.3	63.4	0.0	0.0	0.0	0.0	1.3	0.1	0.1	0.0	0.7	0.0	0.0
B 52	Anorthosite	0.2	79.9	2.1	3.1	6.7	0.0	6.4	0.5	0.3	0.1	0.0	0.0	0.0	0.0
B 53	Amphibolite	1.1	45.6	0.4	3.5	46.2	0.2	2.6	0.3	0.1	0.0	0.0	0.0	0.0	0.0
B-54	Metadiabase	0.8	33.4	0.0	12.3	30.7	0.0	0.0	3.5	1.5	0.0	0.0	17.8	0.0	0.0
B 55	Metadiabase	0.4	27.9	0.0	16.4	3.8	25.4	21.6	4.2	0.0	0.0	0.0	0.0	0.0	0.0
B 56	Granite	22.1	3.8	73.5	0.5	0.0	0.0	0.0	0.0	0.1	0.0	0.0	0.0	0.0	0.0
B 57	Amphibolite	0.5	42.4	0.3	1.9	49.7	2.2	1.7	0.0	0.2	0.0	0.0	1.1	0.0	0.0
B 58	Granite	20.3	11.5	62.9	4.4	0.0	0.0	0.3	0.5	0.0	0.1	0.0	0.0	0.0	0.0
B 59	Amphibolite	1.1	29.0	0.0	0.5	61.4	0.1	5.5	1.9	0.1	0.0	0.0	0.4	0.0	0.0
B 60	Granite	25.4	1.5	73.8	0.8	0.0	0.0	0.0	0.2	0.0	0.1	0.0	0.1	0.1	0.0

Table 3.1 (cont)

Sample lithology	Qtz	Plg	Ksp	Bio	Hb	Px	Gt	Opq	Ap	Zir	Sph	Chl	Mus	Epi
B-61 Granite	25.6	15.2	47.7	4.8	4.1	0.0	0.0	2.5	0.1	0.1	0.0	0.3	0.1	0.0
B-62 Granodiorite	25.2	67.3	0.5	7.1	0.0	0.0	0.0	0.0	0.1	0.0	0.3	1.3	0.2	0.0
B-63 Granodiorite	22.1	58.1	9.6	4.5	3.3	0.5	0.3	0.3	0.1	0.1	0.0	1.1	0.0	0.0
B-64 Granite	40.4	5.1	52.3	0.3	0.0	0.0	0.1	0.8	0.0	0.0	0.0	0.0	0.0	0.0
B-65 Granite	20.5	29.8	26.2	7.4	10.5	0.0	0.0	5.1	0.3	0.2	0.0	0.0	0.0	0.0
B-66 Granite	20.2	39.8	29.5	6.6	1.4	0.0	0.1	2.0	0.3	0.1	0.0	0.0	0.0	0.0
B-67 Granite	40.4	9.8	47.7	1.6	0.0	0.0	0.0	0.4	0.1	0.0	0.0	0.0	0.0	0.0
B-68 Granite	40.6	6.5	47.4	4.2	0.0	0.0	0.0	0.0	0.1	0.1	0.8	0.0	0.3	0.1
B-69 Granite	21.8	1.9	59.7	9.5	5.9	0.0	0.0	0.0	0.2	0.1	0.7	0.2	0.0	0.0
B-70 Granodiorite	40.8	38.1	5.2	8.5	6.0	0.0	0.0	0.0	0.1	0.0	0.6	0.0	0.0	0.7
B-71 Marble	( Calcite	95.9				3.6	0.0	0.0	0.0	0.0	0.0	0.0	0.5	0.0
B-72 Dunite	( Olivine	98.4				0.0	0.0	0.0	0.1	0.0	0.0	0.0	0.0	0.0
B-73 Anorthosite	0.9	78.8	4.9	2.0	4.5	4.2	3.5	0.8	0.1	0.0	0.0	0.2	0.1	0.0
B-74 Amphibolite	8.1	26.3	0.0	21.3	42.9	0.0	0.0	0.0	0.2	0.2	0.5	0.0	0.5	0.0
B-75 Amphibolite	2.3	63.5	0.0	0.0	10.4	20.2	3.5	0.0	0.1	0.0	0.0	0.0	0.0	0.0
B-77 Anorthosite	0.0	94.3	0.0	0.0	3.0	2.2	0.0	0.0	0.0	0.0	0.0	0.5	0.0	0.0
B-78 Diorite	7.0	67.2	1.8	7.6	14.9	0.0	0.7	0.0	0.2	0.1	0.1	0.4	0.0	0.0
B-79 Granodiorite	38.6	49.8	6.4	5.3	0.0	0.0	0.0	0.0	0.1	0.1	0.0	0.0	0.0	0.0
B-80 Anorthosite	0.3	79.4	4.1	4.5	10.9	0.0	0.4	0.0	0.2	0.0	0.0	0.0	0.2	0.0
B-81 Granite	38.8	20.8	25.5	3.8	0.0	0.0	0.0	1.0	0.1	0.0	0.0	0.0	0.0	0.0
B-82 Diorite	11.6	58.8	0.0	0.0	16.2	0.0	10.3	2.9	0.2	0.0	0.0	0.0	0.0	0.0
B-83 Diorite	7.9	71.0	0.3	10.4	8.6	0.0	0.0	0.6	0.3	0.0	0.4	0.5	0.0	0.1
B-84 Amphibolite	1.5	48.4	0.0	0.0	45.1	0.0	0.0	0.0	0.1	0.0	4.9	0.0	0.0	0.0

Abbreviations as follows: Qtz, quartz; Plg, plagioclase; Ksp, k-feldspar; Bio, biotite; Hb, hornblende; Px, pyroxene; Gt, garnet; Opq, opaque oxides; Ap, apatite; Zir, zircon; Sph, sphene; Chl, chlorite; Mus, muscovite; Epi, epidote.

### Granitic to Intermediate Orthogneiss

Fifty-one samples of orthogneiss were collected for velocity measurements. These include single cycle plutonic rocks and granitic-intermediate orthogneisses from different gneiss associations. Many of these rocks have well developed foliations and some of them show beautiful quartz ribbons. The foliation is usually defined by shape fabrics within the LS scheme such as quartz blades or feldspar augen, preferred orientation of biotite and hornblende or compositional layering. Although the gneisses have clearly experienced high finite strains, most of them display granoblastic textures and all minerals show limited amounts of optically visible intragranular deformation except for a few samples in which quartz exhibits undulatory extinction and subgrain development.

Based on the I.U.G.S. classification scheme, the orthogneiss samples are classified into three groups (Fig. 3.2): (1) granite (36 samples), (2) granodiorite and tonalite (9 samples) and (3) diorite and quartz diorite (6 samples). Accessory minerals in these rocks include biotite, hornblende, opaque oxides, sphene, apatite, zircon and chlorite. There is no significant secondary mineral alteration within these samples. It is notable that there are quite a few samples in the granitic group having high contents of K-feldspar.

Samples B-33 (granite) and B-82 (diorite) are mylonites taken from the Parry Sound shear zone. They differ from other

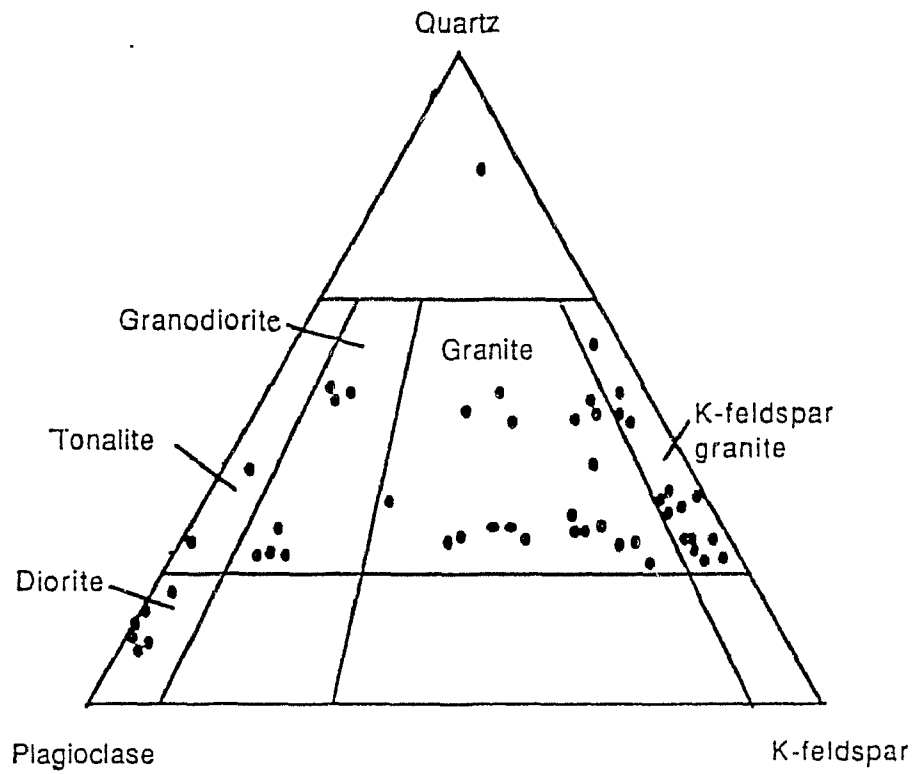


Fig. 3.2 Ternary diagram for the orthogneiss samples.



samples in this group in their fine grain size and strong tectonite fabrics. Samples B-58, 59, 65 and 66, taken from the Central Britt shear zone, are not true mylonites, but their distinct fine grain size and porphyroclastic textures indicate that they have suffered strong deformation.

### Paragneiss

A mica + garnet content greater than 15% is used as the criterion to distinguish paragneiss from orthogneiss. Six samples (B-19, 22, 26, 30, 38 and 39,) are classified as paragneiss. Typical features of these samples include well developed foliation defined by biotite preferred orientation, biotite layering and quartz ribbons. Sample B-38, taken near the Central Britt shear zone, is a fine-grained rock with a strong tectonite fabric indicating high finite strain. There is no visible foliation in sample B-26, but it has a well developed lineation defined by the (001) trend of biotite.

The mineralogy of the paragneiss samples is more varied than that of orthogneiss. Plagioclase, potassium feldspar, quartz and biotite are the principal rock-forming minerals and muscovite, garnet and hornblende are locally present in significant amounts. Common accessory minerals include opaque oxides, apatite and zircon.

### Mafic and Ultramafic Rocks

As described in chapter one, three distinct types of mafic rocks occur within the region, including: (1) small

bodies of amphibolite that resemble early mafic dikes or sills that have been dismembered (Culshaw et al., 1988), (2) equant masses or dikes of metadiabase and (3) metagabbro bodies.

Twelve samples (B-23, 31, 32, 34, 37, 45, 53, 57, 59, 74, 75 and 84) of amphibolite were collected. Well developed foliation defined by hornblende and biotite preferred orientation and quartz ribbons are typical features of these samples. Quartz undulatory extinction is observed in samples B-32, 34 and 75 and the plagioclase has bent twins in samples B-31 and 75. Samples B-59, 74 and 84, which were taken from shear zones, are fine-grained and have mylonitic features. All of the amphibolites consist predominantly of plagioclase and hornblende but biotite occurs in most samples and garnet, opaque oxides, apatite, sphene and chlorite are locally present as accessory minerals. Sample B-31 has an unusually high garnet content (13.9%) and sample B-32 has a high pyroxene content (27%).

Samples B-13, 42, 54 and 55 are metadiabases. Although B-13 is weakly foliated, there is no clear evidence of GFTZ-style deformation in these rocks, and they display original ophitic textures. Sample B-13 has hornblende, plagioclase, pyroxene and garnet as its major minerals and minor amounts of opaque oxides and biotite. The hornblende is found as an alteration product of pyroxene and as inclusions in large garnet crystals. Plagioclase, pyroxene, biotite and garnet are the major minerals in samples B-42 and 55; corona

structures and garnet rims are observed in both samples. Sample B-54 has a distinctive mineralogy compared to the other metadiabase rocks. It lacks pyroxene and garnet, and instead, has a high content (17.8%) of chlorite produced by alteration.

Anorthosite occurs at several locations in the area as bodies and sheets of various sizes (see chapter one). Four samples (B-52, 73, 77 and 80) were collected to represent this lithology. Although plagioclase predominates (>79%), hornblende is present in all samples. Minor amounts of other minerals including biotite, garnet, pyroxene, chlorite and muscovite are locally present. All samples are weakly foliated due to hornblende and biotite preferred orientation. Hornblende and biotite layering and banding are observed in samples B-52 and B-77.

Sample B-72 is a dunite taken from the Parry Sound Shear Zone 20 km northeast of Parry Sound. It consists predominantly of olivine (98.4%) and minor apatite.

#### Experimental Methods

The measurement of seismic wave velocity is basically an application of the pulse transmission technique (Birch, 1960) in which an electrical pulse is applied to a transducer at one end of a specimen and the resulting disturbance is transmitted through the specimen to a receiving transducer where the mechanical signal is converted to an electrical

signal, then amplified and displayed on an oscilloscope. The velocity is obtained from the travel time and the length of the specimen after correction for system delays.

#### Specimen preparation

To prepare the samples for velocity measurement, each specimen was cut into right cylinders approximately 2.54 cm in diameter and 3.8 cm in length. Three mutually perpendicular cores were taken from those rock samples in which both foliation and lineation were developed (Fig. 3.3). One core was taken normal to the foliation plane of the rock (core A) and two were taken within the foliation plane: one parallel to the lineation (B) and one normal to the lineation (C). If the rock was foliated but not lineated, core B was arbitrarily placed in the foliation plane and core C was not taken. For a few rock samples that displayed neither foliation nor lineation, such as B-3, 42 and 55, only one core was cut in an arbitrary direction because such rocks are generally seismically isotropic. Smooth parallel core ends were produced by machine lapping to ensure accurate bulk density estimations and velocity measurements. The bulk density of each core was calculated from its mass and dimensions.

Following the density measurements, each core was jacketed in copper foil and thin (0.005 mm) brass foil shims were placed on the core ends to provide a ground for the transducers. For  $V_p$ , the jacketed sample was placed between

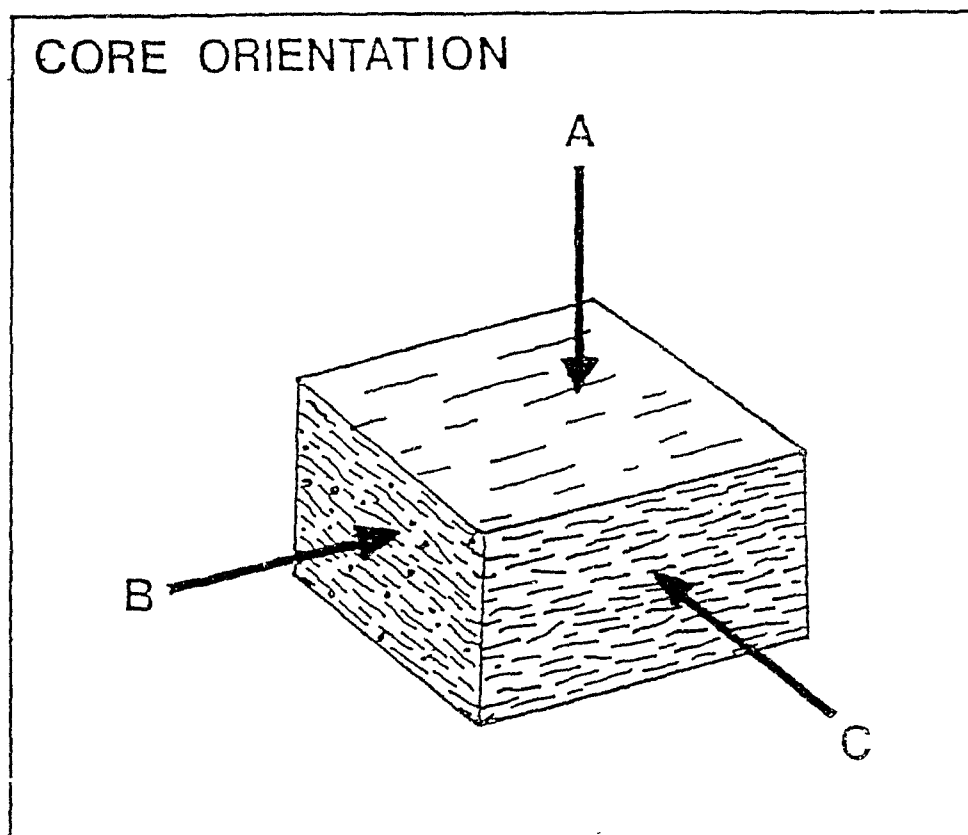


Fig. 3.3 Schematic diagram showing core orientation conventions from Burke (1991). The "A" direction is normal to the foliation, "B" is parallel to the lineation, if present, and "C" is normal to the lineation.

two piezoelectric transducers made of lead zirconate with a resonant frequency of 1 MHz. For  $V_s$ , 1 MHz lead zirconate titanate transducers were used, with the vibration direction oriented with respect to foliation and/or lineation. Then the transducers were backed with brass electrodes. Tight gum-rubber tubing was used to hold the sample assembly together (Fig. 3.4) and to prevent saturation of the core by the pressure fluid.

### Velocity Measurements

The sample assemblies (up to four at a time) were put in a sample holder and then placed in a large pressure vessel where hydrostatic confining pressures up to 600 MPa were generated using an air-driven fluid pump in conjunction with a multi-stage fluid intensifier system. The pressure fluid was a low viscosity oil (ESSO MONOPLEX). A strain gauge on the high pressure side of the intensifier was used to monitor the pressure and display it digitally.

With the sample holder sealed in the vessel, the sending transducer was activated by a +50v spike and the signal from the receiving transducer was stacked over 400 pulse repetitions to reduce the signal to noise ratio before being displayed on a Nicolet digital oscilloscope. The first break of the waveforms was manually picked in order to determine the travel time of the pulse through the specimen. Velocities were then calculated at selected pressures and smooth velocity-pressure curves were fit to the data.

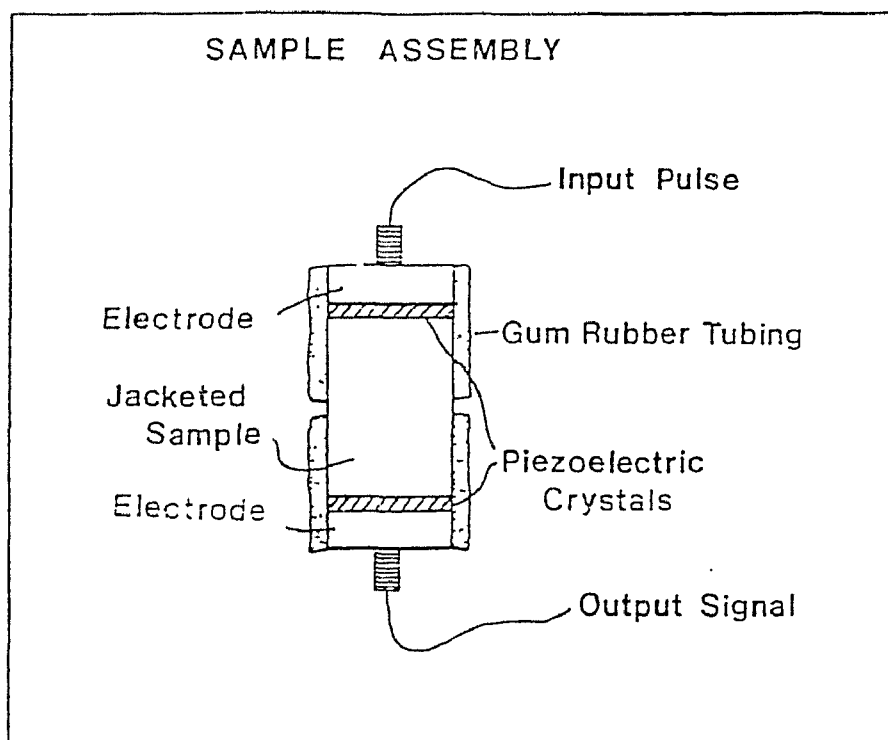


Fig. 3.4 Schematic diagram of the sample assembly from Burke (1991) showing the jacketed sample placed between transducers and electrodes. The tubing holds the assembly together and prevents saturation of the sample with the pressure fluid.

As noted by many investigators (e.g. Birch, 1961), the velocity measured during initial pressurization is commonly lower than the velocity measured as pressure is decreased (Fig. 3.5). This phenomenon, termed velocity hysteresis, is observed in rocks at pressures below 200 MPa and is attributed to the sealing of microcracks at high pressures (Birch, 1961; Gardner et al., 1965) because it is not observed in either single crystals (McSkimin and Andreatch, 1962) or in fused quartz samples with air bubbles (Peselnick and Wilson, 1968). Only velocities obtained during depressurization are reported here since they are reproducible and considered representative of in situ conditions (Burke, 1991).

Errors in velocity measurement may arise from several sources: (1) Errors in measuring core length and travel time. Core lengths are accurate to 0.005 cm and travel time to 2.5 nanoseconds. This results in velocity measurements which are accurate to 0.4 per cent for standard length cores (Burke, 1991). (2) Changes in sample length at elevated confining pressure. No corrections were made for this effect in the present study because it is significant only in the calculation of pressure derivatives (e.g. Brace, 1965) at the pressures considered here. The absolute error associated with the pulse transmission technique is generally regarded to be less than 0.5% for  $V_p$  and 1% for  $V_s$  (Christensen and Shaw, 1970).



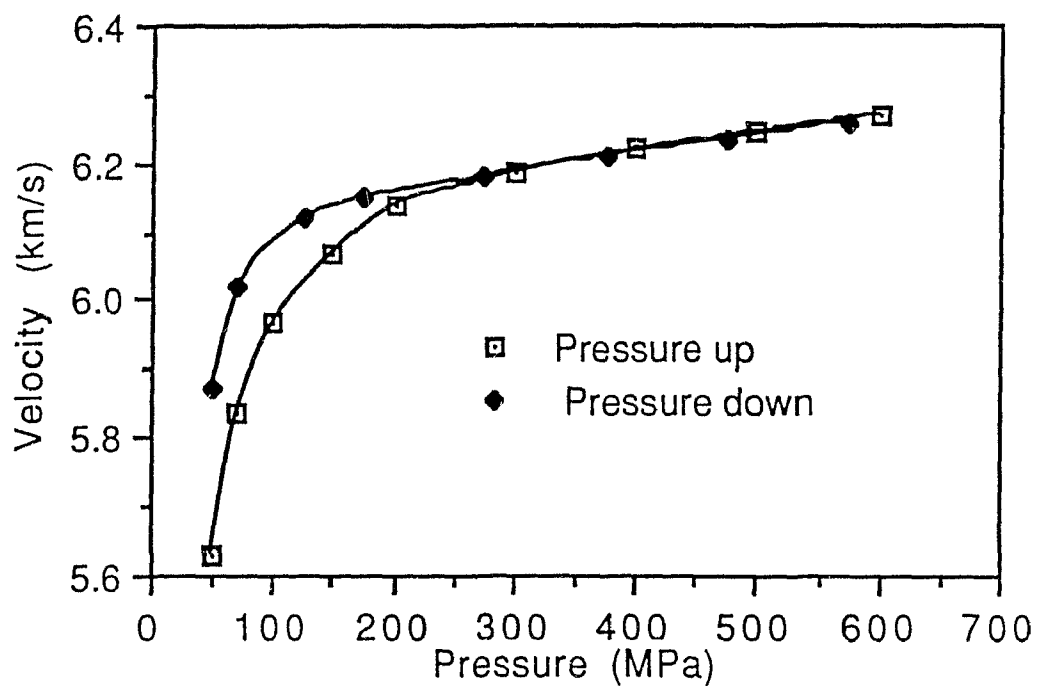


Fig. 3.5 Compressional wave velocity as a function of confining pressure for sample B-43, showing the typical initial increase in velocity with increasing pressure and linear behavior at high pressures. At low pressures, the velocity measured during initial pressurization is lower than the velocity measured as pressure is decreased.

## Experimental Results

Compressional wave velocities for eighty samples and shear wave velocities for seven selected samples are summarized as a function of pressure, propagation direction and vibration direction in Tables 3.2 and Table 3.3, respectively. The samples chosen for  $V_s$  measurement were those with average values of  $V_p$  closest to the mean  $V_p$  calculated for that lithology. (Velocity data for samples B-12, 17, 27 and 76 were not obtained due to saturation during the experiments or to break-up during preparation). The mean velocities shown in Table 3.2 and Table 3.3 were obtained from the relations

$$V_p \text{ (mean)} = (V_A + V_B + V_C)/3 \quad (1)$$

and

$$V_s \text{ (mean)} = (V_{AB} + V_{AC} + V_{BA} + V_{BC} + V_{CA} + V_{CB})/6 \quad (2),$$

where the first letter indicates the propagation direction and the second (in the case of  $V_s$ ) indicates the vibration direction. For transversely isotropic samples in which velocities were measured in only two directions, the mean values were obtained from

$$V_p \text{ (mean)} = (V_A + 2V_B)/3 \quad (3)$$

and

$$V_s \text{ (mean)} = (V_{AB} + V_{BA} + V_{BC})/3 \quad (4)$$

Table 3.2 Densities and Compressional Wave velocities of Britt Samples at Various Confining Pressures.

Sample	Lithology	Density	Pressure, MPa							
		g/cm <sup>3</sup>	20	40	60	80	100	200	400	600
B-1A	Granodiorite	2.746	5.87	6.71	6.07	6.11	6.13	6.16	6.20	6.23
B		2.709	5.71	5.88	5.97	6.02	6.07	6.16	6.20	6.24
Ave.		2.728	5.76	5.92	6.00	6.06	6.09	6.16	6.20	6.24
B-2A	Granite	2.698	5.38	5.88	6.03	6.09	6.12	6.17	6.21	6.24
B		2.697	6.08	6.34	6.41	6.44	6.48	6.53	6.56	6.58
Ave.		2.698	5.85	6.19	6.28	6.32	6.36	6.42	6.44	6.47
B-3	Metadiabase	3.243	6.45	6.70	6.81	6.89	6.94	7.02	7.08	7.11
B-4A	Granite	2.695	5.66	5.85	5.91	5.96	5.98	6.03	6.11	6.18
B		2.696	5.69	5.88	5.99	6.03	6.06	6.12	6.15	6.23
Ave.		2.696	5.69	5.87	5.96	6.01	6.03	6.09	6.14	6.21
B-5A	Granite	2.625	5.60	5.96	6.13	6.23	6.30	6.42	6.48	6.52
B		2.627	5.70	5.99	6.16	6.22	6.27	6.38	6.43	6.48
Ave.		2.626	5.67	5.98	6.15	6.22	6.28	6.39	6.45	6.49
B-6A	Granodiorite	2.730	5.61	5.96	6.14	6.23	6.27	6.38	6.44	6.48
B		2.784	5.93	6.20	6.83	6.33	6.36	6.43	6.51	6.56
Ave.		2.757	5.82	6.12	6.23	6.30	6.33	6.42	6.49	6.53
B-7A	Granodiorite	2.716	5.39	5.61	5.73	5.79	5.82	5.92	5.97	6.00
B		2.614	6.24	6.46	6.56	6.59	6.62	6.73	7.71	6.74
Ave.		2.665	5.96	6.18	6.28	6.32	6.36	6.42	6.46	6.49
B-8A	Granite	2.643	5.42	5.80	5.99	6.08	6.14	6.27	6.32	6.34
B		2.679	5.70	6.00	6.11	6.18	6.22	6.31	6.36	6.39
Ave.		2.661	6.61	6.93	6.07	6.15	6.19	6.30	6.35	6.37
B-9A	Granite	2.633	5.47	5.77	5.87	5.94	5.98	6.04	6.08	6.12
B		2.616	5.20	5.70	5.93	6.04	6.13	6.26	6.34	6.36
C		2.612	5.98	6.14	6.19	6.22	6.24	6.27	6.32	6.36
Ave.		2.620	5.55	5.87	6.00	6.07	6.12	6.19	6.25	6.28
B-10A	Granite	2.661	5.90	6.10	6.16	6.19	6.21	6.24	6.28	6.32
B		2.668	5.95	6.14	6.20	6.24	6.26	6.30	6.31	6.33
C		2.661	5.61	5.96	6.03	6.07	6.10	6.19	6.24	6.27
Ave.		2.663	5.82	6.07	6.13	6.17	6.19	6.24	6.28	6.31
B-11A	Granite	2.662	5.76	5.93	5.99	6.02	6.03	6.07	6.14	6.20
B		2.663	5.75	5.82	5.96	6.04	6.09	6.20	6.26	6.32
Ave.		2.663	5.64	5.86	5.97	6.03	6.07	6.16	6.22	6.28

Sample	Lithology	Density g/cm <sup>3</sup>	Pressure, MPa							
			20	40	60	80	100	200	400	500
B-13A	Amphibolite	3.075	6.30	6.40	6.43	6.45	6.47	6.50	6.53	6.57
B		3.061	6.60	6.90	7.02	7.08	7.11	7.18	7.22	7.24
C		3.105	6.42	6.53	6.58	6.61	6.63	6.67	6.73	6.77
Ave.		3.080	6.44	6.61	6.68	6.71	6.74	6.79	6.83	6.86
B-14A	Granodiorite	2.684	5.69	6.00	6.12	6.18	6.22	6.26	6.31	6.36
B		2.683	5.74	6.08	6.15	6.18	6.23	6.32	6.38	6.42
Ave.		2.684	5.72	6.05	6.14	6.18	6.23	6.30	6.36	6.40
B-15A	Granite	2.626	5.58	5.80	5.97	6.06	6.12	6.20	6.25	6.30
B		2.612	5.56	5.88	6.02	6.09	6.13	6.20	6.25	6.30
Ave.		2.624	5.57	5.86	6.00	6.08	6.13	6.20	6.25	6.30
B-16A	Diorite	2.776	5.62	5.76	5.82	5.86	5.89	5.97	6.05	6.11
B		2.790	6.26	6.34	6.42	6.45	6.47	6.52	6.56	6.59
Ave.		2.783	6.05	6.15	6.22	6.25	6.28	6.34	6.39	6.43
B-18A	Granite	2.603	5.34	5.75	5.98	6.05	6.09	6.14	6.15	6.17
B		2.597	5.43	5.75	5.94	6.02	6.06	6.13	6.18	6.23
C		2.608	5.38	5.82	5.99	6.03	6.06	6.13	6.12	6.22
Ave.		2.603	5.38	5.77	5.97	6.04	6.07	6.13	6.17	6.21
B-19A	Paragneiss	2.712	5.92	6.01	6.08	6.14	6.20	6.29	6.37	6.45
B		2.739	5.85	6.02	6.09	6.14	6.17	6.22	6.27	6.29
Ave.		2.726	5.87	6.02	6.09	6.14	6.18	6.24	6.30	6.35
B-20A	Granite	2.526	5.98	6.22	6.30	6.36	6.39	6.48	6.53	6.56
B		2.675	5.85	6.20	6.29	6.34	6.37	6.44	6.49	6.52
Ave.		2.601	5.89	6.21	6.29	6.35	6.38	6.45	6.50	6.53
B-21A	Granite	2.591	5.34	5.59	5.73	5.78	5.82	5.87	5.96	5.99
C		2.605	5.20	5.44	5.59	5.71	5.79	5.97	6.06	6.12
Ave.		2.598	5.25	5.49	5.64	5.73	5.80	5.94	6.03	6.08
B-22A	Paragneiss	2.762	5.32	5.54	5.63	5.68	5.72	5.79	5.88	5.93
B		2.757	5.47	5.73	5.83	5.92	5.97	6.08	6.16	6.22
Ave.		2.760	5.42	5.67	5.76	5.84	5.89	5.98	6.07	6.12
B-23	Metadiabase	3.003	6.54	6.77	6.91	6.98	7.02	7.11	7.18	7.22
B-24A	Granite	2.710	5.75	5.89	5.95	5.98	6.00	6.05	6.10	6.14
B		2.714	6.00	6.11	6.16	6.20	6.22	6.28	6.34	6.37
C		2.711	5.46	5.60	5.65	5.70	5.73	5.82	5.86	5.90
Ave.		2.712	5.74	5.87	5.92	5.96	5.98	6.05	6.10	6.14

Sample	Lithology	Density g/cm <sup>3</sup>	Pressure, MPa							
			20	40	60	80	100	200	400	600
B-25A	Diorite	2.779	5.50	5.82	6.03	6.14	6.23	6.36	6.46	6.51
B		2.763	5.87	6.10	6.21	6.28	6.33	6.45	6.56	6.60
C		2.755	5.32	5.66	5.85	5.98	6.06	6.23	6.35	6.41
Ave.		2.766	5.56	5.86	6.03	6.13	6.21	6.35	6.46	6.51
B-26A	Paragneiss	2.704	5.12	5.50	5.76	5.84	5.89	6.01	6.11	6.19
B		2.684	5.86	6.20	6.33	6.37	6.41	6.49	6.57	6.63
C		2.688	5.02	5.57	5.84	5.98	6.03	6.18	6.25	6.26
Ave.		2.692	5.33	5.76	5.98	6.06	6.11	6.23	6.31	6.36
B-28A	Granite	2.683	5.18	5.68	5.96	6.08	6.16	6.29	6.34	6.72
B		2.683	5.30	5.90	6.10	6.16	6.20	6.28	6.37	6.42
C		2.691	5.56	6.01	6.24	6.31	6.40	6.51	6.56	6.59
Ave.		2.686	5.53	5.86	6.10	6.19	6.25	6.36	6.42	6.46
B-29A	Granite	2.714	5.77	6.25	6.35	6.40	6.43	6.48	6.51	6.54
B		2.716	6.00	6.18	6.25	6.28	6.31	6.36	6.41	6.46
C		2.691	5.56	6.01	6.24	6.31	6.40	6.51	6.56	6.59
Ave.		2.714	5.90	6.21	6.30	6.34	6.37	6.43	6.48	6.52
B-30A	Paragneiss	2.808	5.52	5.73	5.88	5.96	6.01	6.14	6.18	6.20
B		2.811	6.23	6.30	6.34	6.36	6.38	6.43	6.48	6.52
C		2.791	5.88	6.02	6.07	6.10	6.13	6.20	6.29	6.35
Ave.		2.803	5.52	6.02	6.10	6.15	6.17	6.25	6.32	6.36
B-31A	Amphibolite	3.091	6.25	6.37	6.44	6.50	6.53	6.60	6.67	6.70
B		3.017	6.21	6.35	6.42	6.46	6.49	6.55	6.60	6.64
Ave.		3.054	6.22	6.36	6.43	6.47	6.50	6.57	6.62	6.66
B-32A	Amphibolite	3.044	6.40	6.51	6.58	6.62	6.65	6.71	6.74	6.77
B		3.037	6.89	7.00	7.04	7.10	7.13	7.18	7.25	7.27
Ave.		3.041	6.73	6.84	6.90	6.94	6.97	7.02	7.08	7.10
B-33A	Granite	2.645	5.46	5.78	5.90	5.96	5.99	6.06	6.14	6.16
B		2.654	5.57	5.84	5.96	6.03	6.07	6.14	6.20	6.25
C		2.651	5.82	6.06	6.15	6.20	6.24	6.30	6.35	6.38
Ave.		2.650	5.62	5.89	6.01	6.06	6.10	6.17	6.23	6.26
B-34A	Amphibolite	2.955	6.26	6.31	6.35	6.37	6.39	6.43	6.50	6.58
C		2.958	6.33	6.39	6.44	6.89	6.50	6.57	6.66	6.74
Ave.		2.957	6.31	6.36	6.41	6.45	6.46	6.52	6.61	6.69
B-35A	Granite	2.625	5.55	5.76	5.88	5.96	6.01	6.09	6.15	6.19
B		2.679	5.60	5.84	5.93	6.00	6.05	6.16	6.24	6.28
Ave.		2.665	5.58	5.81	5.92	5.99	6.04	6.14	6.21	6.25

Sample	Lithology	Density	Pressure, MPa							
		g/cm <sup>3</sup>	20	40	60	80	100	200	400	600
B-36A	Granite	2.625	5.87	6.02	6.10	6.16	6.19	6.25	6.28	6.31
B		2.630	5.77	5.95	6.03	6.06	6.09	6.15	6.22	6.26
Ave.		2.628	5.80	5.97	6.05	6.09	6.12	6.19	6.24	6.28
B-37A	Amphibolite	2.910	5.95	6.09	6.16	6.20	6.22	6.26	6.32	6.35
B		2.927	6.56	6.67	6.74	6.79	6.82	6.91	6.96	7.00
C		2.894	6.98	7.10	7.14	7.16	7.17	7.21	7.24	7.27
Ave.	2.910	6.50	6.62	6.68	6.72	6.74	6.79	6.84	6.87	
B-38A	Paragneiss	2.804	5.58	5.71	5.77	5.82	5.84	5.89	5.94	5.98
B		2.785	6.32	6.39	6.44	6.47	6.50	6.58	6.68	6.75
C		2.802	6.28	6.44	6.50	6.54	6.56	6.63	6.71	6.78
Ave.	2.797	6.06	6.18	6.24	6.28	6.30	6.37	6.44	6.50	
B-39A	Paragneiss	2.879	5.77	5.92	6.06	6.15	6.19	6.25	6.42	6.47
B		2.860	6.29	6.43	6.52	6.57	6.61	6.83	6.74	6.79
Ave.		2.870	6.12	6.26	6.37	6.43	6.47	6.54	6.63	6.68
B-40A	Grafite	2.666	5.14	5.52	5.74	5.86	5.94	6.08	6.18	6.24
B		2.654	5.76	6.06	6.18	6.25	6.29	6.37	6.43	6.46
Ave.		2.660	5.55	5.88	6.03	6.12	6.17	6.27	6.35	6.39
B-41A	Granite	2.679	5.65	5.82	5.89	5.92	5.95	6.01	6.08	6.11
B		2.679	5.61	5.82	5.94	6.00	6.05	6.11	6.17	6.20
Ave.		2.676	5.62	5.82	5.92	5.97	6.02	6.08	6.14	6.17
B-42A	Metadiabase	3.188	6.54	6.57	6.60	6.62	6.64	6.70	6.77	6.81
B-43A	Granite	2.649	5.53	5.81	5.99	6.05	6.10	6.17	6.22	6.27
B		2.659	5.84	6.08	6.19	6.24	6.26	6.30	6.35	6.40
C		2.660	5.28	5.74	5.95	6.07	6.14	6.25	6.29	6.32
Ave.	2.656	5.55	5.88	6.04	6.12	6.17	6.24	6.29	6.33	
B-44A	Granodiorite	2.721	5.75	5.92	6.03	6.09	6.13	6.22	6.27	6.31
B		2.686	5.82	5.99	6.08	6.13	6.16	6.21	6.28	6.31
Ave.		2.704	5.80	5.97	6.06	6.12	6.15	6.21	6.28	6.31
B-45A	Metadiabase	3.052	6.68	6.72	6.75	6.76	6.77	6.80	6.84	6.86
B-46A	Granite	2.748	5.82	6.00	6.07	6.11	6.14	6.19	6.24	6.28
B		2.732	5.71	5.85	5.94	5.98	6.01	6.06	6.11	6.15
C		2.737	5.86	5.99	6.08	6.12	6.14	6.19	6.23	6.26
Ave.	2.739	5.80	5.95	6.03	6.07	6.10	6.15	6.19	6.23	
B-47A	Granite	2.673	5.90	6.09	6.16	6.21	6.25	6.33	6.37	6.40
B		2.666	5.84	6.02	6.07	6.13	6.15	6.21	6.26	6.31
Ave.		2.760	5.86	6.04	6.10	6.15	6.18	6.25	6.30	6.34

Sample	Lithology	Density	Pressure, MPa							
		$\rho/\text{cm}^3$	20	40	60	80	100	200	400	600
B-48A	Diorite	2.773	5.59	5.90	6.04	6.11	6.15	6.21	6.28	6.32
B		2.802	5.92	6.15	6.32	6.41	6.46	6.53	6.59	6.64
C		2.771	5.80	6.03	6.15	6.22	6.26	6.34	6.41	6.45
Ave.		2.782	5.77	6.03	6.17	6.25	6.29	6.36	6.43	6.47
B-49A	Granite	2.627	5.49	5.83	5.98	6.03	6.07	6.11	6.14	6.16
B		2.603	5.39	5.69	5.84	5.90	5.93	5.98	6.02	6.05
C		2.611	5.60	5.85	6.00	6.08	6.12	6.17	6.21	6.26
Ave.		2.629	5.49	5.79	5.94	6.00	6.04	6.09	6.12	6.16
B-50	Granite	2.612	5.62	5.84	5.93	5.98	6.01	6.10	6.15	6.20
B-51A	Granite	2.645	5.70	5.89	6.00	6.07	6.12	6.20	6.25	6.29
B		2.664	5.50	5.74	5.86	5.93	5.98	6.06	6.11	6.16
Ave.		2.655	5.57	5.79	5.91	5.98	6.03	6.11	6.16	6.20
B-52A	Anorthosite	2.900	6.64	6.78	6.83	6.86	6.87	6.91	6.95	6.99
B		2.859	6.80	6.95	6.99	7.01	7.02	7.04	7.07	7.09
Ave.		2.880	6.75	6.89	6.94	6.96	6.97	7.00	7.03	7.06
B-53A	Amphibolite	2.980	6.30	6.51	6.60	6.64	6.68	6.74	6.80	6.85
B		2.985	6.77	6.95	7.01	7.05	7.04	7.11	7.15	7.19
Ave.		2.983	6.61	6.80	6.87	6.91	6.94	6.99	7.03	7.08
B-54A	Metadiabase	3.047	6.06	6.12	6.15	6.18	6.20	6.25	6.30	6.33
B-55A	Metadiabase	3.174	6.01	6.33	6.50	6.63	6.69	6.82	6.91	6.95
B-56A	Granite	2.706	5.45	5.72	5.84	5.92	5.96	5.05	6.12	6.15
B		2.613	5.45	5.72	5.84	5.90	5.96	6.05	6.12	6.15
Ave.		2.660	5.55	5.77	5.86	5.93	5.96	6.02	6.07	6.11
B-57A	Amphibolite	2.918	5.93	6.08	6.17	6.21	6.23	6.29	6.35	6.39
B		2.928	6.61	6.71	6.77	6.80	6.82	6.86	6.91	6.96
C		2.937	6.77	6.84	6.91	6.95	6.98	7.05	7.11	7.15
Ave.		2.928	6.44	6.54	6.62	6.65	6.68	6.73	6.79	6.83
B-58A	Granite	2.659	4.85	5.26	5.46	5.57	5.64	5.84	5.96	6.03
B		2.635	5.10	5.40	5.62	5.77	5.88	6.12	6.27	6.31
C		2.636	5.03	5.35	5.51	5.65	5.74	5.95	6.10	6.15
Ave.		2.643	4.99	5.34	5.53	5.66	5.75	5.97	6.11	6.16
B-59A	Amphibolite	3.031	6.18	6.35	6.44	6.89	6.52	6.57	6.64	6.69
B		3.044	6.68	6.78	6.83	6.87	6.89	6.93	6.98	7.00
Ave.		3.038	6.51	6.64	6.70	6.74	6.77	6.81	6.87	6.90
B-60A	Granite	2.589	5.60	5.89	5.89	6.03	6.07	6.15	6.20	6.22
B		2.602	5.60	5.93	6.10	6.16	6.20	6.25	6.33	6.39
C		2.610	5.56	5.81	5.94	6.05	6.07	6.13	6.20	6.25
Ave.		2.603	5.59	5.88	6.01	6.07	6.11	6.18	6.24	6.29

Sample	Lithology	Density	Pressure, MPa							
		g/cm <sup>3</sup>	20	40	60	80	100	200	400	600
B-61A	Granite	2.718	5.66	5.90	6.01	6.06	6.10	6.17	6.23	6.27
B		2.713	5.77	5.96	6.03	6.07	6.10	6.14	6.20	6.24
C		2.716	5.45	5.74	5.90	6.00	6.04	6.14	6.21	6.26
Ave.		2.716	5.63	5.87	5.98	6.04	6.08	6.15	6.21	6.26
B-62A	Granodiorite	2.728	5.77	5.91	5.96	5.99	6.01	6.07	6.12	6.17
B		2.720	5.72	5.82	5.87	5.90	5.92	5.97	6.03	6.08
Ave.		2.724	5.74	5.85	5.90	5.93	5.95	6.00	6.06	6.11
B-63A	Granodiorite	2.708	5.66	5.89	6.03	6.10	6.14	6.23	6.31	6.36
B		2.722	5.65	5.94	6.10	6.20	6.27	6.38	6.44	6.48
Ave.		2.715	5.65	5.92	6.08	6.17	6.23	6.33	6.40	6.44
B-64B	Granite	2.615	5.23	5.60	5.80	5.94	6.01	6.09	6.20	6.25
C		2.618	5.00	5.55	5.83	5.93	5.99	6.10	6.18	6.23
Ave.		2.617	5.11	5.57	5.81	5.93	6.00	6.10	6.19	6.24
B-65A	Granite	2.785	5.13	5.50	5.73	5.83	5.91	6.06	6.17	6.22
B		2.784	5.64	5.93	6.10	6.18	6.23	6.37	6.46	6.49
Ave.		2.785	5.47	5.79	5.98	6.06	6.12	6.27	6.36	6.40
B-66A	Granite	2.658	5.15	5.53	5.71	5.82	5.90	6.04	6.13	6.18
B		2.664	5.42	5.73	5.90	6.01	6.09	6.23	6.31	6.35
C		2.674	5.52	5.80	5.96	6.07	6.12	6.25	6.33	6.37
Ave.		2.665	5.36	5.69	5.86	5.97	6.04	6.17	6.26	6.30
B-67A	Granite	2.566	5.02	5.49	5.77	5.89	5.77	6.11	6.20	6.23
B		2.604	5.50	6.09	6.20	6.22	6.26	6.30	6.35	6.39
Ave.		2.585	5.35	5.89	6.06	6.11	6.17	6.24	6.30	6.34
B-68A	Granite	2.635	5.31	5.63	5.72	5.76	5.79	5.85	5.92	6.00
B		2.635	5.59	6.02	6.23	6.30	6.34	6.42	6.49	6.50
Ave.		2.635	5.50	5.89	6.06	6.12	6.16	6.23	6.30	6.33
B-69A	Granite	2.710	5.59	5.84	5.97	6.04	6.09	6.21	6.24	6.26
B		2.721	5.68	5.85	5.95	6.00	6.04	6.10	6.15	6.20
Ave.		2.716	5.65	5.85	5.96	6.01	6.06	6.14	6.18	6.22
B-70A	Granodiorite	2.720	5.74	5.95	6.05	6.09	6.12	6.17	6.21	6.25
B		2.731	6.02	6.19	6.26	6.29	6.32	6.39	6.46	6.52
C		2.725	5.69	5.92	6.02	6.05	6.07	6.10	6.14	6.17
Ave.		2.725	5.82	6.02	6.11	6.14	6.17	6.22	6.27	6.31
B-71A	Marble	2.731	5.89	6.14	6.27	6.35	6.39	6.46	6.53	6.56
B		2.751	6.37	6.62	6.75	6.83	6.88	6.73	7.01	7.05
Ave.		2.741	6.21	6.46	6.59	6.67	6.72	6.80	6.85	6.89
B-72A	Dunite	3.373	7.25	7.60	7.45	7.82	7.89	8.02	8.09	8.14
B-73B	Anorthosite	2.861	6.56	6.65	6.68	6.70	6.71	6.77	6.82	6.86
C		2.871	6.40	6.50	6.54	6.57	6.58	6.63	6.71	6.78
Ave.		2.866	6.48	6.57	6.61	6.63	6.65	6.70	6.77	6.82
B-74A	Amphibolite	2.769	5.73	5.87	5.94	5.98	6.01	6.06	6.10	6.14
B		2.818	6.15	6.29	6.35	6.39	6.43	6.47	6.51	6.55
C		2.836	6.30	6.47	6.34	6.57	6.59	6.64	6.70	6.74



Sample	Lithology	Density	Pressure, MPa							
		$g/cm^3$	20	40	60	80	100	200	400	600
B-75A	Amphibolite	2.847	6.35	6.63	6.73	6.81	6.81	6.87	6.94	6.99
B		2.806	6.77	6.68	6.91	6.94	6.96	7.00	7.41	7.09
C		2.854	6.59	6.76	6.84	6.90	6.94	6.99	7.08	7.15
Ave.		2.836	6.57	6.75	6.83	6.87	6.90	6.95	7.02	7.08
B-77A	Anorthosite	2.738	6.80	6.97	7.03	7.06	7.08	7.13	7.17	7.20
B		2.762	6.75	6.93	7.01	7.05	7.07	7.13	7.18	7.20
Ave.		2.750	6.77	6.94	7.02	7.05	7.07	7.13	7.18	7.20
B-78A	Diorite	2.838	5.85	6.03	6.08	6.11	6.14	6.17	6.20	6.22
B		2.844	6.33	6.45	6.51	6.53	6.55	6.01	6.64	6.67
Ave.		2.841	6.17	6.31	6.37	6.39	6.41	6.46	6.49	6.52
B-79A	Granodiorite	2.663	5.87	6.01	6.08	6.11	6.13	6.19	6.24	6.29
B		2.660	5.99	6.14	6.20	6.23	6.25	6.31	6.36	6.40
Ave.		2.662	5.95	6.10	6.16	6.19	6.21	6.27	6.32	6.36
B-80A	Anorthosite	2.778	6.04	6.35	6.47	6.51	6.53	6.58	6.62	6.66
B		2.626	5.60	5.84	5.93	6.01	6.07	6.15	6.21	6.26
Ave.		2.784	6.35	6.61	6.72	6.77	6.79	6.83	6.88	6.91
B-81A	Granite	2.629	5.70	5.90	5.99	5.99	6.01	6.03	6.08	6.13
B		2.626	5.60	5.84	5.93	6.01	6.07	6.15	6.21	6.26
Ave.		2.627	5.72	5.91	5.98	6.03	6.06	6.11	6.17	6.22
B-82A	Diorite	2.927	5.50	5.88	6.05	6.13	6.18	6.28	6.36	6.42
B		2.941	5.83	6.05	6.20	6.35	6.43	6.60	6.89	6.73
C		2.932	5.60	5.90	6.07	6.17	6.26	6.45	6.59	6.65
Ave.		2.932	5.64	5.94	6.11	6.22	6.29	6.44	6.55	6.60
B-83A	Diorite	2.837	6.09	6.28	6.33	6.34	6.38	6.42	6.47	6.50
B		2.831	6.14	6.28	6.34	6.38	6.41	6.45	6.48	6.52
Ave.		2.834	6.12	6.28	6.34	6.37	6.40	6.44	6.48	6.51
B-84A	Amphibolite	3.141	6.26	6.46	6.51	6.55	6.58	6.65	6.71	6.73
B		3.118	7.00	7.13	7.20	7.23	7.26	7.32	7.39	7.44
C		3.090	7.03	7.16	7.20	7.22	7.24	7.30	7.37	7.43
Ave.		3.116	6.76	6.91	6.97	7.00	7.03	7.09	7.16	7.20

---

Velocity in km/s.

Table 3.3 Shear Wave Velocities and Poisson's Ratios of Selected Britt Samples at Various Confining Pressures

Sample	Lithology	Density $\rho/\text{cm}^3$	Poisson's ratio	Pressure, MPa				
				60	100	200	400	600
B-11AB	Granite	2.662		3.44	3.47	3.52	3.54	3.56
	BA	2.663		3.47	3.51	3.54	3.57	3.60
	BC	2.663		3.57	3.61	3.65	3.68	3.71
	mean	2.663	0.251	3.49	3.53	3.57	3.60	3.62
B-14AB	Granodiorite	2.684		3.56	3.59	3.61	3.62	3.63
	BA	2.683		3.56	3.59	3.63	3.64	3.65
	BC	2.683		3.64	3.70	3.72	3.74	3.75
	mean	2.683	0.253	3.59	3.63	3.65	3.67	3.68
B-26AB	Paragneiss	2.704		3.31	3.38	3.44	3.48	3.50
	AC	2.704		3.27	3.33	3.39	3.44	3.46
	BA	2.688		3.33	3.41	3.49	3.51	3.54
	BC	2.688		3.47	3.54	3.60	3.64	3.67
	CA	2.684		3.36	3.41	3.47	3.50	3.51
	CB	2.684		3.39	3.44	3.50	3.53	3.56
	mean	2.692	0.276	3.36	3.42	3.48	3.52	3.54
B-55AB	Metadiabase	3.174	0.279	3.69	3.74	3.78	3.82	3.85
B-77AB	Anorthosite	2.783		3.75	3.78	3.81	3.84	3.87
	BA	2.762		3.78	3.81	3.83	3.86	3.89
	BC	2.762		3.74	3.78	3.81	3.84	3.87
	mean	2.754	0.295	3.76	3.79	3.82	3.85	3.88
B-78AB	Diorite	2.834		3.51	3.55	3.61	3.63	3.65
	BA	2.844		3.60	3.63	3.66	3.68	3.69
	BC	2.844		3.88	3.91	3.93	3.95	3.96
	mean	2.841	0.253	3.66	3.70	3.73	3.75	3.76
B-84AB	Amphibolite	3.141		3.85	3.87	3.90	3.92	3.94
	AC	3.141		3.81	3.83	3.86	3.89	3.91
	BA	3.044		3.85	3.87	3.90	3.93	3.94
	BC	3.044		4.16	4.18	4.21	4.25	4.28
	CA	3.090		3.83	3.85	3.87	3.90	3.91
	CB	3.090		4.12	4.14	4.17	4.21	4.24
	mean	3.092	0.270	3.94	3.96	3.99	4.02	4.04

Velocities in km/s. The first letter denotes propagation direction and the second letter, vibration direction.

The Apparent Poisson's ratio values presented in Table 3.3 were calculated from the mean values of  $V_p$  and  $V_s$ .

#### Velocity-Pressure Relationships

For all samples there is an initial increase in velocity with increasing pressure (Fig. 3.5). The velocity-pressure curves then become nearly linear at pressures above about 200 MPa. The initial velocity increase at pressures below 200 MPa has been related to the closure of microcracks (Birch, 1960, 1961; Christensen, 1965; Walsh, 1965), and the linear behavior at higher pressure reflects the intrinsic properties of the rocks, allowing the assessment of the effects of preferred mineral orientation and mineral composition (Christensen, 1965; Walsh, 1965).

Although the magnitude of the initial velocity increase is nearly constant regardless of wave propagation direction within a single rock, there appears to be a weak dependence on lithology and texture. The average differences in velocity ( $V_p$ ) between 20 MPa and 200 MPa for individual lithologies are given in Table 3.4. Rocks with granoblastic textures and original igneous textures show a larger initial increase, while rocks with textures which have been modified by directed stress show a smaller increase, probably due to preferred alignment of crystallographic axes with similar compressibilities.

Table 3.4 Average Velocity Increase (Vp) of Individual Lithologies from 20-200 MPa.

<u>Lithology</u>	<u>Sample number</u>	<u>Velocity increase, km/s</u>
Granite	36	0.58±0.03
Granodiorite	9	0.51±0.03
Diorite	6	0.51±0.08
Paragneiss	6	0.49±0.06
Metadiabase	5	0.45±0.11
Amphibolite	11	0.29±0.06
Anorthosite	4	0.33±0.03

Compressional Wave Velocity-Density Relationships

As demonstrated by Birch (1961), the velocities of rocks at high pressure tend to increase with density for rocks of the same mean atomic weight and to decrease with increasing mean atomic weight. As can be seen in Figure 3.6, in which the average compressional wave velocity at 600 MPa is plotted against bulk density for all samples, the Britt domain rocks display a similar trend. The linear regression fit to this data is

$$V_p = 1.637\rho + 1.961 \quad (5)$$

with a correlation coefficient of 0.793. This line nearly coincides with Burke's (1991) fit for GFTZ rocks to the northwest. Figure 3.6 also shows the  $m = 21$  and  $m = 22$  lines of constant mean atomic weight of Birch (1961). Although most of the data in this study fall between the  $m = 21$  and  $m = 22$  lines, two anomalous groups of samples fall well outside these limits. Samples B-3, 31, 42, 54 and 55 fall below the  $m = 22$  line, while samples B-71, 75, 77 and 81 lie above the  $m = 21$  line.

In order to discern the lithologic controls on compressional wave velocity and bulk density, the average  $V_p$  and density values of the Britt lithologies are given in Table 3.5. The different lithologic groups are also shown in Figure 3.7 as a function of density and velocity at 600 MPa. Excluding samples B-72, an ultramafic rock, and B-54, a

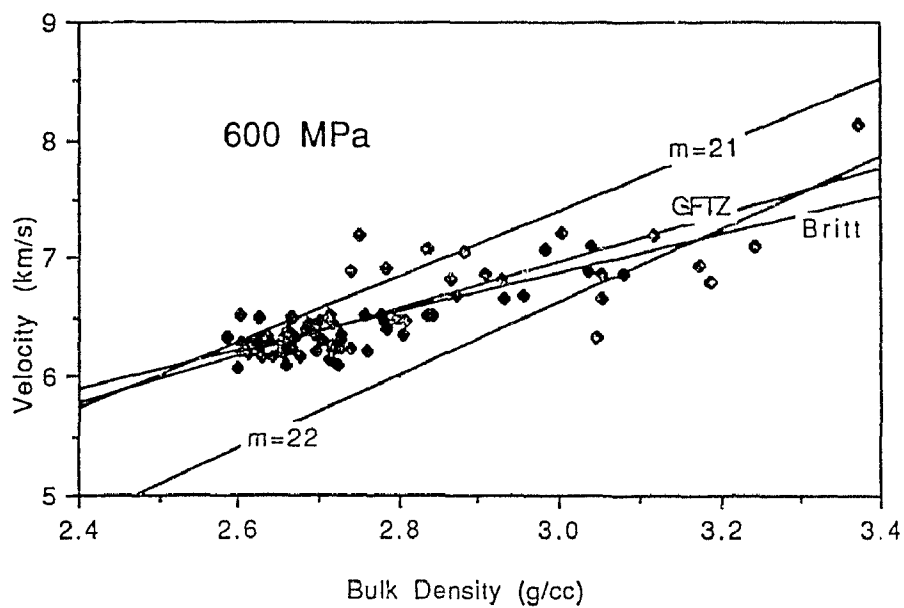


Fig. 3.6 Average velocity ( $V_p$ ) plotted against bulk density for all Britt samples measured. The line marked "Britt" is the best linear fit to this data set and the line marked "GFTZ" is Burke's fit for GFTZ rocks. Lines of constant mean atomic weight from Birch (1961).

Table 3.5 Average Densities and Compressional Wave Velocities of Britt Lithologies.

Lithology	Sample Mean Density		Pressure, MPa				
	number	$\rho/\text{cm}^3$	60	100	200	400	600
Granitic gneiss	36	2.651+0.04	5.99	6.11	6.19	6.25	6.29+0.11
Granodioritic gneiss	9	2.707+0.03	6.11	6.19	6.26	6.32	6.35+0.12
Marble	1	2.741	6.59	6.72	6.80	6.85	6.89
Paragneiss	6	2.775+0.05	6.09	6.19	6.27	6.35	6.39+0.12
Anorthosite	4	2.820+0.01	6.82	6.87	6.92	6.97	7.00+0.13
Dioritic gneiss	6	2.823+0.05	6.21	6.31	6.40	6.47	6.51+0.06
Amphibolite	11	2.973+0.08	6.72	6.78	6.81	6.90	6.92+0.15
Metadiabase (alt.)	1	3.047	5.15	6.20	6.25	6.30	6.33
Metadiabase	5	3.148+0.07	6.60	6.70	6.78	6.84	6.88+0.14
Dunite	1	3.373	7.75	7.89	8.02	8.09	8.14

Velocity in km/s

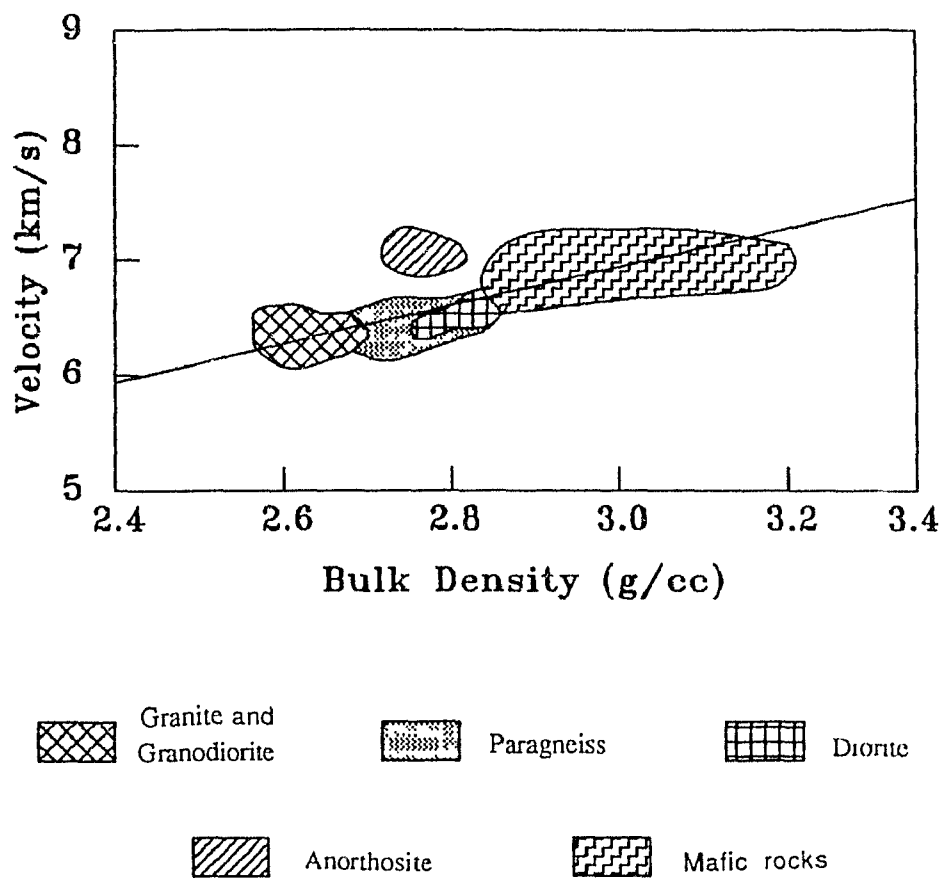


Fig. 3.7 Schematic diagram showing velocity - bulk density fields of Britt rocks. All data were used to define these fields, except B-71 (dunite) and B-54 (a chlorite rich metabasalt). Solid line represents best fit to data from Figure 3.6.



mafic rock with a large chlorite content, five lithologic fields are defined by the data.

Although the individual lithologic fields are not tightly constrained, most of the variations can be interpreted in terms of differences in modal mineral composition and metamorphic alteration. The granite-granodiorite field covers an area with a density range of 2.60-2.77 g/cc and a compressional wave velocity range of 6.02-6.53 km/s. This velocity range is due largely to variations in the proportions of K-feldspar (slow) and plagioclase (slow to fast, depending on %An) contents. The diorite samples form the most tightly constrained field in Figure 3.7, with velocity ranging from 6.43-6.60 km/s and density from 2.78-2.92 g/cc. Sample B-82 has a high (10.8%) garnet content which elongates the density range of this field.

Although only six paragneiss samples were examined in this study, they show considerable scatter, overlapping parts of the diorite and granite-granodiorite fields, with density ranging from 2.70-2.88 g/cc and velocity from 6.12-6.68 km/s. This large range is also likely due to variations in modal composition. Sample B-38 is the fastest sample due to its high plagioclase (53.5%) and hornblende (5.9%) content. The high K-feldspar (40.2%) and relatively high opaque oxide content in sample B-22 seem to be responsible for its low velocity.

Anorthosites and mafic rocks occupy two distinct high density, high velocity fields. Although just four samples of anorthosite were examined (B-52, 73, 77 and 80), they cover a large area, with density ranging from 2.76-2.88 and velocity from 6.82 (B-73) to 7.2 km/s (B-77). Sample B-73 has a relatively high K-feldspar (4.9%) and opaque oxide (3.5%) content, while sample B-77 has a plagioclase content of 94.3% (the highest of the anorthosites).

The mafic samples have the largest field, with velocities ranging from 6.66-7.22 km/s and densities from 2.83-3.24 g/cc. Detailed examination of the data shows that the mafic rocks occupy two subfields (Fig. 3.8) based on their garnet+opaque+biotite contents. The samples falling above the  $m=22$  line are amphibolites, while most of those falling below the line have a relatively high content of garnet+opaques (which are dense) and biotite (which is slow). B-54 is especially slow because it also contains abundant chlorite. B-75 is a plagioclase-rich metagabbro and B-72 (not shown) is dense and fast because it is composed entirely of olivine.

#### Poisson's Ratio

As recently demonstrated by Salisbury and Fountain (in press) for samples from the Kapuskasing Uplift, an even more effective way to discern lithologies using velocities is to plot  $V_p$  vs  $V_s$  and Poisson's ratio as in Figure 3.9. Although the data presented (Tables 3.2 and 3.3) are limited by the

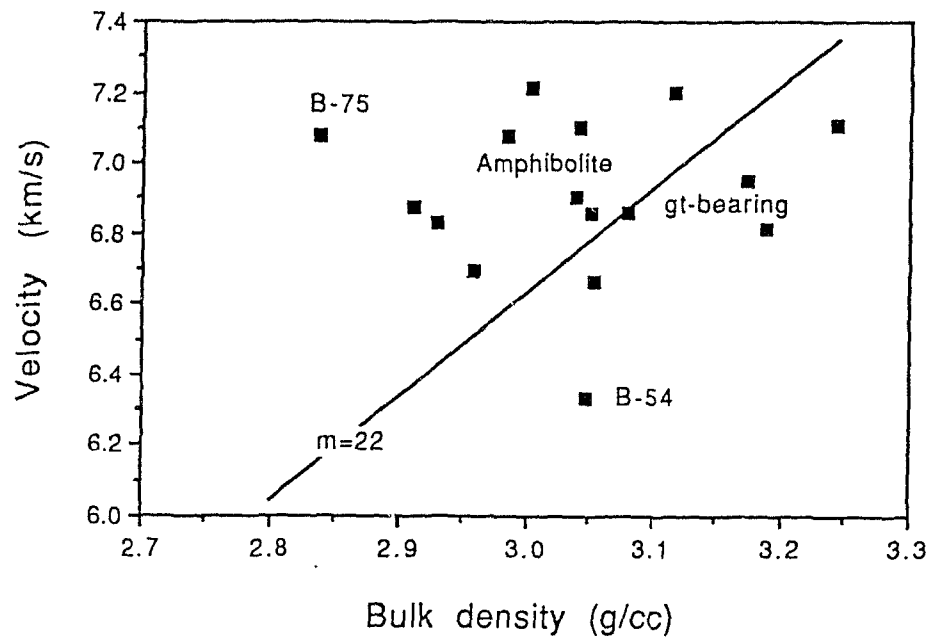


Fig. 3.8 Average compressional wave velocity at 600 MPa plotted against bulk density for all mafic samples. A subfield defined by samples with a high modal garnet+opaque oxide content falls below the  $m=22$  line.

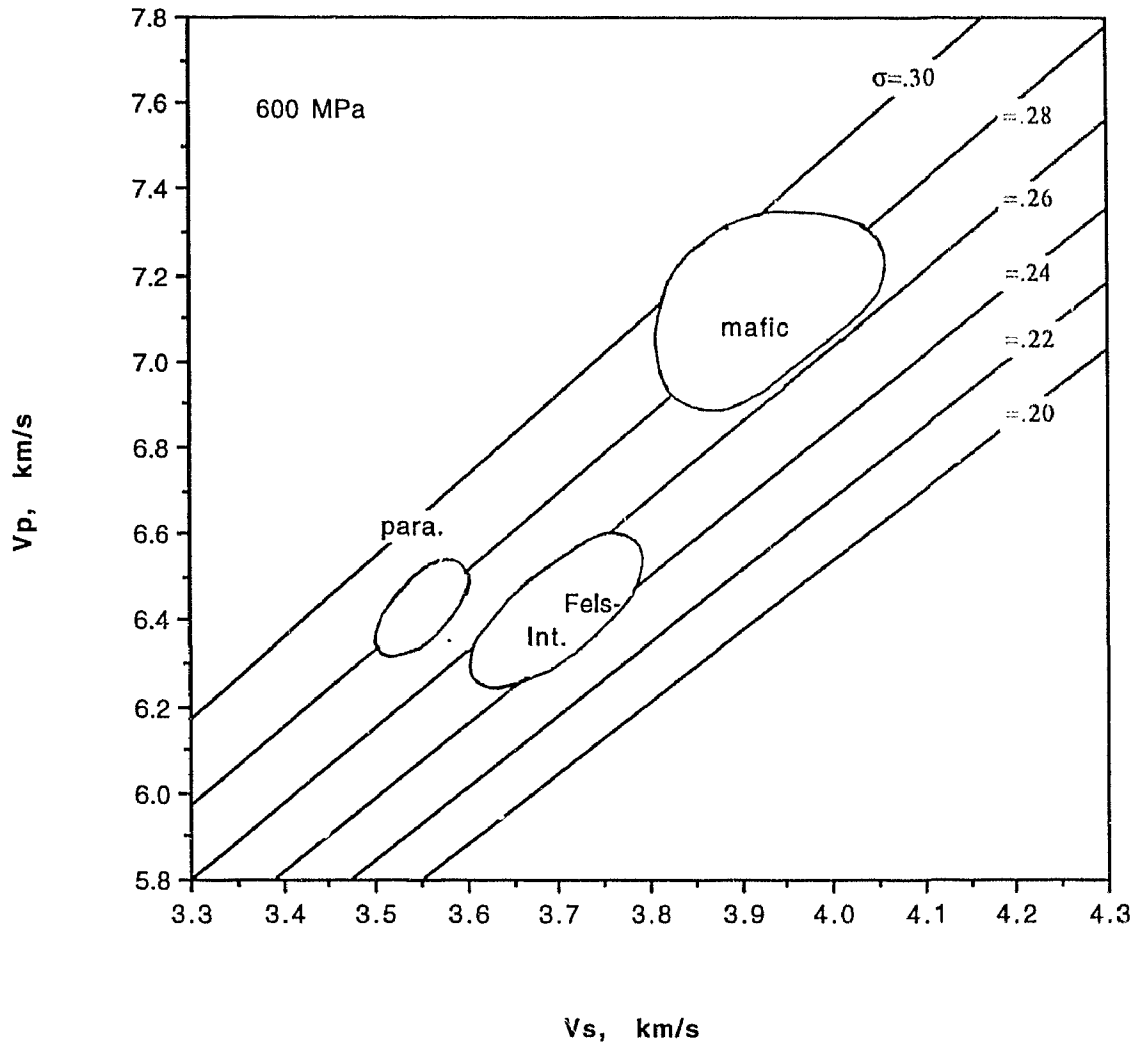


Fig. 3.9 Schematic diagram showing  $V_p$  -  $V_s$  fields of Britt rocks. Fels-Int.=felsic-intermediate gneiss, para=paragneiss, mafic=mafic gneiss,  $\sigma$ =Poisson's ratio.

small number of shear wave velocities measured, several distinct fields are obvious: (1) Mafic rocks have higher  $V_p$  and  $V_s$  values than any other lithology and a wide range of  $\sigma$  values. (2) Felsic rocks have low  $V_p$  and  $V_s$  values and can be subdivided on the basis of  $\sigma$ , with granites and granodiorites having low values (0.25) and paragneisses, high values (0.28). Since  $\sigma$  is relatively insensitive to pressure, it can potentially be used in conjunction with  $V_p$  and  $V_s$  data, as a petrologic discriminator in interpreting refraction velocities.

#### Seismic Anisotropy and Shear Wave Splitting

Velocity anisotropy was observed in most samples of foliated and/or lineated rocks and in some it was quite strong. It is calculated as the per cent difference between the maximum and minimum velocity with respect to the mean velocity (Birch, 1961). Compressional and shear wave anisotropy values at different confining pressures are listed in Tables 3.6 and 3.7, respectively. In most samples, the  $V_p$  anisotropy decreases sharply with increasing pressure until a stable value is reached (Fig. 3.10). Strong anisotropy at low confining pressure is believed to be related to oriented fractures and microcracks while stable values at high pressures reflect the preferred orientation of anisotropic minerals (Christensen, 1965).

As noted by Burke (1991), granitic to granodioritic orthogneisses commonly show very small  $V_p$  anisotropy at high

Table 3.6 Vp Anisotropy of Britt Samples

Sample	Lithology	Pressure, MPa				
		60	100	200	400	600
B- 2	Granite	6.1	5.7	5.8	5.4	5.3
B- 7	Granodiorite	13.2	12.7	11.7	11.5	11.4
B- 9	Granite	5.2	4.2	3.7	4.2	3.8
B-13	Amphibolite	8.8	9.5	10.0	10.1	9.8
B-16	Diorite	9.6	9.2	8.7	8.0	7.5
B-19	Paragneiss	0.2	0.5*	1.1*	1.6*	2.4*
B-21	Granite	2.5*	0.5*	1.7	1.7	2.1
B-22	Paragneiss	3.5	4.2	4.9	4.8	4.7
B-24	Granite	8.8	8.2	7.6	7.9	7.6
B-25	Diorite	6.0	4.3	3.5	3.3	2.9
B-26	Paragneiss	9.4	8.5	7.7	7.3	6.9
B-28	Granite	4.6	3.8	3.6	3.4	3.4
B-30	Paragneiss	7.5	6.0	5.0	4.7	5.0
B-33	Granite	4.2	4.1	3.9	3.4	3.5
B-34	Amphibolite	1.4	1.7	2.1	2.4	2.4
B-37	Amphibolite	14.7	14.1	14.0	13.5	13.4
B-38	Paragneiss	11.7	11.4	11.6	12.0	12.3
B-39	Paragneiss	7.2	6.5	6.6	4.8	4.8
B-40	Granite	7.3	5.7	4.6	3.8	3.3
B-43	Granite	4.0	2.6	2.2	2.2	2.1
B-46	Granite	2.3*	2.1*	2.1*	2.1*	2.1*
B-48	Diorite	4.5	4.9	5.0	4.8	4.9
B-49	Granite	2.7	3.1	2.8	3.1	3.4
B-51	Granite	2.4*	2.3*	2.3*	2.3*	2.1*
B-53	Amphibolite	6.0	5.6	5.3	5.1	4.8
B-57	Amphibolite	11.2	11.2	11.3	11.2	11.1
B-58	Granite	2.9	4.2	4.7	5.1	4.5
B-59	Amphibolite	5.8	5.5	5.3	4.9	4.5
B-60	Granite	2.7	2.1	1.9	2.1	2.7
B-65	Granite	6.2	5.2	4.9	4.6	4.2
B-66	Granite	4.3	3.6	3.4	3.2	3.0
B-67	Granite	7.1	4.5	3.0	2.4	2.5
B-68	Granite	8.4	8.9	9.1	9.0	7.9
B-70	Granodiorite	3.9	4.1	4.7	5.1	5.5
B-71	Marble	7.3	7.3	7.6	7.0	7.1
B-74	Amphibolite	9.6	9.1	9.1	9.3	9.3
B-75	Amphibolite	2.6	2.2	1.9	2.0	2.3
B-78	Diorite	6.8	6.4	6.7	6.8	6.9
B-80	Anorthosite	5.7	5.7	5.6	5.7	5.5
B-81	Granite	1.8	1.7	2.1	2.3	2.3
B-82	Diorite	2.5	4.0	5.0	5.0	4.7
B-84	Amphibolite	9.9	9.7	9.4	9.5	9.9

Anisotropy in %; \* denotes fast in A direction.

Table 3.7 Vs Anisotropy of Selected Britt Samples

Sample	Lithology	Pressure, MPa				
		60	100	200	400	600
B-11	Granite	3.3	4.0	3.6	3.9	4.1
B-14	Granodiorite	2.2	3.0	3.0	3.3	3.3
B-26	Paragneiss	6.0	6.1	6.0	5.7	6.0
B-77	Anorthosite	1.1	0.8	0.5	0.5	0.5
B-78	Diorite	10.1	9.7	8.6	8.5	8.2
B-84	Amphibolite	8.8	8.8	8.8	9.0	9.2

---

Anisotropy in %.

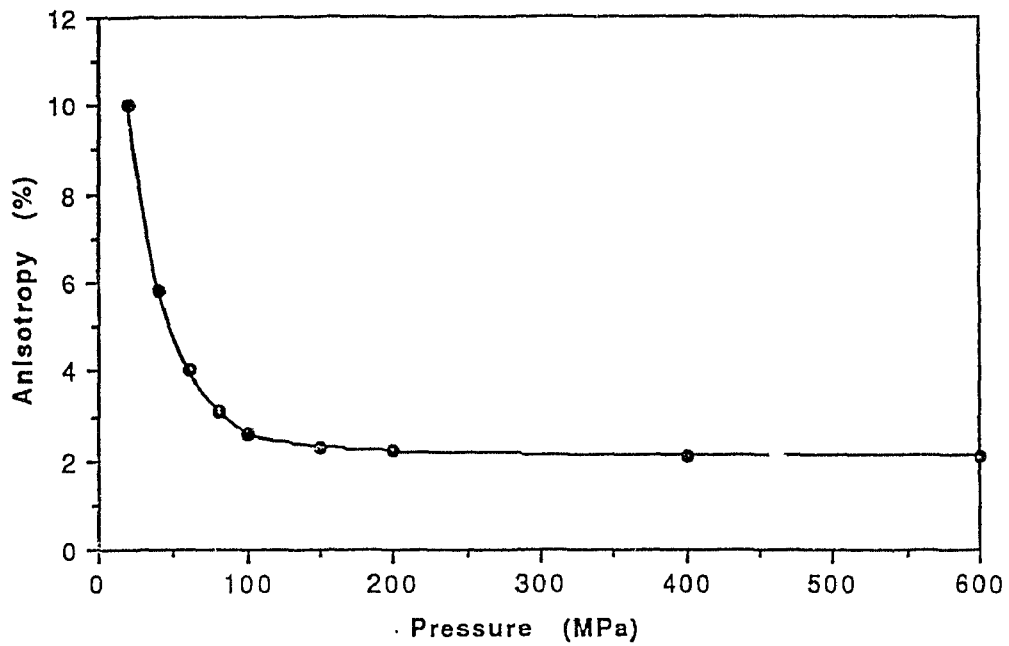


Fig. 3.10 Anisotropy of compressional wave velocity plotted against confining pressure for sample B-43. Note typical decrease in anisotropy with increasing pressure.



pressures regardless of the extent of tectonic deformation (Table 3.8). Even mylonite samples such as B-33 and B-66 show little anisotropy (3.5 and 3.0%, respectively, at 600 MPa). Low anisotropy values for granitic rocks are related to the lack of strongly anisotropic minerals (mica, hornblende) (Alexandrov and Ryzhova, 1961a, 1961b). Although single feldspar crystals can be fairly anisotropic (Alexandrov and Ryzhova, 1962), they generally show little or no preferred orientation, even in mylonitic rocks.

While most of the felsic samples are isotropic, a number of granitic gneiss samples (B-5, 20, 46, 47, 51, 61, 62 and 69) are fast perpendicular to foliation (\* in Table 3.7). Thin section studies show that quartz and feldspars in these samples are weakly aligned with their long axes parallel to foliation. The anisotropy of these rocks may thus be due to the weak alignment of plagioclase c (fast) axes perpendicular to foliation.

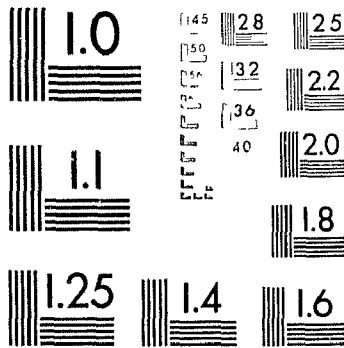
The anisotropy of the dioritic orthogneisses is moderate, ranging from 2.9% to 7.5%, with the fast direction parallel to foliation. The anisotropy values for individual samples of these rocks can be related to their biotite + hornblende content and the degree of preferred orientation. Sample B-16, which shows strong anisotropy (7.5%), has a high biotite + hornblende content (22.9%) and is well oriented. The low anisotropy of B-25 is due to its low biotite + hornblende content and very weak preferred orientation.

Table 3.8 Average Vp Anisotropy of Britt Lithologies.

Lithology	Sample Number	Average Anisotropy %
Granitic gneiss	36	1.1±0.04
Granodiorite gneiss	9	2.2±0.05
Diorite gneiss	6	4.3±0.09
Paragneiss	6	5.2±0.06
Amphibolite	11	5.9±0.07
Metadiabase	6	0.0
Anorthosite	4	2.0±0.03
Marble	1	7.1

2

PM-1 3½"x4" PHOTOGRAPHIC MICROCOPY TARGET  
NBS 1010a ANSI/ISO #2 EQUIVALENT



PRECISION<sup>SM</sup> RESOLUTION TARGETS

The paragneiss samples generally show stronger Vp anisotropy than the orthogneisses due to their high mica contents (>13%) and well-developed foliation. Sample B-38, the most anisotropic sample, is a mylonitic rock with an anisotropy value of 12.8%. Most samples are fast parallel to foliation but sample B-19 is fast perpendicular to foliation, probably due to quartz and feldspar preferred orientation.

To evaluate mica's contribution to the Vp anisotropy of the paragneiss samples, the relationships between modal mica, the degree of mica alignment and anisotropy are plotted in Figure 3.11. The alignment lines were obtained from the relation,

$$\text{Anisotropy} = \frac{3V_1CA(V_{\max}-V_{\min})}{3V_{\max}V_{\min}(1-C) + V_1CA(2V_{\max}+V_{\min})} \quad (6)$$

where  $V_1$  is the velocity of a quartz-feldspar aggregate and is considered equal to the mean velocity of biotite (Christensen, 1965),  $V_{\max}$  and  $V_{\min}$  are the maximum and minimum compressional wave velocities of mica, respectively,  $C$  is the modal content of mica and  $A$  is the percentage of mica alignment determined from fabric analysis (eg. Fig. 3.12) and the relation

$$A = \frac{4}{N\pi} \sum_{i=1}^n X_i \left( \frac{\pi}{4} - \alpha_i \right) \quad (7)$$

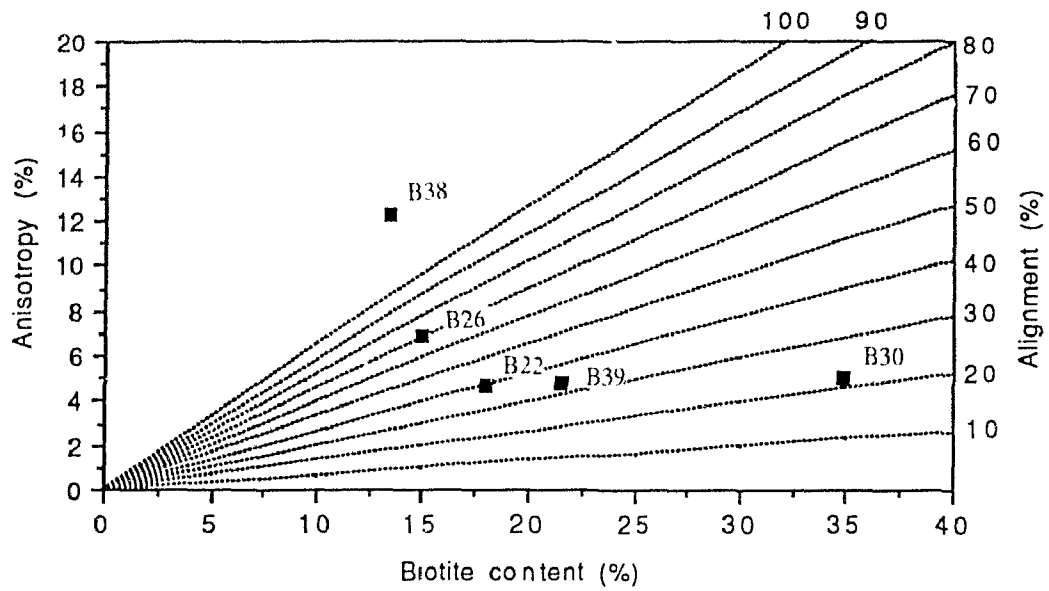


Fig. 3.11 Relationships between anisotropy, modal biotite and biotite alignment for paragneisses. Dotted lines are the solutions to equation 6 (see text).

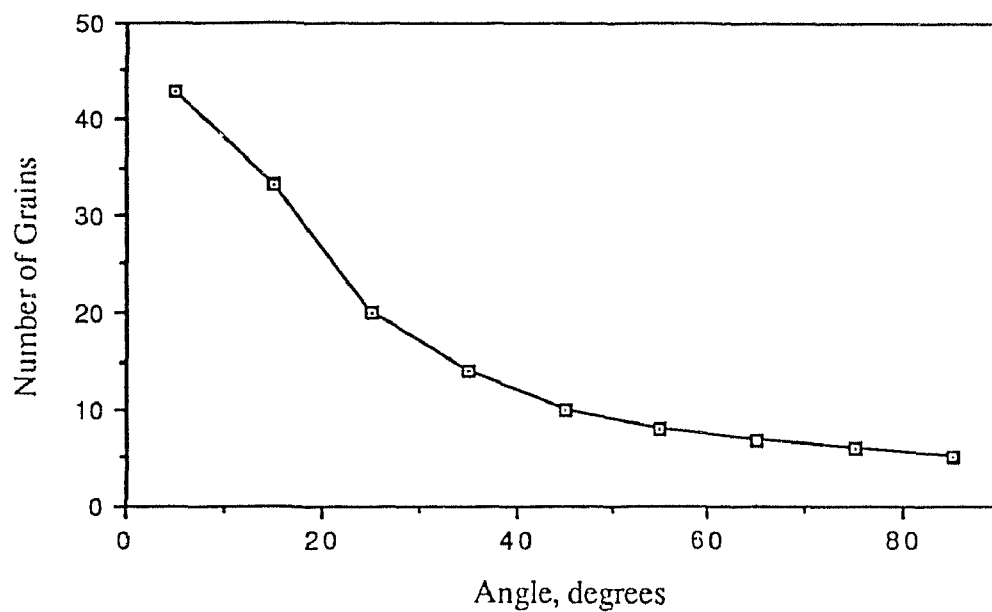


Fig. 3.12 Number of biotite grains versus angle between mica (001) and foliation plane in the plane normal to the "B" direction for sample B-22. Note preferred orientation of biotite. 150 biotite grains were measured.

where N is the total number of grains counted,  $\alpha$  is the angle between the mica {001} plane and the foliation plane within a plane perpendicular to foliation, X is the number of grains with angle  $\alpha$  and  $\alpha_i$  was taken from  $0^\circ$  to  $90^\circ$  in  $10^\circ$  intervals ( $X_i$  is actually the number of grains from  $\alpha_i - 5^\circ$  to  $\alpha_i + 5^\circ$ ). If  $V_l = 6.02$  km/s,  $V_{max} = 7.83$  km/s and  $V_{min} = 4.21$  km/s (Alexandrov and Ryzhova, 1961b), then equation (6) becomes

$$\text{Anisotropy} = \frac{21.8CA}{33.0 + 6.89CA} \quad (8)$$

Any two of three variables, anisotropy, modal content and percentage of alignment can be plotted against each other on this diagram (Fig. 3.11) to find the third. Then the contribution of mica to the anisotropy of the rock can be obtained by comparing the observed and calculated values.

Table 3.9 presents the results of this analysis for four paragneiss samples. Since the differences between the calculated and observed anisotropy values for samples B-22, 30 and 39, are small, the anisotropy of these samples is almost entirely related to biotite preferred orientation. Sixty three per cent of the total anisotropy of sample B-38 is related to biotite alignment and 37% appears to be related to other factors, probably hornblende alignment.

Ten mafic rock samples show anisotropy ranging from 2.3% (B-75) to 13.4% (B-37), many having values greater than 9%. Modal hornblende is plotted against anisotropy in Figure 3.13

Table 3.9 Contribution of Biotite to Anisotropy of Selected Paragneiss Samples.

Sample	Modal biotite content	Alignment	Anisotropy		Contribution
	(%)	(%)	obs.	calcu.	(%)
B-22	18.0	41.0	4.7	4.8	100
B-30	34.8	22.0	5.0	5.0	100
B-38	13.4	89.0	12.3	7.0	63
B-39	21.5	33.0	3.8	4.6	96



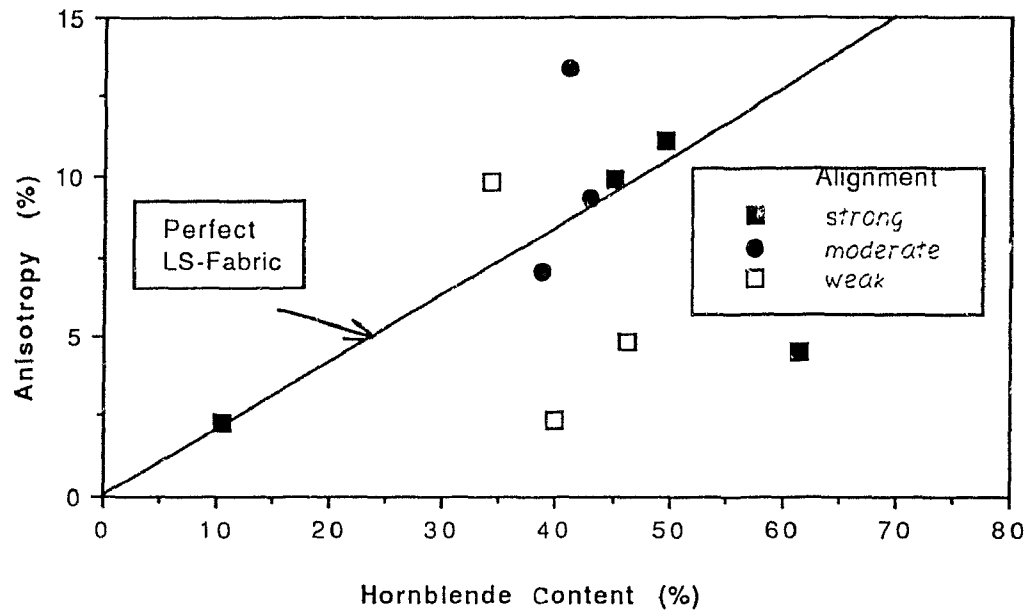


Fig. 3.13 Compressional wave velocity anisotropy plotted against modal hornblende for mafic rocks, excluding isotropic samples. Anisotropy tends to increase with hornblende content and alignment. The line marked perfect LS-Fabric is the variation in anisotropy with hornblende content expected for perfect hornblende alignment in an LS fabric.

for these ten mafic samples. Although quantitative evaluations were not applied for hornblende in this study, anisotropy tends to increase with increasing hornblende content and preferred orientation, suggesting that hornblende dominates the anisotropy in these rocks. However, samples B-13, 37 and 74 have higher anisotropy than might be expected from their moderate (B-37) and weak (B-13,74) hornblende preferred orientations. A greater abundance of biotite in B-37 (7%) and B-74 (21.3%) likely contributes to the anisotropy of these two samples while compositional layering (hornblende and biotite) in sample B-13 is probably the reason for its strong anisotropy. Sample B-59 has a lower anisotropy than expected from its strong hornblende preferred orientation, probably due to plagioclase and quartz preferred alignment.

Shear wave splitting is also a common feature of foliated and/or lineated rocks. It is defined as the difference between the maximum and minimum velocities observed for two orthogonally polarized waves travelling in the same propagation direction. Table 3.10 shows Vs splitting for six Vs samples. The maximum splitting is observed (or estimated) in the "B" direction for rocks with S-fabrics (B-11, 14 and 78) and in the "C" direction for rock with L-fabrics (B-26). Splitting in the "B" and "C" directions is almost the same for samples with LS-fabrics (B-84). It is also inferred from Table 3.10 that the maximum splitting is proportional to the Vs anisotropy of the rock as a whole.

Table 3.10 Shear Wave Splitting of Selected Britt rocks at 600 MPa.

Sample	Lithology	Anisotropy %	Propagation Direction		
			A	B	C
B-11	Granite	4.1	(0.00)	0.11	(0.00)
B-14	Granodiorite	3.3	(0.00)	0.10	(0.00)
B-26	Paragnies	6.0	0.04	0.05	0.13
B-77	Anorthosite	0.5	(0.00)	0.02	(0.00)
B-78	Diorite	8.2	(0.00)	0.27	(0.00)
B-84	Amphibolite	9.2	0.03	0.34	0.33

Splitting in km/s. Values in parentheses estimated on basis of Vp symmetry.

### Average Properties of the Britt Domain

The laboratory studies discussed above represent one of the most comprehensive velocity studies ever undertaken in Precambrian middle crust of felsic-intermediate composition. The study thus provides quantitative information on the average velocity of one of the most common terranes in the shields and on the range on velocity associated with anisotropy and mineralogical variation. In order to compare with in situ data, the average  $V_p$ ,  $V_s$ ,  $\rho$ ,  $\sigma$  and anisotropy of the Britt domain were estimated from the average properties and area-weighted means of each major lithology (e.g. Fountain, et al., 1991) and the results are presented in Table 3.11. The estimated abundances of the four major rock types used in the calculations are granite (45%), granodiorite (40%), diorite (11%) and mafic rocks (4%). Rather than point count the geological map, the abundances of the individual lithologies used in the calculation were loosely based on a cross-section measured along the Key River (Appendix I) and personal communication with Dr. N. Culshaw. This was necessary to ensure that small mafic bodies and dikes, which are not shown on the geologic map, were adequately represented in the statistics.

Two implications can be drawn from the results in Table 3.11. (1) The average values of the seismic properties of rocks from the Britt domain are close to those of granodiorite. If the Britt domain has the same composition at depth and is homogeneous at the scale of seismic refraction

Table 3.11 Average Properties of Britt Domain from Laboratory Measurements.

Parameters	Pressure, MPa		
	100	200	600
Vp - A	6.11	6.19	6.29
Vp - B	6.23	6.31	6.41
Vp - C	6.21	6.29	6.39
Vp (mean)	6.18	6.26	6.36
Vs - A	3.53	3.57	3.61
- B	3.63	3.67	3.70
- C	3.63	3.67	3.70
Vs (mean)	3.60	3.63	3.67
Anisotropy (Vp)	2.0	1.9	1.9
Anisotropy (Vs)	2.8	2.7	2.5
$\sigma$	0.24	0.25	0.25
$\rho$	( 2.70 g/cm <sup>3</sup> )		

Vp, Vs in km/s and A, B, C denote propagation directions;  
 $\sigma$  - Poisson's ratio;  $\rho$ -density; Anisotropy in %.

experiments, such experiments should give the same velocities and Poisson's ratios. (2) While  $V_p$  anisotropy is weakly developed in the vertical plane (~2%), since the regional foliation is horizontal or shallow-dipping, the Britt domain should be essentially transversely isotropic.

Chapter 4  
REFRACTION EXPERIMENT AND COMPARISON WITH  
LABORATORY DATA

Laboratory velocities may not be representative of regional in-situ velocities because of the effects of large scale variations in petrology with depth, regional variations in structure, lithology and fabric and local variations in pore fluids and fracture porosity. Therefore, a comparison of laboratory and in-situ data is necessary to understand the effects of these features on regional velocity structure and to determine the over all petrology of the crust as a function of depth (e.g. Fountain and Salisbury, 1990; Burke, 1991). In order to obtain such information, the author participated in the 1992 LITHOPROBE Abitibi-Grenville refraction experiment and analyzed the data for the Britt domain.

1992 Lithoprobe Abitibi-Grenville  
Refraction Experiments

The 1992 Abitibi-Grenville refraction survey was a multi-purpose, multi-agency scientific project conducted by LITHOPROBE. The major participants of this project were the Geological Survey of Canada, the United State Geological Survey and five Canadian universities including Dalhousie

University. Four refraction lines were carried out in the Grenville and Superior geological provinces of the Canadian Shield in Ontario and Quebec (Fig. 4.1). Line AB, which extends from Parry Sound through the Britt domain and across the GFTZ to the north of the Sudbury basin, was examined in preliminary fashion along its entire length and the Britt domain was analyzed in detail.

#### Data Acquisition

There were 10 shot points and 270 recording sites along line AB with an average shot spacing of about 27 km and a recorder spacing of about 1 km. Seismic energy was generated at each shot point by detonation of Hydromex T3 in drill holes approximately 40 m in depth and 20.4 cm in diameter. Detailed information on the depth and charge size of individual shots along line AB is given in Table 4.1.

Four types of recording systems were provided by the GSC and USGS for the survey. The GSC instruments included single component PRS1 and three component PRS4 seismographs with 2 Hz L4C detectors. The PRS seismometers recorded the seismic wave digitally at a sampling rate of 120 Hz. These instruments were managed in the field using LithoSEIS software. For further information regarding the PRS seismometers and LithoSEIS software, see Asudeh et al. (1992,1993). The USGS instruments included vertical component SGR seismometers with single 2 Hz geophones and vertical



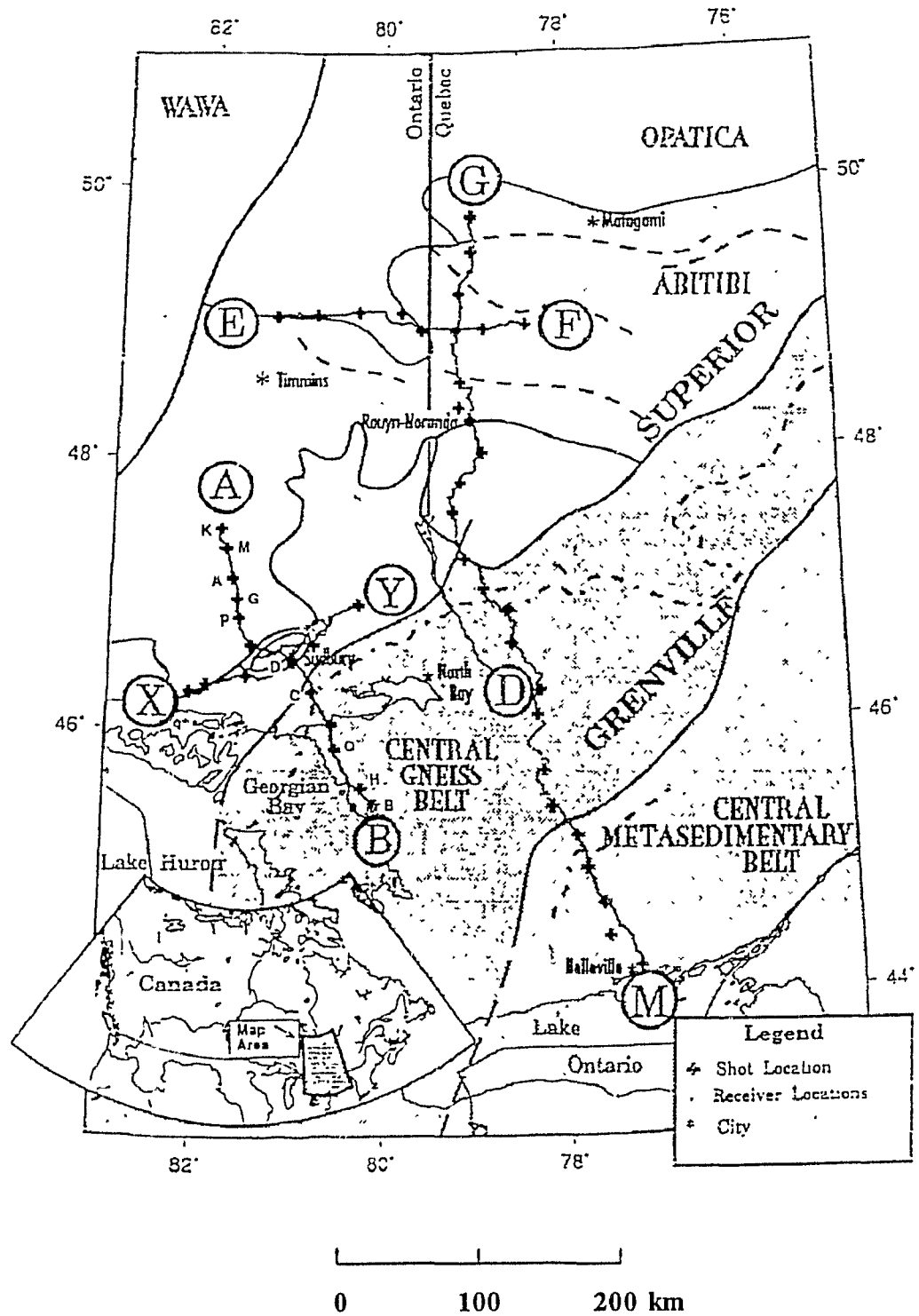


Fig. 4.1 Location of the 1992 Abitibi-Grenville seismic refraction survey with regional geology (R. Irving, et al., 1993).

Table 4.1 Depth and charge size of individual shots along line AB.

<u>Shot name</u>	<u>Shot ID</u>	<u>Letter Designation</u>	<u>Depth(m)</u>	<u>Weight(kg)</u>	<u>Distance(km)</u>
AB0	0030	K	43	800.0	0
AB1	0035	M	35	400.0	16
AB2	0031	A	35	400.0	39
AB3	0036	G	35	400.0	58
AB4	0044	P	35	400.0	71
AB6	0041	D	43	800.0	121
AB7	0043	C	35	400.0	156
AB8	0040	Q	35	400.0	208
AB9	0039	H	35	400.0	243
AB10	0042	B	43	1500.0	265

component SGR seismographs with a string of 8 Hz geophones. These instruments recorded and stored vertical displacement data on cassette tapes at a sampling rate of 125 samples per second.

The recording and shot sites were located using GPS receivers operating in the differential mode with accuracies better than 10 meters (R. Irving et al., 1993). The Geocentric Earth Orbiting Satellite (GEOS) clock was used to provide absolute shot time information and to correct for seismograph clock drift. More detailed information on the data acquisition is provided by R. Irving et al., (1993).

#### Data Processing

The corrections and processing applied to the field data include (1) resampling and combination of the GSC and USGS data; (2) SEG Y formatting and taping; (3) time corrections and filtering. Due to the different sampling rates between the GSC (120 s/sec) and USGS (125s/sec) data, resampling had to be done before merging. This, together with SEG Y formatting, shot time corrections and taping were done by GSC scientists. Clock corrections and frequency filtering were applied to the raw data tapes distributed by the LITHOPROBE Seismic Processing Centre before the data were interpreted. Topographic corrections were not applied to the data presented here because there is little relief along line AB (<300 m, giving a maximum travel time error of about 0.1 s).

After all corrections had been applied to the data, vertical component in-line data for each shot gather along line AB were plotted with reduction velocities of 7 km/s for  $V_p$  and 4 km/s for  $V_s$  and are presented in Figures 4.2 and 4.3, respectively, and in Appendix I.

### Data interpretation

#### *Travel Time Fit*

The program MODEL (Reid and Keen, 1990) was used in the data interpretation. The program uses travel time fitting techniques for 2-D refraction interpretation and can be run interactively on workstations. Several first order features can be recognized directly from the record sections, including (1) two crustal first arrivals ( $P_g$ ), (2) mantle refractions ( $P_n$ ) and a marked velocity asymmetry between stations south and north of shot C which is located on the Grenville Front. Based on these first arrival characteristics, a fairly simple 2-D velocity model was constructed as an initial input model (not presented here) consisting of a two-layer crust, a flat Moho and a vertical boundary within the crust at shot C, and the program was used to calculate the travel times for each captured ray travelling through the model. The calculated travel time curves were then superimposed on the recorded sections and the initial model was changed incrementally until a best fit was reached. The model parameters to be adjusted included

Fig. 4.2 Vertical component, in-line seismic record sections for each shot point along line AB plotted at a reduction velocity of 7 km/s. A 2-12 Hz band-pass filter was applied to the data. P-wave travel time curves calculated from the best fit model in Figure 4.4 are superimposed on the sections. Ray diagrams showing areas sampled by captured rays follow each section.

Shot K

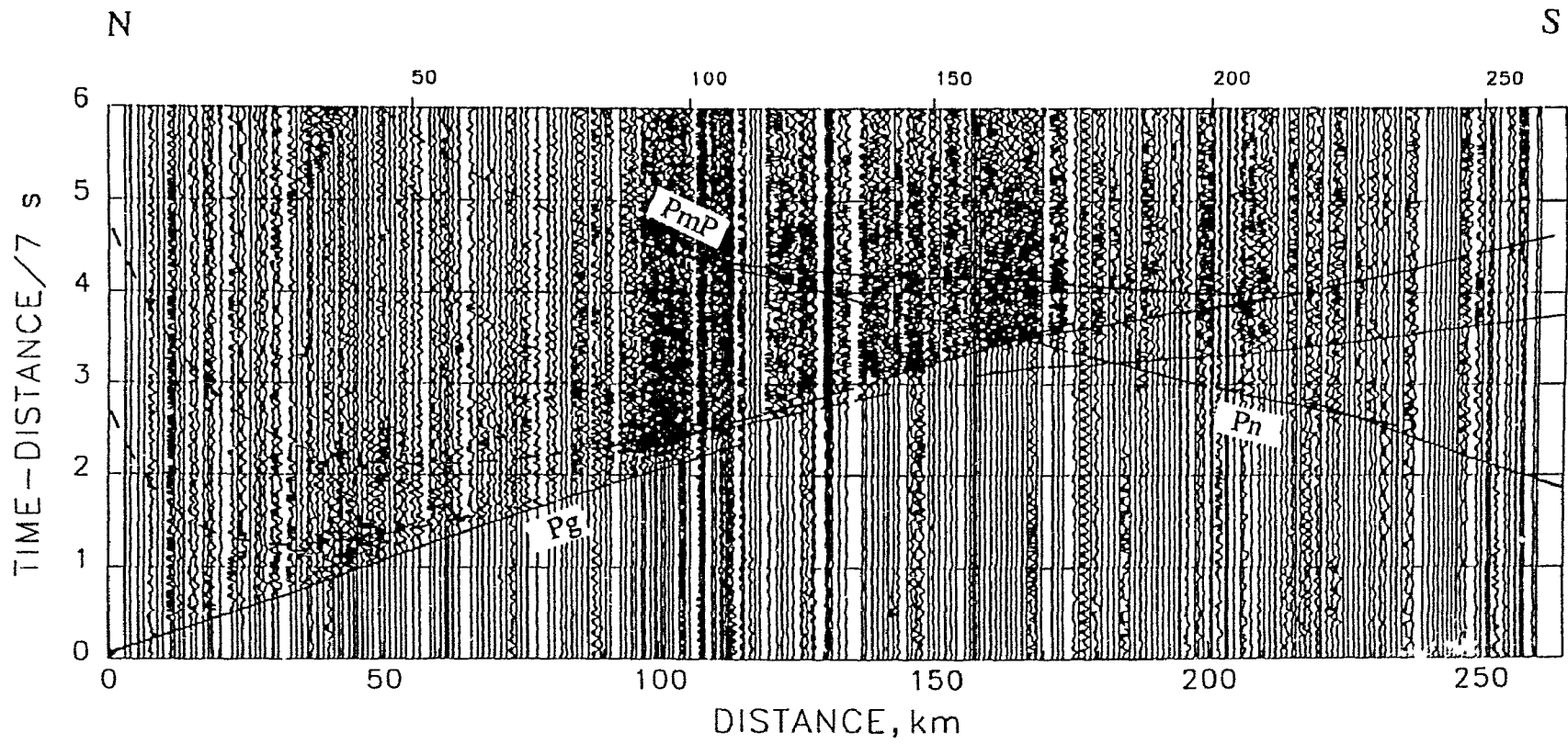


Fig. 4.2

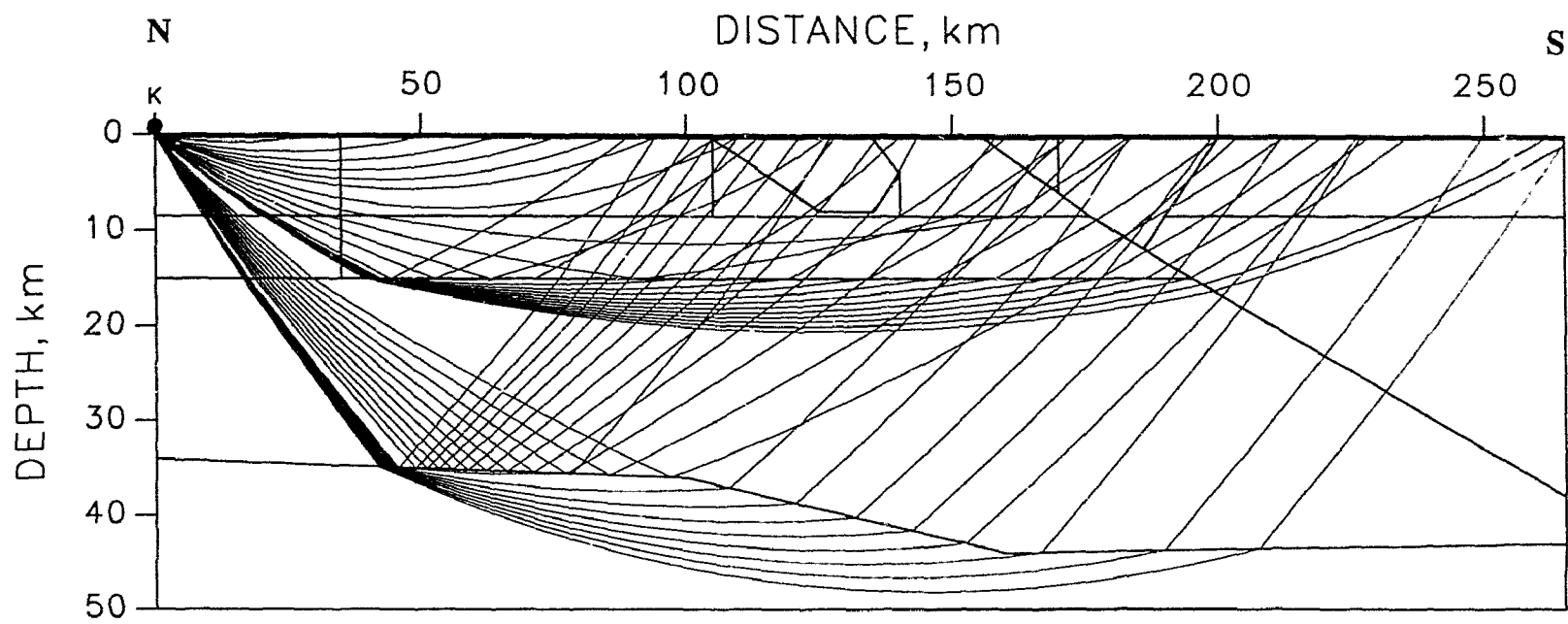


Fig. 4.2

Shot M

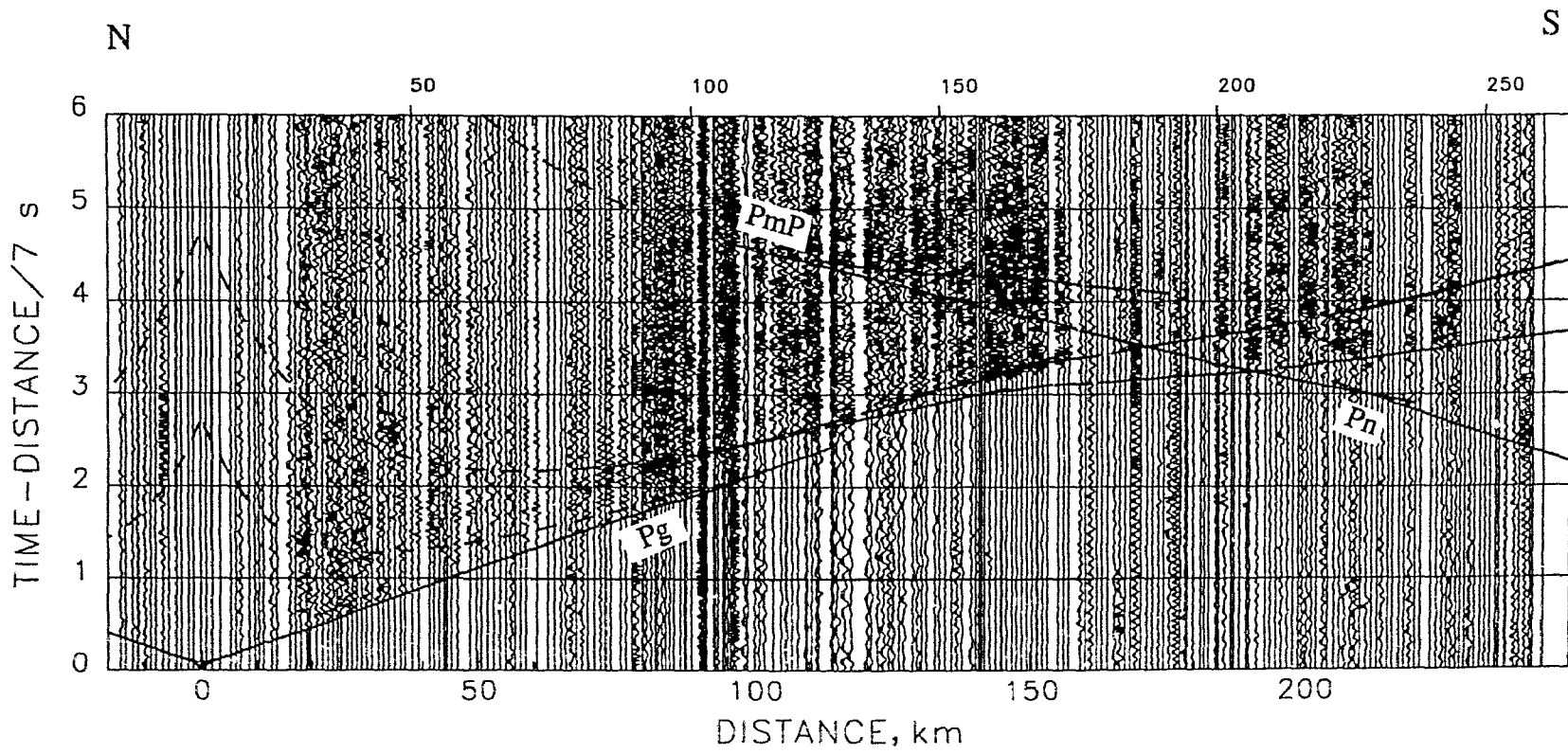


Fig. 4.2



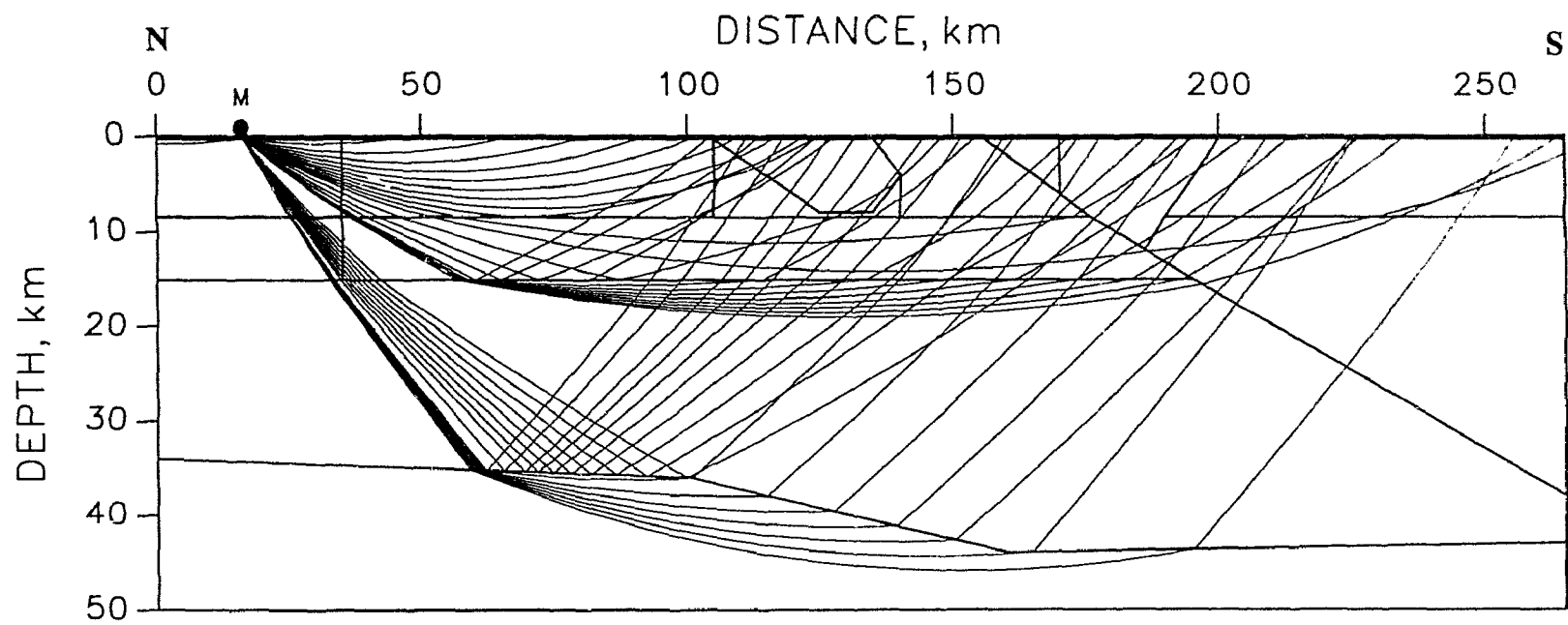


Fig. 4.2

Shot A

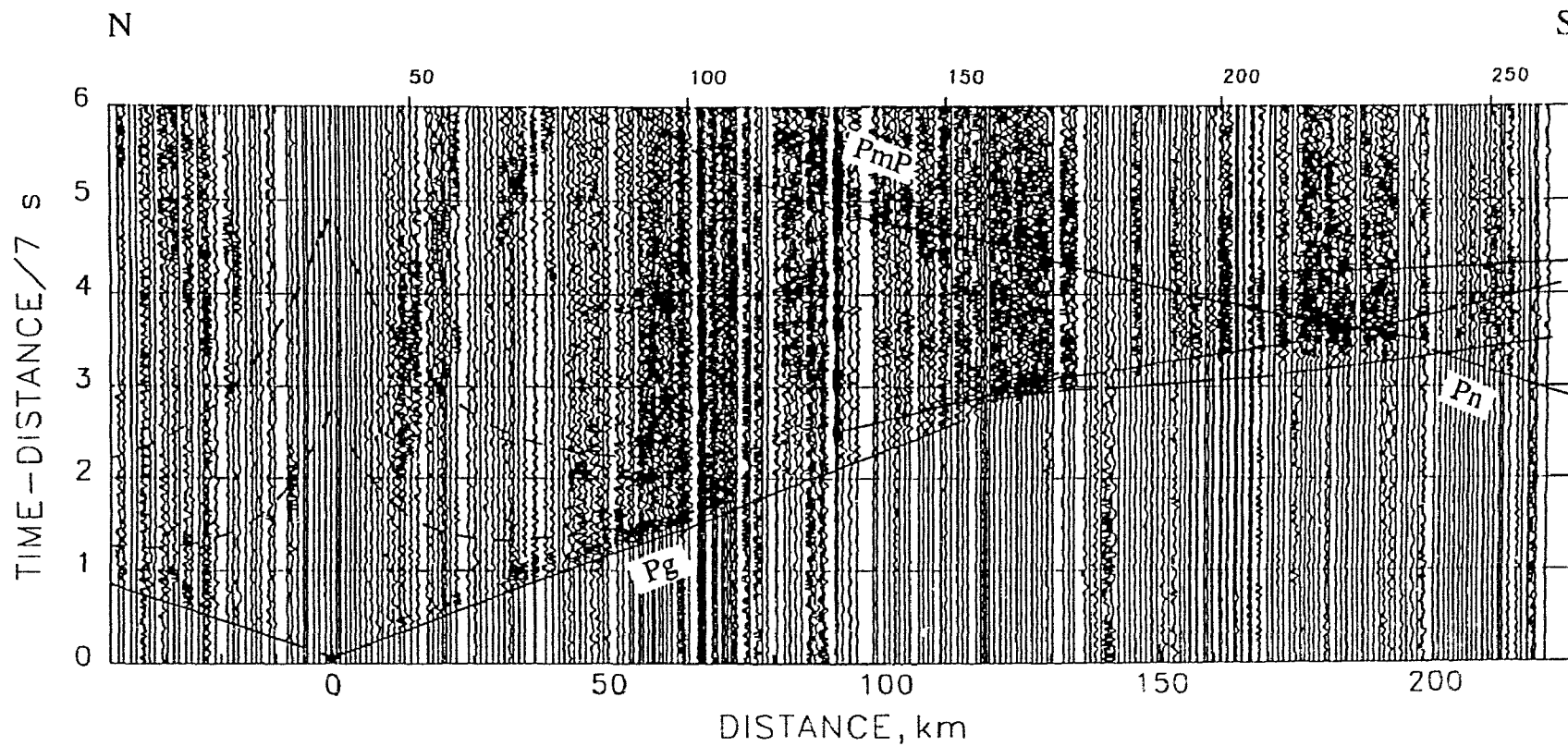


Fig. 4.2

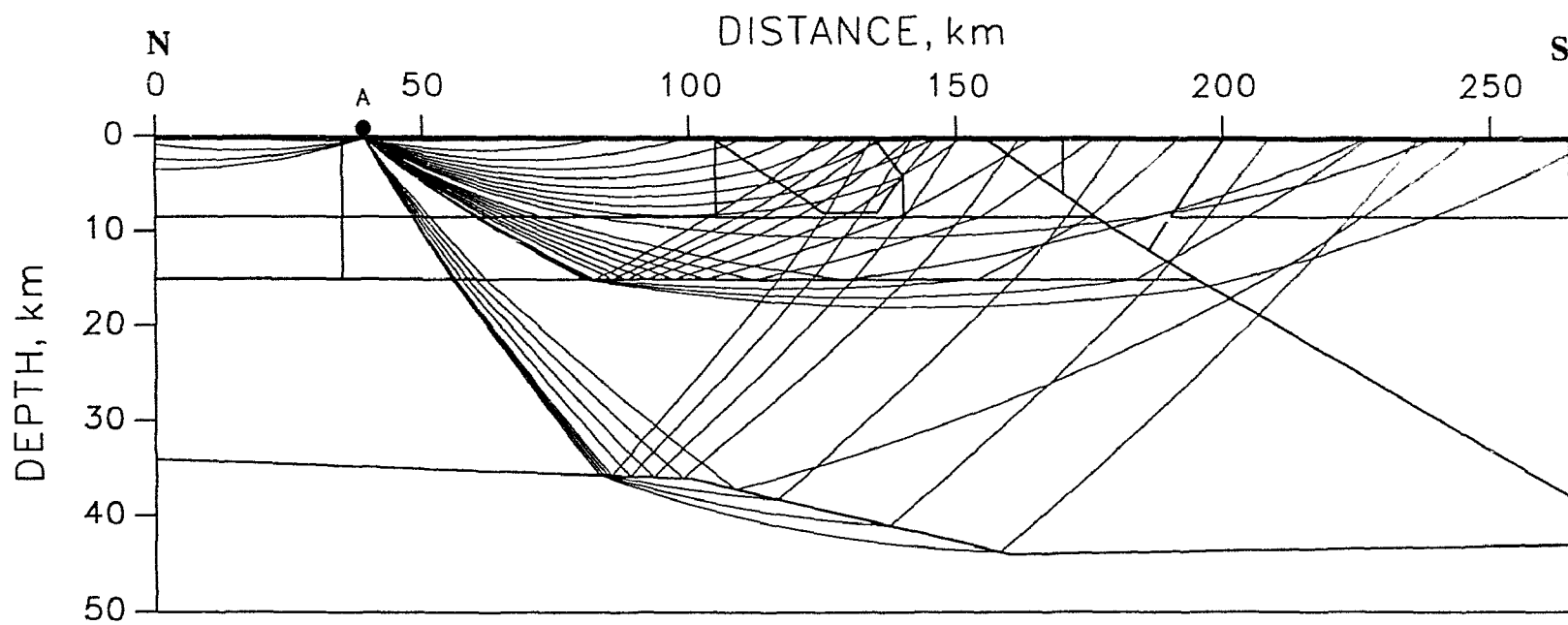


Fig. 4.2

Shot G

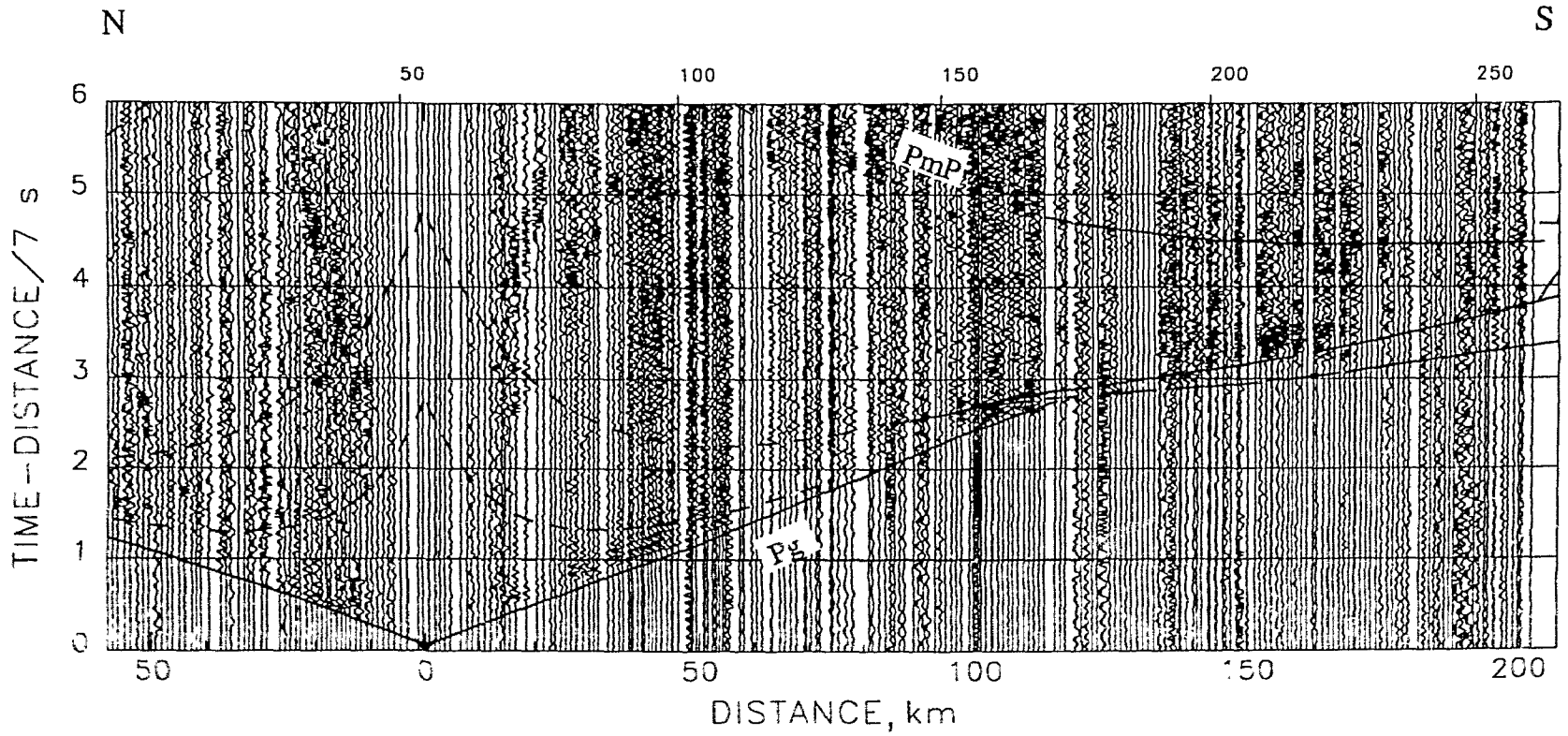


Fig. 4.2

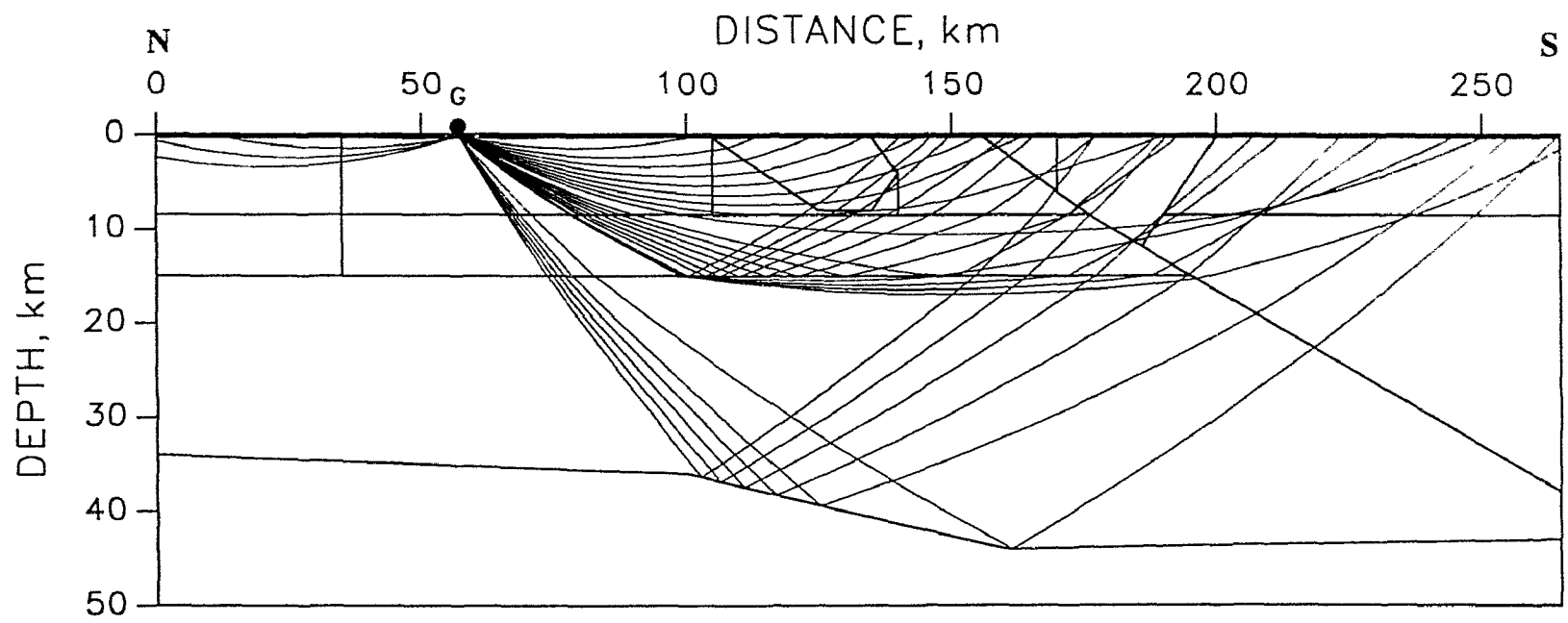


Fig. 4.2

Shot P

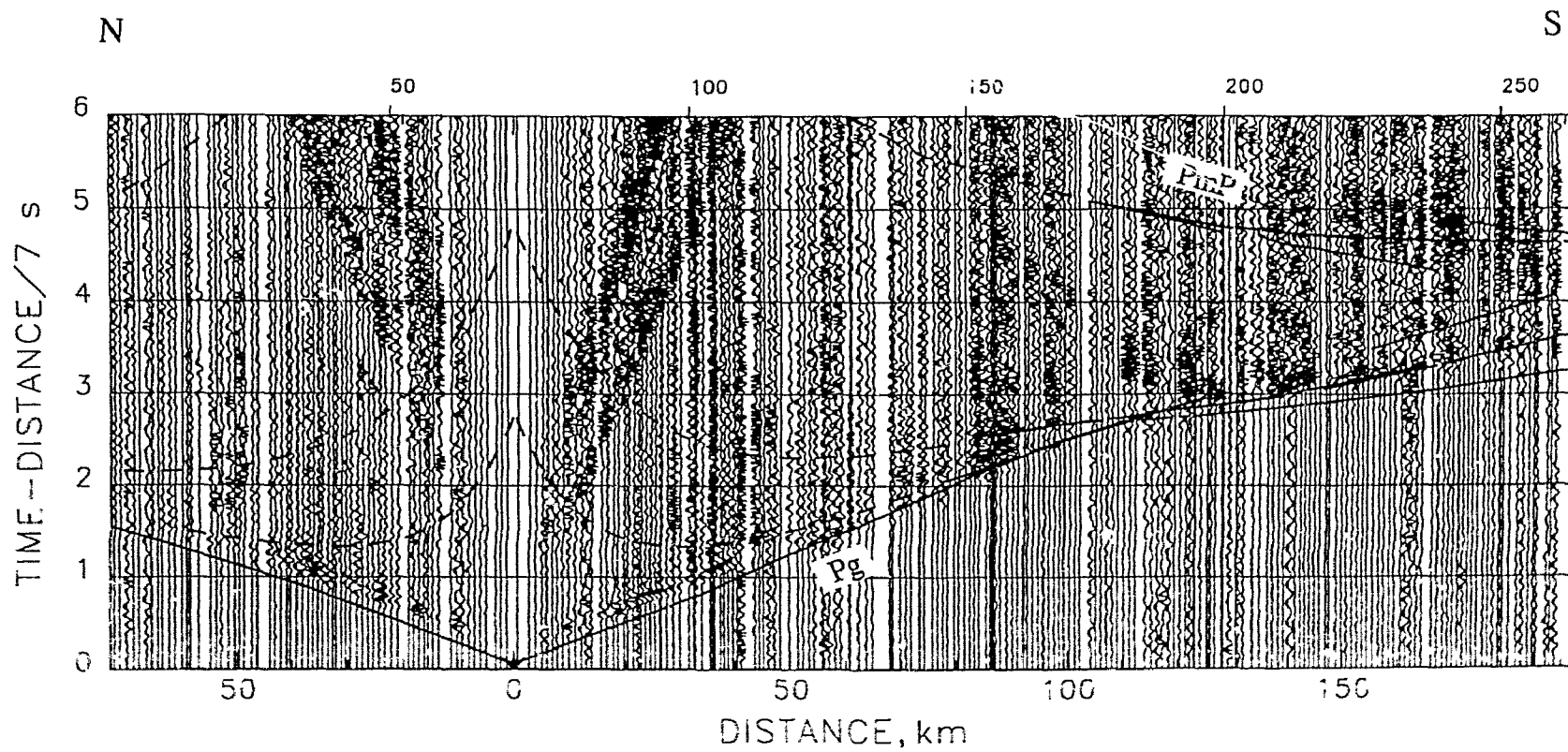


Fig. 4.2

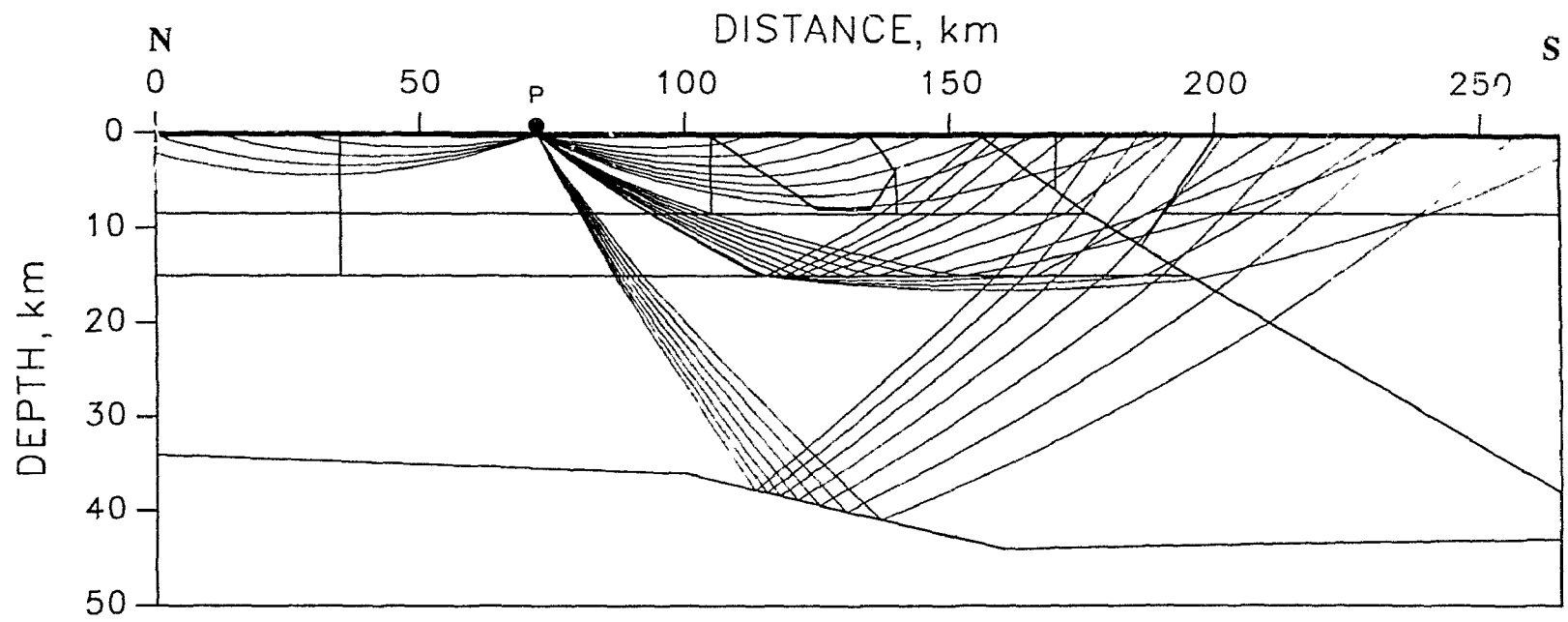


Fig. 4.2

# Shot D

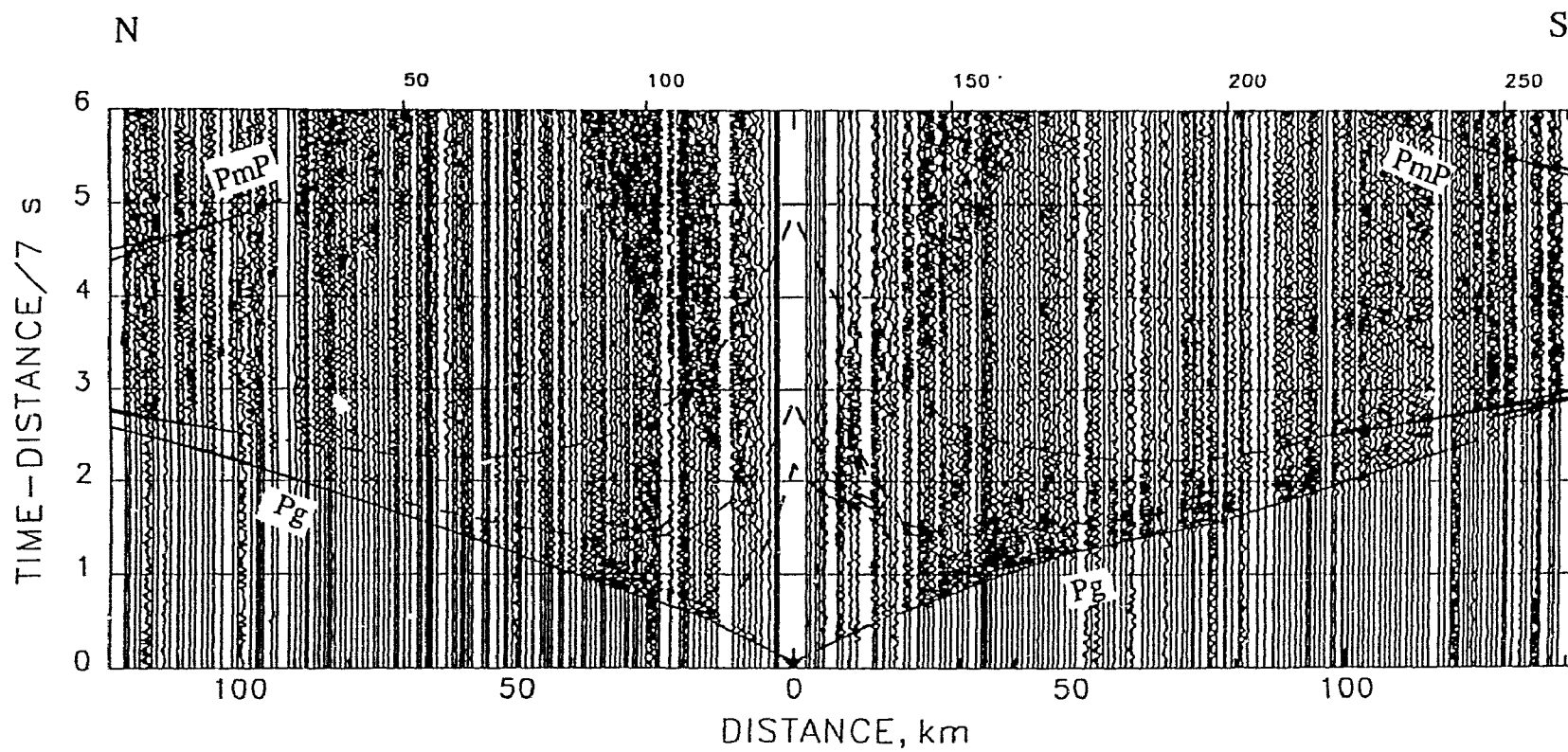


Fig. 4.2



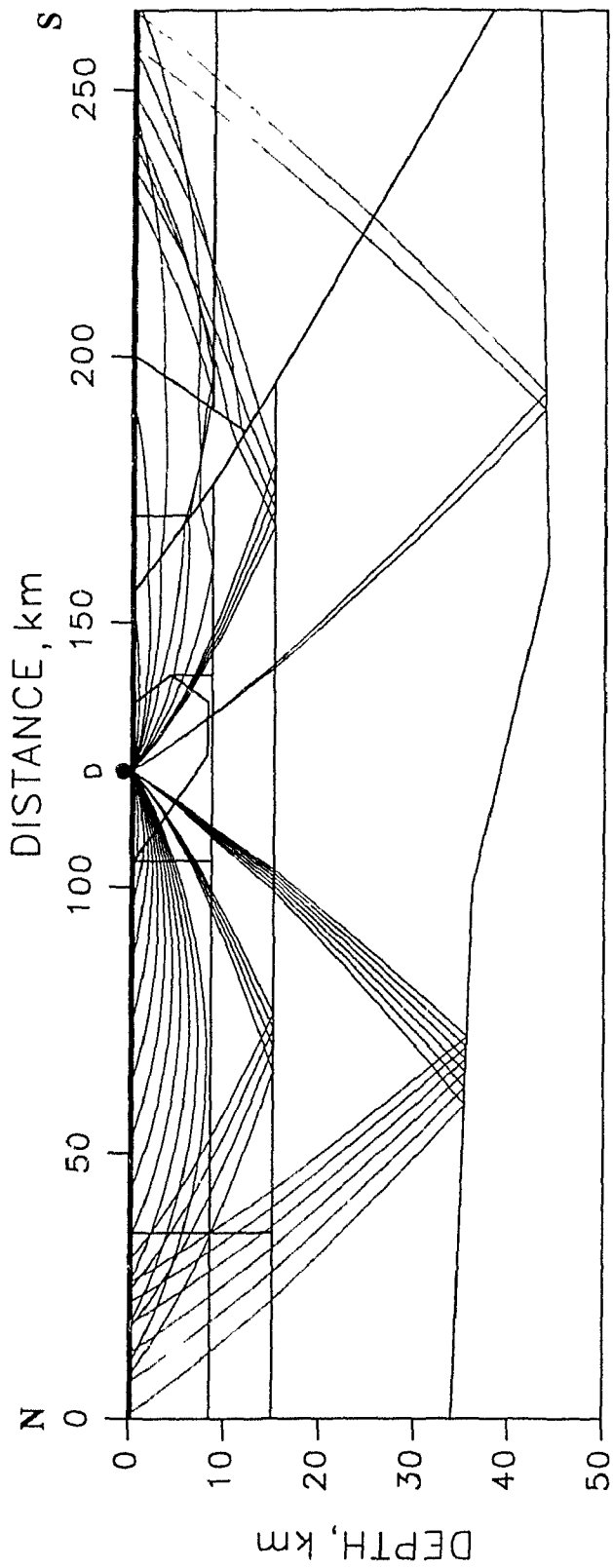


Fig. 4.2

Shot C

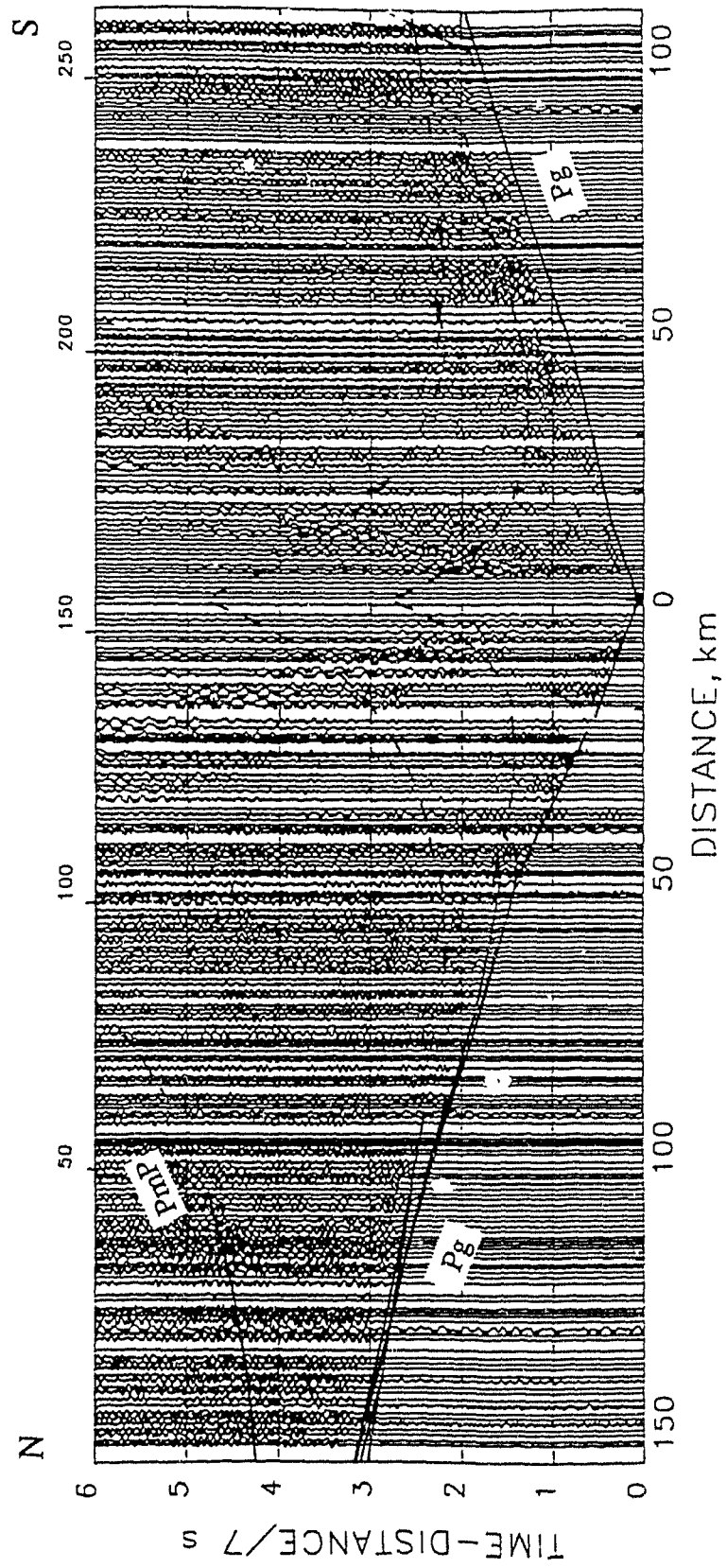


Fig. 4.2

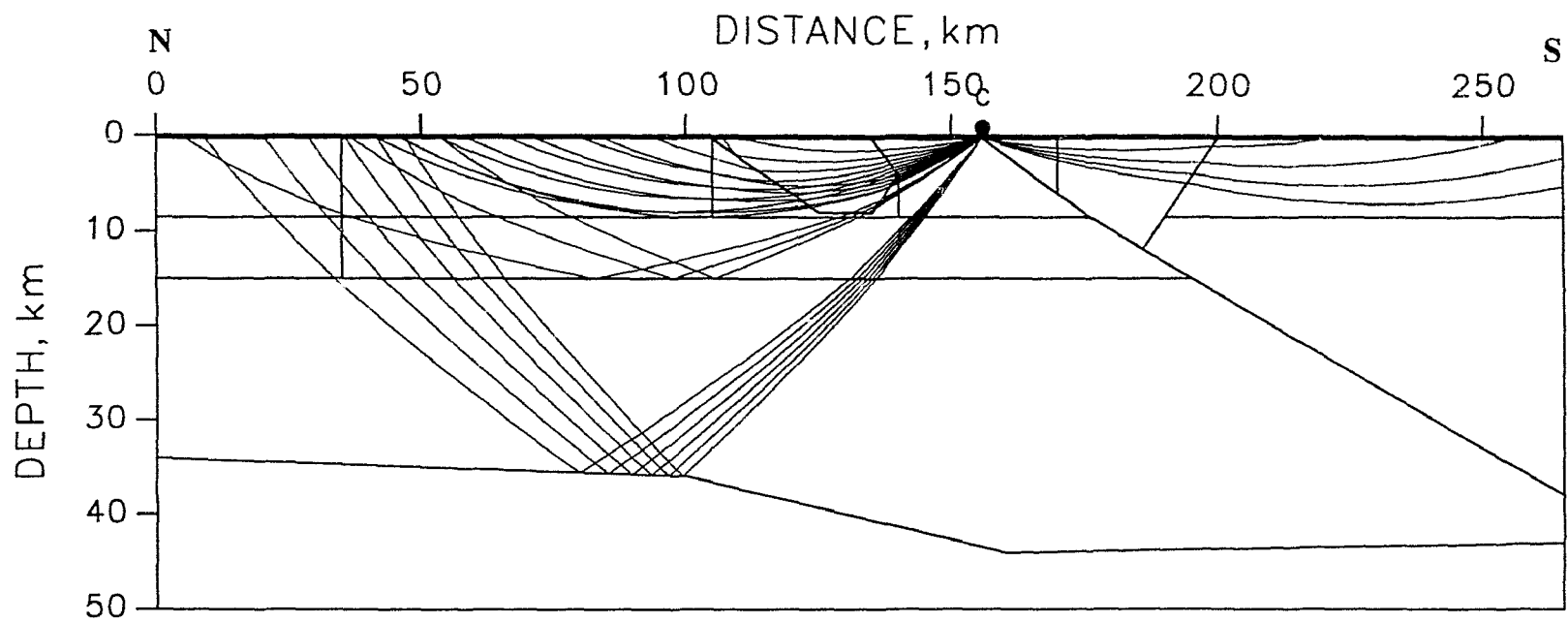


Fig. 4.2

Shot Q

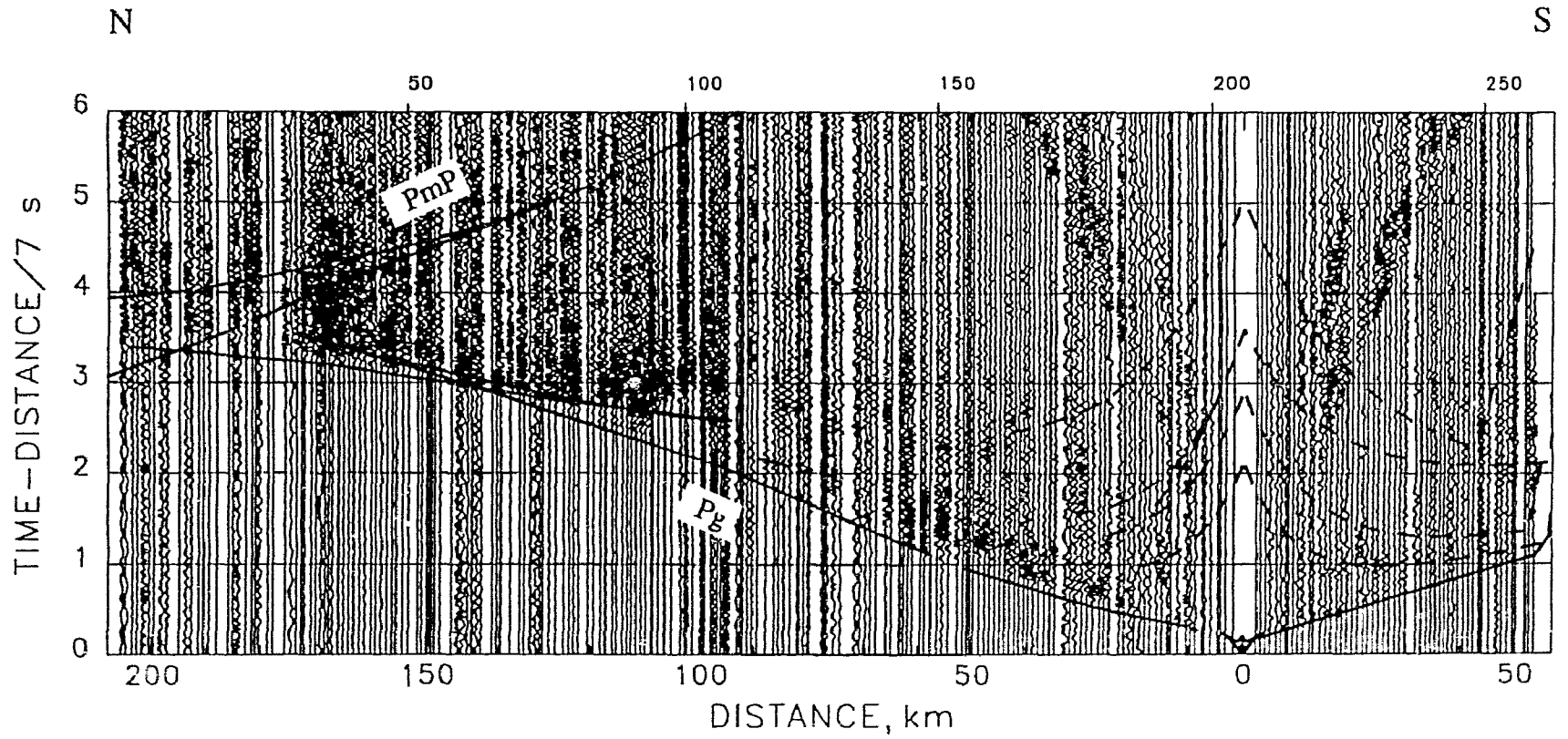


Fig. 4.2

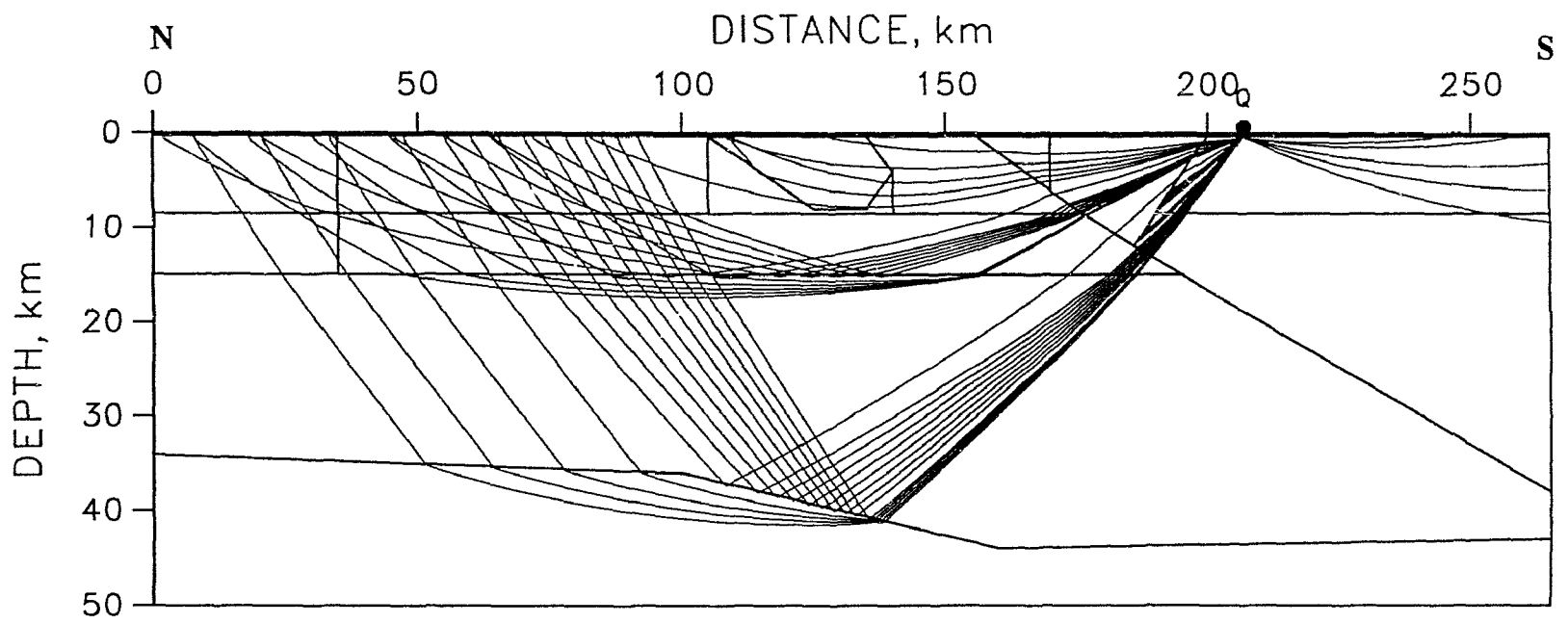


Fig. 4.2

Shot H

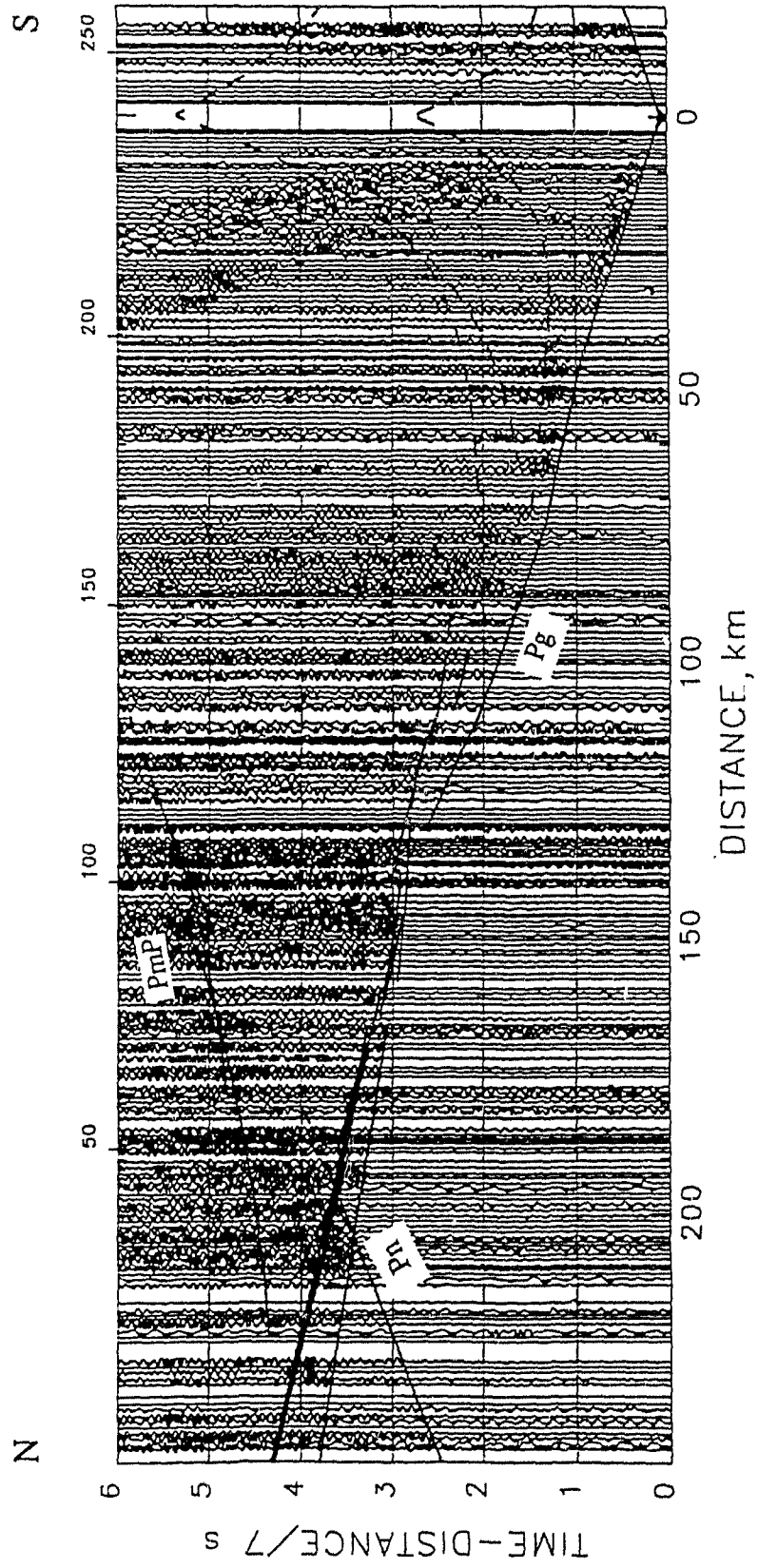


Fig. 4.2

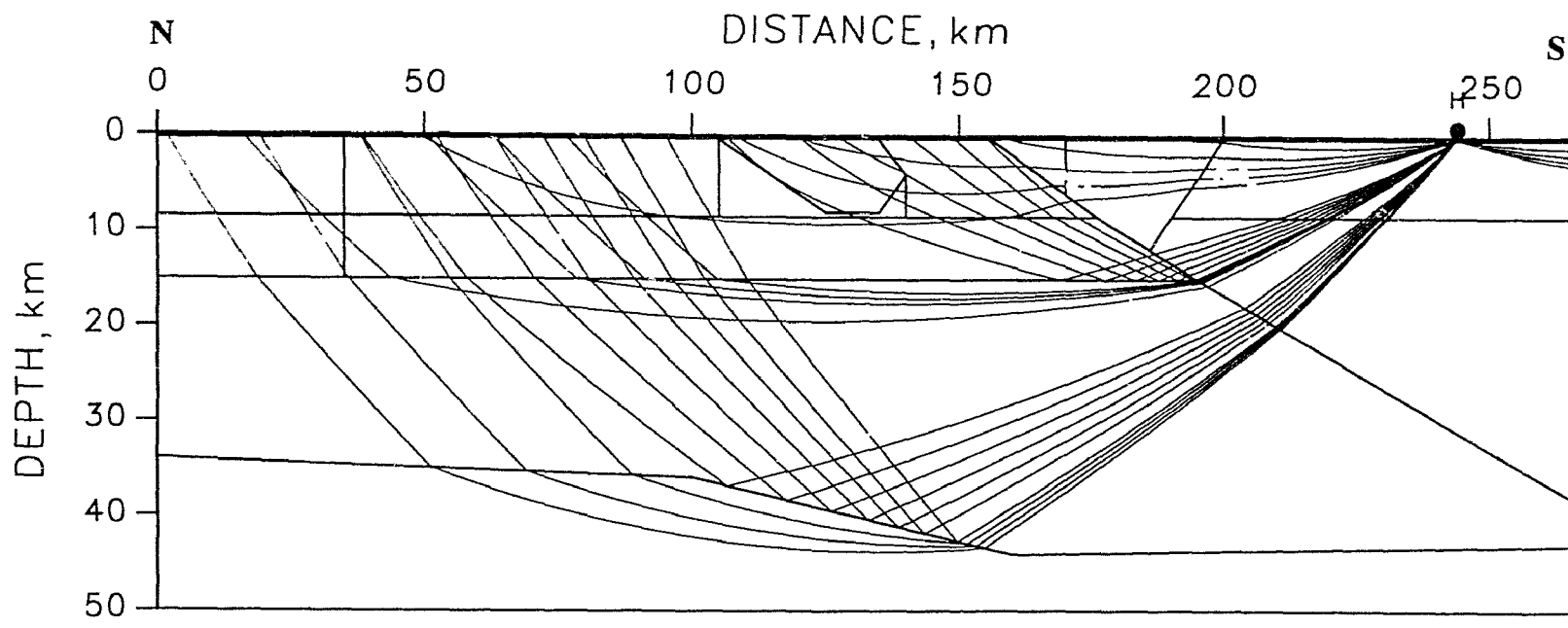


Fig. 4.2

# Shot B

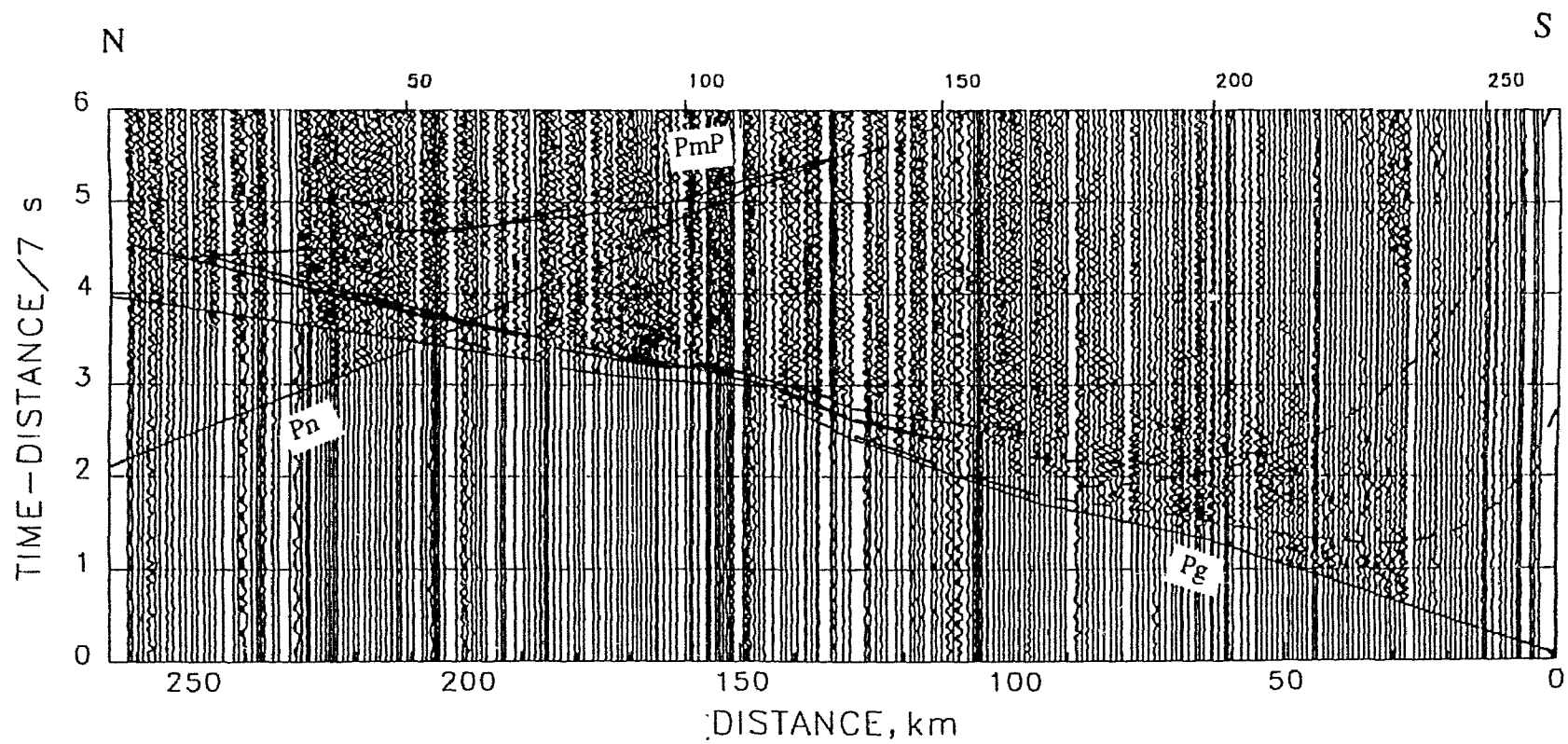


Fig. 4.2



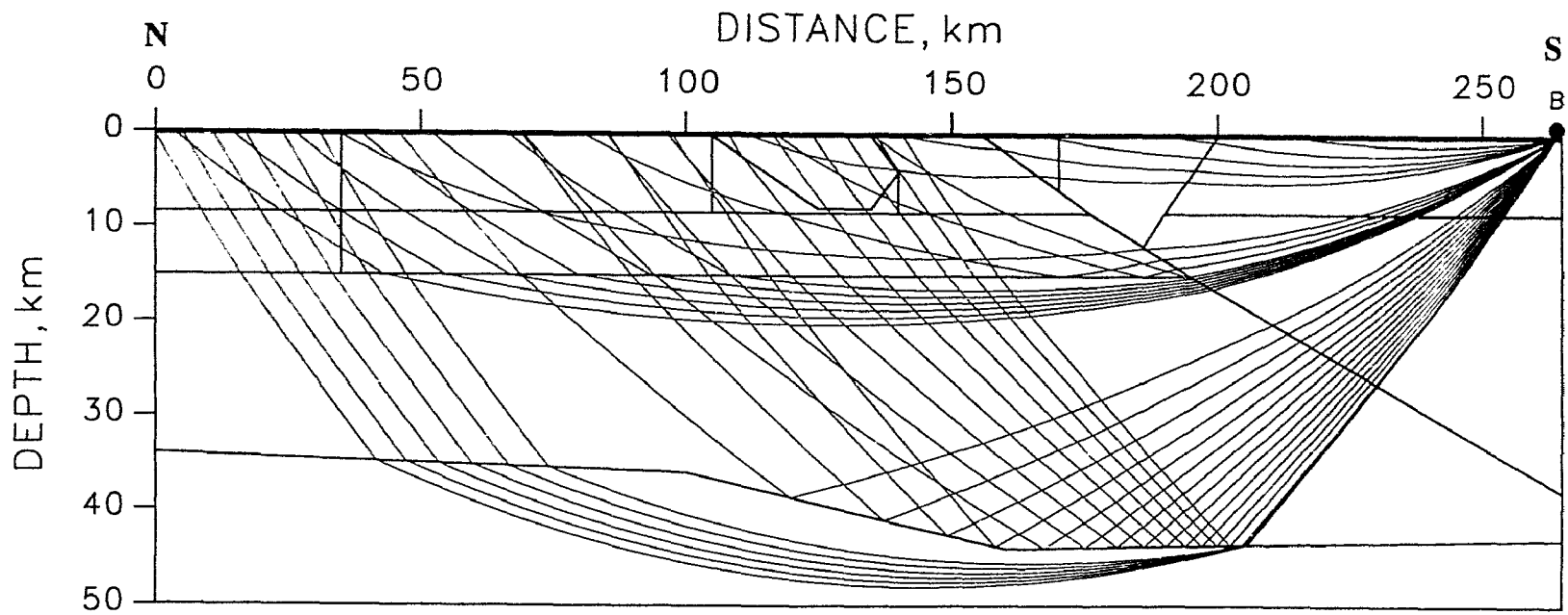


Fig. 4.2

Fig. 4.3 Vertical component, in-line seismic record section for selected shot points along line AB plotted at a reduction velocity of 4 km/s. A 2-12 Hz band-pass filter was applied to the data. S-wave travel time curves calculated from the model in Figure 4.4 are superimposed on the sections.

Shot K

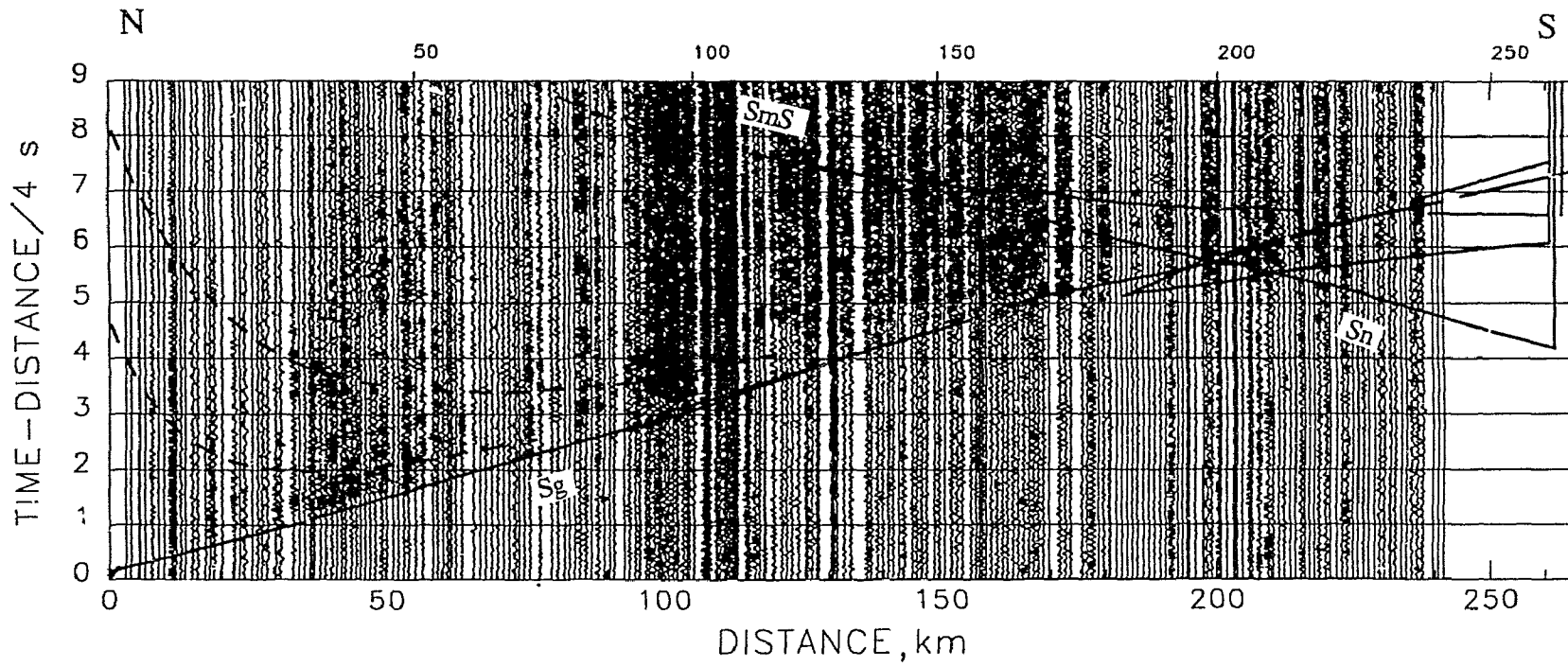


Fig. 4.3

# Shot D

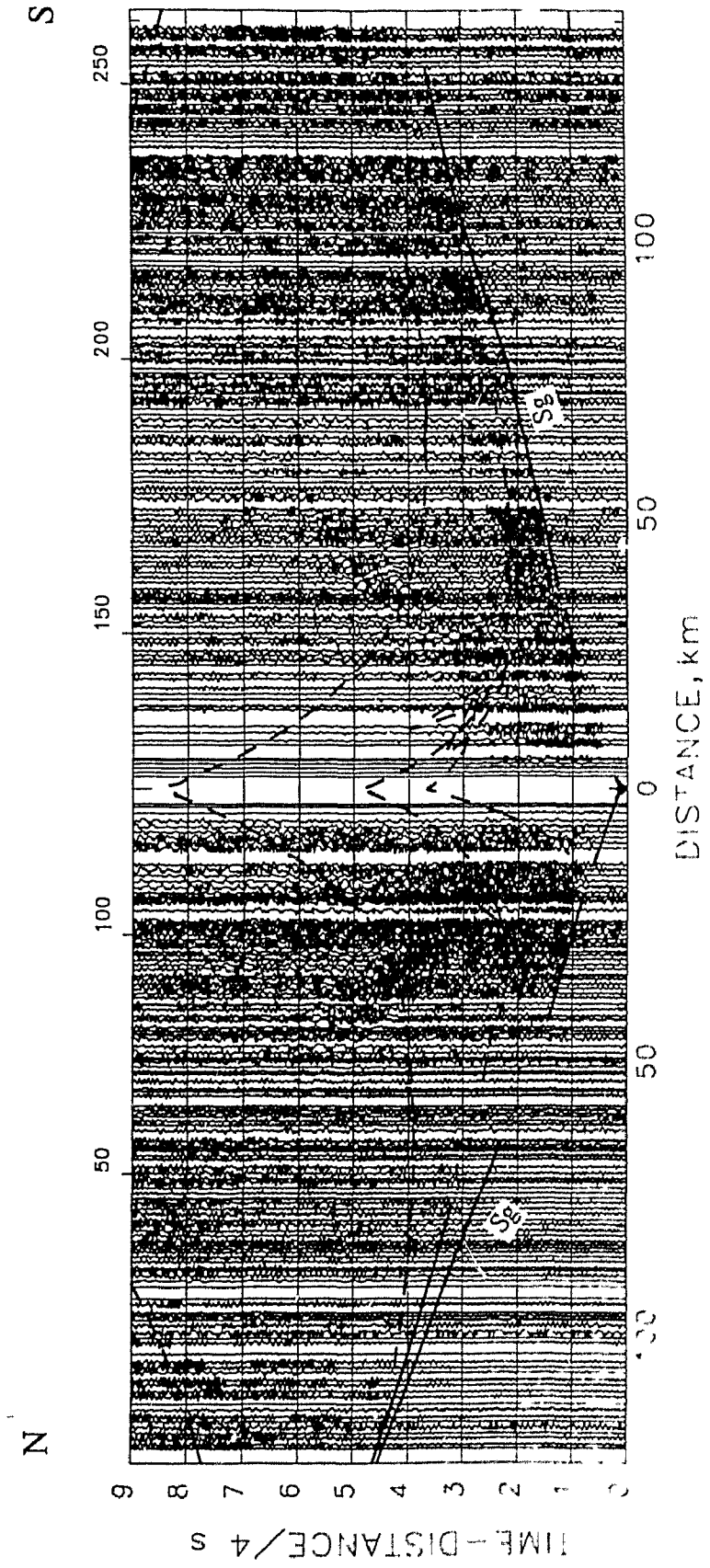


Fig. 4.3

Shot B

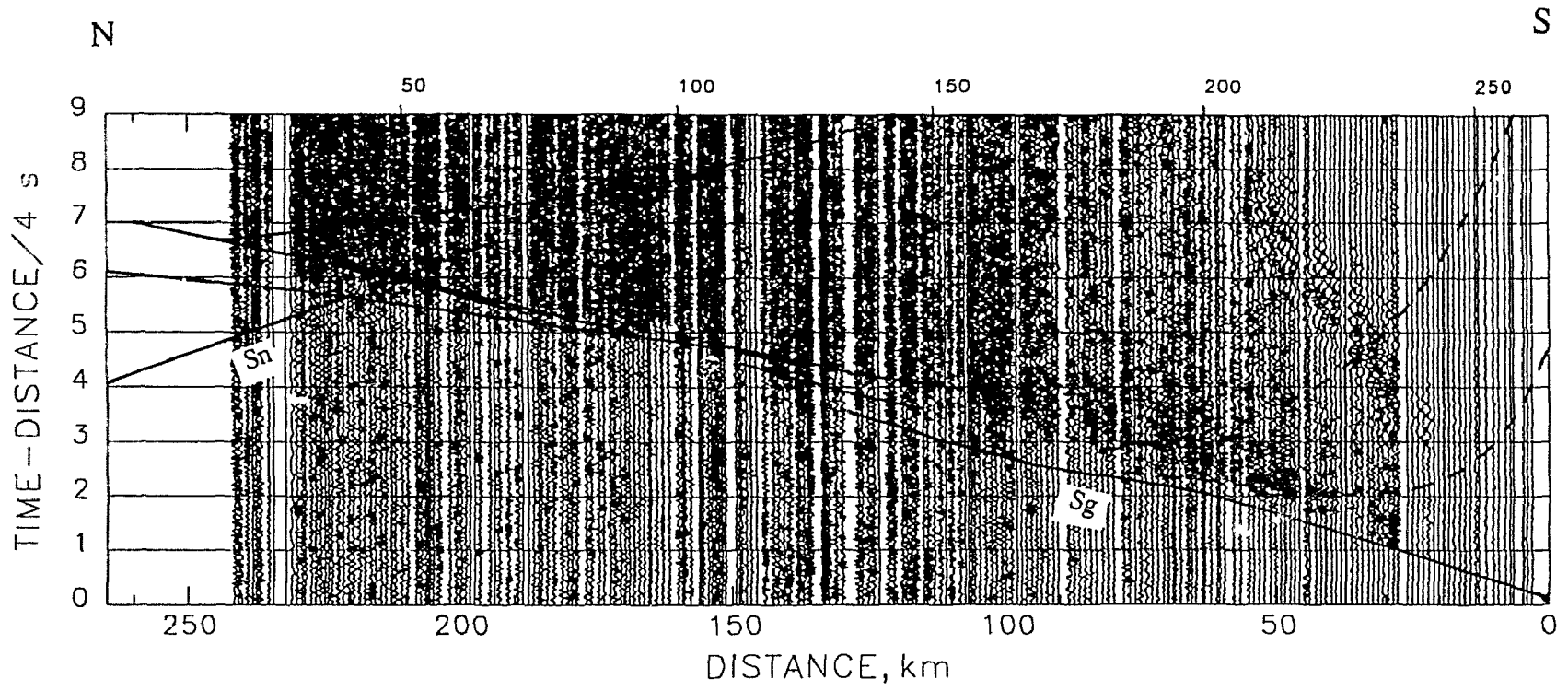
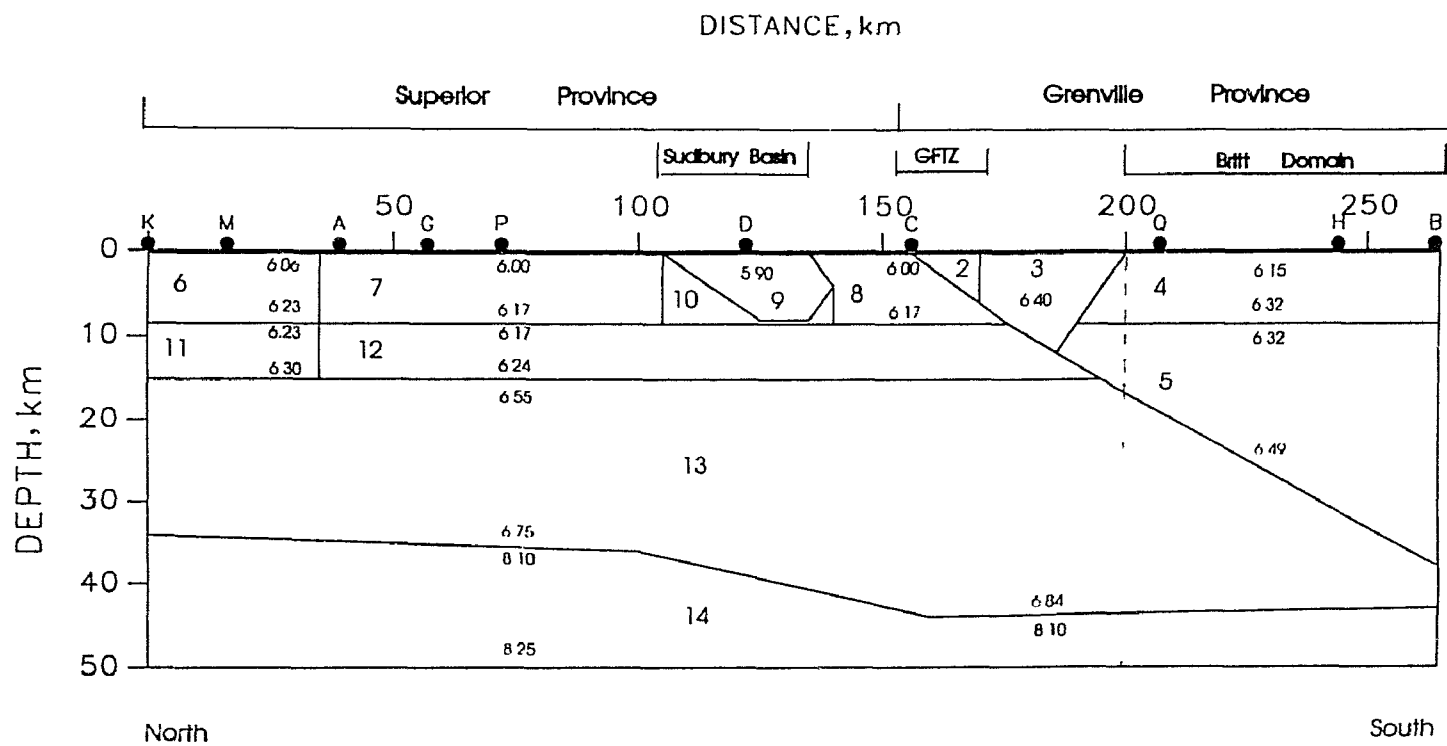


Fig. 4.3

velocity, vertical velocity gradient, their lateral variation and boundary geometry and position. Many of the changes applied to the initial model were suggested by data from other sources: The introduction of a SE-dipping Grenville Front and a low velocity basin north of the Front (the Sudbury Basin) were suggested by surface geology and existing reflection data (Green et al., 1990; Milkereit et al., 1992) and the introduction of mantle topography was suggested by the GLIMPCE data and earlier refraction modelling to the east (Mereu et al., 1986). Other features, however, were dictated by the refraction data alone and were discovered by trial and error. Figure 4.4 shows the resultant layered velocity model and the velocities, gradients and Poisson's ratios of the individual layers are given in Table 4.2. As can be seen in Figures 4.2 and 4.3 and Appendix I, the  $V_p$  and  $V_s$  travel time curves calculated from the resultant model for each shot fit most of the recorded sections quite well. The ray diagrams for each shot are also given in Figure 4.2 to show the area sampled by the captured rays. The travel time fit for some of the S-wave sections is marginal, especially for the  $S_g$  arrivals from shots C and Q (Appendix I). The misfit may be caused by S-wave splitting in a folded medium; laboratory data (Table 3.10) indicate that S-wave splitting is much stronger than P-wave anisotropy for Britt domain rocks. However, three-component data are needed to explain the  $S_g$  irregularity over the Britt domain.

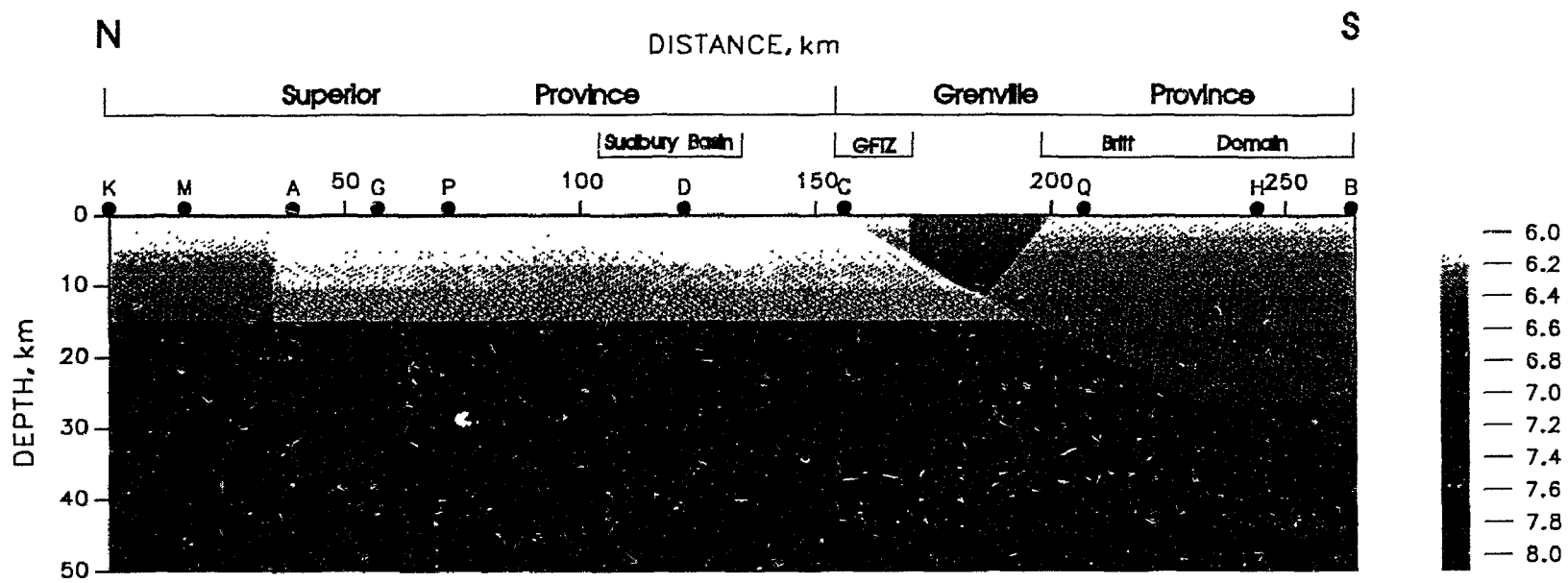
Figure 4.4. Velocity model for refraction line AB. The black dots with letters indicate shot points. a) The numbers denote layer numbers in Table 4.2. P-wave velocities are cited in the model for most layers; other parameters of individual layers are given in Table 4.2. Vertical dashed line shows location of velocity section in Figure 4.9. b) Colour print of the velocity model showing velocity gradients. Velocities in km/s.



(a)

Fig. 4.4





(b)

Fig. 4.4

Table 4.2. Velocities, velocity gradients and Poisson's ratios for individual layers in the model shown in Figure 4.4. Velocities shown are for top of layer. *Notably anisotropic layers are in italics and underlined.*

Layer	South Shots: B, H, O, C, D					North Shot: K, M, A, G, P					Average				
	Vp	g	Vs	g	$\sigma$	Vp	g	Vs	g	$\sigma$	Vp	g	Vs	g	$\sigma$
1	4.50	2.80	2.50	1.50	-	4.50	2.80	2.50	1.50	-	4.50	2.80	2.50	1.50	-
2	<i>6.15</i>	<i>0.02</i>	<i>3.55</i>	<i>0.01</i>	<i>0.25</i>	<i>5.90</i>	<i>0.02</i>	<i>3.45</i>	<i>0.01</i>	<i>0.24</i>	<i>6.07</i>	<i>0.02</i>	<i>3.52</i>	<i>0.01</i>	<i>0.25</i>
3	<i>6.40</i>	<i>0.02</i>	<i>3.68</i>	<i>0.01</i>	<i>0.25</i>	<i>6.10</i>	<i>0.02</i>	<i>3.54</i>	<i>0.01</i>	<i>0.25</i>	<i>6.30</i>	<i>0.02</i>	<i>3.62</i>	<i>0.01</i>	<i>0.25</i>
4	6.15	0.02	3.55	0.01	0.25	6.15	0.02	3.55	0.01	0.25	6.15	0.02	3.55	0.01	0.25
5	6.32	0.01	3.65	.005	0.24	6.32	0.01	3.65	.005	0.25	6.32	0.01	3.65	.005	0.25
6	6.06	0.02	3.55	0.01	0.24	6.15	0.02	3.59	0.01	0.24	6.12	0.02	3.58	0.01	0.24
7	6.00	0.02	3.53	0.01	0.24	6.05	0.02	3.55	0.01	0.24	6.03	0.02	3.54	0.01	0.24
8	<i>6.00</i>	<i>0.02</i>	<i>3.53</i>	<i>0.01</i>	<i>0.24</i>	<i>5.75</i>	<i>0.02</i>	<i>3.45</i>	<i>0.01</i>	<i>0.22</i>	<i>5.92</i>	<i>0.02</i>	<i>3.50</i>	<i>0.01</i>	<i>0.23</i>
9	<i>5.90</i>	<i>0.03</i>	<i>3.50</i>	<i>0.01</i>	<i>0.23</i>	<i>5.80</i>	<i>0.03</i>	<i>3.45</i>	<i>0.01</i>	<i>0.23</i>	<i>5.87</i>	<i>0.03</i>	<i>3.48</i>	<i>0.01</i>	<i>0.23</i>
10	<i>6.20</i>	<i>0.02</i>	<i>3.58</i>	<i>0.01</i>	<i>0.25</i>	<i>6.10</i>	<i>0.02</i>	<i>3.52</i>	<i>0.01</i>	<i>0.25</i>	<i>6.17</i>	<i>0.02</i>	<i>3.56</i>	<i>0.01</i>	<i>0.25</i>
11	6.23	0.01	3.64	.005	0.24	6.31	0.01	3.67	.005	0.24	6.28	0.01	3.66	.005	0.24
12	6.17	0.01	3.60	.005	0.24	6.22	0.01	3.63	.005	0.24	6.20	0.01	3.62	.005	0.24
13	6.55	0.01	3.75	.005	0.26	6.55	0.01	3.75	.005	0.26	6.55	0.01	3.75	.005	0.26
14	8.10	0.01	4.50	.005	0.28	8.10	0.01	4.50	.005	0.28	8.10	0.01	4.50	.005	0.28

Vp - compressional wave velocity in km/s, Vs - shear wave velocity in km/s, g - velocity gradient in s<sup>-1</sup>,  $\sigma$  - Poisson's ratio.

### *Error Analysis of Travel Time Fit*

In order to estimate the limitations of the resultant velocity model, errors of travel time fit are evaluated for features of interest, including the P-wave velocity of the upper crust in the Britt domain (layer 4), the dip of the GFTZ and the Vp anisotropy of layer 3. The method used was to plot the average (RMS) residual times between observed and calculated data against different model input parameters. The parameters resulting in the smallest residual times are considered the best fit and uncertainties of the parameters are estimated using the  $\chi^2$  method (e.g. Osler, 1993).

To determine the accuracy of the compressional wave velocity and velocity gradient derived for the Britt domain, the residuals calculated for various input velocities and gradients are plotted and contoured in Figure 4.5. Rays from shots B and Q at a range of 200-265 km are used for this calculation. The results show that the residual time is much more sensitive to velocity perturbation than to gradient perturbation. The resultant model parameters for this layer fall well within the 20 ms contour which corresponds to a velocity uncertainty of  $\pm 0.03$  km/s and a gradient uncertainty about  $\pm 0.03\text{s}^{-1}$ . Thus the velocity assigned to layer 4 in the velocity model is quite accurate but the gradient could not be well constrained by this test alone. However, the gradient of this layer is well constrained by the residual time contours in Figure 4.6 in which all rays crossing the GFTZ from all shots were included in the calculations. Figure 4.6

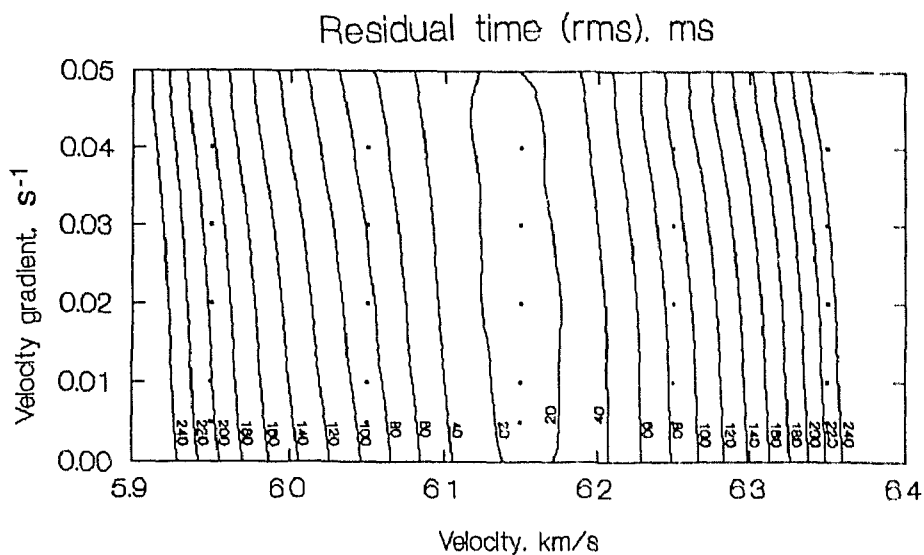


Fig. 4.5 Average residual time plotted against  $V_p$  and  $V_p$  gradient in the Britt domain (layer 4). All rays from shots B and Q at a range of 200-265 km are included in the calculation. Solid squares show models tested.

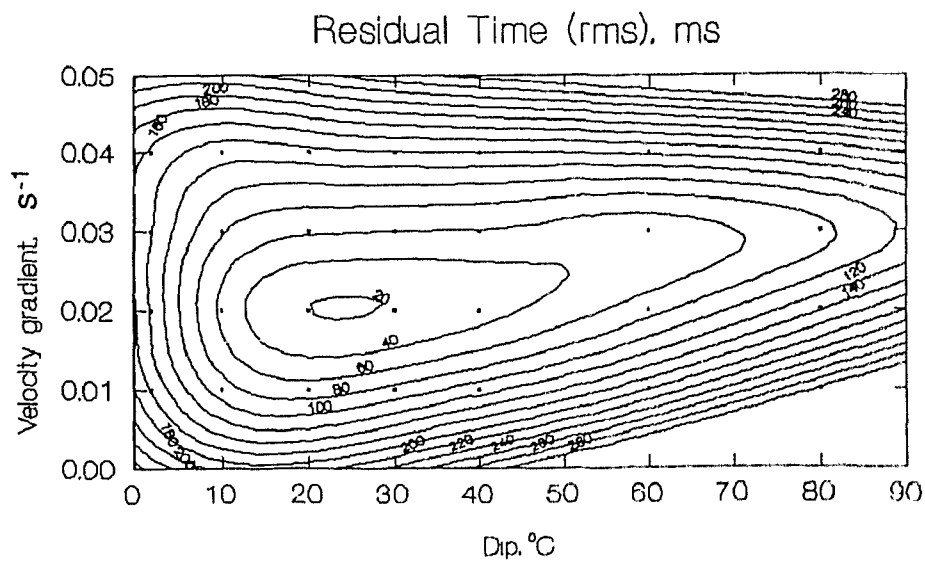


Fig. 4.6 Average residual time plotted against dip of the GFTZ and  $V_p$  gradient in the Britt domain (layer 4). All rays crossing the GFTZ are included in the calculation. Solid squares show models tested.

shows that the residual time is much more sensitive to the gradient of layer 4 than to the dip of the GFTZ. The resultant model, with a gradient of  $0.02\text{s}^{-1}$  and a dip of  $22^\circ$  falls within the 20 ms residual time contour which corresponds to a dip uncertainty of  $\pm 4^\circ$ . These results constrain the dip of the Grenville Front and have been incorporated in the final model shown in Figure 4.4.

In order to test for Vp anisotropy in layer 3, residual times for various combinations of Vp and Vp gradient in layer 3 are plotted in Figure 4.7a for shots B, H, Q and C in the south and Figure 4.7b for shots K, M, A, G and P in the north. All rays traversing layer 3 are included in the calculation. The different Vp values defined by these two plots (6.4 km/s for rays subparallel to foliation, 6.1 km/s for rays subperpendicular to foliation) both have uncertainties of about  $\pm 0.05$  km/s. Figures 4.7a and 4.7b also show that the difference in Vp for the two shot groups cannot be erased by changing gradients.

#### *Synthetic Amplitude Analysis*

Synthetic amplitudes were calculated for selected shots using the program SYNPROC (Reid, 1993) in order to estimate the limitations of the model shown in Figure 4.4 in terms of arrival energies. Three synthetic sections for shots K, D and B are presented in Figures 4.8a, 4.8b and 4.8c, respectively. Comparison with the recorded sections shows that 1) the synthetic Pg arrivals are stronger than the observed arrivals

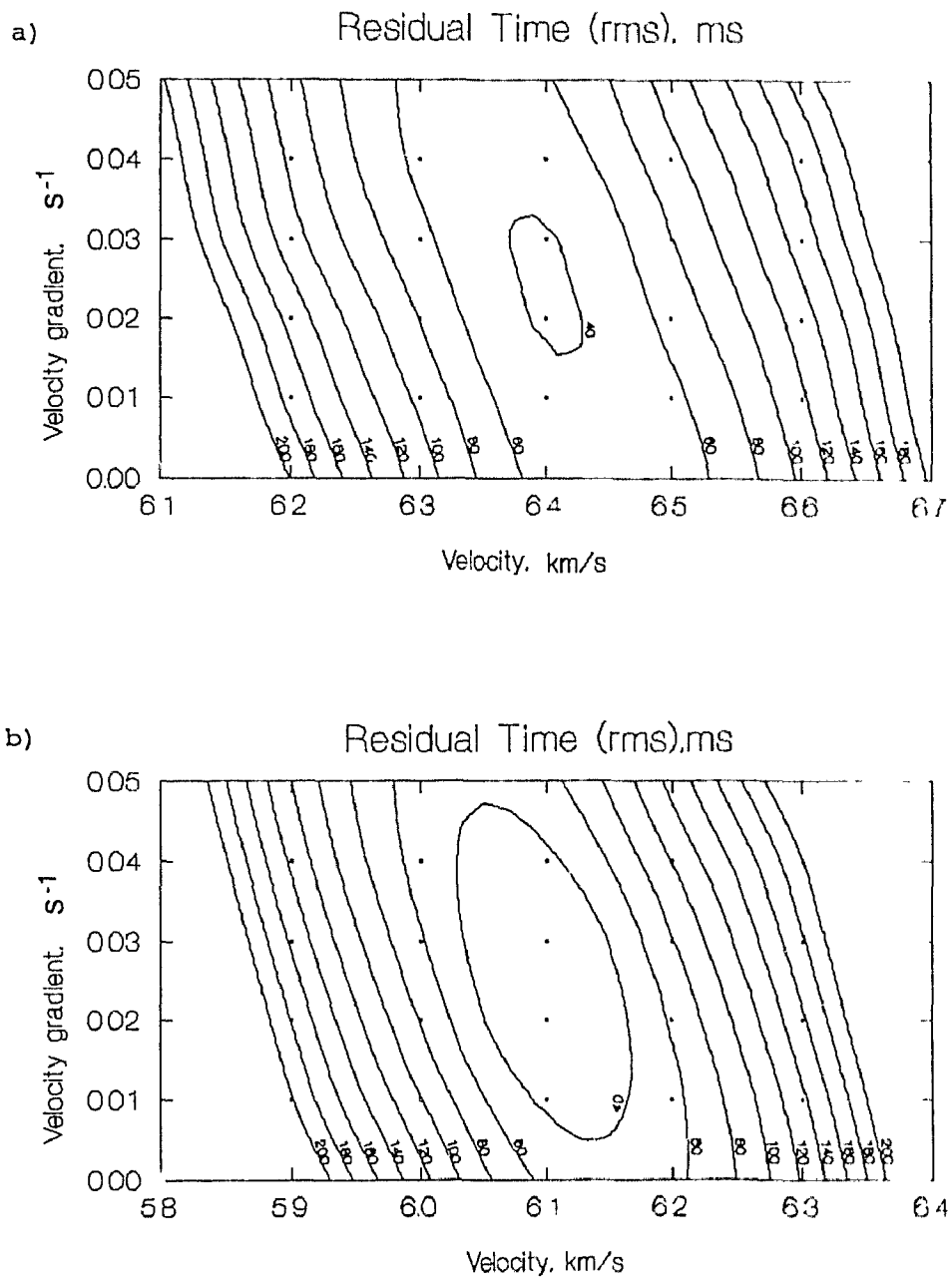


Fig. 4.7 Average residual time plotted against  $V_p$  and  $V_p$  gradient in layer 3. a) Residual time calculated using rays from shots B, H, Q, C, and D which cross layer 3. b) Residual time calculated using rays from shots K, M, A, G, and P which cross layer 3. Solid squares show models tested.

Fig. 4.8. Synthetic seismic refraction profiles for a) shot K, b) shot D and c) shot B using the 2-D velocity-depth model in Fig. 4.4 and Table 4.2. Traces are plotted at a reduction velocity of 7 km/s.

(a) shot K

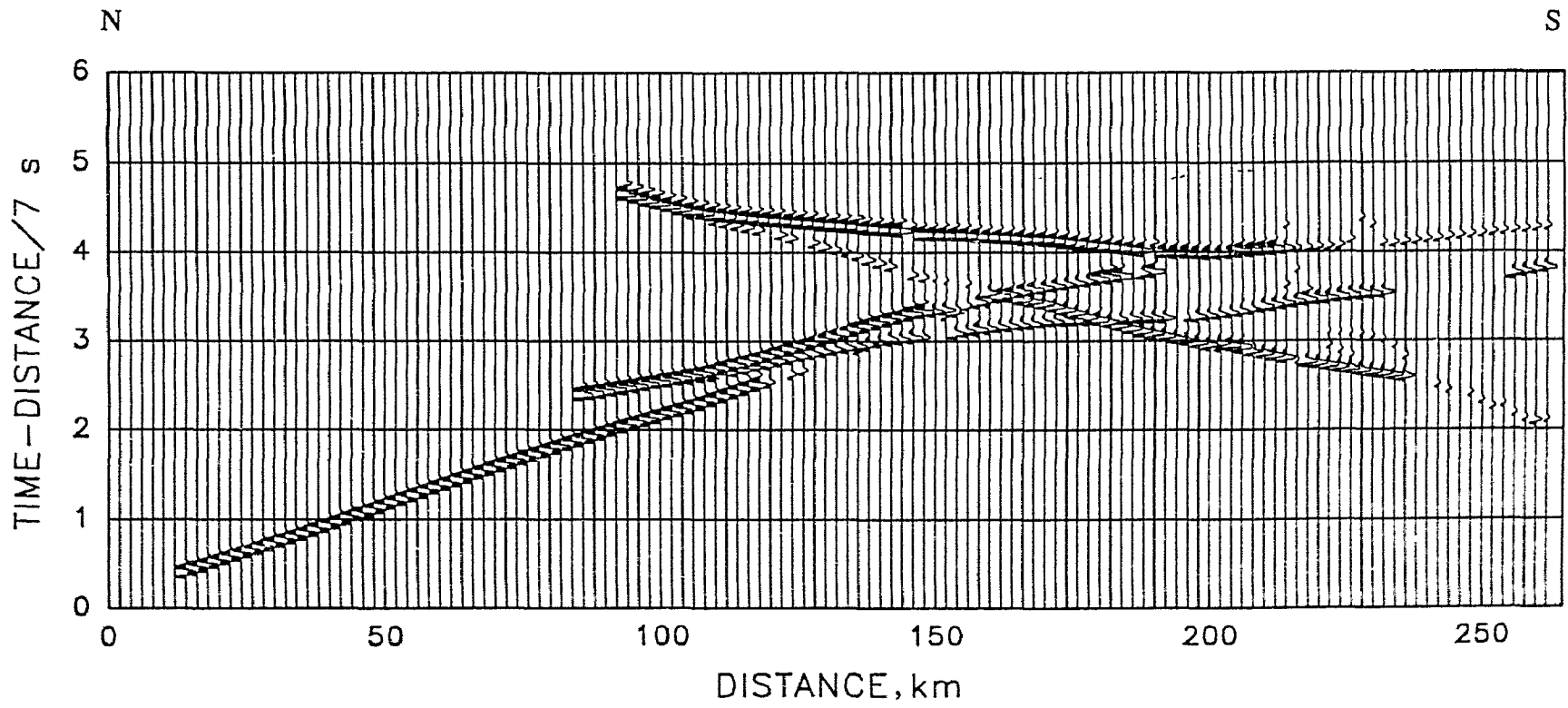


Fig. 4.8



(b) shot D



Fig. 4.8

(c) shot B

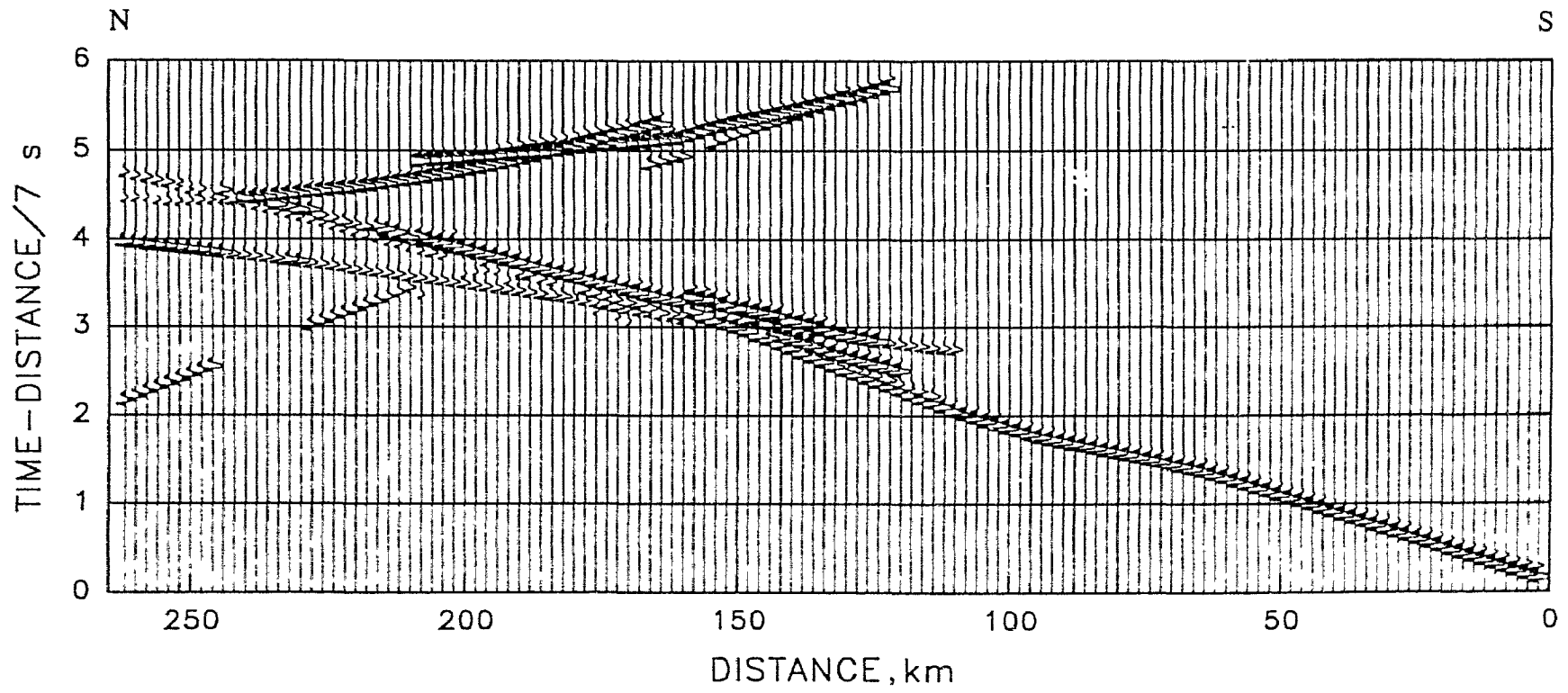


Fig. 4.8

at a range from 0 - 108 km (north of the GFTZ), 2) the synthetic PCP and PmP arrivals are also generally stronger and 3) synthetic later arrivals are much simpler than observed arrivals. These obvious misfits to the recorded data indicate that 1) the velocity gradients in the upper crust north of the GFTZ may be smaller than those in the model, 2) the upper-lower crust boundary and the Moho should be represented as velocity transitions with steep gradients rather than as sharp boundaries, and 3) the crust is generally more complicated than the model, especially in the vicinity of the Sudbury Basin and the GFTZ where strong, complicated later arrivals are recorded through a long time window after the first arrivals. Therefore, the model presented in this study is only a first order result representing regional average velocities and large scale crustal structures.

#### *Interpretation of the Resultant Model*

Due to a lack of velocity information on the weathered layer in this refraction data set, the velocity and thickness of the top layer in the model (layer 1) was based on refraction data from the On-Going Great Lakes Experiment (Burke, 1991) conducted in the GFTZ just west of line AB. Immediately beneath the weathered layer, which was assigned an arbitrary thickness of 300 m, slightly different velocities were obtained for the southern and northern portions of the line. In the Britt domain (layer 4),  $V_p=6.15$

km/s and  $V_s=3.55$  km/s but north of the GFTZ (layers 7 and 8),  $V_p$  averages 6.00 km/s and  $V_s=3.53$  km/s. Velocities increase fairly rapidly with depth in the upper levels of the crust ( $0.02-0.03s^{-1}$ ) and then more slowly in layers 5, 11 and 12 ( $0.01s^{-1}$ ). As shown in Figure 4.4 and Table 4.2, the lower crust (layer 13) is marked by a modest increase in velocity to 6.55 km/s ( $V_p$ ) and 3.75 km/s ( $V_s$ ) both under the Superior Province and where layer 13 extends under the Grenville Province but the crust-mantle boundary is much deeper under the GFTZ and the Britt domain. The Sudbury Basin shows slightly lower velocities than the surrounding granitic gneisses, in agreement with laboratory data (Salisbury et al., 1991) and these gneisses, in turn, display slightly lower velocities than the granodiorite gneisses south of the Front, as would be predicted from the laboratory data (Table 3.5). Also shown in the model is a high velocity block (layer 3) just south of the GFTZ with a velocity as high as 6.4 km/s which coincides with a pronounced gravity high (Ministry of Northern Development and Mines, 1991)). This high velocity block may be related to abundant mafic rocks exposed at the surface. Archean ages (Nd-Sm; A. Dickin, personal communication) have been obtained in this area suggesting that this high velocity block may be a wedge of Superior Province lower crust brought to the surface during thrusting. A similar case can be found in the eastern Grenville Orogen (Rivers, 1994). One of the most interesting results is that the GFTZ (layer 2) and the blocks in its vicinity (3, 8, 9,

10) show notable anisotropy at shallow depths (<8 km), indicating a south-dipping foliation or layering, with  $V_p$  fast parallel to dip. Although weak anisotropy is also likely in the Britt domain (layer 4), it cannot be demonstrated because of the raypath geometry. If the Britt domain is anisotropic, the velocity given for layer 4 in Table 4.2 is probably the fast velocity.

The large scale features shown in the resultant model are consistent with the results of GLIMPCE profile J (Fig. 2.10; Epili and Mereu, 1991), including the overall crustal velocity structure, the velocity discontinuity in the middle crust under the Superior Province and the dip geometry and depths. However, the series of dipping layers detected under the Britt domain along Profile J are not resolved in this study. A possible explanation is given in Chapter 5. COCRUST profile AO (Fig. 2.7; Mereu et al., 1986) shows different features in the CGB to the east, including low velocities near the surface, higher velocities in the middle to lower crust and a very thick crust-mantle transition zone. However, the P-wave velocity structure under the Britt domain determined in this study is very similar to that along COCRUST profile CD further to the east (Fig. 2.7; Mereu et al., 1986).

## Comparison of In-situ and Laboratory Data

Refraction and average laboratory velocities for the Britt domain beneath the weathered layer are summarized along with their estimated errors in Figure 4.9. The refraction velocities at various depths are those determined at a range of 200 km for the northern Britt domain and presented in Table 4.2. The laboratory compressional and shear wave velocity curves are the average velocities calculated for the Britt domain in Chapter 3 (Table 3.11) for different propagation directions using the time average method and the estimated abundances of each major lithologic group. As shown in Figure 4.9, the data fall into three groups: (1) 0-3 km where the fit is poor, (2) 3-15 km where the fit is excellent and, (3) 15 km-Moho where a higher refraction  $V_p$  suggests a change in lithology.

Although geothermal effects on velocity are usually small, especially in shield areas, geothermal corrections were made to the laboratory  $V_p$  data and are shown in Figure 4.10 in order to make a better estimation of the lithology at depth. The corrections were based on the laboratory results of Christensen (1979) (about  $-0.05$  km/s/100<sup>0</sup>C) and an average geothermal gradient of about 10<sup>0</sup>C/km for the Canadian shield (Sass et al., 1968). Only average and fast velocities are given in Figure 4.10 because measured refraction velocities are for sub-horizontal to shallow-dipping ( $\sim 30^0$ ), or fast paths, and vertical or steeply-dipping (slow) paths are not

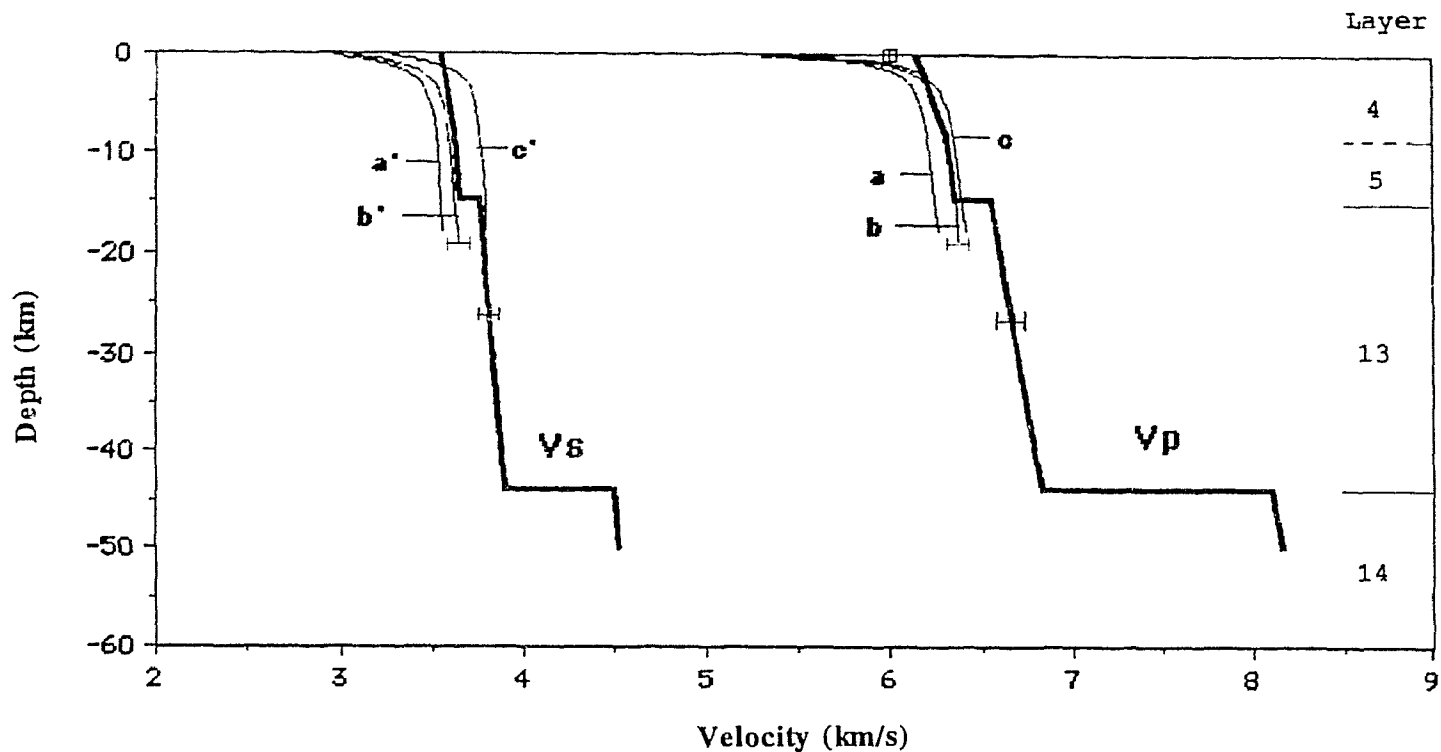


Fig. 4.9 Comparison of laboratory and refraction velocity data for the Britt domain (see Figure 4.4a for location). Heavy lines are compressional ( $V_p$ ) and shear ( $V_s$ ) wave refraction velocities given in Table 4.2 for the northern Britt domain. Layer 13 corresponds to Superior Province lower crust. Laboratory-derived average velocity-depth curves include: a - laboratory dry  $V_p$  in slow direction; b - average laboratory dry  $V_p$ ; c - laboratory dry  $V_p$  in fast direction; a' - average laboratory dry  $V_s$  in slow direction; b' - average laboratory dry  $V_s$ ; c' - average laboratory dry  $V_s$  in fast direction. The square at the top shows wet  $V_p$  in fast direction of sample B44-B at zero pressure (see text). Laboratory velocities at room temperature.

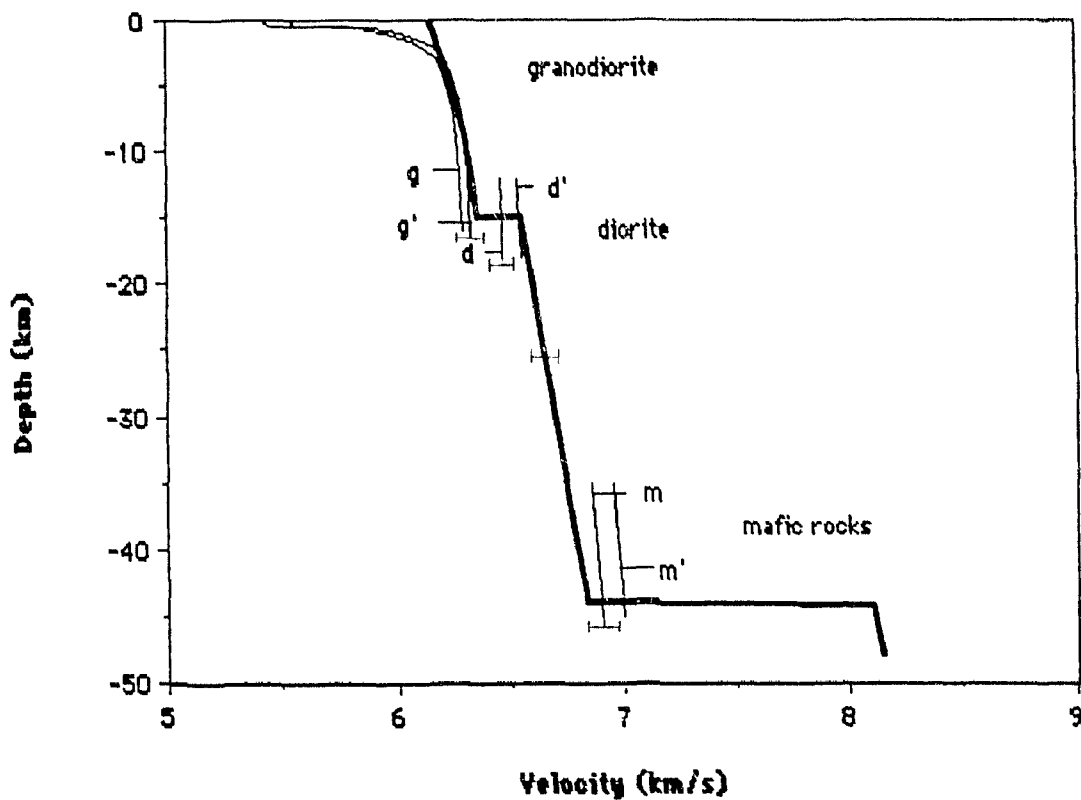


Fig. 4.10 Temperature-corrected laboratory  $V_p$ -depth curves superimposed on refraction  $V_p$ -depth curve with possible lithologies at various depths. Heavy line is refraction  $V_p$  curve and thin lines labelled with letters are laboratory  $V_p$  curves, in which  $g$ ,  $d$  and  $m$  are average velocities of granodiorite, diorite and mafic rocks, respectively and  $g'$ ,  $d'$  and  $m'$  are the average velocities in the fast direction for the same lithologies. The curves for mafic rocks are extrapolations of laboratory data to 1.2 GPa.



applicable in this comparison (note vertical exaggeration in ray diagrams in Figure 4.2).

The following sections discuss the fit of the data in the three depth zones mentioned above plus anisotropy in the GFTZ. Only compressional wave velocities are discussed in detail in these sections due to insufficient laboratory shear wave velocity data. However, the shear wave velocity-depth curves shown in Figure 4.9 have similar features to the compressional wave curves and can be understood in the same terms.

#### 3-15 km Depth Zone

The data obtained at this depth range are considered the most reliable from both the laboratory and refraction points of view, because most surface effects on velocities are minimal at these depths and the intrinsic properties of the rocks are reflected in velocity-pressure-temperature curves which are nearly linear. As shown in Figure 4.10, the laboratory data in this zone are in excellent agreement with refraction. The discrepancy between refraction and laboratory  $V_p$  in the fast direction ( $< 0.02$  km/s) lies within the errors of both techniques. This excellent fit suggests that the average lithology in this depth zone is similar to that at the surface of the Britt domain (granodiorite gneiss). Laboratory and refraction values of  $V_s$  and  $\sigma$  are also consistent with this conclusion and rule out the presence of significant amounts of paragneiss or mafic rocks (their  $\sigma$

values are too high). However, a small discrepancy in P-wave velocities toward the base of this zone suggests a slight increase in mafic lithologies with depth since the velocity exceeds the limits set simply by pressure and temperature.

#### 15 km - Moho

The refraction  $V_p$  shows an abrupt increase at 15 km depth from 6.38 km/s to 6.55 km/s, and then increases linearly to 6.84 km/s at the bottom of the crust. Thus the average laboratory  $V_p$  for the Britt domain no longer fits with the refraction  $V_p$  for this depth zone. However, it should be noted that rocks in this depth zone are not Britt domain rocks, but belong to the lower crust of the Superior Province. The  $V_p$  change most probably reflects a change in lithology. To estimate the lithology at these depths, the average laboratory  $V_p$  for diorite gneiss at 600 MPa and for mafic rocks extrapolated to 1.2 GPa are shown in Figure 4.10. It is found that the average laboratory  $V_p$  of diorite is low but the velocity in the fast direction fits the refraction  $V_p$  very well at the top of this zone. The discrepancy increases linearly with depth to the Moho where the refraction  $V_p$  (6.84 km/s) approaches the average laboratory  $V_p$  of mafic rocks (6.9 km/s after geothermal corrections). Therefore we conclude that the average lithologies in this depth range may correspond to diorite or rocks which are slightly more mafic at the top and end with rocks which are intermediate between diorite and mafic rocks just above the Moho, where the

lithology changes rapidly to ultramafic rocks with a refraction velocity of 8.10 km/s. The increase in  $\sigma$  to about 0.26 in the lower crust is also consistent with a more mafic composition.

#### 0-3 km Zone

As shown in Figure 4.10, laboratory and refraction velocities do not fit well in the top 3 km of the section below the weathered layer. The refraction velocities are generally higher than the laboratory velocities, with the discrepancy for  $V_p$  in the fast direction being as large as 0.5 km/s. There are many possible causes for the misfit including: (1) differences in water saturation, (2) large scale lithologic layering, (3) poor sample coupling or core damage due to weathering, temperature or pressure cycling, leading to anomalously low laboratory velocities at low pressures and (4) errors in refraction data interpretation.

It is well known from laboratory experiments that wet rock samples have much higher velocities than dry samples at low pressures and many rocks in the survey area are believed to be saturated by ground water since the water table is shallow. To see the difference between wet and dry velocities for Britt domain rocks, the velocities of several water-saturated granitic and granodiorite gneiss samples were measured at zero pressure. The results presented in Figures 4.9 and 4.11 for sample B-44, for example, show that saturation causes  $V_p$  to increase from 5.0 to 5.9 km/s at 10

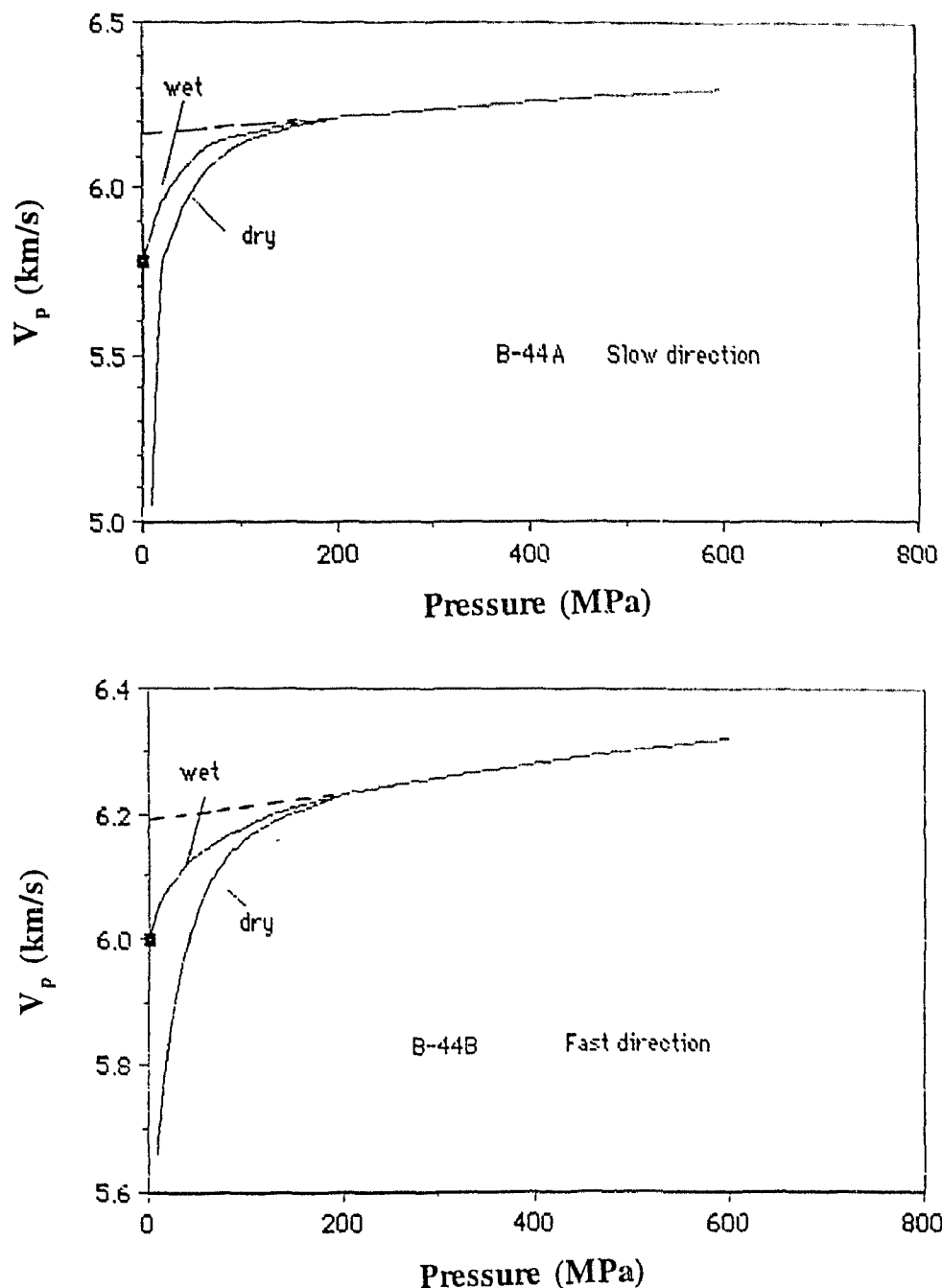


Fig. 4.11. Velocity-pressure plot for sample B44-A (slow direction) and B44-B (fast direction) showing that wet samples have much higher velocities at low pressures and a smaller initial velocity increase than dry samples. The wet velocity values at zero pressure were extrapolated to high pressures based on the fact that wet and dry velocities converge at high pressures (about 200 MPa). Projections of high pressure data to low pressures shown by dashed straight lines.

MPa in the slow direction (perpendicular to foliation) and from 5.7 to 6.05 km/s in the fast direction (parallel to foliation), respectively. As described in Chapter 2, regional foliation in the Britt domain is almost horizontal in the direction of the refraction line. Near-surface refraction velocities, therefore, should be more closely approximated by laboratory velocities measured in the fast direction through water-saturated samples.

A second possibility which should at least be considered is that the discrepancy is caused by large-scale layering. The seismic velocity of a stratified medium with homogeneous, isotropic layers of different velocities, in which the layer thickness is much less than the wavelength, was theoretically evaluated by Postma (1955) and later by Melia and Carlson (1983) in the laboratory. Although these studies were designed to evaluate velocity anisotropy caused by compositional layering, they also showed that the average velocity in such a medium could not be calculated by the time-average method. Instead, they showed that for long wavelengths, the actual velocity is slightly lower than the time-average velocity for the direction perpendicular to the layers and notably higher than the time-average velocity in the direction parallel to layering. Although the Britt domain is not a perfect stratified medium, semi-laminated bodies of various lithologies with thicknesses much less than the wavelength are evident from surface geology. If long-wave theory were used to calculate the average velocity of the

Britt domain, however,  $V_p$  would only be about 0.04 km/s higher than the time-average velocity in the fast direction because the fast mafic layers are not volumetrically significant. Since this represents a maximum increase (the Britt domain is only semi-laminated), layering cannot contribute significantly to the discrepancy.

A third possibility is that the laboratory velocities at low pressures are low due to poor transducer/sample coupling or to microscopic core damage caused by weathering, seasonal temperature cycling (freezing and thawing) or pressure release during erosion (pressure cycling). For these reasons, projections of high pressure data to low pressures are often considered more reliable estimates of velocity than actual measurements at low pressure. As can be seen in Figures 4.9, 4.10 and 4.11, such projections would match refraction velocities closely.

In summary, the difference (0.6 km/s) between laboratory and refraction velocities is probably not significant. The small discrepancy remaining after taking these effects into account can be easily accommodated within the errors of the refraction data, particularly when it is recalled that the velocities and gradients at the top of the section are poorly constrained by the shot spacing along line AB and that the only shallow in-situ gradient information available in the region is for a small area along the GFTZ to the northwest (Burke, 1991).

### Velocity Anisotropy of the Grenville Front Tectonic Zone

It was found that several shallow (< 8 km) layers or blocks coincident with, or close to the GFTZ required different velocities to fit the travel time curves for different groups of shots. As shown in Table 4.2 and demonstrated in a previous section (Error Analysis of Travel Time Fit), these blocks have lower velocities for shots located in the southern portion of the line than for the shots in the north. This geometry-dependent velocity behaviour indicates that these blocks are anisotropic with the fast velocity direction dipping to the south at a low angle and the slow velocity direction being sub-perpendicular to the fast direction.

The laboratory anisotropy data, which show that anisotropy at low pressures is much higher than at elevated pressures, can be used to explain why the anisotropic blocks are restricted to shallow levels of the crust. However it is difficult to make a quantitative comparison between the laboratory and in-situ anisotropy values for two reasons. One is that because of the ray geometry, the velocities given for the individual blocks may not be their fastest and slowest velocities. Another reason is that the in situ anisotropy might include the effects of large scale features such as oriented fractures and lithologic layering or lamination (e.g. Postma, 1955; Melia and Carlson, 1984).

It should be noted that deeper layers or blocks in the model which do not show anisotropy are not necessarily isotropic.



## Chapter 5

### SYNTHETIC REFLECTION MODELLING

Synthetic modelling is widely used in seismic interpretation because it allows us to compare the seismic response of various velocity structures and to select the geologic model or family of models which provides the best fit to recorded data. Although the models obtained by this means are usually non-unique for a specified seismic section, they can often be constrained by other geologic information and used, in turn, to constrain interpretation of deep seismic profiles. In the following section, synthetic modelling will be used to investigate the kinds of structures responsible for the vertical incidence and wide angle reflection patterns observed in the Britt domain. In general, the modelling for the Britt domain was limited to a depth of about 10 km, the maximum depth to which surface geology could be projected using regional dips.

Based on the laboratory velocity and density measurements presented in chapter 3, the reflection coefficients of possible lithologic contacts in the Britt domain are calculated and listed in Table 5.1. Although it is clear from this data that strong reflections potentially exist among the lithologies observed in the region (the mafic lithologies will have strong reflection coefficients against the felsic rocks, for example) and GLIMPCE profile J is far from transparent under the Britt domain despite the

Table 5.1 Possible reflection coefficients for Britt domain rocks at 60 (first value), 200 (second value) and 600 MPa (third value).

	Granitic gneiss	Granodiorite gneiss	Paragneiss	Diorite gneiss	Marble	Anorthosite	Mafic rock
Mafic rock	0.12 0.11 0.11	0.10 0.09 0.09	0.09 0.08 0.08	0.07 0.06 0.06	0.05 0.05 0.05	0.02 0.02 0.02	0.00 0.00 0.00
Anortho- site	0.09 0.09 0.08	0.07 0.07 0.07	0.06 0.06 0.05	0.05 0.04 0.04	0.03 0.02 0.02	0.00 0.00 0.00	
Marble	0.07 0.06 0.06	0.04 0.05 0.05	0.03 0.03 0.03	0.02 0.02 0.01	0.00 0.00 0.00		
Diorite gneiss	0.05 0.05 0.05	0.03 0.03 0.03	0.02 0.02 0.02	0.00 0.00 0.00			
Para- gneiss	0.03 0.03 0.03	0.01 0.01 0.01	0.00 0.00 0.00				
Grano- diorite gneiss	0.02 0.02 0.02	0.00 0.00 0.00					
Granitic gneiss	0.00 0.00 0.00						

predominance of felsic rocks, the absence of continuous reflections raises several questions regarding the nature of the reflections:

(1) Aside from gabbro and anorthosite bodies, most of the mafic rocks reside in subparallel dike swarms. Can these produce significant reflections?

(2) What is the reflection response of such structures to first and second order folding?

(3) Can folded reflectors produce the "shingles" observed in the GLIMPCE line J wide-angle reflection data (Mereu et al., 1990)?

To address these problems, forward modelling techniques were employed using laboratory-derived velocities and densities and surface geology as constraints.

#### Reflectivity of Thin Mafic layers

##### Thin Bed Resolution

The resolution of a single thin layer using seismic reflection techniques is limited by the interference of reflections from the top and bottom of the layer. The results of Ricker (1953) and Widess (1973) suggest that only features on the order of  $1/8$  to  $1/4$  or more of the wavelength of the incident seismic wavelet (typically 15-75m) can be resolved by seismic techniques. An equation relating the bed thickness and reflection amplitude was given by Widess (1973):

$$A' = 2A \sin(2\pi b/\lambda) \quad (9)$$

where  $A'$  is the maximum amplitude of the composite reflected wavelet,  $A$  is the maximum amplitude when the bed is very thick,  $b$  is the bed thickness and  $\lambda$  is the wavelength.

The studies of Christensen and Szymanski (1988), Christensen (1989), Juhlin (1990) and Burke (1991), however, show that the amplitude can be enhanced if a number of thin beds are closely spaced. For the simple case of regularly spaced thin beds,

$$A' = \frac{2A \sin(2\pi b_1/\lambda) \sin[2\pi N(b_1+b_2)/\lambda]}{\sin[2\pi(b_1+b_2)/\lambda]} \quad (10)$$

where  $A'$  is the amplitude of the wavelet reflected from a thin bed cluster,  $A$  is the reflection amplitude from a single thick bed with the same properties as the high velocity layers in the cluster,  $N$  is the number of thin layers,  $b_1$  and  $b_2$  are the thicknesses of the high and low velocity layers respectively, and  $\lambda$  is the wavelength of the incident seismic wavelet (see Appendix II).

#### Model Construction and Modelling Technique

As described in chapter one, irregular clusters of thin (0.1 to several meter thick) mafic dikes commonly occur within the granitic gneisses of the Britt domain, although their abundance varies from place to place depending on the gneiss association. The distribution of these mafic layers was mapped along the Key River (see Figure 3.1 for location)

and the result is shown in Figure 5.1. For ease of presentation, they are shown as clusters rather than individual layers in Figure 5.1, but the detailed sequence is given in Appendix III with the cluster interval noted. To see whether or not the thin mafic layers in this sequence can make significant reflections, a one-dimensional velocity-density-depth model based on this data set was tested. Only one limb of the syncline was used for modelling. The physical properties used for each lithology are the average compressional wave velocities and densities presented in Table 3.5. Only velocities measured at 600 MPa were used because impedance contrasts are relatively insensitive to pressure.

A FORTRAN program (Newseis3) developed by L. Mayer at Dalhousie University was used for this work. The program reads a series of velocity-density-depth measurements and calculates impedances and two-way travel times assuming normal incidence raypath. The program then reads a source function composed of time and amplitude. In order to properly calculate reflection coefficients for convolution, the impedance curve and source function were resampled at equal intervals. Once this was completed, a reflection coefficient series was generated. The reflection coefficients and the source function were then convolved and a synthetic seismogram was generated and plotted. This program was modified by J. Osler at Dalhousie to run interactively on a

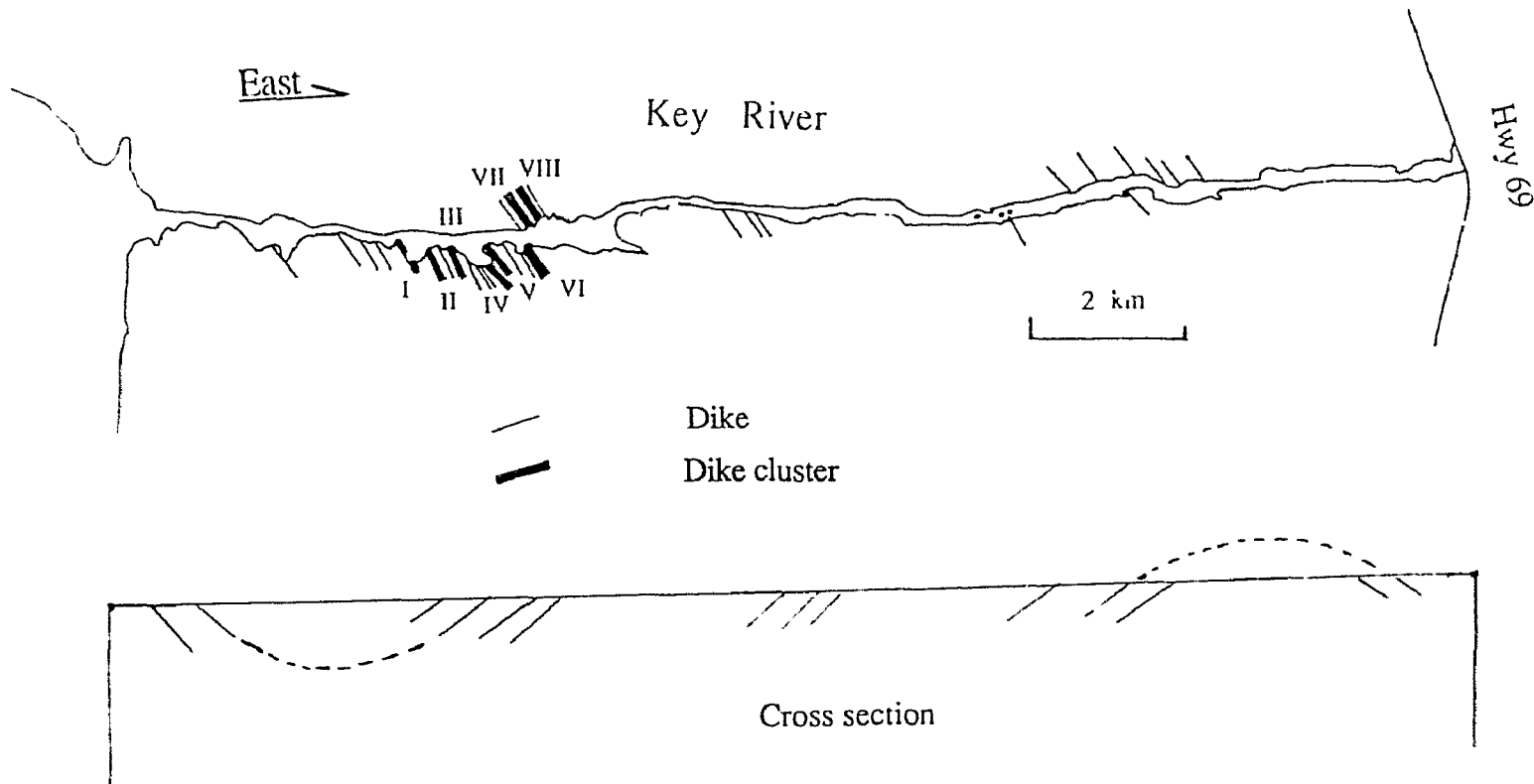


Figure 5.1 Distribution of mafic dikes and amphibolite layers as mapped along Key River in the northern Britt domain. Thin layers are grouped into clusters for ease of presentation; individual layer thicknesses are given in Appendix III.

VAX computer, driving a Tektronics emulator on a PC with output to a screen using NCAR equivalent graphics.

A Ricker wavelet with a central frequency of 30 Hz was used to simulate the source wavelet used for GLIMPCE profile J. The resulting synthetic trace was repeated ten times to simulate a one-dimensional seismic section and displayed at true amplitudes, i.e. no automatic gain control was applied. In order to assess the relative strength of the complicated events generated by thin layers, a 300 meter thick calibration dike was inserted near the top of the model. For the wavelet frequency used, this dike is thick enough to avoid interference between reflections from its top and bottom.

This modelling technique does not incorporate the effects of various phenomena such as geometrical spreading or multiple reflections. These limitations are acceptable because a range-dependent gain is usually applied to 2D reflection data to correct for spreading and multiple reflections are not usually significant due to their small amplitudes (less than 1/10 of the first reflections).

### Modelling Results

Figure 5.2 shows the result of the convolution of the spike reflection coefficient series derived from the observed dike distribution with a Ricker wavelet having a center frequency of 30 Hz. The column on the left shows the

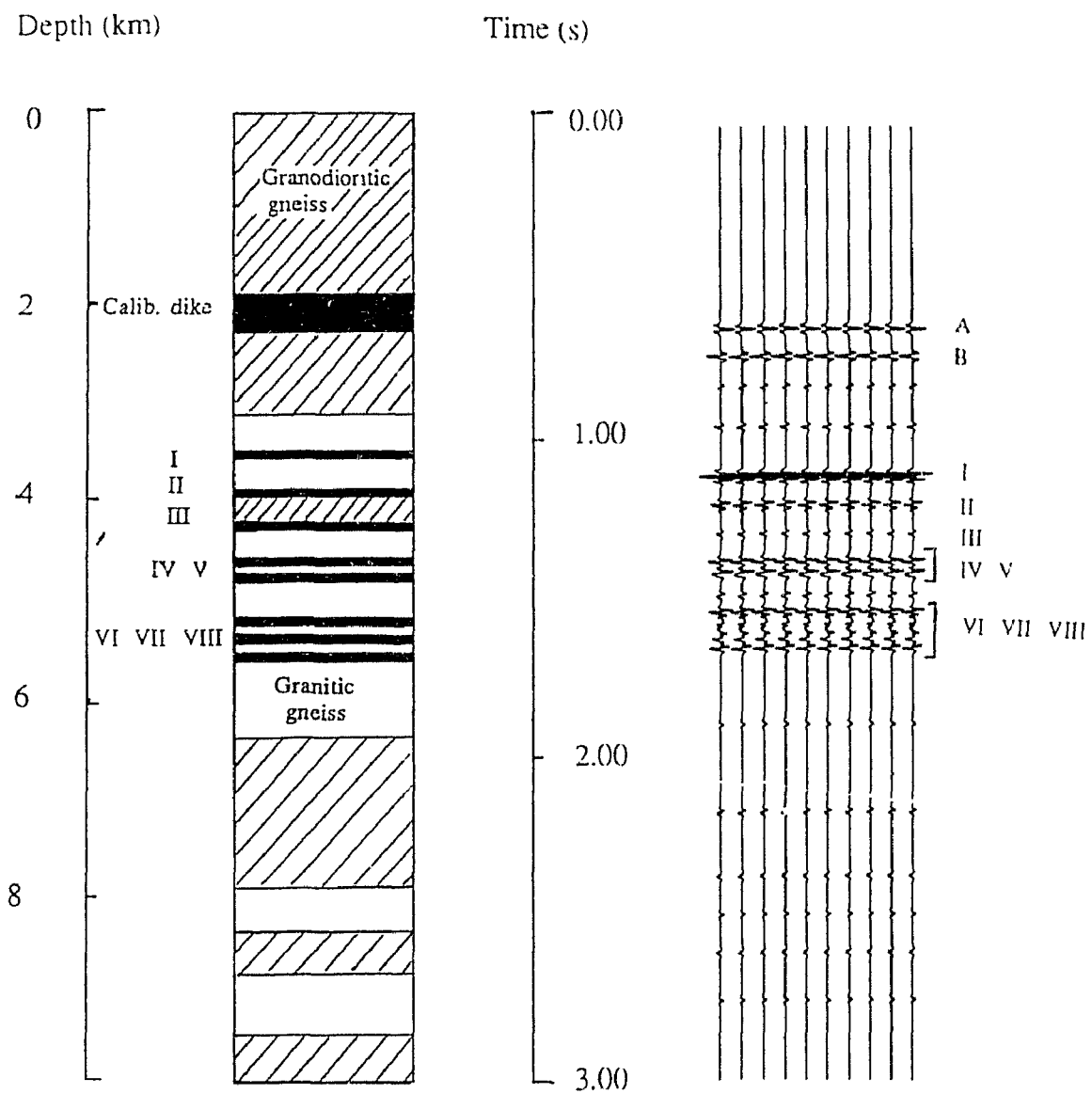


Figure 5.2 One-dimensional seismic section for the detailed mafic layer distribution given in Appendix III. The column on left shows the relative position of mafic layer clusters.



relative positions of the mafic layer clusters for comparison.

The high amplitude reflections labelled A and B near the top of the section resulted from the 300 m thick "calibration dike" inserted in the model. The reflection coefficient at this boundary is 0.09, and there is no interference between the top and bottom of the layer at the frequency and wavelength of the wavelet used.

The amplitudes of the events generated by the thin layer clusters are strongly dependent on the thickness of the individual dikes and their spacing. The event corresponding to cluster I has an extremely large amplitude because there is a 20 m thick dike in the cluster, while cluster III has a small amplitude because the dikes in this cluster are thin (0.1 m) and their spacing intervals are large (average about 0.5 m) with respect to individual dike thicknesses. This result is in agreement with the analysis given in Appendix II. The reflection amplitudes of the other clusters are 1/2 to 3/4 of the amplitude generated by the calibration dike. Since the reflection coefficient of the calibration dike is 0.09, a value that is considered high for deep crustal reflection profiles (Warner, 1990; Burke and Fountain, 1990), it is clear that the clusters can give rise to significant reflections even though the thicknesses of the individual dikes in each cluster are typically much less than that required for the detection of individual dikes.

## Reflection Patterns Due to Lithologic Variation

As described in chapter one, although the lithology of the Britt domain is dominated by granitic gneiss, scattered mafic pods and intermediate bodies a kilometre or more across are quite common in the area. Based on the laboratory-derived reflection coefficients (Table 5.1), these are probably responsible for many of the discontinuous subhorizontal reflections seen on GLIMPCE profile J throughout the Britt domain (Fig. 5.3). The surface geology also shows, however, that some high impedance lithologies, such as the dike clusters, have a large lateral extent and have been incorporated in a series of NW trending folds. Despite their large reflection coefficients against the gneisses, they are not observed on profile J. The following discussion addresses whether or not the lithologic relationships seen in the Britt domain can generate a similar reflection pattern to that observed in profile J, with special reference to the seismic response of folded structures.

### Modelling Technique

The 2-D AIMS software residing on a workstation at Memorial University was used in this work. This program was designed by Geoquest, Inc. for forward seismic modelling and seismic data interpretation. A two-dimensional velocity-density-depth model was first constructed interactively. Then the source-receiver and raypath geometry were specified and

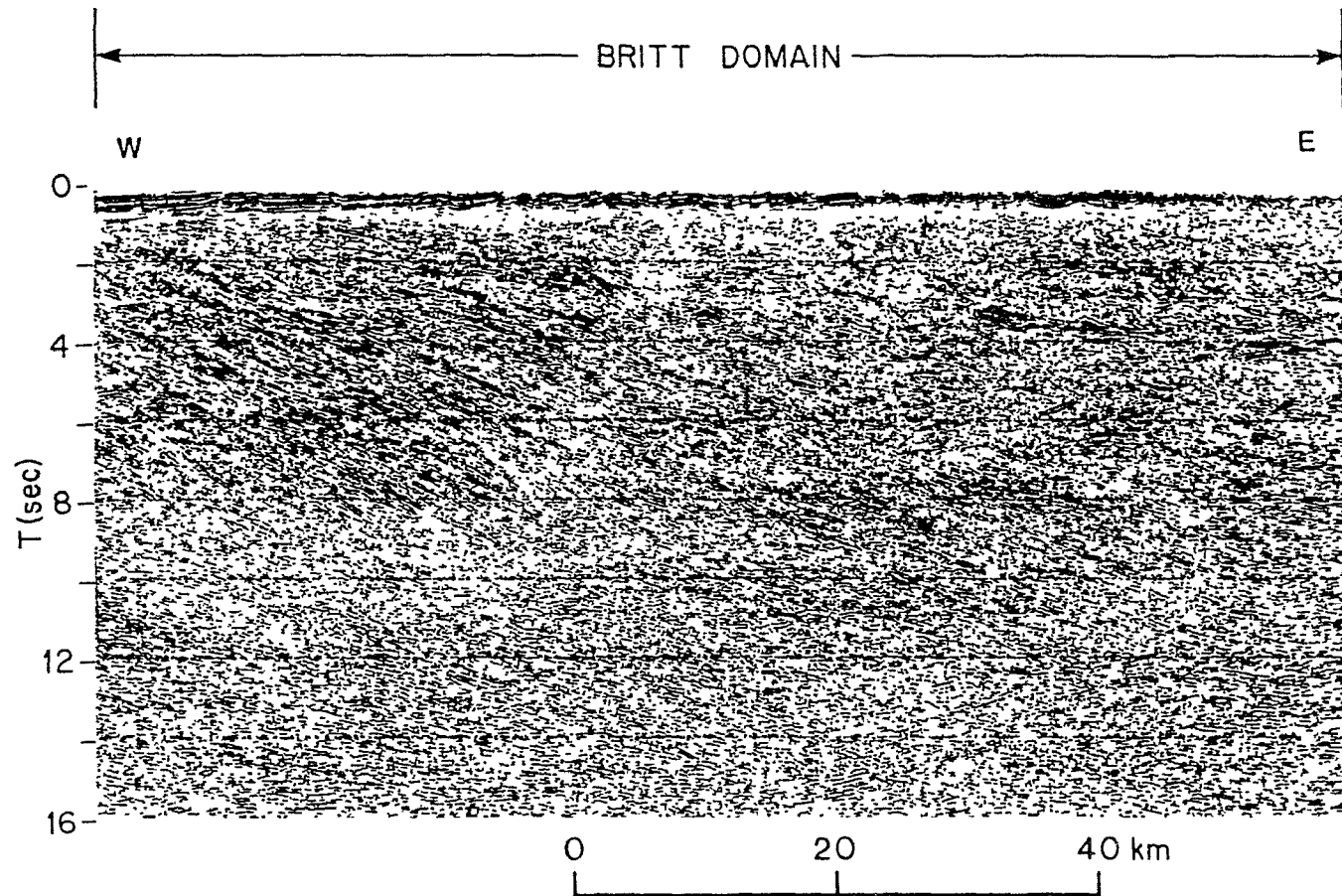


Fig. 5.3 Blue-up of GLIMPCE line J showing discontinuous, subhorizontal reflections under eastern Britt domain.

"working rays" traced through the model. For this study, a zero-offset ray pattern with diffractions was chosen to simulate the near vertical reflection data from GLIMPCE line J. Impedance contrasts and transmission and reflection coefficients for each interface and travel times for each "working ray" were also calculated at this stage.

A series of propagation effects may be considered during vector amplitude calculation depending on the user's specifications. These effects include transmission and reflection effects and geometrical spreading. Results, including travel times and complex vector amplitudes for individual rays generated in the ray generation mode are then convolved with a specified wavelet. As before, a Ricker wavelet having a central frequency of 30 Hz was used in this work. The resulting synthetic section could be displayed in various formats and the SEG-Y or PSC files of the synthetic section could also be generated. The synthetic data generated by AIMS were FK-migrated using the VISTA6.6 software package.

### Folded Structures

As discussed in chapter 2, the principal structural features throughout the Britt domain are folds of various scales. Therefore the first model tested was a simple folded structure was (Fig.5.4). Not surprisingly, this input geometry was easily recovered on the FK migrated synthetic section (Fig. 5.5b). To determine why this kind of structure is not observed on the vertical reflection section, synthetic

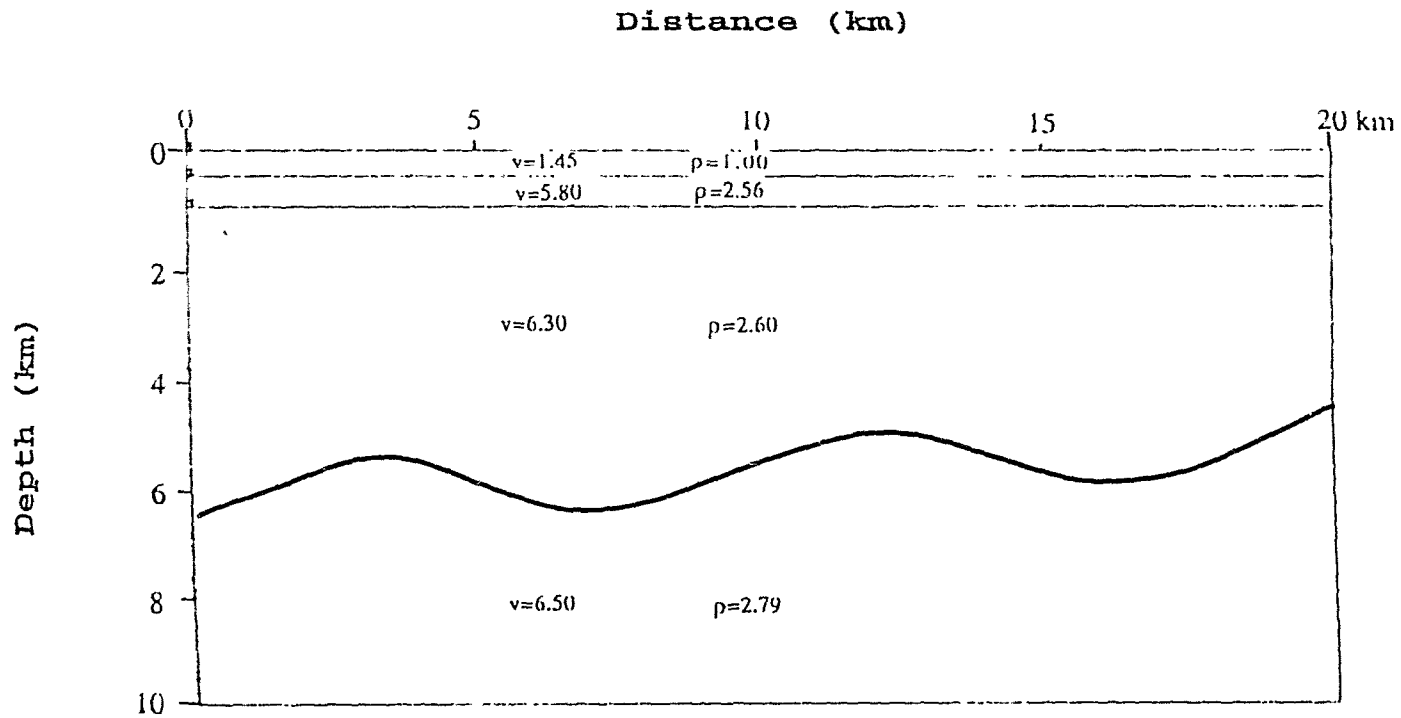


Fig. 5.4 Synthetic model to test the reflection response of a simple fold boundary. Compressional wave velocities ( $V_p$ ) in km/s, densities in  $g/cm^3$ .

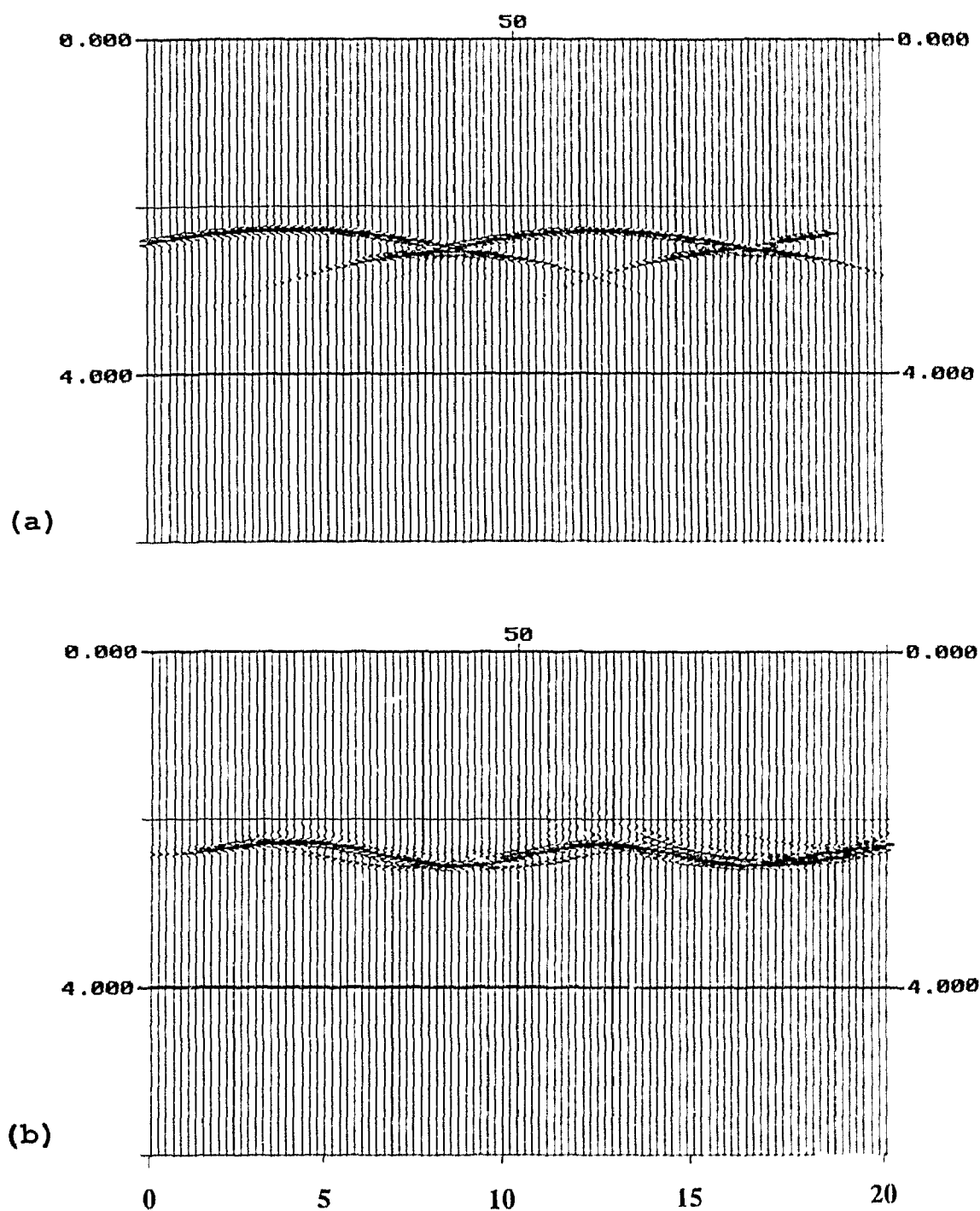


Fig. 5.5 a) Unmigrated and b) F-K migrated synthetic reflection sections for the model shown in Figure 5.4. Vertical scale is two-way travel time in seconds and horizontal scale at top is trace number in 200 meter intervals.

reflection profiles were then generated for a gently folded boundary with superimposed second order folds (rugosity). Figure 5.6 shows the model tested, in which a series of secondary folds are randomly superimposed on a first order folded boundary. The scales of the first and second order folds are based on field observations in the northern Britt domain. Unmigrated and migrated synthetic sections for this model are shown in Figures 5.7 and 5.8, respectively. A series of discontinuous reflections appears on the migrated section (Fig. 5.8) and the input geometry could not be recovered from the profile. It is interesting to note that these reflections bear no resemblance to folds but suggest, instead, the presence of a zone of subhorizontal reflectors. Although this is due in part to spatial aliasing caused by the wide receiver spacing used in the modelling, steeply dipping fold limbs will be difficult to image in any case because the incidence energy is not returned to the surface. In order to exclude spatial aliasing effects, the closer receiver spacing was applied to an equivalent model shown in Figure 5.6. The results shown in Figure 5.9 are somewhat similar to those in Figure 5.7 and 5.8 in terms of discontinuity of reflections.

The seismic effects of discontinuous, high impedance bodies on an underlying reflector were also investigated to simulate the effects of the mafic bodies observed in the Britt domain. The problem was simplified to the "plum

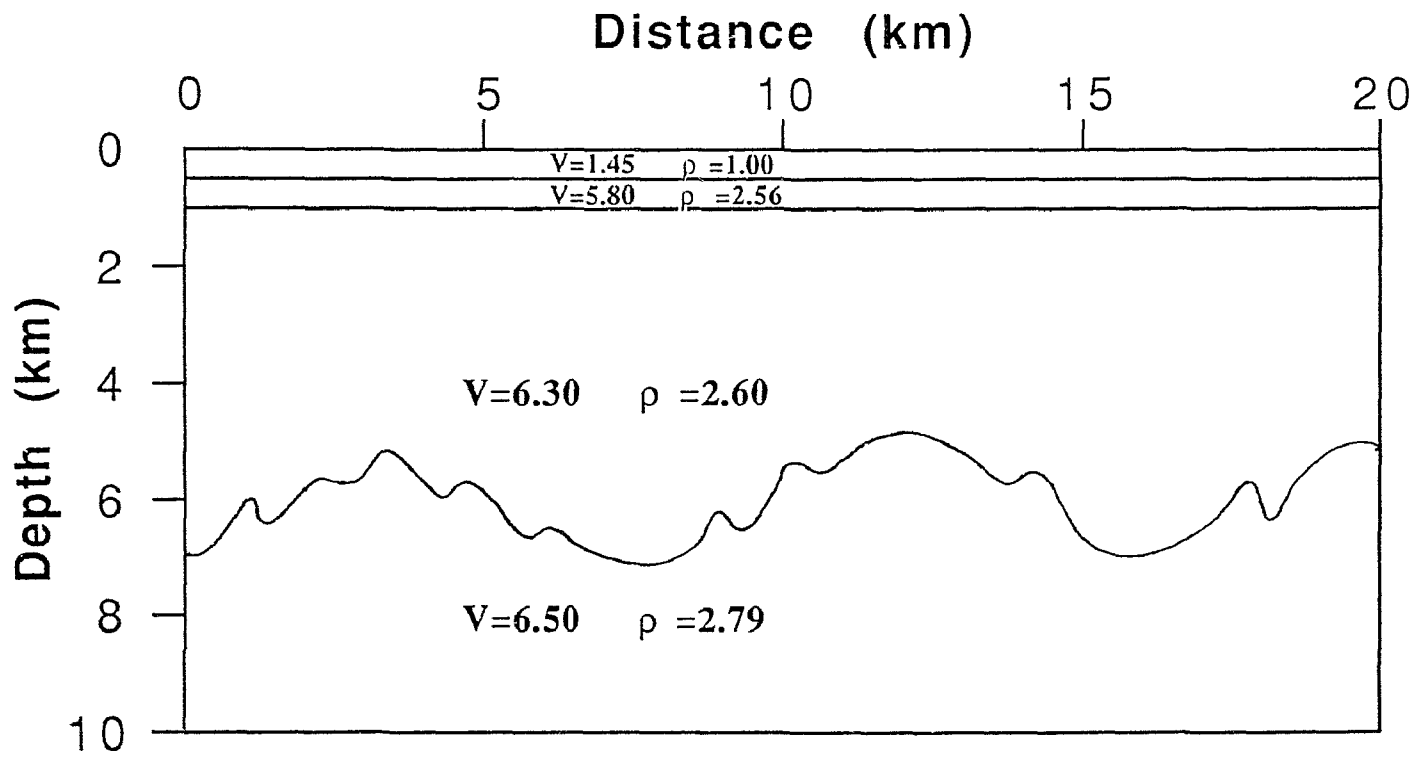


Fig. 5.6 Synthetic model to test the reflection response of second order folds superimposed on a gently folded boundary. Compressional wave velocities ( $V_p$ ) in km/s, densities in  $\text{g/cm}^3$ .



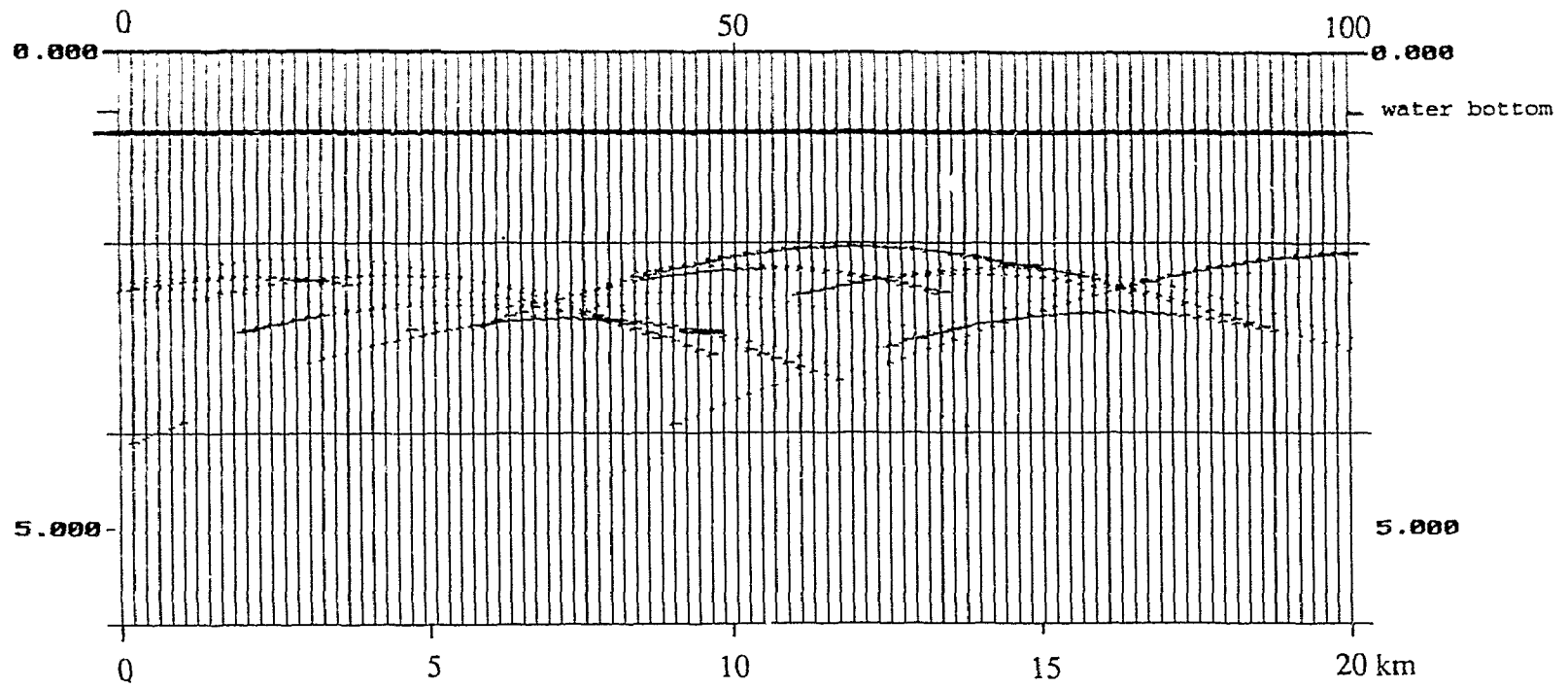


Fig. 5.7 Unmigrated synthetic reflection section for the model shown in Figure 5.6. Vertical scale is two-way travel time in seconds and horizontal scale at top is trace number in 200 meter intervals.

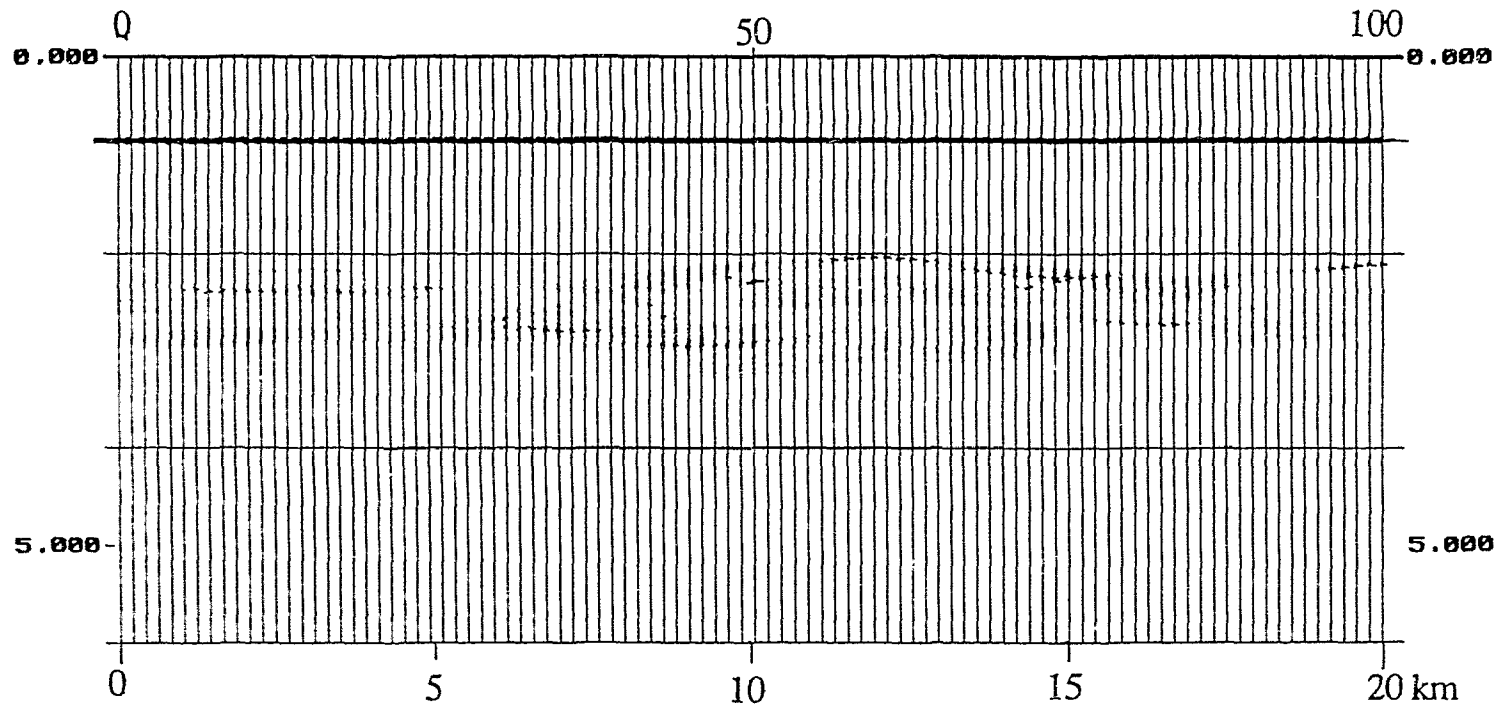


Fig. 5.8 FK-migrated synthetic reflection section for the model shown in Figure 5.6. Vertical scale is two-way travel time in seconds and horizontal scale at top is trace number in 200 meter intervals. Input boundary can not be reconstructed from discontinuous reflections shown. Reflections are more likely to be attributed to subhorizontal lamination even though the basic structure consists of folds.

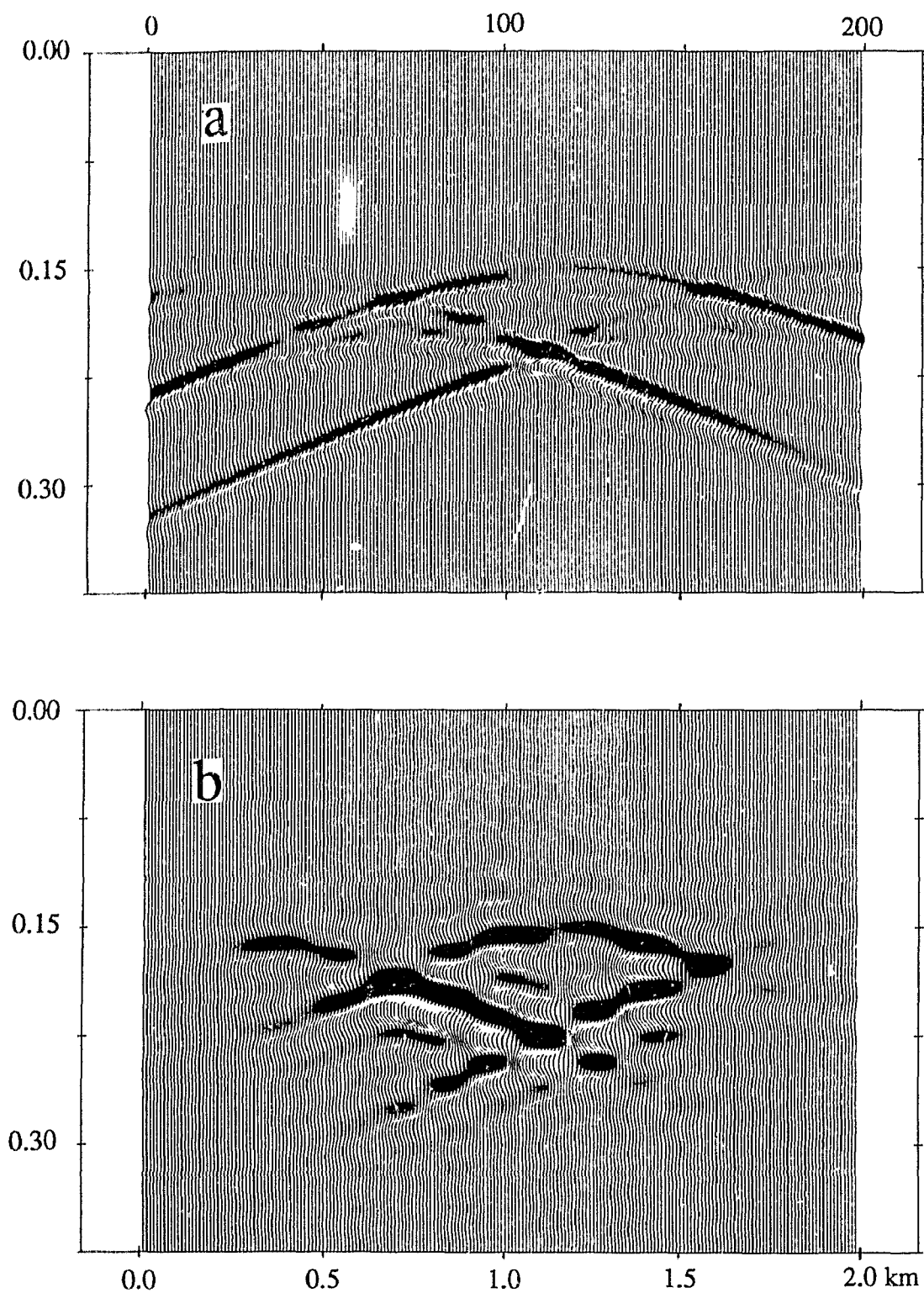


Fig. 5.9 a) Unmigrated and b) migrated synthetic sections for an equivalent model shown in Figure 5.6 with the closer trace spacing. Vertical scale is two-way travel time in seconds and horizontal scale at top is trace number in 10 meters intervals. Input boundary can not be reconstructed from discontinuous reflections shown.

pudding" model shown in Figure 5.10 in which mafic pods imbedded in granite overlie granodiorite. Although the continuous horizontal boundary at 6 km was imaged on the synthetic sections (Fig. 5.11), the reflection amplitudes vary laterally due to acoustic shadowing effects and the travel times are slightly disturbed by pull-up effects. With the above test as background, a series of models specific to the Britt domain was then examined.

### Hypothetical Models for the Britt Domain

#### *Model construction*

It is evident that lithologic variation in the northern Britt domain is quite different from that in the south, especially in terms of the abundance of mafic bodies or pods and to a lesser extent, the style and degree of deformation. Therefore, two hypothetical models parallel to Profile J were constructed based on the lithologic and structural variations encountered along two cross-sections through the geological map of Culshaw et al (1989) (Figure 5.12). Figure 5.13 shows the southern Britt model and Figure 5.14 is the northern Britt model. In addition to the large map-scale units and features, the models also include smaller scale units and structural features which are considered to be significant in terms of seismic reflection, such as second order folds (rugosity). These smaller scale features are

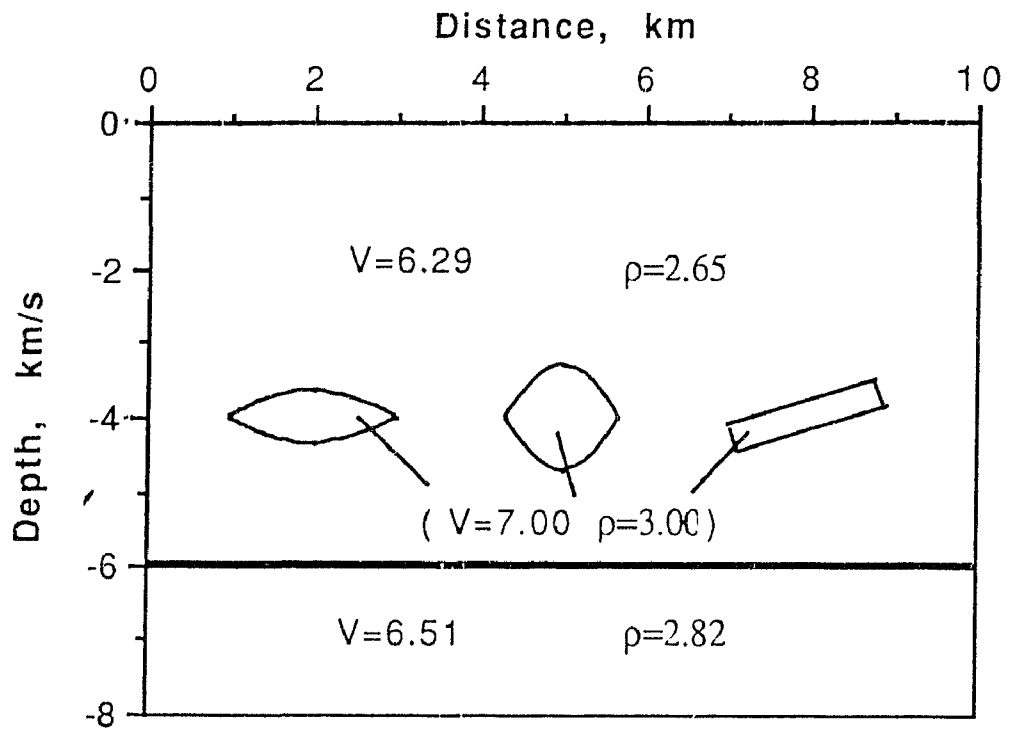
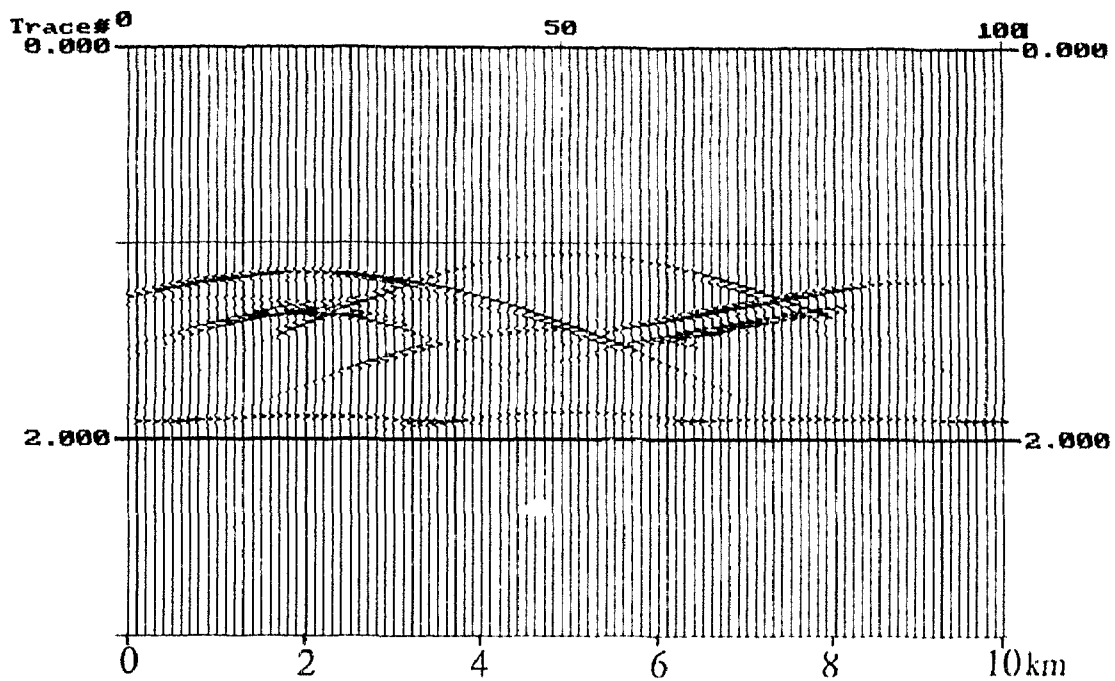
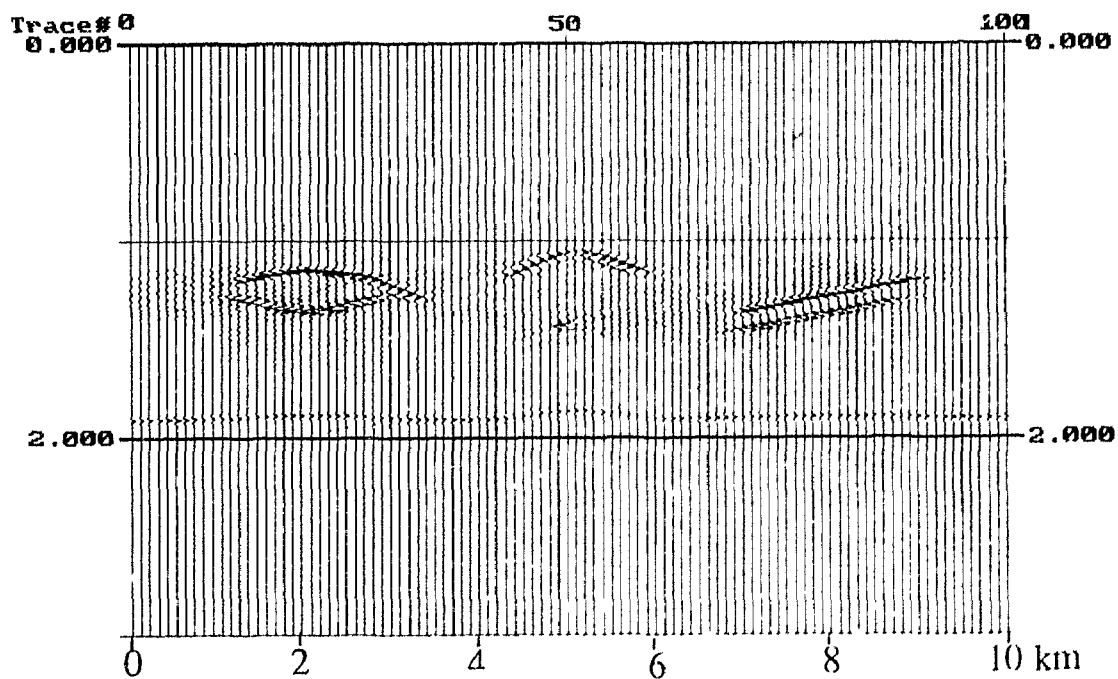


Fig. 5.10 Synthetic model used to test the reflection response of a flat boundary below pods of gabbro.



Unmigrated



FK-migrated

Fig. 5.11 Synthetic reflection sections for the model shown in Figure 5.10. Vertical scale is two-way travel time in seconds. Pods show as isolated reflections and continuous boundary has been segmented by shadowing and pull-up effects.

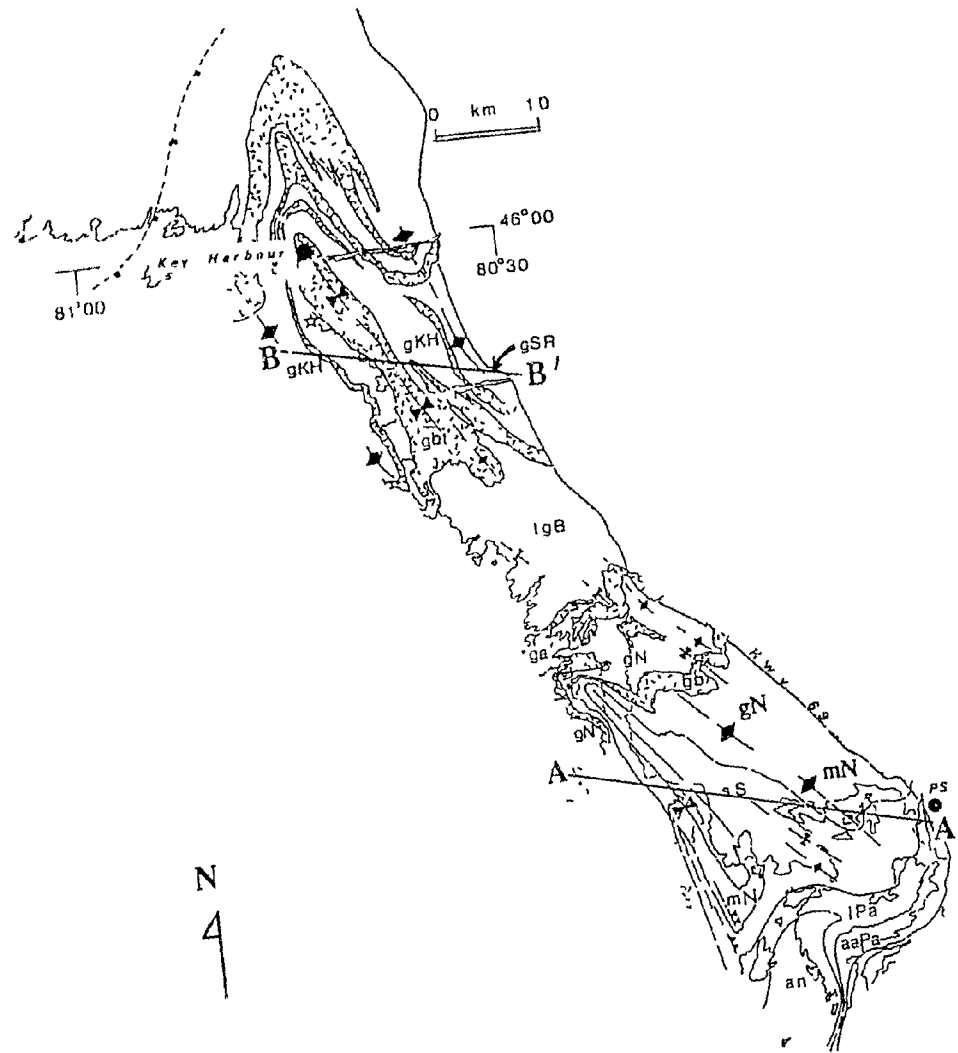


Fig. 5.12 Location of two cross sections used to construct the southern Britt model (A-A') shown in Figure 5.13 and the northern Britt model (B-B') in Figure 5.14. Symbols as in Figure 2.3.

### Southern Britt Velocity-Depth Model

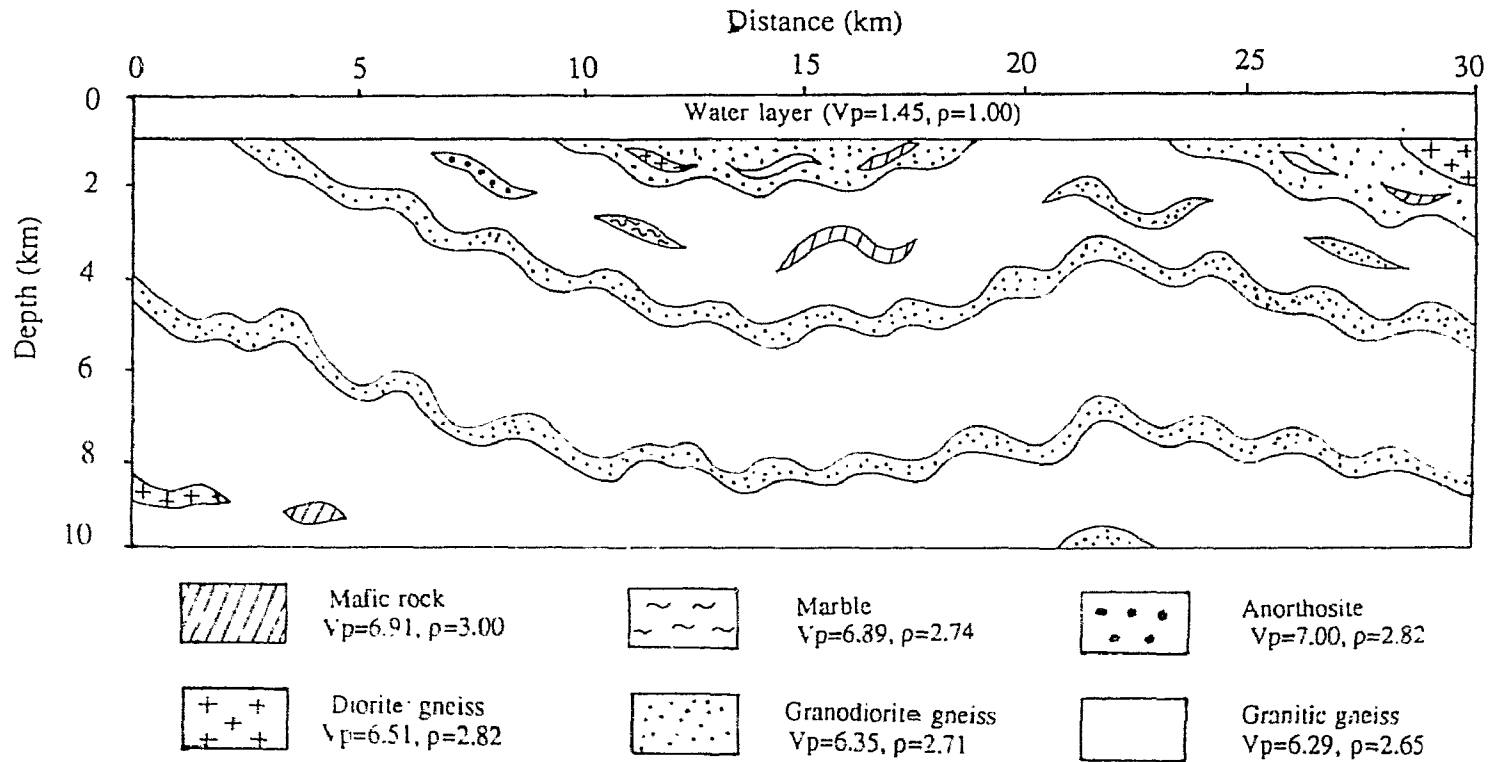


Fig. 5.13 Hypothetical two-dimensional model of lithologic and physical property variation in the southern Britt domain based on geology along profile A-A' in Figure 5.12. Compressional wave velocities in km/s; densities in  $g/cm^3$ .



### Northern Britt Velocity-Depth Model

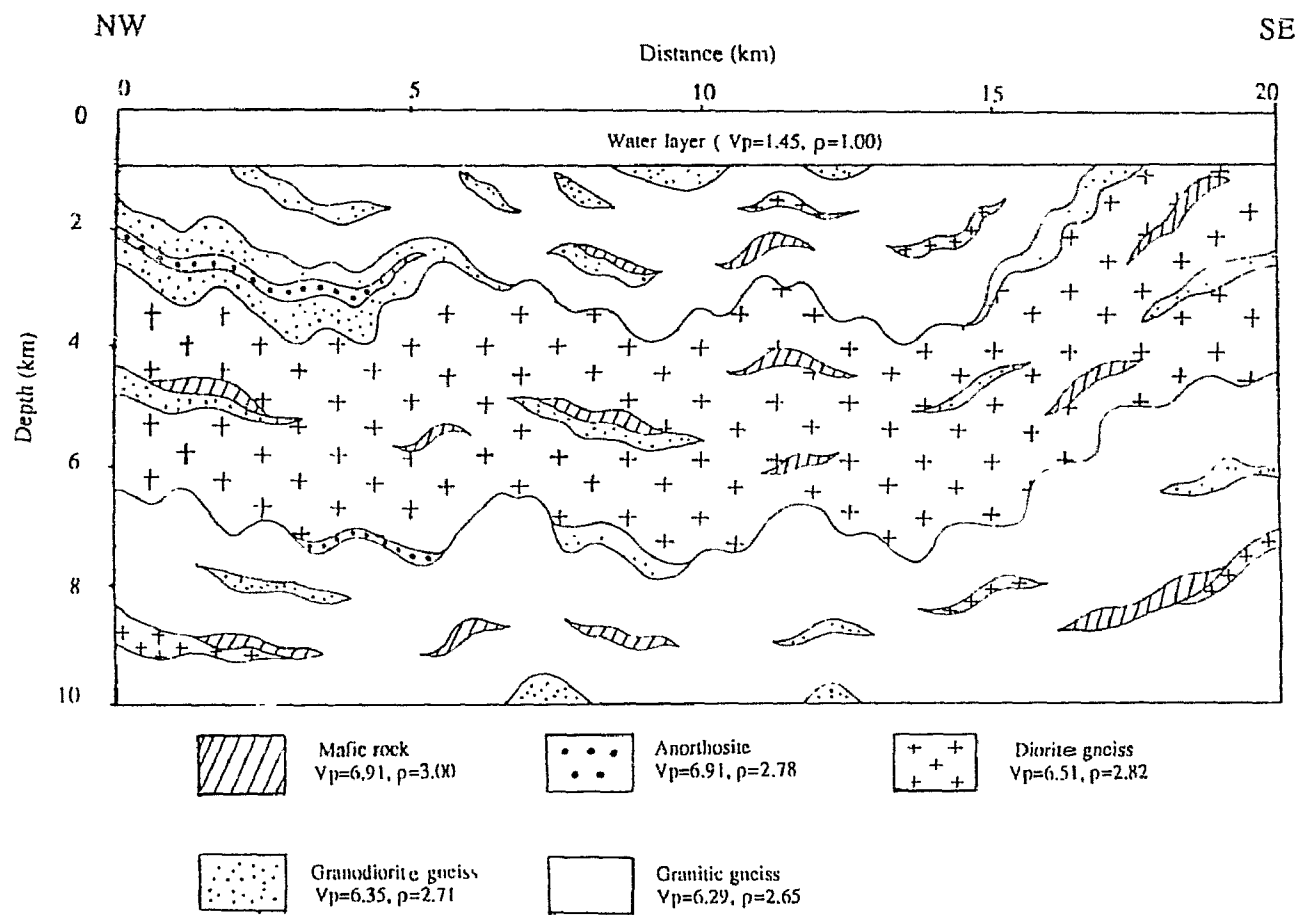


Fig. 5.14 Hypothetical two-dimensional model of lithologic and physical property variation in the northern Britt domain based on geology along profile B-B' in Figure 5.12. Compressional wave velocities in km/s; densities in  $g/cm^3$ .

loosely based on outcrop observations and the descriptions of Culshaw, et al (1988, 1989).

As can be seen in the Figures 5.13 and 5.14, the two models are quite different. The southern Britt model, which represents the less deformed, allochthonous upper deck of the Britt domain, contains six different lithologies including: (1) granitic gneiss, (2) granodiorite gneiss, (3) diorite gneiss, (4) mafic rocks, (5) marble and (6) anorthosite, the first three in first and second order folds, the last three in both pods and folds. The northern Britt model, which represents the more tightly folded, parautochthonous lower deck includes the same lithologies but lacks marble. As for the thin layer modelling, the compressional wave velocities used were the average laboratory-derived velocities at 600 MPa for the individual lithologies discussed in chapter three. Paragneiss was not included in the velocity-depth models because its P-wave velocity and density are similar to those of granodiorite gneiss and diorite gneiss. A 1 km-thick water layer was added at the top of each model to simulate the acquisition conditions of profile J.

In interpreting the results of modelling it should be remembered that the lithologies and structural features at depth in the models are only estimates due to the limited subsurface information available. The purpose of the modelling is not to produce a synthetic reflection profile which is faithful to specific events on profile J, but to

explore the types of structures which might produce the kinds of reflection patterns observed.

### *Synthetic Sections*

Figures 5.15 and 5.16 show the zero-offset, unmigrated synthetic seismic sections generated from the southern and northern Britt models, respectively. Both sections show that significant reflections are generated at the boundaries between structures composed of (1) mafic rocks and the other lithologies, (2) diorite gneiss and the other lithologies, (3) anorthosite and the other lithologies, and (in the southern Britt domain) between (4) marble and granitic gneiss. All other contacts generate only low amplitude reflections due to their low reflection coefficients. The first order folds can be discerned in the southern traverse but the second order folds can be detected in neither.

FK migration was applied to the synthetic sections generated from the input models and the results are shown in Figures 5.17 and 5.18, respectively. The synthetic section for the southern Britt model shows mostly low amplitude reflections because the dominant lithologies (such as the Nadeau Island Association) include relatively few mafic-intermediate bodies or pods. Interestingly, the first order folds can be detected clearly as strings of discontinuous reflections off the peaks and troughs of second order folds, but the second order folds themselves can not be identified

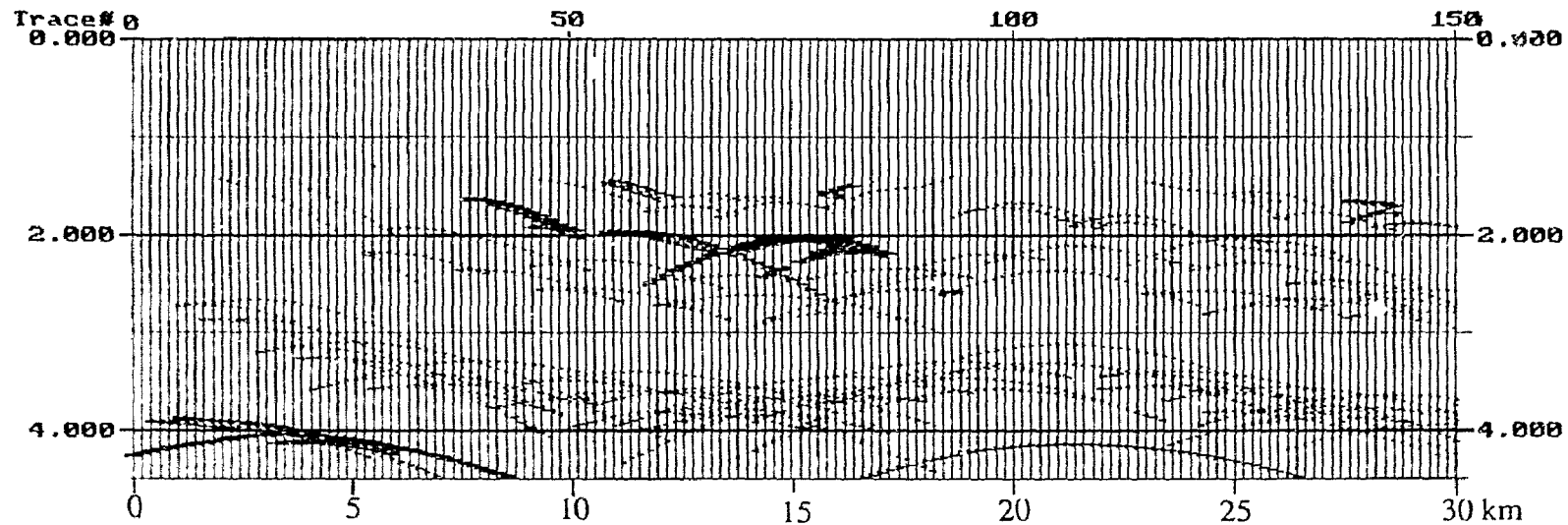


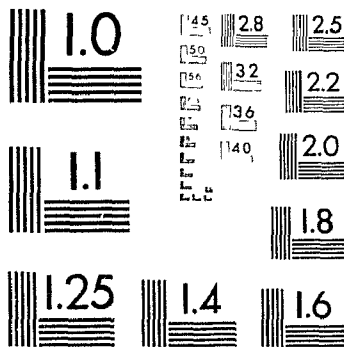
Fig. 5.15 Unmigrated synthetic reflection section for the model shown in Figure 5.13. Vertical scale is two-way travel time in seconds and horizontal scale at top is trace number in 200 meter intervals. See text for discussion. First order folds can be discerned but second order folds are represented by parabolas off peaks and troughs.

3

OF/DE

3

PM-1 3½"x4" PHOTOGRAPHIC MICROCOPY TARGET  
NBS 1010a ANSI/ISO #2 EQUIVALENT



PRECISION<sup>SM</sup> RESOLUTION TARGETS

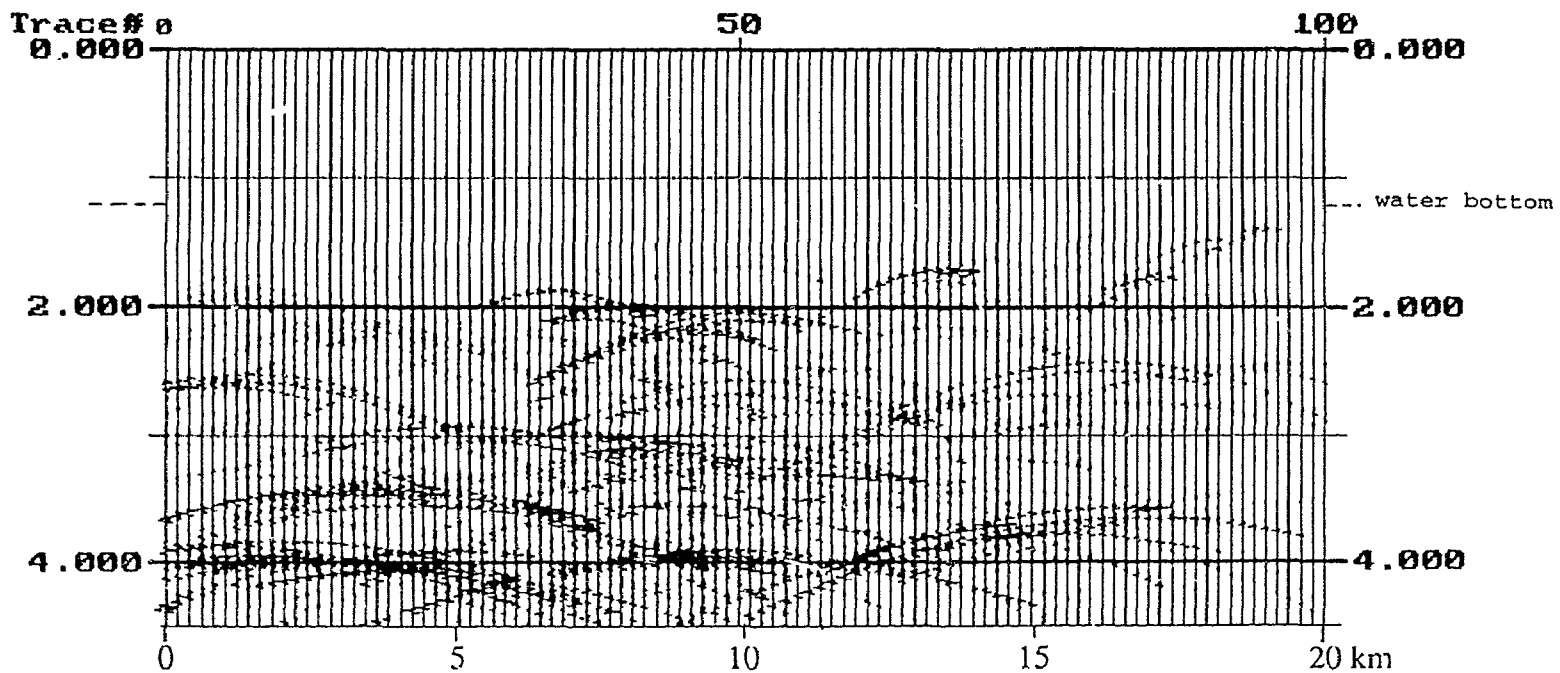


Fig. 5.16 Unmigrated synthetic reflection section for the model shown in Figure 5.14. Vertical scale is two-way travel time in seconds and horizontal scale at top is trace number in 200 meter intervals. See text for discussion. Overall structure is undiscernible.

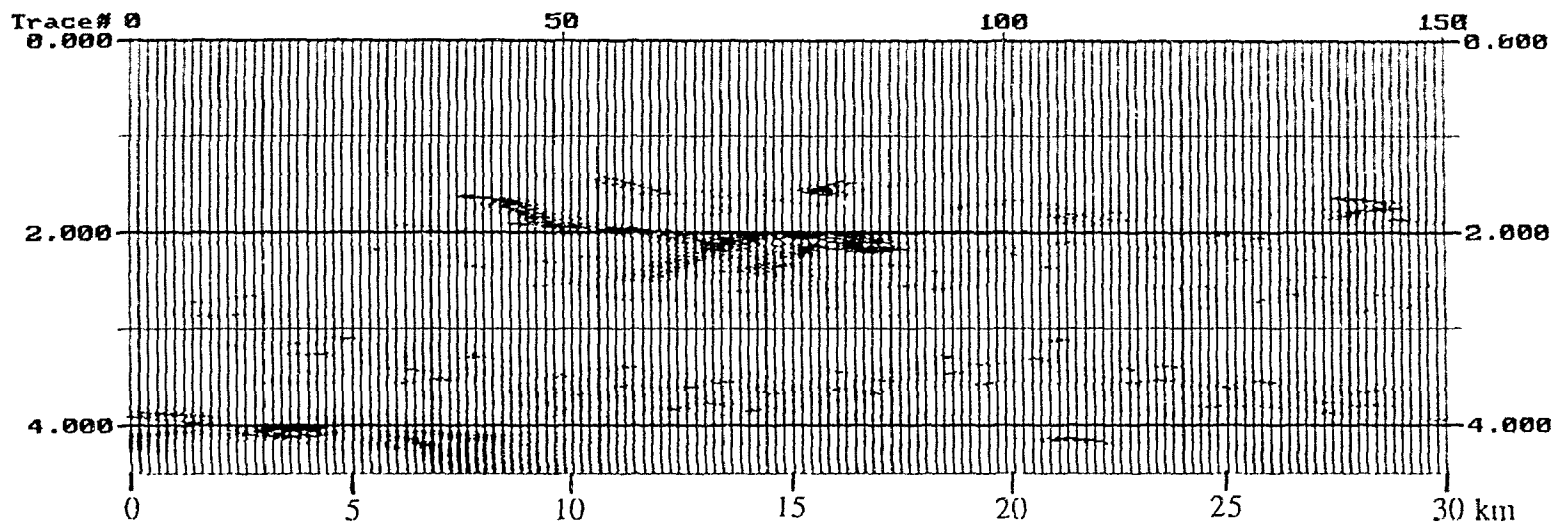


Fig. 5.17 FK-migrated synthetic reflection section for the model shown in Figure 5.13. Migration velocities are 90% of RMS velocities. Vertical scale is two-way travel time in seconds and horizontal scale at top is trace number in 200 meter intervals. First order folds can be discerned; second order fold axes marked by discontinuous reflections at peaks and troughs.

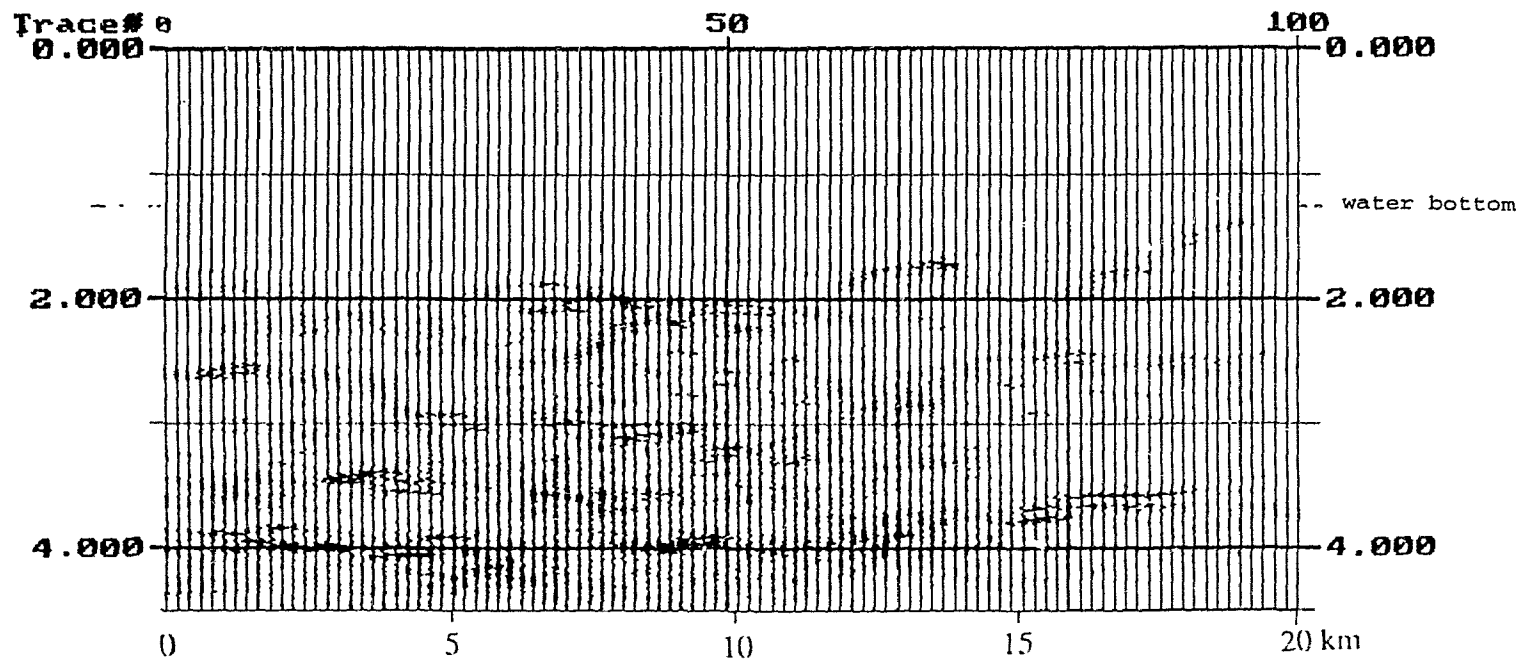


Fig. 5.18 FK-migrated synthetic reflection section for the model shown in Figure 5.14. Migration velocities are 90% of RMS velocities. Vertical scale is two-way travel time in seconds and horizontal scale at top is trace number in 200 meter intervals. Overall structure remains obscure; reflections are discontinuous.



as folds because of aliasing and energy-shedding off steep fold limbs.

The synthetic section generated from the northern Britt model is characterized by discontinuous scattered reflections similar to those in the eastern portion of GLIMPCE profile J. Neither the first nor the second order folds can be identified with any certainty, either because of the increased rugosity of the model or because the folds are partially obscured by mafic bodies, which are more abundant in the northern model. To test the relative importance of these two factors, a simplified model (Fig. 5.19) based on the northern Britt model, but with no second-order folds, was tested for comparison with the rugose model (Figures 5.14, 5.16 and 5.18) and the actual reflection data (Figure 2.8 and 5.3). The synthetic sections generated from this model are shown in Figure 5.20 (unmigrated) and 5.21 (migrated). These sections show that although the reflections from this simplified model are more continuous than either the observed reflections on line J or the reflections generated from the northern Britt model with both first and second-order folds, continuous folded boundaries still cannot be identified. This result indicates that both rugosity and the presence of mafic bodies contribute to the discontinuous nature of the reflections in the northern Britt domain model.

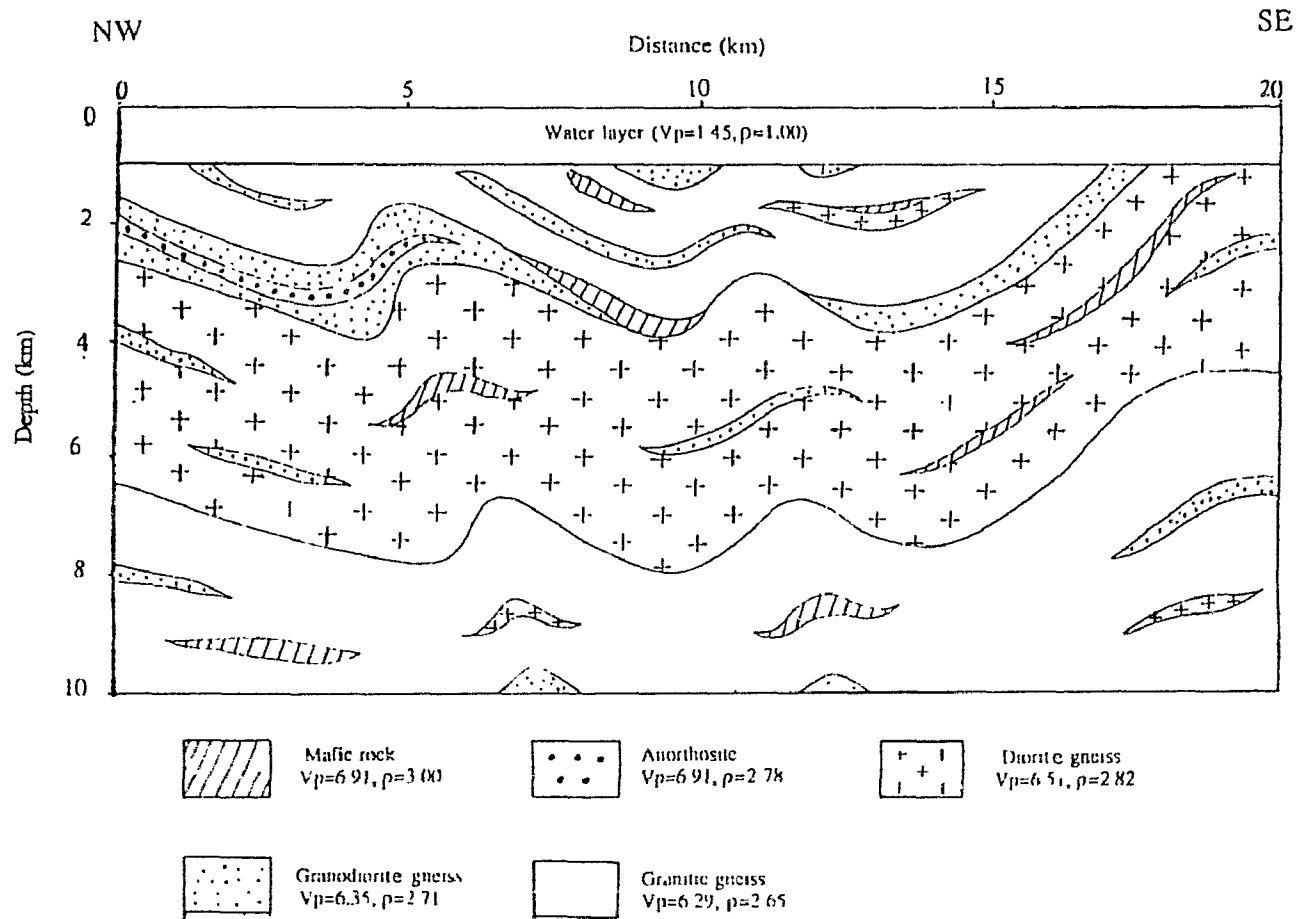


Fig. 5.19 Hypothetical model of lithologic and physical property variation in the northern Britt domain based on geology along profile B-B', but with no second order folds associated with lithologic boundaries. Compressional wave velocities in km/s; densities in  $g/cm^3$ .

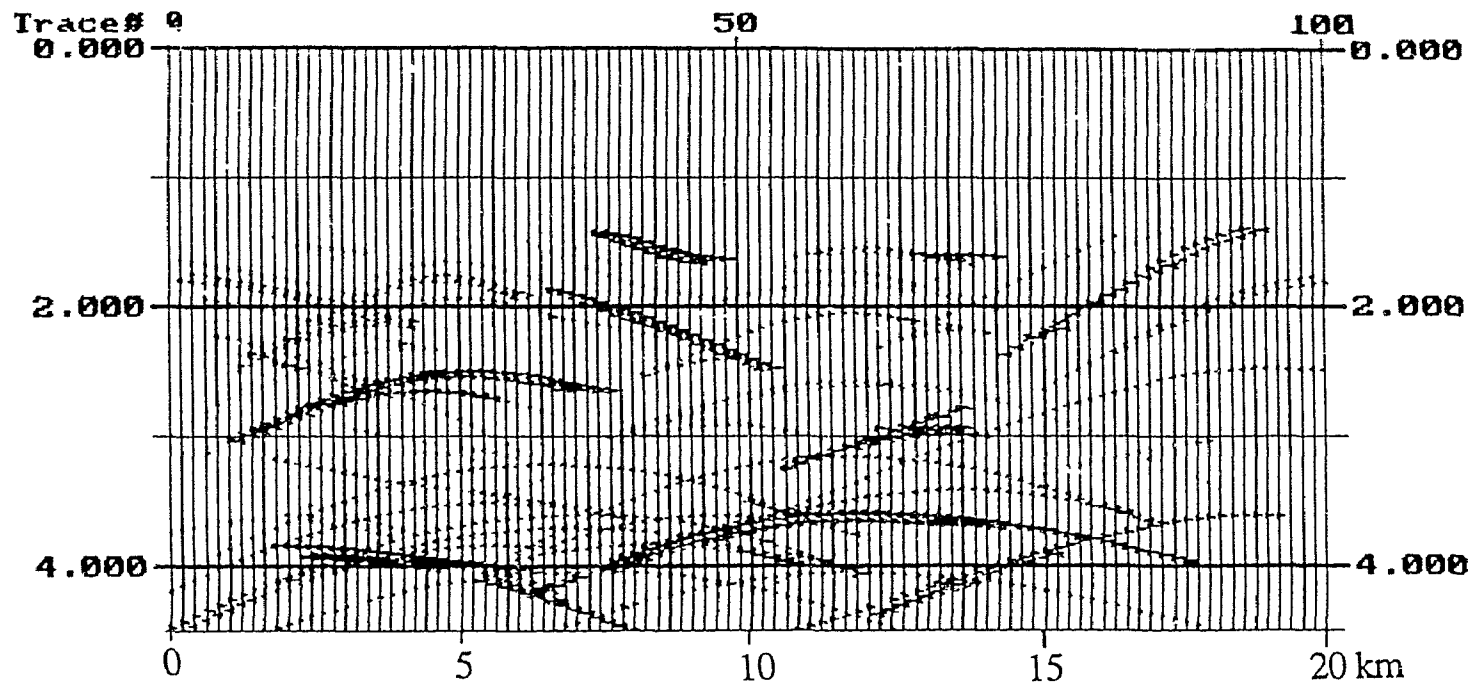


Fig. 5.20 Unmigrated synthetic reflection section for the model shown in Figure 5.19. Vertical scale is two-way travel time in seconds and horizontal scale at top is trace number in 200 meter intervals.

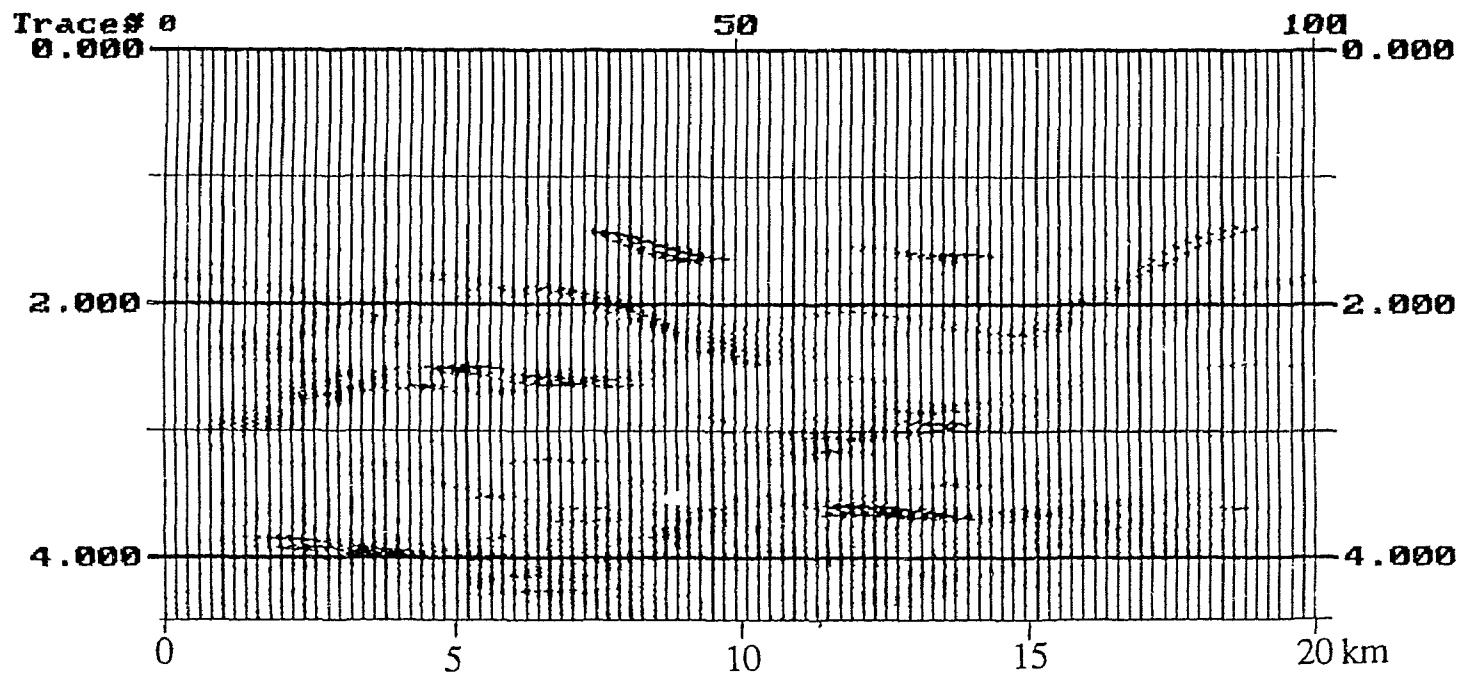


Fig. 5.21 FK-migrated synthetic reflection section for the model shown in Figure 5.19. Migration velocities are 90% of RMS velocities. Vertical scale is two-way travel time in seconds and horizontal scale at top is trace number in 200 meter intervals. Reflections are much more continuous than in Figure 5.18 and input model can be loosely discerned from reflections.

### *Discussion*

It is clear that an interpretation based on the synthetic data alone would not correctly represent the input model geometry. In particular, the continuous folded boundaries (reflection coefficient = 0.05) in the northern Britt model lose their continuity completely, even for migrated sections. The similarity of profile J to the synthetic reflection profile for the northern Britt model suggests that the lithology and structure under profile J throughout most of the Britt domain may resemble the northern model more closely than the southern model. This would be consistent with recent interpretations of the southern Britt domain as a thin-skinned allochthon overlying the northern Britt parautochthon (Culshaw et al., in press). It is thus concluded that if continuous, gently folded boundaries are present under the Britt domain, they are probably not resolved on profile J due to the presence of second-order folds along the boundaries and/or impedance inhomogeneities above the boundaries.

### Wide-angle Reflection Character of Folded Structures

#### The Problem

As described in chapter two, refraction/ wide-angle reflection data along profile J through the Britt domain display complex "shingle-like" Pg phases (Fig. 2.9). Although

the dipping reflector geometry suggested by Mereu and others (1990) could successfully explain these arrivals, it is not a unique solution. The geological data and the results of near-vertical reflection modelling suggest an alternative interpretation.

Considering that major structures of the Britt domain are characterized by a series of folds, a generalized simple fold model (Fig. 5.22) was tested. The wavelength and amplitude of the folds, which are the key parameters in the modelling, are loosely based on the surface geologic data. The object of the modelling was not to interpret specific wide angle reflection events along profile J but to explore the cause of shingling in wide angle reflection profiles.

#### Modelling technique

The modelling package SEIS81 developed by V. Cerveny and I. Psencik was used in this work for offset reflection modelling. The package was designed for the numerical modelling of seismic wave fields in two-dimensional, laterally varying layered structures using the ray method, and it consists of five programs: Seis81, Smooth, Rayplot, Syntpl and Seisplot.

The basic computation was performed by the program Seis81, which includes approximation of interfaces and velocity distribution, two-point ray tracing, standard ray tracing, dynamic ray tracing and evaluation of amplitudes. The program Smooth was used for the preparation of a smooth

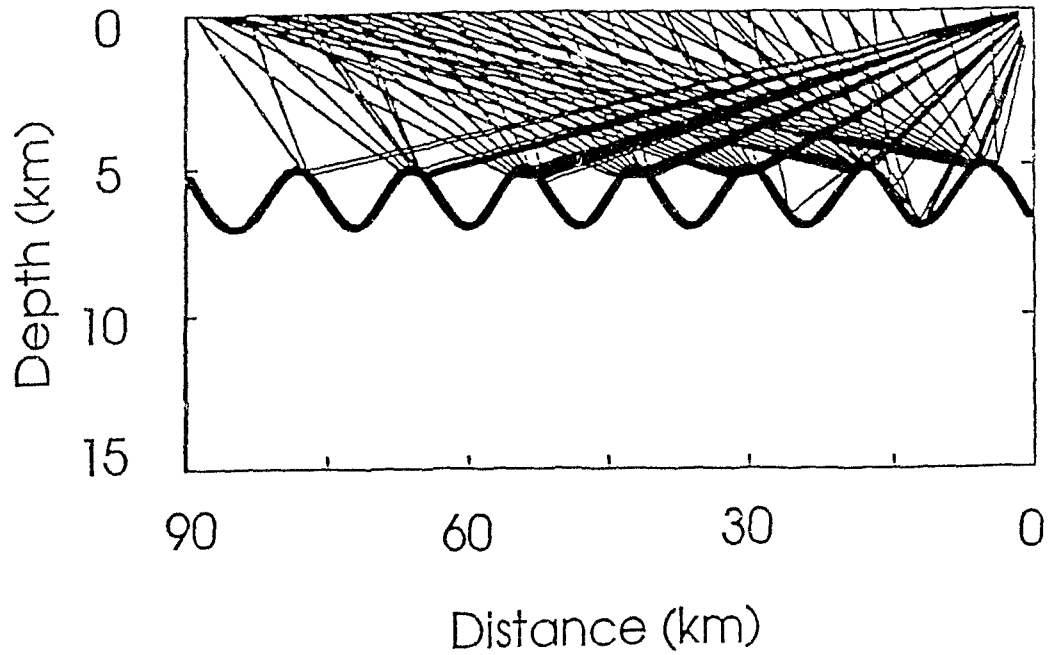


Fig. 5.22 Synthetic model used to test wide-angle reflection response of a folded structure. Compressional wave velocity and density above the boundary are 6.15 km/s and 2.65 g/cm<sup>3</sup>, and below the boundary are 6.40 km/s and 2.80 g/cm<sup>3</sup>, respectively.

velocity input file for the program Seis81. Ray diagrams, time-distance and amplitude-distance curves were produced and plotted using the program Rayplot. The program Syntpl computed synthetic seismograms from the data generated in Seis81. The output file of Syntpl contains synthetic seismograms which may be further processed and plotted using Seisplot.

### Results

The ray diagram and synthetic wide angle reflection profile generated for a line perpendicular to the fold axes are shown in Figures 5.22 and 5.23, respectively. The reduction velocity for displaying the synthetic data was 6.5 km/s. The results show clearly that "shingle-like" arrivals may be generated from a single folded boundary, because only the limbs of folds which dip toward the source reflect rays to the surface (Fig. 5.22).

The results also show that the length and dips of the shingles decrease with increasing distance. On the other hand, if the shingles resulted from a series of dipping layers due to wide-angle effects (Mereu et al., 1990), the length and slope should increase with increasing distance. This characteristic may help to identify the geometry responsible for generating a specific set of shingles. In the case of those shown on the refraction/wide-angle reflection section recorded at station 3 on profile J (Fig. 2.9), folds seem to be responsible.



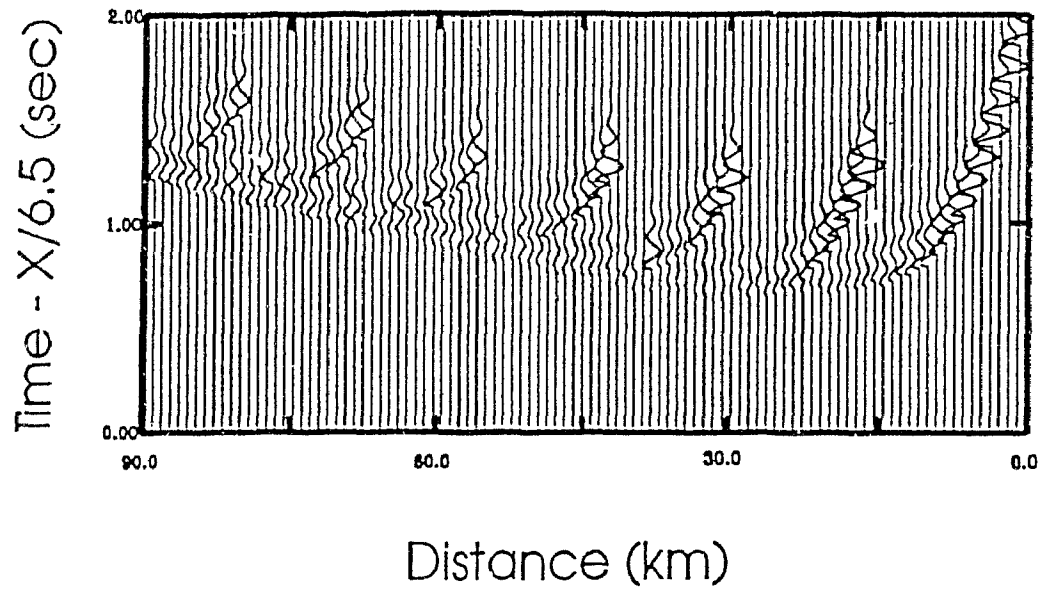


Fig. 5.23 Synthetic seismic section for the model shown in Figure 5.18 showing "shingles" corresponding to wide-angle reflections from the limbs of folds which dip toward source.

It is obvious that for folded boundaries, a reverse record section should show shingles which dip in the opposite direction, while simple dipping boundaries should not generate shingles at all. Unfortunately, this critical information is not available in the data set for profile J. Although record station 2 is located on the north-west side of the Britt domain, the east-dipping geometry and high reflectivity of the intervening Grenville Front Tectonic Zone caused poor reception of energy reflected from the Britt domain.

## Chapter 6

### CONCLUSIONS

This study has provided laboratory compressional and shear wave velocity data for various lithologies and in-situ refraction velocity information for the Britt domain in the Central Gneiss Belt, southwestern Grenville Province, a representative sample of Precambrian middle continental crust. The lithologies of the Britt domain at depth have been estimated through a comparison of laboratory and refraction data. Possible causes of the Britt domain reflectivity found along GLIMPCE profile J were evaluated based on laboratory-derived reflection coefficients and surface geology, using one-D and two-D zero-offset reflection modelling. A new interpretation of the 'shingles' observed on profile J is suggested from wide-angle reflection modelling. The results of this research are summarized below.

#### Laboratory Seismic Properties of Britt Domain Rocks

Figure 6.1 shows the average compressional wave velocity for each lithology in the Britt domain as a function of pressure, along with the time-average velocity of the Britt domain as a whole calculated from the relative abundance of each exposed lithology. In this section, the results of

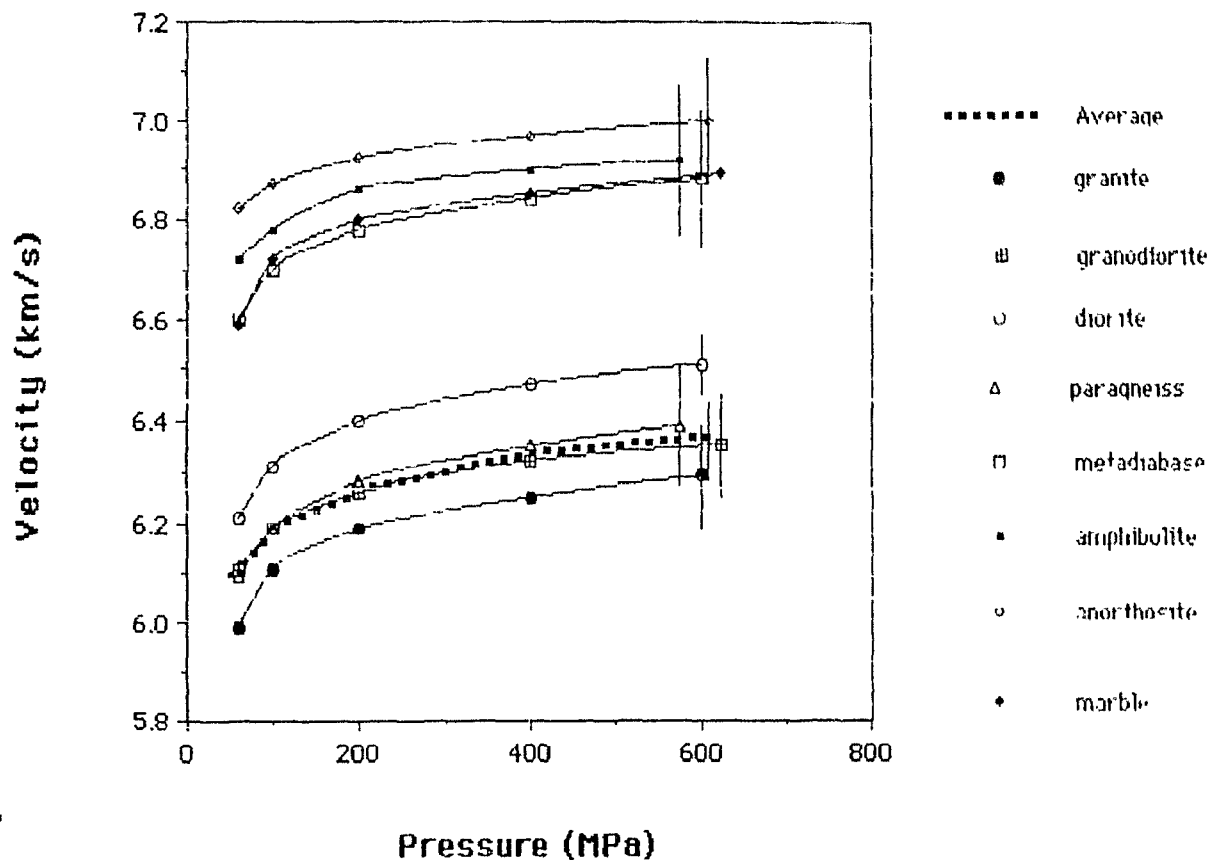


Fig. 6.1 Average P-wave velocity-pressure curves for major lithologies in the Britt Domain. Error bars show standard deviations at 600 MPa.

laboratory studies on the seismic properties of the Britt domain rocks are summarized.

#### Granitic Gneisses

The average compressional wave velocity of the granitic gneisses, the most abundant lithology in the Britt domain (~45%), is  $6.29 \pm 0.11$  at 600 MPa and the average density is  $2.65 \pm 0.04$  g/cm<sup>3</sup>. The range in velocity exhibited by these rocks is probably due to their range of quartz and feldspar contents and variations in feldspar composition. The average shear wave velocity of a representative sample is 3.62 km/s at 600 MPa, giving a Poisson's ratio of 0.25. Vp anisotropy in these rocks is generally small (1.1% on average) due to their low content of anisotropic minerals such as mica and hornblende. Some samples are fast perpendicular to foliation, probably due to quartz and feldspar alignment. The low anisotropy of the granitic gneisses, even highly strained ones, implies that significant reflections would be difficult to develop internally in this lithology.

#### Granodiorite Gneisses

The granodiorite gneisses, including tonalites, which constitute ~40% of the Britt domain, have an average compressional wave velocity of  $6.36 \pm 0.12$  km/s at 600 MPa and an average bulk density of  $2.71 \pm 0.03$  g/cm<sup>3</sup>. The average shear wave velocity of a representative sample is 3.68 km/s, giving a Poisson's ratio of 0.25. Like granitic gneiss, the

anisotropy of these rocks is also weak (2.7% on average) due to the lack of strongly anisotropic minerals.

#### Diorite Gneisses

The diorite gneiss samples (~11%) have a narrow range in modal mineralogy and, consequently, a narrow range in seismic velocity and density. The average compressional wave velocity of these rocks at 600 MPa is  $6.51 \pm 0.06$  km/s and the average density is  $2.82 \pm 0.05$  g/cm<sup>3</sup>. The mean shear wave velocity of a representative sample is 3.76 km/s, giving a Poisson's ratio of 0.25. Seismic anisotropy in these rocks is higher (4.3% on average), due to their higher content of anisotropic minerals such as mica and hornblende.

#### Paragneisses

Paragneiss samples exhibit a wide range in compressional wave velocity due to their wide range in modal mineralogy. The average  $V_p$  of these rocks is  $6.39 \pm 0.12$  km/s at 600 MPa and the average density is  $2.78 \pm 0.05$  g/cm<sup>3</sup>. Seismic anisotropy in these rocks is relatively strong (5.2% on average) due to their high biotite content. The average shear wave velocity measured for a selected paragneiss sample is 3.54 km/s with obvious splitting for different propagation and vibration directions. Because of their similar P-wave velocities, the paragneisses were included with the granodiorites for purposes of regional velocity calculation, but the two lithologies can be easily distinguished using

shear wave data and Poisson's ratios (paragneiss has a much higher  $\sigma$ ).

### Mafic Rocks

There are two distinct sub-groups of mafic rocks in the Britt domain (totalling ~4%), amphibolite and metadiabase. The amphibolite samples have an average compressional wave velocity of  $6.92 \pm 0.15$  km/s at 600 MPa and an average bulk density of  $2.97 \pm 0.08$  g/cm<sup>3</sup>. These rocks usually exhibit strong seismic anisotropy (5.9%) which depends on the hornblende content and its degree of preferred orientation. The average compressional wave velocity for the metadiabase samples at 600 MPa is  $6.88 \pm 0.14$  km/s and the average bulk density is  $3.15 \pm 0.07$  g/cm<sup>3</sup>. No significant seismic anisotropy was found for metadiabase due to the preservation of ophitic textures. Shear wave velocities averaged 3.85 km/s and 4.04 km/s for representative samples of metadiabase and amphibolite, respectively, giving Poisson's ratio values of 0.28 and 0.27.

### Other Lithologies

Other lithologies which are less abundant include anorthosite, marble and dunite. The anorthosites have an average compressional wave velocity of  $7.00 \pm 0.13$  km/s at 600 MPa and an average density of  $2.82 \pm 0.01$  g/cm<sup>3</sup>. Seismic anisotropy in these rocks is weak (2.0%) due to the lack of preferred crystal orientation. The average shear wave

velocity measured for anorthosite is 3.88 km/s at 600 MPa, giving a Poisson's ratio of 0.295. The compressional wave velocity for marble is 6.89 km/s at 600 MPa and the observed anisotropy is 7.1%. The dunite sample was isotropic with a compressional wave velocity of 8.1 km/s.

### Summary

The average seismic properties of the rocks from the Britt domain are closely related to their modal mineralogies and textures. As many researchers have noted (e.g. Kern and Schenk, 1985), the low average velocity of granitic gneisses ( $V_p = 6.29$  km/s) corresponds to a high quartz and feldspar content, while abundant modal hornblende, plagioclase, garnet and pyroxene explain the higher velocities (6.82-7.00 km/s) of the mafic rocks and anorthosites.  $V_p$  anisotropy depends largely on the modal content and alignment of mica and hornblende. Thus, amphibolite and paragneiss demonstrate strong anisotropy (5-6%) while the granitoid rocks are nearly isotropic (~1%). Similar results were reported for rocks from the GFTZ (Burke, 1991). As demonstrated by Christensen and Fountain (1975), Kern and Richter (1981) and Kern and Schenk (1985), the modal content of plagioclase is generally proportional to Poisson's ratio, but a high modal content of quartz tends to lower the value.

The time-average velocities of the Britt domain are 6.36  $\pm$  0.06 km/s for  $V_p$  and 3.68 km/s for  $V_s$ , giving a Poisson's ratio of 0.25. These properties are consistent with a bulk



composition of granodiorite near the surface. The average  $V_p$  anisotropy is weak (2.0% at 600 MPa). Since the regional foliation is nearly horizontal or shallow-dipping, the crust will be weakly anisotropic, with  $V_p$  fast in the horizontal direction.

Impedance contrasts which are likely to make significant reflections lie between (1) mafic rocks (including anorthosite) and granitic-granodiorite gneiss ( $R=0.08-0.11$  at 600 MPa) and (2) intermediate gneiss and all other lithologies ( $R=0.05-0.07$ ) except granodiorite gneiss, paragneiss and marble ( $R=0.01-0.03$ ).

#### Results from 1992 Abitibi-Grenville Refraction Experiment

The primary results from the 1992 Abitibi-Grenville refraction line AB, summarized in Figure 6.2, include:

(1) Below the surface layer, which is estimated to be only 300 meters thick, the Britt domain has a uniform velocity structure to a depth of ~ 15 km with a compressional wave velocity of 6.15 km/s and a shear wave velocity of 3.55 km/s near the surface and linear vertical velocity gradients of  $0.02\text{s}^{-1}$  and  $0.01\text{s}^{-1}$ , respectively.

(2) The upper crust in the Superior province has slightly lower velocities ( $V_p=6.05$  km/s,  $V_s=3.45$  km/s) than the upper crust of the Britt domain. At 15 km depth, the compressional and shear wave velocities in both provinces increase fairly abruptly to 6.55 and 3.75 km/s, respectively.

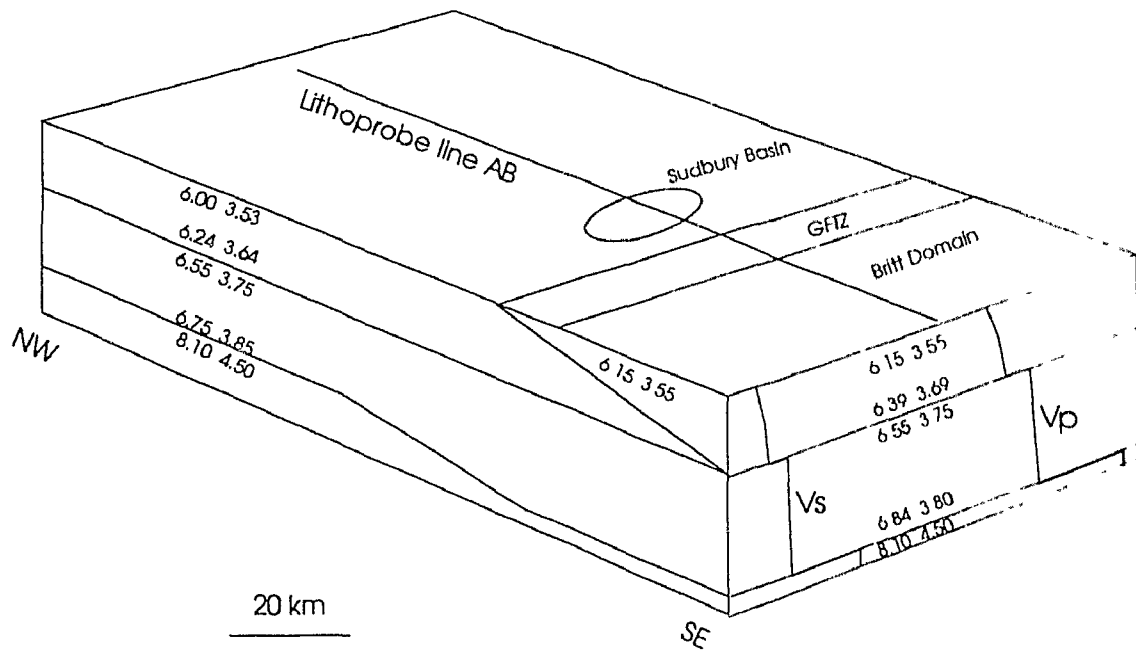


Fig. 6.2 Schematic diagram showing velocity structure beneath Abitibi-Grenville line AB.

(3) A high velocity block with a compressional wave velocity of 6.4 km/s near the surface is found immediately south of the Grenville Front Tectonic Zone in the Britt domain where it coincides with a pronounced gravity high.

(4) The Sudbury Basin shows slightly lower velocities than the surrounding gneisses, in agreement with laboratory data (Salisbury et al., 1992).

(5) The Grenville Front Tectonic Zone exhibits pronounced seismic anisotropy at shallow depths (< 8 km), with Vp fast down and to the south, indicating south-dipping foliation, in agreement with surface geology and reflection data.

(6) The Moho is much deeper beneath the Britt domain (44 km) than beneath the Superior province (34 km), in accord with results from profile J.

Comparison of the refraction and laboratory data shows that:

(1) An excellent fit exists between laboratory and refraction data below 3 km where the intrinsic properties of rocks control refraction velocities. The misfit within the upper 3 km can be easily explained by surface effects.

(2) Although slight variations in lithology exist, the principal lithology exposed in the Britt domain is granodiorite gneiss. While other interpretations are possible, the simplest interpretation of the fit between laboratory and refraction data is that granodiorites are representative of

the entire upper crust of the Britt domain above the Grenville Front Tectonic Zone. The laboratory-derived Poisson's ratio value for granodiorites from the Britt domain (0.25) also fits that from the refraction experiment (0.25) quite well. The value for paragneiss does not.

(3) The lower crust beneath the Grenville Front Tectonic Zone in the central Britt domain, which actually belongs to the Superior province, appears to be composed of diorite at the top but becomes increasingly mafic toward the Moho.

(4) The refraction structure is consistent with crustal-scale thrusting to the NW as imaged to the south on profile J.

## Synthetic Reflection Modelling and Data Interpretation

### Reflectivity

#### *Thin Mafic Layers*

As noted above, the strongest impedance contrasts in the Britt domain are between felsic to intermediate rocks and mafic rocks, with the latter residing mostly in thin dikes. The reflectivity of the thin mafic layers in the Britt domain was tested through one-dimensional reflection modelling. At the same time, a theoretical analysis of the reflectivity of thin layer clusters as a function of layer thickness and spacing was also made and the results are summarized as equation 5.1. Both real data modelling and theoretical results suggest that thin mafic layers in the Britt domain

are one of the possible causes of the observed reflections on GLIMPCE line J. However, the horizontal extent of many of these clusters is small with respect to the size of a Fresnel zone, especially at large depths. Their contribution to the observed reflectivity is therefore uncertain.

#### *Larger Scale Lithologic Contacts*

Two dimensional zero-offset synthetic reflection sections (Fig. 5.17 and 5.18) show that significant reflections are generated at the boundaries between (1) mafic rocks and all other lithologies, (2) diorite gneisses and all other lithologies, (3) anorthosites and all other lithologies and between (4) marble and granitic gneiss (in the southern Britt domain). All other lithologic contacts only generate low amplitude reflections due to their low reflection coefficients. Taking the relative abundance of individual lithologies into account, however, mafic rocks (pods or sills) are probably responsible for much of the Britt domain reflectivity, especially at greater depth. By comparing the synthetic sections with profile J, it is concluded that the lithologies under most of profile J are similar to those in the northern Britt domain, rather than the southern region, which is consistent with an allochthonous origin of the upper levels of the crust south of the Central Britt Shear Zone.

### Reflection Patterns

As shown in Figure 5.3, sub-horizontal, discontinuous and scattered reflections characterize the Britt domain reflectivity. However, surface geology shows that some high impedance lithologies have a large lateral extent and are incorporated in a series of NW-trending folds. Modelling suggests that these continuous boundaries and folded structures may not be observed on profile J because of (1) scattering by second order folds (rugosity) superimposed on the boundaries and (2) shadowing and pull-up effects caused by impedance inhomogeneities above the boundaries. The reflections from fold limbs tend to be muted, leaving peaks and troughs which merge laterally into pseudo-horizontal reflectors at depth. Another reason for the sub-horizontal characteristics of the reflections along line J is that the line cuts the folds at an angle which is oblique to the fold axes (Fig. 6.3).

### 'Shingles' on Profile J

Wide-angle reflection modelling suggests that the "shingles" observed along profile J (Mereu et al., 1990) may be caused by folded reflectors. This interpretation is also supported by surface geology, near vertical reflection data (sub-horizontal rather than dipping reflections in the Britt domain itself), the characteristics of the shingles themselves (their lengths and dips decrease with increasing

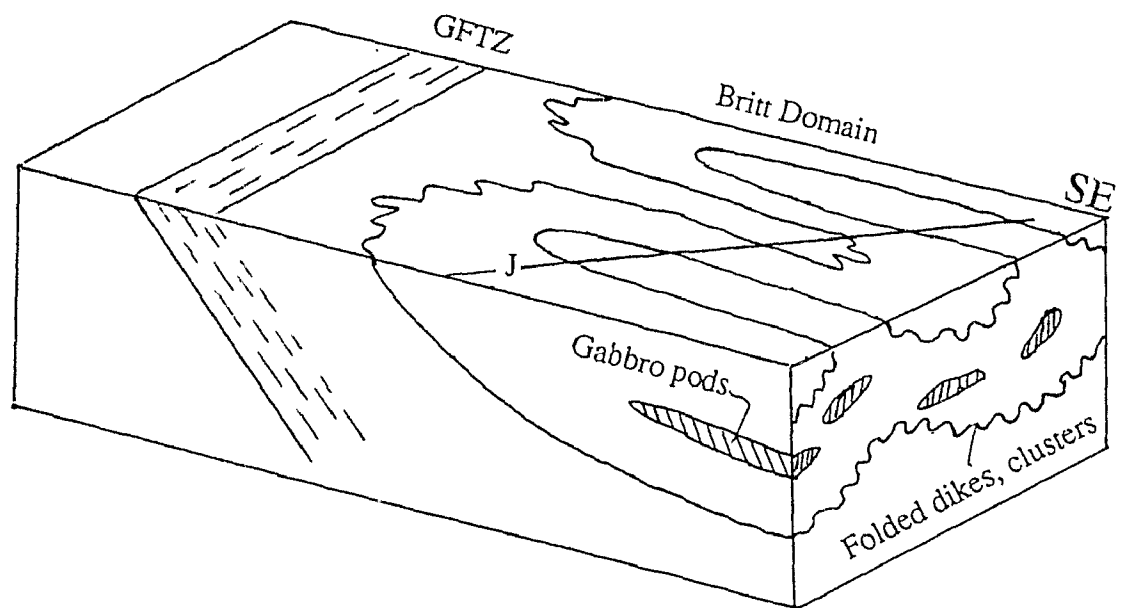


Fig. 6.3. Schematic diagram showing reflection geometry along GLIMPCE profile J.

distance from the source) and new refraction data collected along the axis of the folds (no 'shingles' are observed).

Discussion on the Nature of Seismic Reflectivity  
in the Continental Crust

As noted at the beginning of this study, various hypotheses have been proposed for the origin of deep crustal reflections, including (1) fluid layers, (2) mylonite zones and (3) lithologic layering. Mooney and Meissner (1992) argue for a multi-genetic origin for these reflections and propose that the dense, subhorizontal sets of reflections observed in the lower crust are caused by lamination of crustal materials with different seismic properties. However, as they also noted, it is difficult to attribute subhorizontal reflections under orogens to such a cause because lamination usually implies an extensional environment.

While this study supports, by extrapolation, the conclusion that lithologic layering can cause lower crustal reflectivity, simple lamination is not necessarily the sole cause of subhorizontal reflections. The modelling results presented here show that complex folded structures also make subhorizontal, discontinuous reflections, but they may be shorter and less dense than those caused by simple lamination. Interestingly, the reflections observed in shields and orogens are shorter and less dense (except in shear zones) than those observed in extensional regions



(Mooney and Meissner, 1992). Therefore seismic laminae may well be correlated with laminated lower crust in extensional regions such as rifts, but to complex folded structures beneath both ancient and modern orogens.

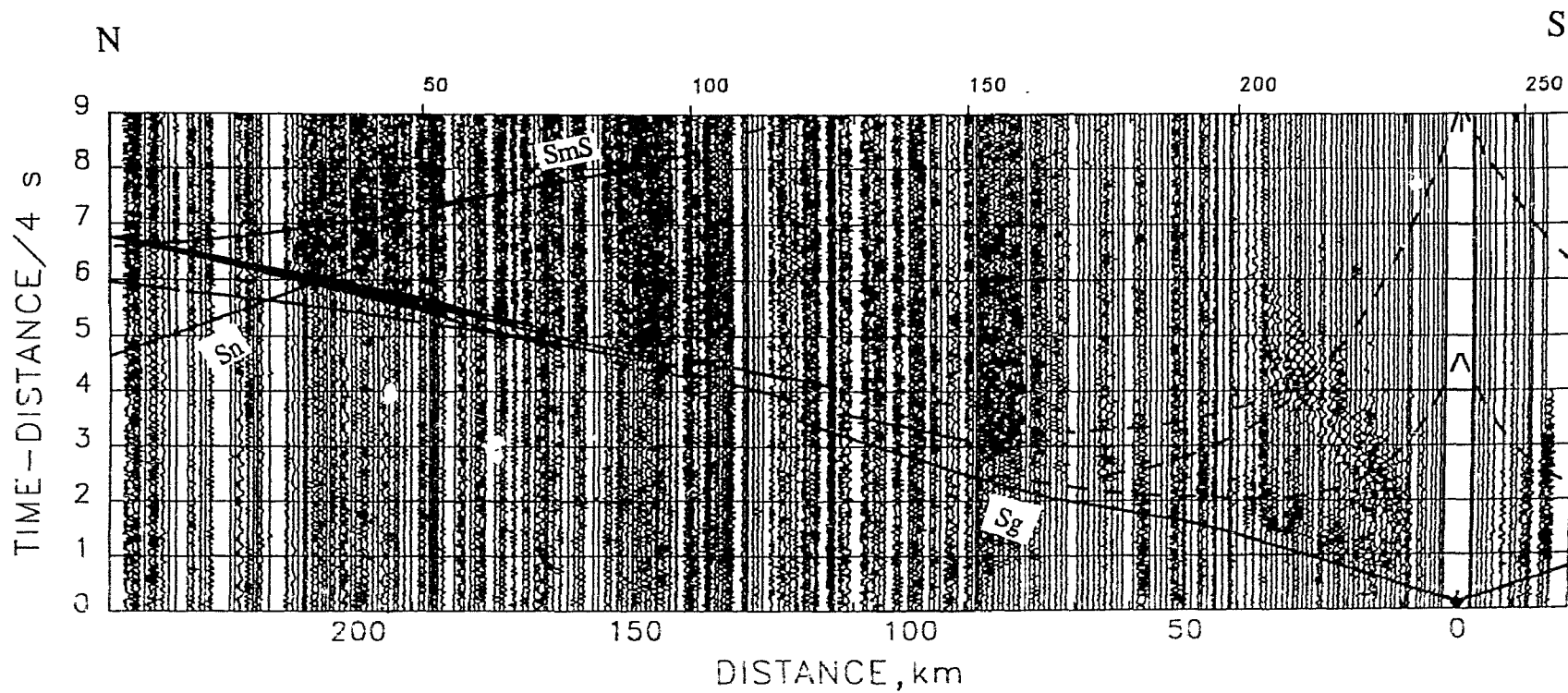
If reflective lower crust can be attributed to different types of structures, as discussed above, refraction velocities may also be different because of anisotropy, with velocities being faster in the horizontal direction in laminated lower crust than in complexly folded lower crust. According to long-wave theory (Postma, 1955; Melia and Carlson, 1984), a horizontally laminated medium will have a fairly large anisotropy which depends on the relative proportions of its constituent high and low velocity layers and their velocity contrasts, with the fast direction being horizontal or parallel to layering even if the constituent layers are isotropic. Thus, in principle, the bimodal velocity distribution of continental lower crust (Holbrook et al., 1992) does not necessarily correspond to differences in bulk composition but may be related in part to structure (note that high velocity lower crust is usually correlated with extensional environments, where laminations are expected, and low velocity lower crust with orogens) (Holbrook et al., 1992). Consequently, it can be argued that refraction velocities obtained from laminated lower crust may be biased toward the fast direction in a layered medium, and thus, should not be correlated directly with bulk composition. Even if lower crustal velocities in orogens

prove to be more representative of in situ averages, estimates of bulk composition (e.g. Holbrook et al., 1992) should be constrained both by observed reflectivity and velocity.

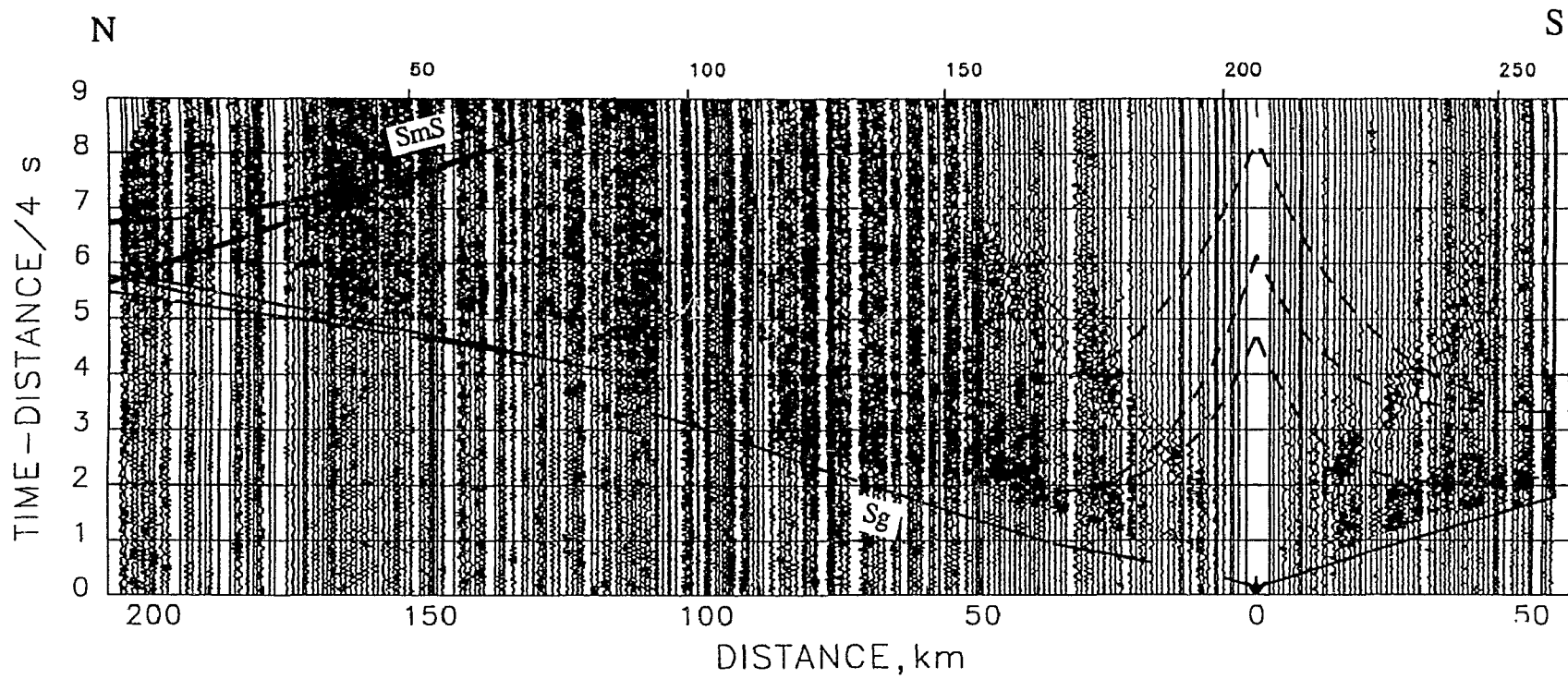
## Appendix I

Vertical component, in-line seismic sections of each shot gather along line AB, plotted at a reduction velocity of 4 km/s. A 2-12 Hz band pass filter has been applied to the data.  $V_s$  travel time curves calculated from the model in Figure 4.2 are superimposed on the sections.

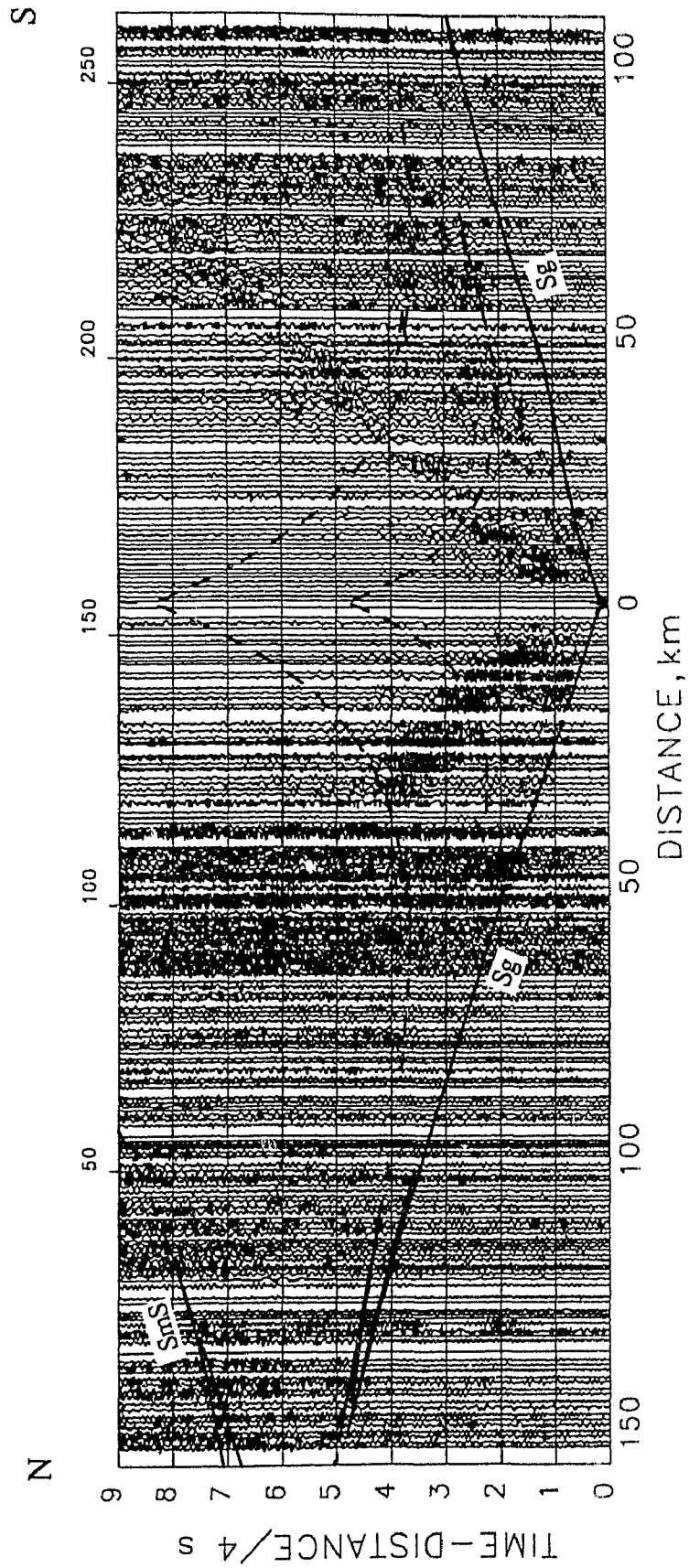
# Shot H



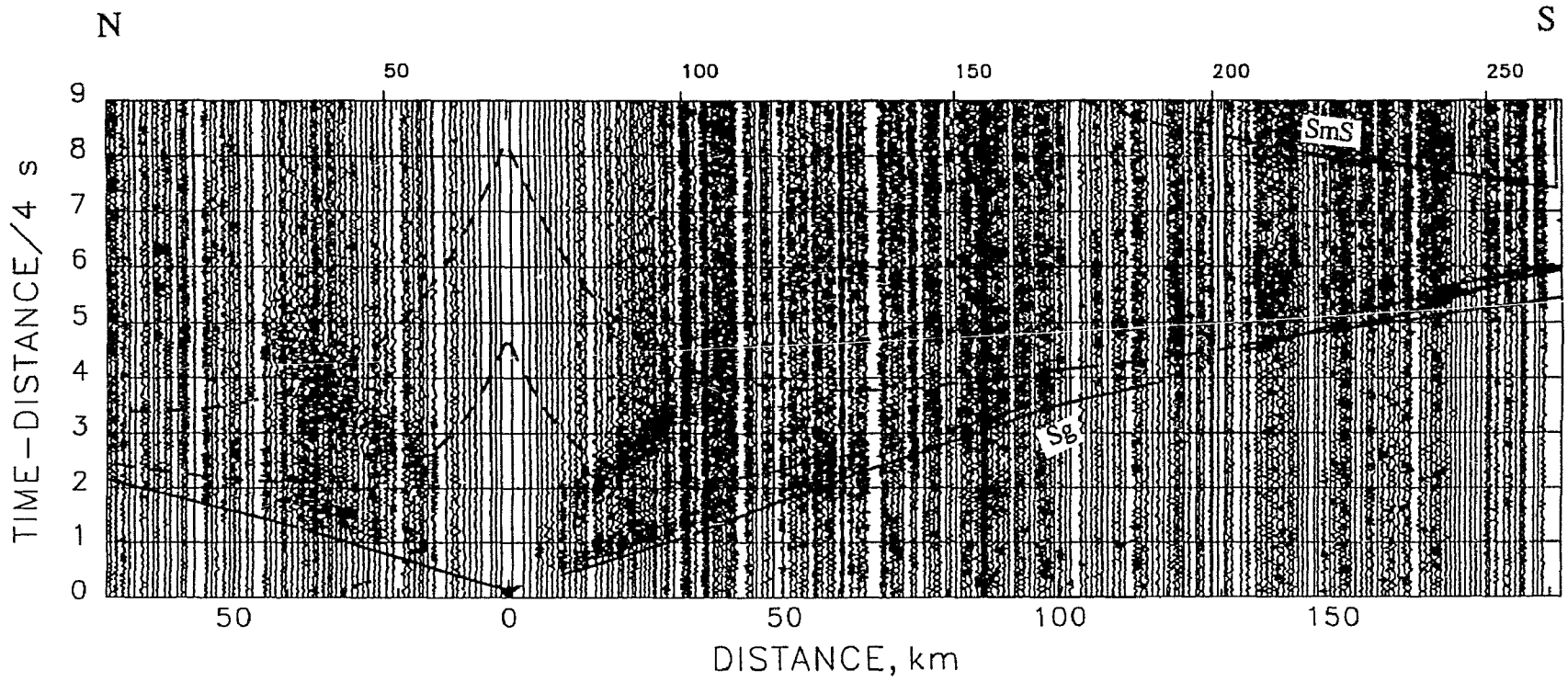
Shot Q



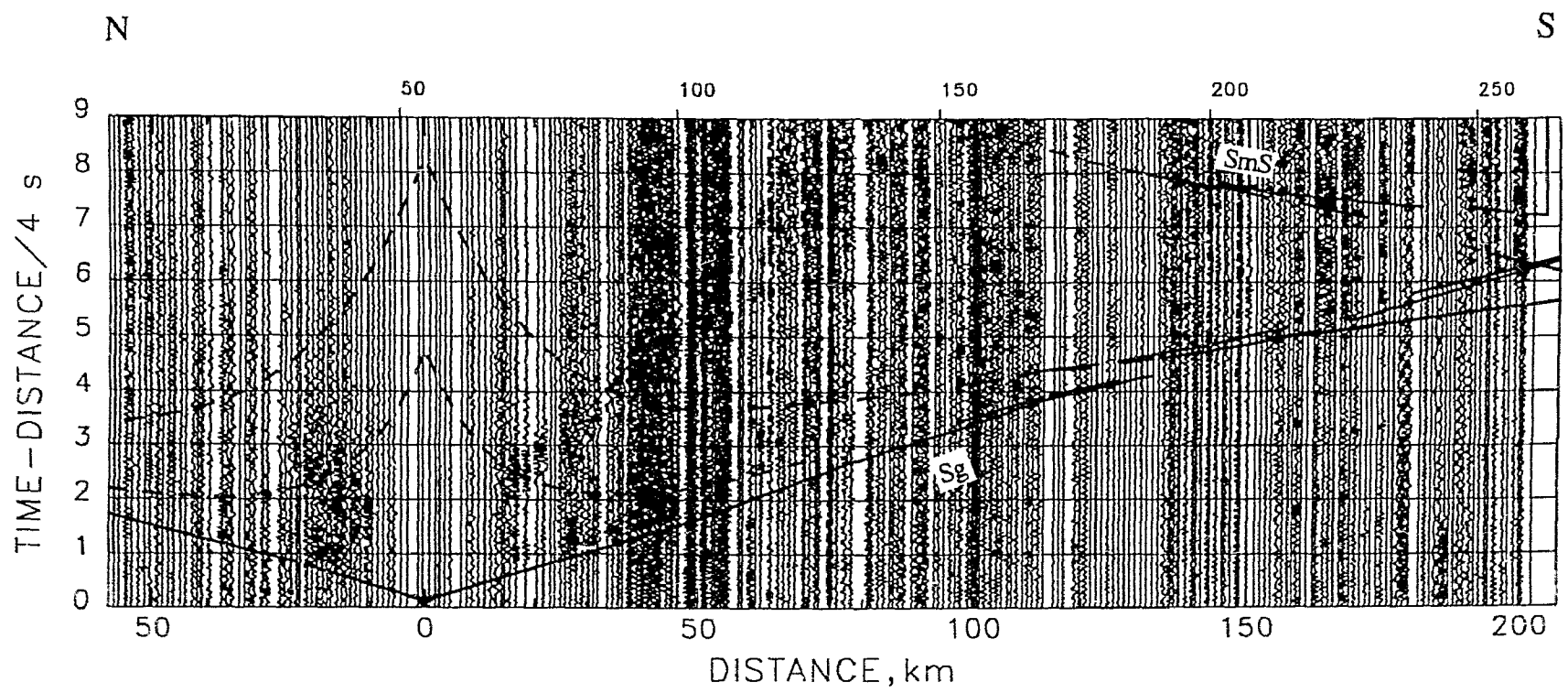
# Shot C



Shot P

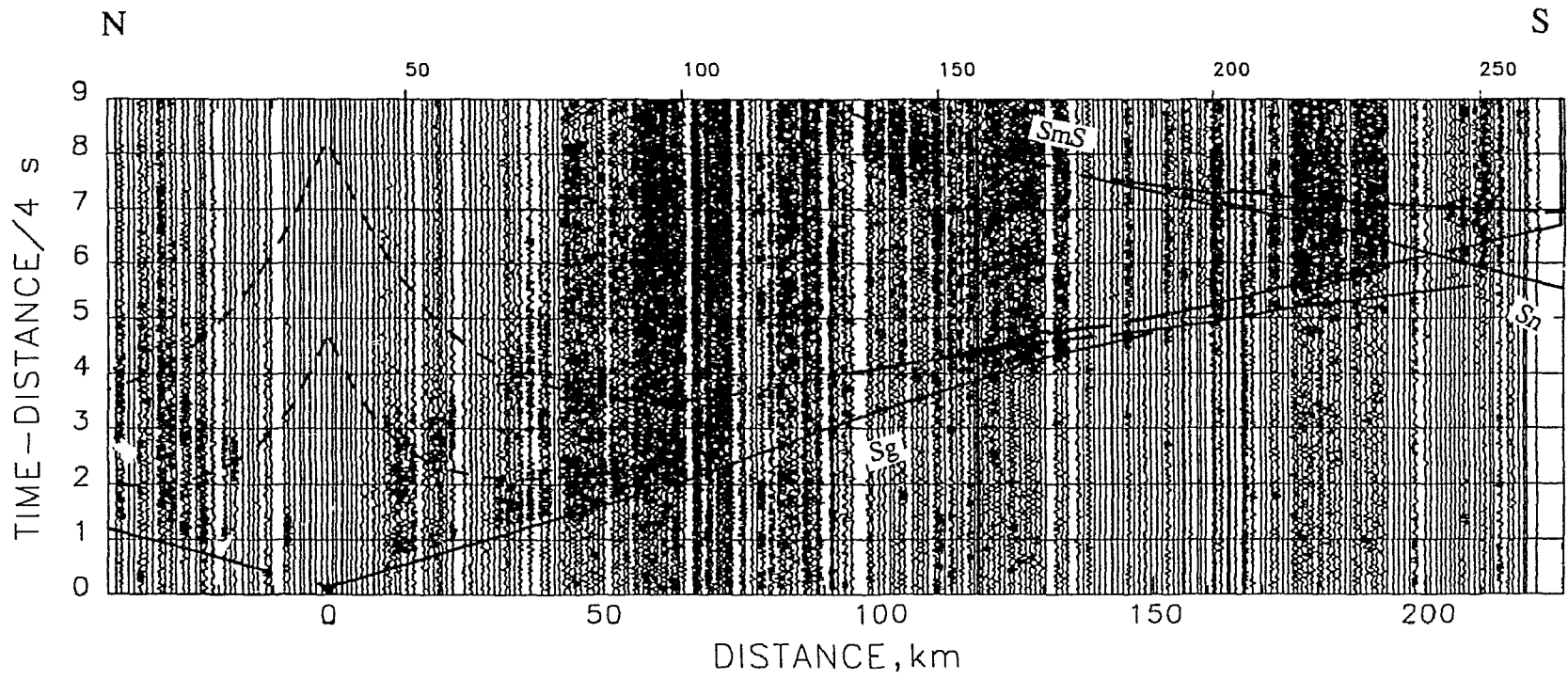


# Shot G

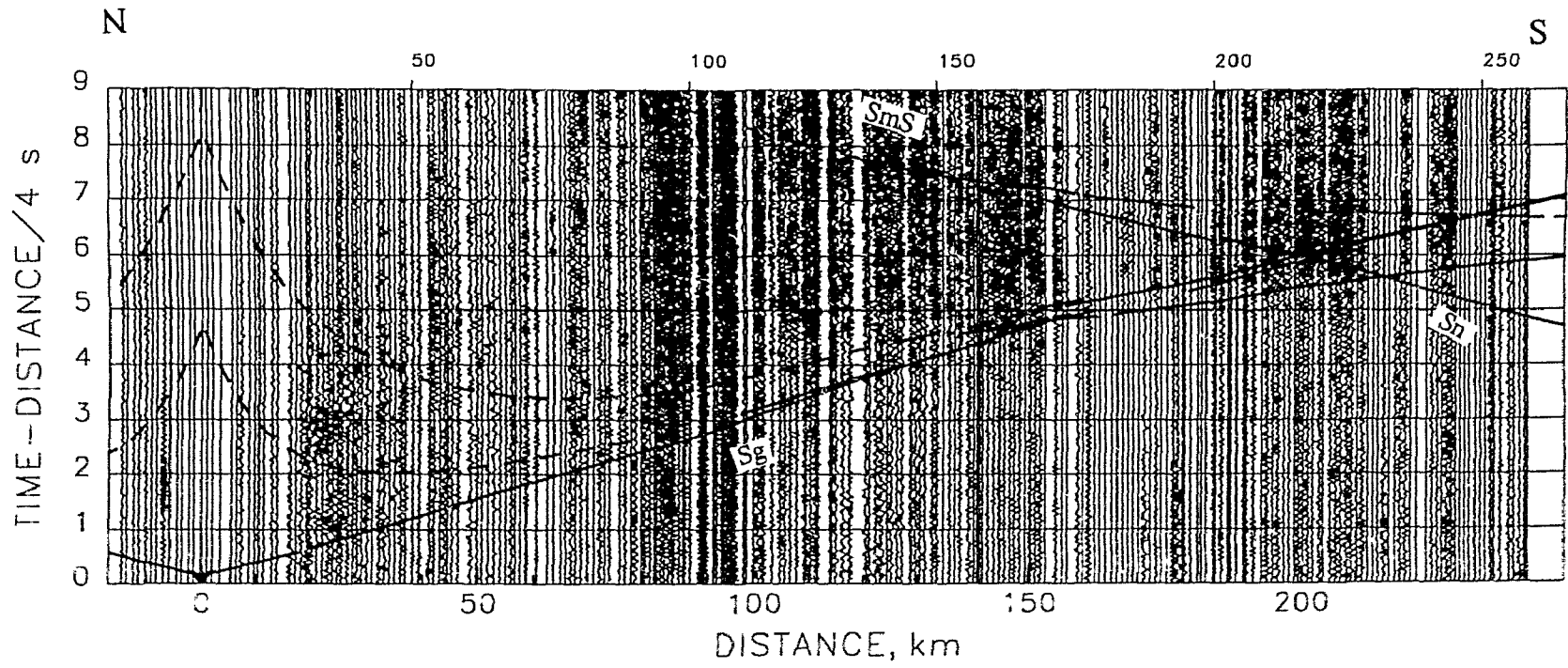




Shot A



# Shot M



## Appendix II

### Reflectivity of Regularly Spaced Thin Layers

A wavelet reflected from a single thin bed can be approximated as (Widess, 1955)

$$R = (2A \sin 2\pi b_1 / \lambda_1) \sin 2\pi / \tau \quad (A-1)$$

where  $A$  is the maximum reflection amplitude when the bed is very thick,  $b_1$  is the bed thickness,  $\tau$  is the period of the incident wavelet and  $\lambda_1$  is the wavelength. The term in brackets is approximately the maximum amplitude of the wavelet.

Now we consider the effect of a number of regularly spaced thin layers on the amplitude of the reflected wavelet. To the first order of approximation, the wavelets reflected from each thin layer are identical except for time differences. The wavelet reflected from a thin layer cluster is then,

$$R_d = \sum_{i=1}^N R_i = \sum_{k=0}^N (\hat{A} \sin 2\pi(t + k\Delta t) / \tau) \quad (A-2)$$

where  $\hat{A} = 2A \sin 2\pi b_1 / \lambda_1$ ,  $N$  is the number of layers and  $\Delta t$  is the time difference between two successive wavelets. By expanding equation (A-2), we obtain,

$$R_d = \sum_{k=0}^N (\dot{A} \sin 2\pi t/\tau \cos 2\pi k \Delta t/\tau + \dot{A} \cos 2\pi t/\tau \sin 2\pi k \Delta t/\tau)$$

$$R_d \stackrel{\omega=2\pi/\tau}{=} \dot{A} \sin \omega t \sum_{k=0}^N \cos \omega k \Delta t + \dot{A} \cos \omega t \sum_{k=0}^N \sin \omega k \Delta t$$

$$R_d = \dot{A} \sin \omega t \sin \frac{1}{2} N \omega \Delta t \cdot \frac{\cos \frac{1}{2} (N+1) \omega \Delta t}{\sin \frac{1}{2} \omega \Delta t} + \dot{A} \cos \omega t \sin \frac{1}{2} N \omega \Delta t \cdot \frac{\sin \frac{1}{2} (N+1) \omega \Delta t}{\sin \frac{1}{2} \omega \Delta t}$$

$$R_d = \frac{\dot{A} \sin \frac{1}{2} N \omega \Delta t}{\sin \frac{1}{2} \omega \Delta t} [\sin \omega t \cos \frac{1}{2} (N+1) \omega \Delta t + \cos \omega t \sin \frac{1}{2} (N+1) \omega \Delta t]$$

$$R_d = \left( \dot{A} \cdot \frac{\sin \frac{1}{2} N \omega \Delta t}{\sin \frac{1}{2} \omega \Delta t} \right) \sin [\omega t + \frac{1}{2} (N+1) \omega \Delta t] \quad (A-3)$$

The term in brackets is approximately the maximum reflection amplitude  $A_d$  and the time difference  $\Delta t$  can be calculated from

$$\Delta t = b_1/v_1 + b_2/v_2$$

where  $b_1$  and  $b_2$  are the thicknesses of the high and low velocity layers and  $v_1$  and  $v_2$ , their P-wave velocities, respectively.

Rewriting the maximum reflection amplitude we obtain,

$$A_d = 2A \sin 2\pi b_1/\lambda_1 \frac{\sin 2\pi N(b_1/\lambda_1 + b_2/\lambda_2)}{\sin 2\pi(b_1/\lambda_1 + b_2/\lambda_2)} \quad (A-4)$$

where  $\lambda_1$  and  $\lambda_2$  are the wavelengths calculated from  $v_1$  and  $v_2$ , respectively. To the first order of approximation,

$$\lambda_1 \approx \lambda_2 \approx \lambda$$

where  $\lambda$  is the wavelength of the incident wavelet. Then

equation (A-4) becomes

$$A_d = 2A \sin 2\pi b_1 / \lambda_1 \frac{\sin 2\pi N(b_1 + b_2) / \lambda}{\sin 2\pi(b_1 + b_2) / \lambda} \quad (A-5)$$

Equation (A-5) shows that the maximum reflection amplitude from a thin layer cluster is proportional to the thickness ( $b_1$ ) and the number ( $N$ ) of the high velocity layers and inversely proportional to the thickness ( $b_2$ ) of the low velocity layers, provided both high and low velocity layers are thin. For a thin layer cluster composed of  $b_1 = 1$  m,  $b_2 = 1$  m and  $N = 10$ , and an incident wavelet with a predominant frequency of 100 Hz, the maximum reflection amplitude is about 0.9 A; if  $b_2$  is increased to 1.5 m, then the amplitude is 0.56 A.

Note that transmission loss was not considered in this approximation.

Appendix III

Detailed Distribution of Mafic layers Along Key River

Thickness(m)	Lithology	Cluster
950.0	Granodiorite gneiss	
1.0	Mafic dike	
625.0	Granodiorite gneiss	
0.1	Mafic dike	
1.0	Granodiorite gneiss	
3.5	Mafic dike	
249.0	Granitic gneiss	
0.2	Mafic dike	
4.5	Granitic gneiss	
0.3	Mafic dike	
145.0	Granitic gneiss	
1.4	Mafic gneiss	
73.0	Granitic gneiss	
20.0	Mafic dike	
2.4	Granitic gneiss	
0.4	Mafic gneiss	
0.4	Granitic gneiss	
6.7	Mafic dike	
5.0	Granitic gneiss	
0.3	Mafic dike	
1.6	Granitic gneiss	
0.3	Mafic dike	
2.0	Granitic gneiss	
0.2	Mafic dike	
20.0	Granitic gneiss	
2.5	Mafic dike	
0.5	Granodiorite gneiss	
0.3	Granitic gneiss	
0.4	Mafic dike	
0.2	Granodiorite gneiss	
0.2	Granitic gneiss	
1.2	Mafic dike	
0.5	Granodiorite gneiss	
0.3	Granitic gneiss	
0.4	Mafic dike	
0.2	Granodiorite gneiss	
0.2	Granitic gneiss	
1.2	Mafic dike	
0.5	Granodiorite gneiss	
0.8	Mafic dike	
0.3	Granodiorite gneiss	
0.2	Granitic gneiss	
0.7	Mafic dike	
0.5	Granodiorite gneiss	
1.7	Mafic dike	
215.0	Granitic gneiss	



0.1	Mafic dike	II
3.2	Granitic gneiss	
1.0	Mafic dike	
7.2	Granodiorite gneiss	
2.3	Mafic dike	
0.9	Granodiorite gneiss	
0.3	Mafic dike	
0.8	Granodiorite gneiss	
3.5	Mafic dike	
8.9	Granodiorite gneiss	
0.3	Mafic dike	
15.0	Granodiorite gneiss	
0.1	Granitic gneiss	
2.5	Granodiorite gneiss	
0.1	Granitic gneiss	
2.1	Granodiorite gneiss	
0.2	Granitic gneiss	
1.0	Granodiorite gneiss	
0.1	Granitic gneiss	
0.3	Granodiorite gneiss	
0.2	Granitic gneiss	
0.3	Granodiorite gneiss	
0.4	Granitic gneiss	
0.1	Granodiorite gneiss	
0.8	Granitic gneiss	
0.2	Granodiorite gneiss	
0.7	Granitic gneiss	
0.1	Granodiorite gneiss	
1.3	Granitic gneiss	
3.2	Mafic dike	
1.1	Granitic gneiss	
0.2	Mafic dike	
0.9	Granitic gneiss	
0.3	Mafic dike	
1.5	Granitic gneiss	
0.3	Mafic dike	
3.7	Granitic gneiss	
0.1	Mafic dike	
0.9	Granitic gneiss	
3.5	Mafic dike	
115.0	Granodiorite gneiss	
0.9	Mafic dike	
120.0	Granodiorite gneiss	
0.1	Mafic dike	III
0.3	Granitic gneiss	
0.1	Mafic dike	
0.3	Granitic gneiss	
0.2	Mafic dike	
0.4	Granitic gneiss	
0.1	Mafic dike	
0.3	Granitic gneiss	
0.1	Mafic dike	
0.3	Granitic gneiss	
0.3	Granitic gneiss	

0.2	Mafic dike
1.0	Granitic gneiss
0.1	Mafic dike
0.5	Granitic gneiss
0.2	Mafic dike
0.4	Granitic gneiss
0.1	Mafic dike
0.5	Granitic gneiss
0.2	Mafic dike
0.3	Granitic gneiss
0.1	Mafic dike
0.4	Granitic gneiss
0.2	Mafic dike
0.3	Granitic gneiss
0.1	Mafic dike
0.3	Granitic gneiss
0.2	Mafic dike
0.5	Granitic gneiss
0.2	Mafic dike
0.4	Granitic gneiss
0.1	Mafic dike
2.6	Granitic gneiss
0.2	Mafic dike
0.5	Granitic gneiss
0.1	Mafic dike
0.9	Granitic gneiss
0.2	Mafic dike
0.4	Granitic gneiss
0.1	Mafic dike
0.3	Granitic gneiss
0.2	Mafic dike
0.4	Granitic gneiss
0.2	Mafic dike
5.1	Granitic gneiss
0.2	Mafic dike
0.3	Granitic gneiss
0.3	Mafic dike
4.9	Granitic gneiss
0.2	Mafic dike
1.5	Granitic gneiss
0.3	Mafic dike
2.0	Granitic gneiss
0.2	Mafic dike
1.5	Granitic gneiss
0.2	Mafic dike
2.1	Granitic gneiss
0.3	Mafic dike
1.9	Granitic gneiss
0.2	Mafic dike
1.1	Granitic gneiss
0.2	Mafic dike
105.0	Granitic gneiss
0.5	Mafic dike

III



30.0	Granitic gneiss	IV	
0.8	Mafic dike		
90.0	Granitic gneiss		
0.8	Mafic dike		
15.0	Granitic gneiss		
2.1	Mafic dike		
1.0	Granitic gneiss		
0.6	Mafic dike		
1.2	Granitic gneiss		
0.3	Mafic dike		
1.0	Granitic gneiss		
2.9	Mafic dike		
95.0	Granitic gneiss		V
0.8	Mafic dike		
1.2	Granitic gneiss		
1.2	Mafic dike		
0.5	Granitic gneiss		
0.1	Mafic dike		
0.8	Granitic gneiss		
0.4	Mafic dike		
0.7	Granitic gneiss		
0.5	Mafic dike		
0.8	Granitic gneiss		
0.9	Mafic dike		
1.5	Granitic gneiss		
0.3	Mafic dike		
0.9	Granitic gneiss		
0.5	Mafic dike		
1.2	Granitic gneiss		
1.3	Mafic dike		
0.6	Granitic gneiss		
0.1	Mafic dike		
0.7	Granitic gneiss		
0.3	Mafic dike		
1.8	Granitic gneiss		
0.5	Mafic dike		
0.3	Granitic gneiss		
0.4	Mafic dike		
1.3	Granitic gneiss		
1.0	Mafic dike		
0.8	Granitic gneiss		
0.6	Mafic dike		
0.5	Granitic gneiss		
0.3	Mafic dike		
10.2	Granitic gneiss		
0.5	Mafic dike		
1.3	Granitic gneiss		
0.8	Mafic dike		
0.3	Granitic gneiss		
0.5	Mafic dike		
1.0	Granitic gneiss		
0.7	Mafic dike		
0.8	Granitic gneiss		

0.6	Mafic dike	V
0.5	Granitic gneiss	
0.2	Mafic dike	
1.0	Granitic gneiss	
0.3	Mafic dike	
0.7	Granitic gneiss	
0.2	Mafic dike	
199.0	Granitic gneiss	
3.0	Mafic dike	
120.0	Granitic gneiss	
3.1	Mafic dike	VI
30.0	Granitic gneiss	
2.5	Mafic dike	
0.8	Granitic gneiss	
1.5	Mafic dike	
0.4	Granitic gneiss	
0.5	Mafic dike	
1.2	Granitic gneiss	
2.1	Mafic dike	
19.0	Granitic gneiss	
0.8	Mafic dike	
15.5	Granitic gneiss	
1.1	Mafic dike	
0.6	Granitic gneiss	
0.8	Mafic dike	
0.3	Granitic gneiss	
0.9	Mafic dike	
0.7	Granitic gneiss	
2.1	Mafic dike	
1.5	Granitic gneiss	
0.8	Mafic dike	
0.4	Granitic gneiss	
1.9	Mafic dike	
20.0	Granitic gneiss	
0.5	Mafic dike	
12.8	Granitic gneiss	
0.4	Mafic dike	
5.0	Granitic gneiss	
4.5	Mafic dike	
2.5	Granitic gneiss	
1.7	Mafic dike	
3.5	Granitic gneiss	
2.2	Mafic dike	
5.1	Granitic gneiss	
0.2	Mafic dike	
2.1	Granitic gneiss	
0.1	Mafic dike	
3.0	Granitic gneiss	
0.2	Mafic dike	
0.8	Granitic gneiss	
1.2	Mafic dike	
2.2	Granitic gneiss	
2.5	Mafic dike	

2.5	Granitic gneiss	VII
0.1	Mafic dike	
2.2	Granitic gneiss	
0.2	Mafic dike	
1.8	Granitic gneiss	
0.1	Mafic dike	
3.1	Granitic gneiss	
0.2	Mafic dike	
4.0	Granitic gneiss	
0.2	Mafic dike	
16.5	Granitic gneiss	
3.6	Mafic dike	
59.0	Granitic gneiss	
0.5	Mafic dike	
3.0	Granitic gneiss	VIII
0.3	Mafic dike	
2.2	Granitic gneiss	
0.3	Mafic dike	
2.5	Granitic gneiss	
0.2	Mafic dike	
0.8	Granitic gneiss	
0.3	Mafic dike	
0.5	Granitic gneiss	
0.2	Mafic dike	
4.2	Granitic gneiss	
3.6	Mafic dike	
5.4	Granitic gneiss	
2.5	Mafic dike	
4.5	Granitic gneiss	
1.5	Mafic dike	
2.7	Granitic gneiss	
2.5	Mafic dike	
5.5	Granitic gneiss	
1.8	Mafic dike	
4.9	Granitic gneiss	
5.4	Mafic dike	
6.6	Granitic gneiss	
3.8	Mafic dike	
9.2	Granitic gneiss	
3.1	Mafic dike	
5.8	Granitic gneiss	
2.5	Mafic dike	
3.9	Granitic gneiss	
1.6	Mafic dike	
4.2	Granitic gneiss	
2.5	Mafic dike	
3.8	Garnitic gneiss	
1.1	Mafic dike	
7.2	Granitic gneiss	
2.3	Mafic dike	
4.4	Granitic gneiss	
0.8	Mafic dike	
3.5	Granitic gneiss	

2.6	Mafic dike
1.9	Granitic gneiss
1.4	Mafic dike
5.6	Granitic gneiss
2.8	Mafic dike
4.7	Granitic gneiss
1.5	Mafic gneiss
3.6	Granitic gneiss
2.3	Mafic dike
4.1	Granitic gneiss
3.1	Mafic dike
750.0	Granitic gneiss
870.0	Granodiorite gneiss
1.1	Mafic dike
180.0	Granodiorite gneiss
0.8	Mafic dike
150.0	Granodiorite gneiss
1.2	Mafic dike
305.0	Granodiorite gneiss
375.0	Granitic gneiss
380.0	Granodiorite gneiss
205.0	Granitic gneiss
0.1	Mafic dike
20.0	Granitic gneiss
0.1	Mafic dike
5.5	Granitic gneiss
0.1	Mafic dike
6.4	Granitic gneiss
0.1	Mafic dike
8.5	Granitic gneiss
0.1	Mafic dike
255.0	Granitic gneiss
950.0	Granodiorite gneiss
20.0	Mafic dike
600.0	Granitic gneiss
1.0	Mafic dike
300.0	Granitic gneiss
20.0	Mafic dike
50.0	Granitic gneiss
3.5	Mafic dike
200.0	Granitic gneiss
1.5	Mafic dike
250.0	Granitic gneiss
1.0	Mafic dike
205.0	Granitic gneiss
1.0	Mafic dike
1500.0	Granitic gneiss

VIII

### References

- Alexandrov, K.S. and T.V.Ryzhova, 1961a, Elastic properties of rock forming minerals, 1, Pyroxenes and amphibolites, Bull. Acad. Sci. USSR Geophys. Ser., 9, 1165-1168.
- Alexandrov, K.S. and T.V.Ryzhova, 1961b, Elastic properties of rock forming minerals, 2, layered silicates, Bull. Acad. Sci. USSR Geophys. Ser., 11, 871-875.
- Alexandrov, K.S. and T.V.Ryzhova, 1962, Elastic properties of rock forming minerals, 3, feldspars, Bull. Acad. Sci. USSR Geophys. Ser., 2, 129-131.
- Allmendinger, R.W., K.D.Nelson, C.J.Potter, M.Barazangi, L.D.Brown and J.E.Oliver, 1987, Deep seismic reflection characteristics of the continental crust, Geology, 15, 289-386.
- Anovitz, L.M. and E.J.Essene, 1990, Themobarometry and pressure-temperature paths in the Grenville Province of Ontario, J. Petrology, 31, 197-241.
- Asudeh, I., F.Anderson, J.Parmelee, S.Vishnubhatla, P.Munro and J.Thomas, 1992, A Portable Refraction Seismograph PRS1., Geological Survey of Canada, Open File Report 2478, 47 pp.
- Asudeh, I., C.Spencer, and R. Wetmiller, in press, Litho SEIS User Manual, Geological Survey of Canada, Open File Report.
- Baer, A.J., 1981, A Grenville model of Proterozoic plate tectonics, in Precambrian Plate Tectonics, ed. by A. Kroner, Elsevier, New York, 351-385.
- Behrendt, J.C., A.G.Green, W.F.Cannon, D.R.Hutchinson, M.W.Lee, B.Milkereit, W.F.Agena and C.Spencer, 1988, Crustal structure of the midcontinental rift system: Results from GLIMPCE deep seismic reflection profiles, Geology, 16, 81-85.
- Bethune, K.M., A.Davidson and F.O.Dudas, 1990, Structure and metamorphism of the Sudbury dykes: Constraints on tectonic evolution of the Grenville Front south of Sudbury, Ontario, Geological Association of Canada/ Mineralogical Association of Canada Joint Annual Meeting, Program with abstracts, vol. 15, A10.

- Birch, F., 1960, The velocity of compressional waves in rocks to 10 kilobars, part 1, *J. Geophys. Res.*, **66**, 2199-2224.
- Birch, F., 1961, The velocity of compressional waves in rocks to 10 kilobars, part 2, *J. Geophys. Res.*, **65**, 1083-1102.
- Brace, W., 1965, Some new measurements of linear compressibility of rocks, *J. Geophys. Res.*, **70**, 319-398.
- Burke, M., 1991, Reflectivity of highly deformed terranes based on laboratory and in situ velocity measurements from the Grenville Front Tectonic Zone, Central Ontario, Canada, Ph.D thesis, Dalhousie Univ., 238 pp.
- Christensen, N.I., 1965, Compressional wave velocities in metamorphic rocks to 10 kilobars, *J. Geophys. Res.*, **70**, 6147-6164.
- Christensen, N.I., 1979, Compressional wave velocities in rocks at high temperatures and pressures, critical thermal gradients and crustal low-velocity zones, *J. Geophys. Res.* **84**, 6849-6857.
- Christensen, N.I., 1989, Reflectivity and seismic properties of the deep continental crust, *J. Geophys. Res.* **94**, 17795-17804.
- Christensen, N.I., 1989, Pore pressure, seismic velocities and crustal structure, in Geophysical Framework of the United States, GSA. Mem., vol.172, ed. by L.C.Pakiser and W.D. Mooney, 783-798.
- Christensen, N.I. and D.M.Fountain, 1975, Constitution of the lower continental crust based on experimental studies of seismic velocities in granulite, *Geol. Soc. Am. Bull.*, **86**, 227-236.
- Christensen, N.I. and G.Shaw, 1970, Elasticity of mafic rocks from the mid-Atlantic Ridge, *Geophys. J.*, **20**, 271-284.
- Christensen, N.I. and D.Szymanski, 1988, Origin of reflections from the Brevard Fault Zone, *Geophys. J.*, **20**, 271-284.
- Corrigan, D., 1990, Geology and U-Pb geochronology of the Key Harbour area, Britt Domain, Southwest Grenville Province, MSc. Thesis, Dalhousie Univ., Halifax, 165pp.

- Corrigan, D., N.G.Culshaw and J.K.Mortensen, in press, Pre-Grenville evolution and Grenvillian overprinting of the Parautochthonous Belt in the Key Harbour area, Ontario: U-Pb and structural constraints, *Can. J. Earth Sci.*
- Corriveau, L., 1990, Proterozoic subduction and terrane amalgamation in the southwestern Grenville Province, Canada: Evidence from ultrapotassic to shoshonitic plutonism, *Geology*, **18**, 614-617.
- Culshaw, N.G., G.Check, D.Corrigan, J.Drage, R.Gover, M.J.Haggart, P.Wallace and N.Wodicka, 1988, Georgian Bay Geological Synthesis: Key Harbour to Dillon, Grenville Province of Ontario, in *Current Research*, part C, Geological Survey of Canada Paper 88-1C, 129-133.
- Culshaw, N.G., G.Check, D.Corrigan, J.Drage, R.Gover, M.J.Haggart, P.Wallace and N.Wodicka, 1989, Georgian Bay geological synthesis: Dillon to Twelve Mill Bay, Grenville Province of Ontario, in *Current Research*, part C, Geological Survey of Canada Paper 89-1C, 157-163.
- Culshaw, N.G., D.Corrigan, R.A.Jamieson, J.Ketchum, P.Wallace and N.Wodicka, 1991, Traverse of the Central Gneiss Belt, Grenville Province, Georgian Bay. In: *Geological Society of Canada - Mineralogical Society of Canada - Society of Economic Geologists, Joint Annual Meeting*, Toronto, 91, Field Trip B3: Guidebook, 32 pp.
- Culshaw, N.G., A.Davidson and L.Nadeau, 1983, Structural subdivisions of the Grenville Province in the Parr Sound-Algonquin region, Ontario, in *Current Research*, part B, Geological Survey of Canada Paper 83-B, 243-252.
- Culshaw, N.I., J.Ketchum, N.Wodicka and P.Wallace, in press, Ductile extension following thrusting in the deep crust: Evidence from southern Britt Domain, southwest Grenville Province, Georgian Bay, Ontario, *Can. J. Earth Sci.*
- Culshaw, N.G., P.H.Reynolds and G.Check, 1991, A  $^{40}\text{Ar}/^{39}\text{Ar}$  study of post-tectonic cooling and uplift in the Britt domain, Grenville Province, Ontario, *Earth and Planet. Sci. Lett.*, **105**, 405-415.

- Davidson, A., 1984, Tectonic boundaries within the Grenville Province of the Canadian Shield, *J. of Geodynamics*, **1**, 433-444.
- Davidson, A., 1986, New interpretations in the southwestern Grenville Province, in The Grenville Province, ed. by J.M.Moore, A.Davidson and A.J.Baer, Geological Association of Canada Spec. Paper 31, 61-74.
- Davidson, A. and K.M.Bethune, 1988, Geology of the north shore of Georgian Bay, Grenville Province of Ontario, in *Current Research*, part C, Geological Survey of Canada Paper 88-1C, 135-144.
- Davidson, A., N.G.Culshaw and L.Nadeau, 1982, A tectonic metamorphic framework for part of the Grenville Province, Parry Sound region, Ontario, in *Current Research*, part A, Geological Survey of Canada Paper 82-1A, 175-190.
- Davidson, A. and O.van Breemen, 1988, Baddeleyite-zircon relationships in coronitic metagabbro, Grenville Province, Ontario: Implications for geochronology, *Contributions to Mineralogy and Petrology*, **100**, 291-299.
- Davidson, A., O.van Breemen and R.W.Sullivan, 1992, Circa 1.75 Ga ages for plutonic rocks from the southern Province and adjacent Grenville Province: What is the expression of the Penokean Orogeny? in *Radiogenic age and isotopic studies*, Report 6, Geological Survey of Canada Paper 92-2.
- Dewey, J.F. and K.C.A.Burke, 1973, Tibetan, Variscan, and Precambrian basement reactivation: Products of continental collision, *J. Geol.*, **81**, 683-692.
- Dobrin, M.B. and C.H.Savit, 1988, Introduction to Geophysical Prospecting, McGraw-Hill, Inc., 312 pp.
- Donaldson, J.A. and E.Irving, 1972, Grenville Front and rifting of the Canadian Shield, *Nature*, **237**, 139-140.
- Easton, R.M., in press, Mesoproterozoic evolution of the southeast margin of Laurentia, in Geology of Ontario, OGS Special Vol. 4, 1302-1313.
- Epili, D. and R.F.Mereu, 1991, The Grenville Front Tectonic Zone: Results from the 1986 Great Lakes onshore seismic wide-angle reflection and refraction experiment, *J. Geophys. Res.*, **96**, 16335-16348.



- Fountain, D.M., 1986, Implications of deep crustal evolution for seismic reflection, in Reflection Seismology: The Continental Crust, ed. by M. Baranganzi and L. Brown, AGU. Geodynamics series, **14**, 1-7.
- Fountain, D.M. and N.I. Christensen, 1989, Composition of the continental crust and upper mantle -- a review, in Geophysical Framework of the Continental United States, ed. by L.C.Pakiser and W.D.Mooney, Geol. Soc. Am., Mem., vol. **172**, 711-742.
- Fountain, D.M., D.T.McDonough and J.M.Gorbam, 1987, Seismic reflection models of continental crust based on metamorphic terranes, Geophys. J. R. Astr. Soc., **89**, 61-66.
- Fountain, D.M., M.H.Salisbury and J.Percival, 1990, Seismic structure of the continental crust based on rock velocity measurements from the Kapuskasing Uplift, J. Geophys. Res., **95**, 1167-1186.
- Gardner, G., M.Wyllie and D.Droschak, 1965, Hysteresis in the velocity-pressure characteristics of rocks, Geophys., **30**, 111-134.
- GLIMPCE seismic refraction working group, 1989, GLIMPCE seismic experiments: Long-offset recordings, EOS. Trans. AGU, **70**, 841, 852-853.
- Green, A.G., M.F.Cannon, B.Milkreit, D.R.Hutchinson, A.Davidson, J.C.Behrendt, C.Spencer, M.W.Lee, P.Morel-a-l' Hussier and W.F.Agena, 1989, A GLIMPCE of the deep crust beneath the Great Lakes, in Properties and Processes of Earth's Crust, ed. by R.F.Mereu, S.Muller and D.M.Fountain, AGU., 65-80.
- Green, A.G., B.Milkereit, J.Percival, A.Davidson, R.Parrish, F.Cook, W.Geis, W.F.Cannon, D.Hutchinson, G.West and R.Clowes, 1990, Origin of deep crustal reflections: seismic profiling across high grade metamorphic terranes in Canada, Tectonophys., **173**, 627-638.
- Green, A. G., B.Milkereit, A.Davidson, C.Spencer, D.R.Hutchinson, W.F.Cannon, M.W.Lee, W.F.Agena, J.C.Hehrendt and W.J.Hinze, 1988, Crustal structure of the Grenville Front and adjacent terranes, Geol, **16**, 788-792.

- Haggart, M.J., R.A.Jamieson, P.H.Reynolds, T.E.Krogh, C.Beaumont and N.G.Culshaw, 1993, Last gasp of the Grenville orogeny - thermochronology of the Grenville Front Tectonic Zone near Killarney, Ontario, *J. Geol.*, **101**, 575-589.
- Hanmer, S.K. and A.Ciesielski, 1984, Structural reconnaissance of the northwest boundary of the Central Metasedimentary Belt, Grenville Province, Ontario, and Quebec, in *Current research, part B, Geological Survey of Canada Paper 84-1B*, 121-131.
- Heaman, L.M. and A.N.LeCheminant, in press, Paragenesis and U-Pb systematics of baddeleyite (ZrO), *Chemical Geol.*
- Holbrook, W.D., W.D.Mooney and N.I.Christensen, 1992, The seismic velocity structure of the deep continental crust, in *Continental Lower Crust*, ed. by M.D.Fountain, R.Aruculus and R.W.Kay, Elsevier, Amsterdam, 1-45.
- Irving, R. and 14 others, 1993, 1992 Lithoprobe Abitibi-Grenville seismic refraction survey: Acquisition and processing report, Open File No. 2627, Geological Survey of Canada, 24 pp.
- Jamieson, R.A., N.G.Culshaw, N.Wodicka, D.Corrigan and J.Ketchum, 1992, Timing and tectonic setting of Grenville metamorphism - constraints from a transect along Georgian Bay, Ontario, *J. Metamorphic Geol.*, **10**, 321-332.
- Jamieson, R.A., N.G.Culshaw and D.Corrigan, in press, Orogenic front to orogenic interior: I. Grenvillian structure and metamorphism near Key Harbour, Georgian Bay, Ontario, *J. metamorphic Geol.*
- Juhlin, C., 1990, Interpretation of the reflections in the Siljan Ring area based on results from the Gravberg-1 borehole, *Tectonophysics*, **173**, 345-360.
- Ketchum, J.W.F., N.G.Culshaw, R.A.Jamieson and L.M.Heaman, 1992, Structure, metamorphism, and geochronology of high grade gneiss within and adjacent to the Central Britt Shear Zone, Central Gneiss Belt, southwest Grenville Province, Geological Association of Canada / Mineralogical Association of Canada Joint Meeting, Program with Abstracts, **17**, A57.

- Ketchum, J.W.F., N.G.Culshaw, L.M.Heaman, T.E.Krogh and R.A.Jamieson, 1993, Late orogenic ductile extension in the middle Proterozoic Grenville orogen: An example from Ontario, Canada, Abstract in Late Orogenic Extension in Mountain Belts, ed. by M.Seranne and J.Malavieille, Document du BRGM France, **219**, 108-109.
- Ketchum, J.W.F., R.A.Jamieson, L.M.Heaman, N.G.Culshaw and T.E.Krogh, in press, 1.45 Ga granulites in the southwestern Grenville Province: Geologic setting, P-T conditions, and U-Pb geochronology, *Geology*.
- Kern, H. and A.Richter, 1981, Temperature derivatives of compressional and shear wave velocities in crustal and mantle rocks at 6 kbar confining pressure, *J. Geophys.*, **49**, 47-56.
- Kern, H. and V.Schenk, 1985, Elastic wave velocities in rocks from a lower crustal section in southern Calabria (Italy), *Earth Planet. Sci. Lett.*, **40**, 147-160.
- Krogh, T.E., 1971, The Grenville Front interpreted as an ancient plate boundary, in Carnegie Inst. Washington Yearbook, **70**, 239-240.
- Krogh, T.E., 1989, U-Pb systematics of zircon and titanite in metasediments and gneisses near the Grenville Front Tectonic Zone, Ontario, Geological Association of Canada/ Mineralogical Association of Canada, Program with Abstracts, vol. 14, A52.
- Krogh, T.E., F.Corfu, W.D.Davis, G.R.Dunning, L.M.Heaman, S.L.Kamo, N.Machado, J.D.Greenough and E.Nukamura, 1987, Precise U-Pb isotopic ages of diabase dykes and mafic to ultramafic rocks using trace amounts of baddeleyite and zircon, in Diabase Dyke Swarms, ed. by H.C.Halls and W.F.Fahrig, Geological Association of Canada Spec. Paper 34, 147-152.
- Linda, F.M., M.D.Thomas and A.Davidson, 1983, Geological significance of Bouguer gravity anomalies in the region of the Parry Sound Domain, Grenville Province, Ontario, in *Current Research, Part B*, Geological Survey of Canada Paper 83-1B, 261-266.
- McEachern, S.L. and O.van Breemen, 1993, Age of deformation within the Central Metasedimentary Belt boundary thrust zone, southwest Grenville Orogeny: Constraints on the collision of the Mid-Proterozoic Elzevir terrane, *Can. J. Earth Sci.* **30**, 1155-1165.

- McGrath, P.H., D.W.Halliday and B.Felix, 1988, Coastal gravity survey, Georgian Bay, Ontario, in Current Research, Part C, Geological Survey of Canada Paper 88-1c, 145-149.
- McSkimin, H. and P.Andreatch, 1962, Analysis of the pulse superposition method for measuring ultrasonic wave velocities as a function of temperature and pressure, J. Aconst. Soc. Amer., **34**, 609-673.
- Meissner, R., 1986, The Continental Crust: A Geological Approach, Academic Press, New York, 426 pp.
- Meissner, R., TH. Wever and P.Sadowiak, 1990, Reflection patterns in the Variscan mountain belts and adjacent areas: An attempt for a pattern recognition and correlation to tectonic units, Tectonophys, **173**, 361-378.
- Melia, P.J. and R.L.Carlson, 1984, An experimental test of P-wave anisotropy in stratified media, Geophysics, **49**, 374-378.
- Mereu, R.F., D.Epili and A.G.Green, et al., 1990, Pg-shingles: Preliminary results from the onshore GLIMPCE refraction experiment, Tectonophys., **173**, 617-626.
- Mereu, R.F. and Ojo, S.B., 1981, The scattering of seismic waves through a crust and upper mantle with random lateral and vertical inhomogeneities, Phys. of Earth and Planet. Int., **26**, 233-240.
- Mereu, R.F., D.Wang, O.Kuhn, D.A.Forsyth, A.G.Green, P.Morol, G.G.R.Buchbinder, D.Crossley, E.Schwarz, R.duBerger, C.Brooks and R.Clowes, 1986, The 1982 COCRUST seismic experiment across the Ottawa-Bonnechere graben and Grenville Front in Ontario and Quebec, Geophys. J. R. Astron. Soc., **84**, 491-514.
- Ministry of Northern Development and Mines of Ontario, 1991, Vertical Magnetic Gradient of Ontario, Map 2591, 1:1000000
- Mooney, W.D. and R.Meissner, 1991, Continental crustal evolution observation, EOS. Trans. AGU., **72**, 537.
- Mooney, W.D. and R.Meissner, 1992, Multi-genetic origin of crustal reflectivity: A review of seismic reflection profiling of the continental lower crust and Moho, in Continental Lower Crust, ed. by D.M.Fountain, R.Arculus and R.W.Kay, 45-79.

- Nadeau, 1990, Tectonic, thermal and magmatic evolution of the Central Gneiss Belt, Huntsville region, southwestern Grenville orogeny, Ph.D thesis, Carleton University, Ottawa, 269.
- Nockolds, S.R., 1954, Average compositions of some igneous rocks, GSA. Bull., **65**, 1007-1032.
- Poldervaart, A., 1955, Chemistry of the Earth's crust, in Crust Of the Earth, A. Poldervaart, ed., GSA. Spec. Paper **62**, 119-144.
- Postman, G.W., 1955, Wave propagation in a stratified medium, Geophysics, **20**, 780-806.
- Reid, I, 1993, Velocity structure of reflective lower crust beneath the Grand Banks of Newfoundland, J. Geophys. Res., **98**, 9845-9859.
- Reid, I. and C.E.Keen, 1990, Deep crustal structure beneath a rifted basin: Results from seismic refraction measurements across the Jeanne d'Arc Basin, offshore eastern Canada, Can. J. Earth Sci. **27**, 1462-1471.
- Ricker, N., 1953, Wavelet construction, wavelet expansion and the control of seismic resolution, Geophys., **18**, 796-792.
- Rivers, T., J.Martignole, C.F.Gower and A.Davidson, 1989, New tectonic subdivisions of the Grenville Province, southeast Canadian Shield, Tectonics, **8**, 63-84.
- Ryzhova, T.V., 1964, Elastic properties of plagioclases, Bull. Acad. Sci. USSR Geophys. Ser., **7**, 633-635.
- Sadowiak, P., 1991, Seismic reflectivity patterns: comparative investigations of Europe and North America, in Continental lithosphere: Deep Seismic Reflections, ed. by R. Meissner, AGU., Washington, D.C., 315 pp.
- Salisbury, M. and D.Fountain, in press, The seismic velocity and Poisson's ratio structure of the Kapuskasing uplift from laboratory measurements, Can. J. Earth Sci..
- Salisbury, M.H., R.Iulicucci and C.Long, in press, Velocity and reflection structure of the Sudbury structure from laboratory measurements, Geophys. Res. Lett..

- Schwerdtner, W.M., 1987, Interplay between folding and ductile shearing in the Proterozoic crust of the Muskoka-Parry Sound region, Central Ontario, *Can. J. Earth Sci.*, **24**, 1507-1525.
- Stockwell, C.H., 1964, Fourth report on structural provinces, orogenies and time-classification of rocks of the Canadian Precambrian shield, in Age Determinations and Geological Studies, Part II, Geological Survey of Canada Paper 64-17, 1-21.
- Stockwell, C.H., 1982, Proposals for time classification and correlation of Precambrian rocks and events in Canada, Geological Survey of Canada Paper 80-19, 135 pp.
- Telford, W.M., L.D. Geldart and R.E. Sheriff, 1990, *Applied Geophysics*, Cambridge Univ. Press, 770 pp.
- Van Breemen, O., A. Davidson, W.D. Loveridge and R.D. Sullivan, 1986, U-Pb zircon geochronology of Grenville tectonites, granulites and igneous precursors, Parry Sound, Ontario, in The Grenville Province, ed. by J. M. Moore, A. Davidson and A.J. Baer, Geological Association of Canada Spec. Paper 31, 191-207.
- Van Breemen, O. and A. Davidson, 1990, U-Pb zircon and baddeleyite ages from the Central Gneiss Belt, Ontario, in Radiogenic Age and Isotopic Studies, Geological Survey of Canada Paper 89-2, 85-92.
- Walsh, J.B., 1965, The effect of cracks on the compressibility of rocks, *J. Geophys. Res.*, **70**, 381-390.
- Warner, M., 1990, Basalts, water, or shear zones in the lower continental crust?, *Tectonophys.*, **173**, 163-174.
- White, D., M. Easton, N. Culshaw, B. Milkereit, D. Forsyth, S. Carr, A. Green and A. Davidson, in Press, Seismic images of the Grenville orogen in Ontario, *Can. J. Earth Sci.*.
- Widess, M.B., 1973, How thin is a thin bed? *Geophys.*, **38**, 1176-1180.
- Windley, B.F., 1986, Comparative tectonics of the western Grenville and the western Himalaya, in The Grenville Province, ed. J.M. Moore, A. Davidson and A.J. Baer, Geological Association of Canada Spec Paper 31, 341-348.

- Woussen, G., W.D.Roy, E.Dimroth and E.H.Chown, 1986, Mid-Proterozoic extensional tectonics in the core zone of the Grenville Province, in The Grenville Province, ed. by J.M.Moore, A.Davidson and A.J.Baer, Geological Association of Canada Spec. Paper 31, 297-311.
- Wynne-Edwards, H.R., 1972, The Grenville Province, in Variations in Tectonic Styles in Canada, ed. by R.A.Price and R.J.W.Douglas, Geological Survey of Canada Spec. Paper 11, 263-334.
- Wynne-Edwards, H.R., 1976, Proterozoic ensialic orogenesis: The millipede model of ductile plate tectonics, *Amer. J. Sci.*, **276**, 927-953.
- Young, G.M., 1980, The Grenville orogenic belt in the north Atlantic continents, *Earth Sci. Rev.*, **16**, 277-288.